Sensorless Control of Permanent-Magnet Synchronous Motor Drives

By

P. D. Chandana Perera

Dissertation submitted to the Faculty of Engineering & Science at Aalborg University
in partial fulfillment of the requirements for the degree of
doctor of philosophy in Electrical Engineering

INSTITUTE OF ENERGY TECHNOLOGY
AALBORG UNIVERSITY
AALBORG, DENMARK
DECEMBER 2002

Aalborg University
Institute of Energy Technology
Pontoppidanstræde 101
DK-9220 Aalborg East
Denmark.

Printed in Denmark by Arco Grafisk A/S, Skive

Second print, February 2003

ISBN 87-89179-41-2

Preface

This thesis is submitted to the Faculty of Engineering and Science at Aalborg University in partial fulfillment of the requirements for the Ph.D. degree in Electrical Engineering.

The project has been followed by three supervisors: Professor Frede Blaabjerg, Associate Professor John K. Pedersen, both from Institute of Energy Technology (IET) at Aalborg University, and External Professor Paul Thøgersen who is Manager of Control Engineering at Danfoss Drives A/S. I would like to thank all of them for their support and their response to my work during the project period.

This project has been a part of Danfoss Professor Programme at Aalborg University. I greatly appreciate the financial support given from Danfoss Professor Programme to carry out this research project.

I would like to thank Professor Thomas Jahns and Professor Robert Lorenz for their support and their discussions with me during my two month stay at University of Wisconsin in Madison. During that period, I had the opportunity to learn about carrier signal injection method for position and velocity estimation of an interior type PM synchronous machine and some other aspects related to PM synchronous machine control, which were invaluable for me.

During the project period, I had many valuable discussions with the colleagues at IET. I want to thank all of them. My thanks are also due to the laboratory staff of IET, who helped me to build the test system for this project. I am also thankful to Dariusz Swierczynski for his assistance to solve some programming problems in the test system during his stay at IET.

Finally, I would like to express my deepest gratitude to my parents and siblings for their constant support and patience.

Aalborg, November 2002

P. D. Chandana Perera

Abstract

The reduced energy consumption is highly demand in motor drives for heating, ventilating, and air conditioning (HVAC) applications. The efficiency advantage makes the permanent-magnet (PM) synchronous machine an attractive alternative to the induction machine in drives for those applications.

In order to use PM synchronous machines in HVAC applications, simple, low-cost control methods are also important for them. The particular requirement in control of PM synchronous machines is the synchronization of the AC excitation frequency with rotational speed. A shaft-mounted position sensor is required for achieving this. This shaft-mounted position sensor increases the cost and reduces the reliability in the drive system. This makes it undesirable for HVAC applications. The objective of this research project is to investigate sensorless control methods for PM synchronous machines with particular attention to HVAC application requirements.

The understanding of the machine model is a key requirement for machine control. The mathematical models for PM synchronous machines are first derived in this thesis. The control properties of PM synchronous machines are discussed and they are compared.

Since high dynamic performance is not a demand for HVAC applications, a suitable control approach for PM synchronous machines is V/f control approach. A substantial part of this thesis is devoted to investigate V/f control approach for PM synchronous machines.

In order to provide basics for designing a V/f controlled drive, the stability characteristics of PM synchronous machines under open-loop V/f control, i.e. without having any feedback for V/f control, is analyzed in this thesis. The linearized machine model is the key to analyze the stability characteristics. The stability analysis show that the PM synchronous machine becomes unstable after exceeding a certain applied frequency under open-loop V/f control.

In order to show how to stabilize the V/f controlled PM synchronous machines for a wide frequency range, a simplified small signal dynamics model for PM synchronous machines is derived in this thesis. With the help of this model it is shown that by modulating the applied frequency proportional to the perturbations in the power the stable operation of the machine can be achieved for a wide frequency range. In voltage source inverter driven drives the DC-link current perturbations can also be used for

this purpose. The implementation of both these methods are discussed in details.

For the V/f controlled drive, a method to calculate the magnitude of the voltage with vector compensation of the stator resistance voltage drop is proposed. The complete V/f controlled drive consists of this voltage calculation algorithm and a stabilizing loop, which modulates the applied frequency proportional to the perturbations in the power. Only two current sensors are required to measure the motor phase currents and no rotor position sensor is required for complete implementation of the drive. This proposed sensorless V/f controlled drive system demonstrates satisfactory performance for HVAC applications.

Besides V/f control approach, the field-oriented control approach for PM synchronous machines is also discussed in the thesis. The control structure and the design of the controllers for field-oriented controlled drive system are described. A rotor position estimation technique for sensorless operation of the field-oriented controlled drive system is studied in details. The estimator uses predictor-corrector method where the difference between the estimated current and the measured current (current error) is used to correct a predicted rotor position. The analysis show that the correction of the predicted rotor position using current errors is possible in the estimation algorithm for non-salient pole PM synchronous machines, however, there are difficulties for salient pole PM synchronous machines. For salient pole PM synchronous machines more investigations are still required for accurate rotor position estimation.

Finally, the comparison shows that the proposed sensorless V/f control approach has some promising features for HVAC applications compared to the sensorless field-oriented control approach investigated in the thesis.

Table of Contents

Nomenclature

Abbreviations

$CSFC$	Constant stator flux control
$CTAC$	Constant torque angle control
DSP	Digital signal processor
EMF	Electromotive force
FOC	Field-oriented control
HPF	High-pass filter
$HVAC$	Heating, ventilating and air conditioning
$IPMSM$	Interior magnets type permanent-magnet synchronous machine
LPF	Low-pass filter
$MTPAC$	Maximum torque per ampere control
PI	Proportional-Integral control
$PMSM$	Permanent-magnet synchronous machine with sinusoidal back-EMF and without damper windings in the rotor
PWM	Pulse width modulation
$SPMSM$	Surface magnets type permanent-magnet synchronous machine
SVM	Space vector modulation
$UPFC$	Unity power factor control
VSI	Voltage source inverter

Symbols

$\underline{a}$	Complex vector operator $e^{j\frac{2\pi}{3}}$
B_m	Viscous friction coefficient
E_m	Magnitude of the rotor permanent-magnet flux induced voltage vector in steady state

E_s	Magnitude of the stator flux linkage induced voltage vector in steady state
i_{as}, i_{bs}, i_{cs}	Instantaneous stator a,b,c phase currents
i^r_{ds}, i^r_{qs}	Instantaneous stator currents in rotor fixed d,q frame
I^r_{ds}, I^r_{qs}	Steady state stator currents in rotor fixed d,q frame
I_s	Magnitude of the stator current vector in steady state
i_{dc}	DC-link current
$\underline{i}_{abcs}$	Stator current vector in stationary reference frame
$\underline{i}^r_{qds}$	Stator current vector in rotor fixed d,q frame
J	Inertia of the motor shaft and the load system
L_d, L_q	Rotor d- and q- axis inductances
L_{ls}	Leakage inductance
L_{md}, L_{mq}	Rotor d- and q- axis magnetizing inductances
n	Pole number of the motor
p	Operator $\frac{d}{dt}$
p_e	Instantaneous power input to the motor
P_e	Steady state power input to the motor
r_s	Stator resistance per phase
s	Laplace operator
T	Sampling period
T_l	Load torque
T_e	Electromagnetic torque produced by the motor
v_{as}, v_{bs}, v_{cs}	Instantaneous stator a,b,c phase voltages
v^r_{ds}, v^r_{qs}	Instantaneous stator voltages in rotor fixed d,q frame
V^r_{ds}, V^r_{qs}	Steady state stator voltages in rotor fixed d,q frame
V_s	Magnitude of the stator voltage vector in steady state
v_{dc}	DC-link voltage
$\underline{v}_{abcs}$	Stator voltage vector in stationary reference frame
$\underline{v}^r_{qds}$	Stator voltage vector in rotor fixed d,q frame
α	Torque angle
δ	Load angle
θ_r	Electrical rotor position

$\lambda_{as}, \lambda_{bs}, \lambda_{cs}$	Stator a,b,c phase flux linkage
$\lambda^r_{ds}, \lambda^r_{qs}$	Stator flux linkage in rotor fixed d,q frame
λ_s	Magnitude of the stator flux linkage vector
$\underline{\lambda}_{abcs}$	Stator flux linkage vector in stationary reference frame
$\underline{\lambda}^r_{qds}$	Stator flux linkage vector in rotor fixed d,q frame
λ_m	Rotor permanent-magnet flux which linkages with stator
ϕ	Power factor angle
ψ	The angle between stator flux linkage vector and the rotor permanent-magnet flux vector
ω_r	Electrical rotor speed
ω_e	Electrical speed of the applied voltage vector to the machine

Subscripts

a, b, c	Stator a,b,c phases
n	Normalized quantity
s	Stator quantity
0	Steady state quantity

Superscripts

r	Rotor fixed reference frame quantity
$\star$	Complex conjugate
$*$	Reference quantity
$\hat{}$	Estimated quantity

Part I

Preliminaries

Chapter 1

Introduction

1.1 Permanent-magnet electric machines

Permanent-magnet (PM) electric machines are doubly excited electric machines, which have two sources of excitation, namely, the armature and the field. In conventional doubly excited electric machines (DC commutator machines and synchronous machines), both of these excitation sources are electric windings connected to an external source of electric energy. In PM electric machines, the field is generated by permanent-magnets eliminating the requirement of field windings and external electrical source for it.

In contrast to the conventional doubly excited electric machines, the copper loss associated with field windings does not exist in PM electric machines increasing the efficiency of the machine. Moreover, the use of permanent-magnets to generate the field allows to design these machines with less weight and compact size compared to the conventional doubly excited electric machines. On the other hand, in PM electric machines the permanent-magnets generate a constant field flux and it cannot be controlled as easy as in conventional doubly excited electric machines changing the field current.

1.1.1 Classification of PM electric machines

In general, PM electric machines can be classified as shown in figure 1.1.

Depending on the design of the machine whether it for DC or AC excitation, PM electric machines can be first classified into two groups, namely, PMDC and PMAC type. The structure of PMDC machines is very similar to the conventional DC commutator machines. The only difference is the use of permanent-magnets in the place of field windings. The commutator and the brushes still exist in these machines and they still suffer the problems associated with conventional DC commutator machines.

The PMAC machines are synchronous machines, which the field is generated by permanent-magnets located in the rotor. In these machines, the commutator and the brushes do not exist making the machine structure very simple and eliminating the

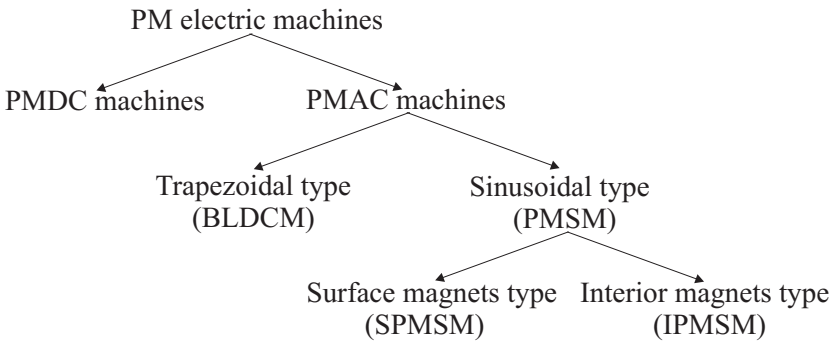

Figure 1.1: *Classification of PM electric machines.*

problems, such as brushwear, high rotor inertia, which associate with PMDC machines. This makes the PMAC machines the most attractive machine type among the PM electric machines. The PMAC machines can be further classified into trapezoidal and sinusoidal types as shown in figure 1.1. The trapezoidal PMAC machines induce a trapezoidal back-EMF voltage waveform in each stator phase winding during rotation, whereas sinusoidal PMAC machines induce a sinusoidal back-EMF voltage waveform. For torque production, the trapezoidal PMAC machines are excited from rectangular current waveforms, whereas sinusoidal PMAC machines require sinusoidal current excitation of the stator. The trapezoidal PMAC machines, which are also called "brushless DC motors" (BLDCM) were developed first because of the simple control of those machines. However, the presence of torque ripples in those drives rejects their usage in high performance motion control applications. The development of sinusoidal PMAC machines came next in late 1970s and 1980s due to the possibility of high performance control of those machines using vector control principles first used for induction machines [1]. The sinusoidal PMAC machines are the most suitable PMAC machine type to compete with the induction machines in the most of the induction machine drive applications. Therefore, they are getting a growing attention in recent years. Since these machines are closely related to the conventional synchronous machines, they are also called PM synchronous machines (PMSMs). It should be mentioned that except for special applications, in general, the PMSMs are not built with damper windings in the rotor, mainly due to the high manufacturing cost. Hereinafter the PMSMs referred to PM synchronous machines without having damper windings in the rotor.

Different rotor configurations exist for PMSMs depending on how the magnets are placed in the rotor [1], [2]. The two common types, namely, surface magnets type and interior magnets type are shown in figure 1.2. In surface magnets type the magnets are mounted on the surface of the rotor core, whereas in interior magnets type the magnets are placed inside the rotor core. Hereinafter the PMSMs with surface magnets rotor configuration are referred to as SPMSMs and PMSMs with interior magnets rotor configuration are referred to as IPMSMs.

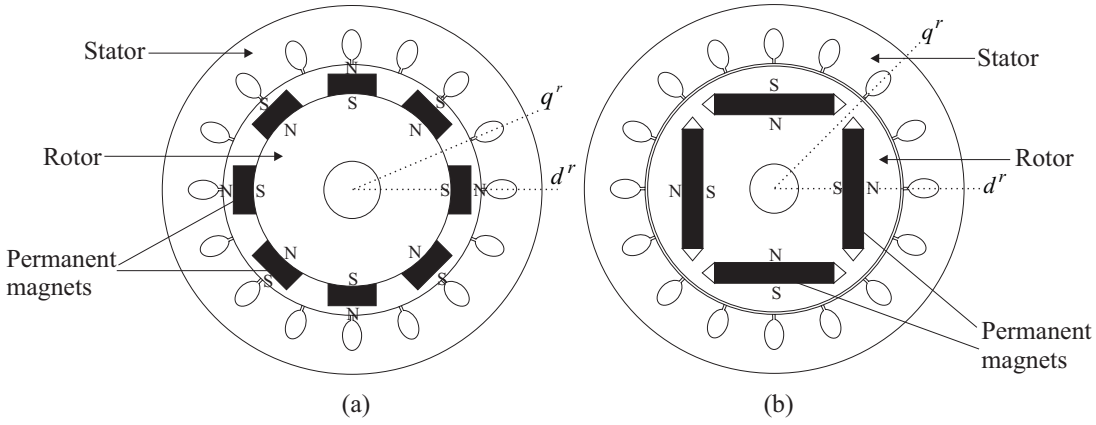

Figure 1.2: *Motor cross sections showing different rotor configurations for PMSMs. (a) Surface magnets type (b) Interior magnets type.*

The interior magnets type rotor configuration brings saliency characteristics to the machine which is not present in a machine with surface magnets type rotor [3]. As shown in figure 1.2(a) and figure 1.2(b), the magnetic flux induced by the magnets defines the rotor direct or d^r-axis radially through the centerline of the magnets. The rotor quadrature or q^r-axis is orthogonally (90 electrical degrees) placed with rotor d^r-axis (Note that for four-pole design this is 45 mechanical degrees as shown in figure 1.2(b)). Since the permeability of permanent-magnets is almost same as the air, in interior magnets type configuration the effective airgap of d^r-axis is increased compared to the q^r-axis. Therefore, the d^r-axis reluctance is higher than the q^r-axis reluctance. This results in the q^r-axis inductance is higher than the d^r-axis inductance, i.e. $L_q > L_d$, in IPMSMs.

1.2 Control fundamentals for PMSMs

Since PMSMs are synchronous machines, the accurate torque can be produced in these machines only when the AC excitation frequency is precisely synchronized with the rotor frequency. Therefore, the fundamental requirement in control design of PMSMs is the assurance of precise synchronization of machine's excitation with the rotor frequency. The direct approach to achieve this requirement is the continuous measurement of the absolute rotor angular position and, the excitation of the machine accordingly as shown in figure 1.3. This concept is also known as self synchronization [1] and it assures that the PMSM does not go out of synchronization during operation.

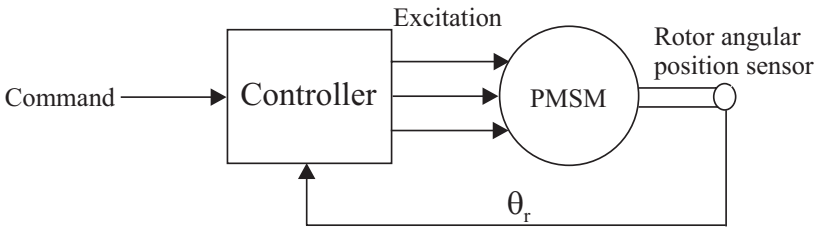

Figure 1.3: *The self synchronization concept for PMSMs, which uses rotor angular position feedback to synchronize the AC excitation and the rotor frequency.*

1.2.1 Basic control methods

V/f control

It is possible to design the IPMSMs with squirrel cage windings (damper windings) in the rotor as shown in figure 1.4. These squirrel cage rotor windings are similar to the induction machine squirrel cage rotor windings and they produce asynchronous torque when the IPM rotor does not rotate in synchronous speed. The asynchronous torque produced by rotor squirrel cage windings during asynchronous operation put back the IPM rotor to the synchronous operation ensuring the synchronous operation of the IPMSM at all the time. This makes the possibility to use simple open-loop V/f control algorithm for this type of IPMSMs as shown in figure 1.4 to achieve speed control for applications like pumps and fans that do not require fast dynamic response [1].

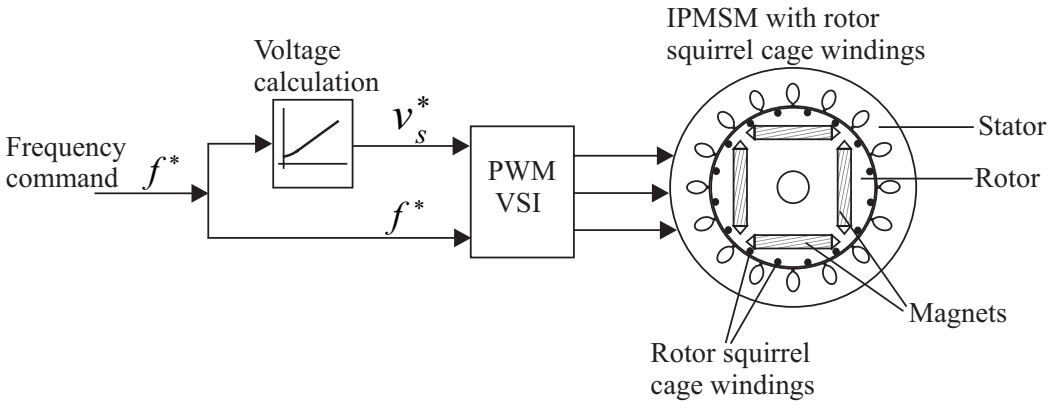

Figure 1.4: *Open-loop V/f control approach, which can be used for IPMSMs with rotor squirrel cage windings.*

Figure 1.4 shown V/f control approach for IPMSMs with rotor cage windings is similar to the one uses in induction machine V/f control (scalar control) approach.

However, one advantage in this drive is, the rotor speed is only dependent on the excitation frequency of the machine and it does not require slip compensation requirement as it does in induction machine drives.

While the IPMSMs with rotor cage windings can be used to control using the configuration shown in figure 1.4, a difficulty can be expected to control the PMSMs without having rotor cage windings using the same control configuration. The non-existence of the rotor cage windings means that the machine does not guarantee the synchronization of the rotor with the excitation frequency and the stable operation. Therefore, to use V/f control approach to the PMSMs without having rotor cage windings requires rotor frequency (rotor speed) information in order to achieve the synchronization between AC excitation frequency and rotor frequency. In this case, the system should be designed to operate in closed-loop manner as shown in figure 1.5.

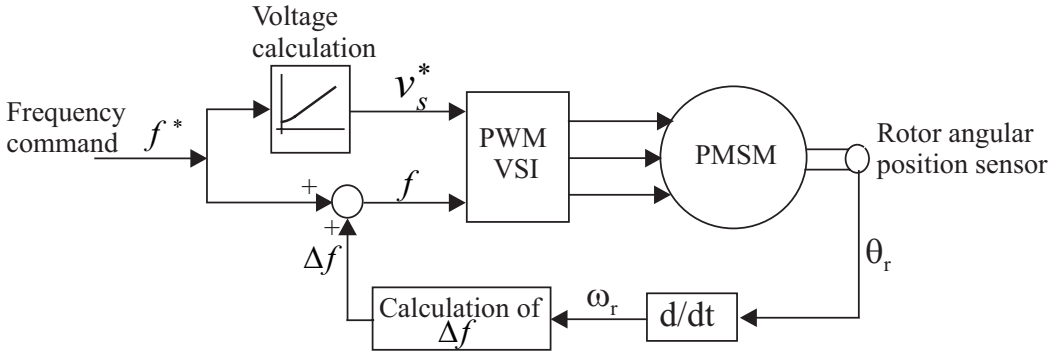

Figure 1.5: *V/f control approach for PMSMs without having rotor cage windings.*

Closed-loop speed and torque control

Better performance compared to the V/f control approach can be achieved incorporating torque and speed control of the machine in the drive controller. The drive control structure with torque and speed controller is shown in figure 1.6. The torque production of PMSMs is related to the stator currents and the torque control incorporates with stator current control requiring stator current feedback to the torque controller as shown in figure 1.6. Moreover, as described in the beginning of this section, to achieve self synchronization, the rotor angular position feedback is also essential for the torque controller.

The stator current control is done in field-oriented frame in the torque controller. Therefore, the PMSM control with this type of torque controller can also be referred to as field-oriented control.

The speed control can be achieved closing the speed feedback loop outside the inner

torque control loop as shown in figure 1.6. The speed feedback can be derived from the same rotor angular position sensor, which is used to obtain the rotor position feedback.

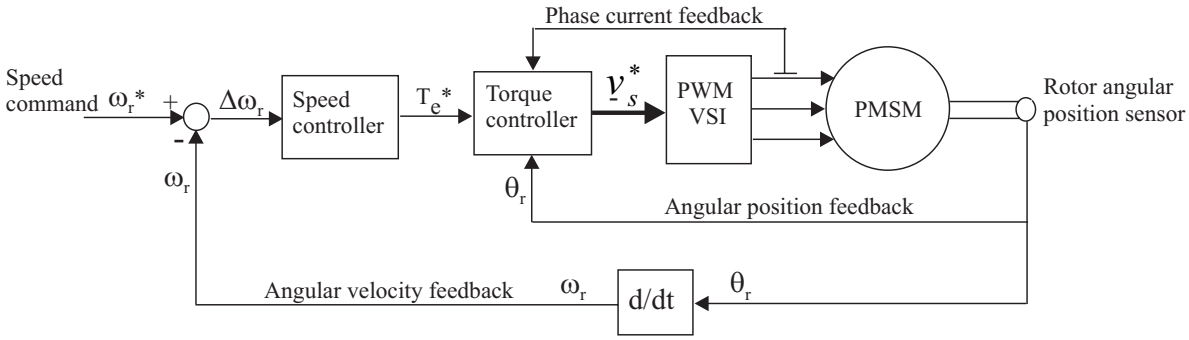

Figure 1.6: *Block diagram of PMSM control scheme incorporating torque and speed controller.*

In order to achieve fast torque control, direct torque control (DTC) of PMSMs is also get some attention recently. Accurate flux estimation and torque estimation are required for DTC. A detailed discussion about DTC of PMSMs can be found in [4].

1.2.2 Rotor position sensor elimination

It is clear from the above discussed control approaches for PMSMs, i.e. the V/f control approach to the PMSMs without having rotor cage windings (figure 1.5) and, the torque and speed control approach (figure 1.6), the requirement of rotor angular position sensor to achieve self synchronization in the control. This shaft mounted position sensor is not desirable in the control system due to number of reasons [5]. The position sensors are expensive and they considerably increase the cost of the drive system. Moreover, a special mechanical arrangement needs to be made for mounting the position sensors and extra signal wires are required from the sensor to the controller. Some type of position sensors are temperature sensitive and their accuracy degrades when the system temperature exceeds the limits. These reasons lead to the elimination of shaft mounted rotor angular position sensor, which is conventionally used for self synchronization in the control system. The control of PMSMs using the same concepts discussed in § 1.2.1 eliminating the rotor angular position sensor is referred to as sensorless control of those machines.

For the V/f control approach shown in figure 1.5 there are possibilities to use other variables rather than rotor speed to achieve self synchronization and stable operation of the PMSM. The measurements from the motor terminals or the DC-link in the inverter may be used for this purpose and this sensorless control approach for PMSMs is shown in figure 1.7.

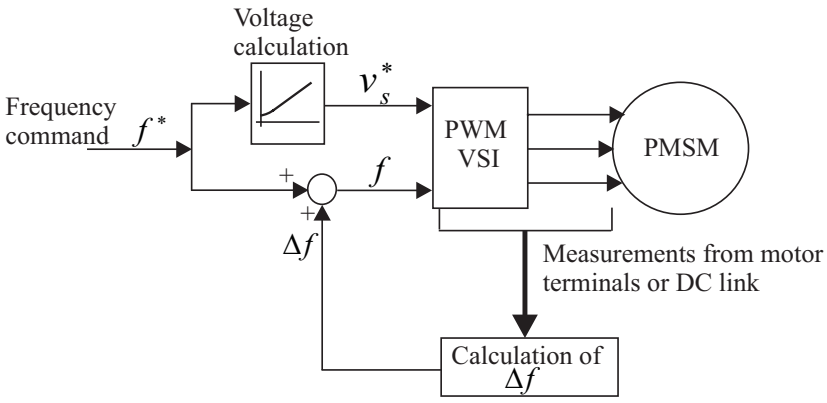

Figure 1.7: *V/f control approach for PMSMs without using rotor position sensor.*

For the torque and speed control approach shown in figure 1.6, the basic method of eliminating the shaft mounted position sensor is, the accurate estimation of rotor angular position and velocity using measurements from the motor terminals or the DC-link. This approach is shown in figure 1.8.

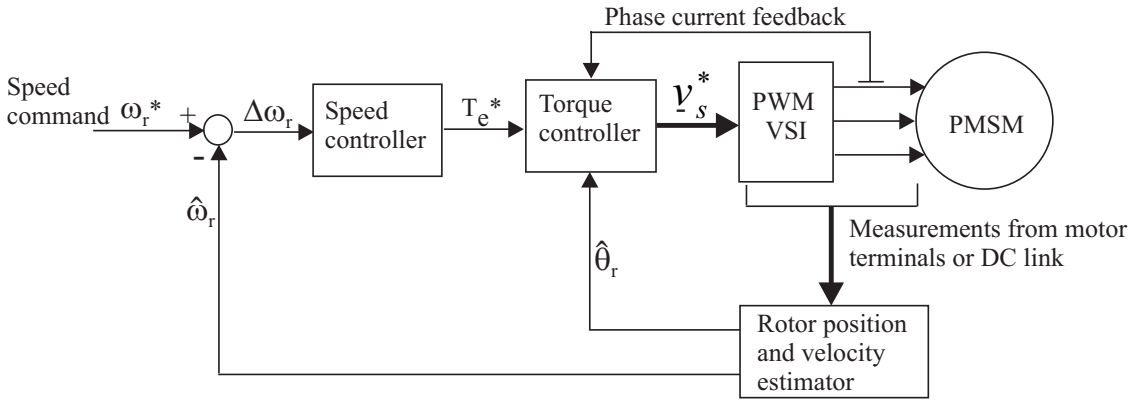

Figure 1.8: *Torque and speed control scheme for PMSMs eliminating rotor angular position sensor.*

1.3 PMSMs versus induction machines

In contrast to the induction machines, the PMSMs do not require magnetizing component of stator current, since the excitation is provided by magnets in those machines. This causes a reduction in stator copper loss in PMSMs. Moreover, the copper loss associated with rotor in induction machines does not exist in PMSMs. This copper loss reduction in stator and rotor significantly improves the efficiency in PMSMs compared to the induction machines. However, it should be mentioned that during flux

weakening regime operation the PMSMs require high stator current to weaken the flux [6],[7], increasing the stator copper loss. This reduces the efficiency of PMSMs during flux weakening regime operation and both PMSMs and induction machines suffer with less efficiency characteristics in that regime operation. This implies that from efficiency point of view the PMSMs are well suited over the induction machines in the applications like pumps and fans, where the machines are operated in constant torque regime.

The growing electrical energy consumption is one of the major problems that world faces at present. Most of this electrical energy is consumed in motor drives and a large fraction of this motor drives consumed energy goes to the induction machine drives with pumps and fans [8]. Therefore, in pumps and fans drives, using PMSMs instead of using induction machines, it can be contributed to reduce the total electrical energy consumption significantly.

Another attractive feature of PMSMs over the induction machines is that the possibility of design them with less weight and volume. Recently, the IPMSMs were designed with significant reduction of weight and volume over the induction machines [9],[10]. Moreover, they also have high torque to inertia (T_e/J) ratio, which is highly attractive for applications that demand fast dynamic response.

Since PMSMs are synchronous machines their control should always be incorporated with self synchronization concept as explained in §1.2. It is not a requirement for induction machine control since they are asynchronous machines. This makes the main difference in control concepts for these two types of machines.

1.4 Objectives and scope of the project

In pumps and fans drives, when PMSMs are used instead of induction machines the improvement of efficiency and its impact to the global energy saving is clear from the discussion in §1.3. This fact is the motivation for this project.

If PMSMs are to be used in pumps and fans drives, they will need control methods, which are more suitable for those applications. This project deals with control of PMSMs focusing on pumps and fans applications.

The PMSMs' basic control methods and the reasons to eliminate the rotor angular position sensor from those methods are discussed in §1.2.1 and §1.2.2 respectively. For the same reasons as described in §1.2.2, it is obvious that the rotor angular position sensor is highly undesirable in pumps and fans applications and sensorless control should be considered.

Both sensorless V/f control approach and sensorless torque and speed control approach (see figure 1.7 and figure 1.8) can be considered as solutions for this project. The sensorless V/f control approach shown in figure 1.7 seems the most suitable control approach for pumps and fans drives due its simplicity. However, this approach is

not widely addressed in the literature so far. Since high dynamic performance of the drive is not a demand for pumps and fans applications simple rotor position and velocity estimation technique may be possible for the sensorless torque and speed control approach.

Considering these facts the objectives of this project are as follows.

- The sensorless V/f control approach shown in figure 1.7 should be given a considerable attention during this project. The modeling of the system and the designing of the whole controller should be presented in detail. The performance of the drive with this control approach should be analyzed.
- The sensorless torque and speed control approach shown in figure 1.8 should be presented with design of various controllers (speed, torque, current) and design of a position and speed estimator. The attention should be paid to the simplicity in position and speed estimating algorithm. The performance of the drive with this control approach should be analyzed.
- A comparison is required for the two control approaches in terms of implementation simplicity and performance.

1.4.1 Limitations

- Only an interior type PM synchronous machine without having cage windings in the rotor is used as the test motor for this project. Recently, the IPMSMs were designed with significantly improved efficiency, less weight and less volume over the induction machines [9],[10]. Therefore, an IPMSM is a good candidate to consider in pumps and fans drives.
- The standard adjustable speed drive converter configuration, i.e. voltage source inverter with diode rectifier, shown in figure 1.9 is used in the motor controller.
- Since the applications are pumps and fans, the control speed range is limited to 10%-100% of rated speed, which is typical for such applications. The flux weakening regime operation of the machine is not considered. During 10%-100% rated speed the controller should be able to overcome 50% of rated load torque step.

1.5 Outline of the thesis

The thesis is organized in the following manner in order to present the work, which has been done in the project. For readability, it is separated into 5 parts including one part for appendices.

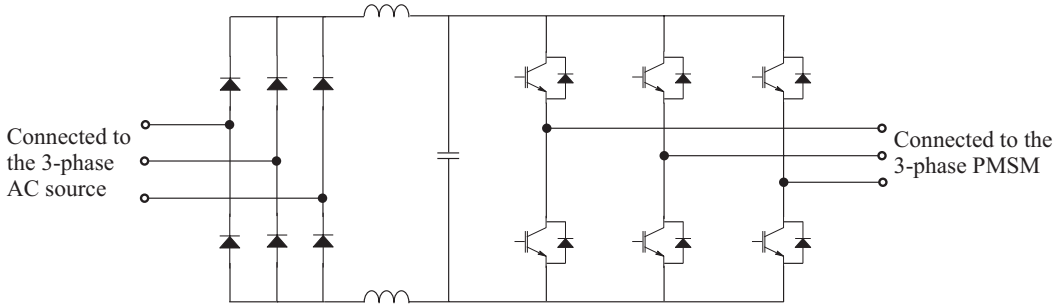

Figure 1.9: *The converter configuration used in the motor controller.*

PART I Preliminaries

Chapter 1. Introduction

This chapter.

Chapter 2. Mathematical Models and Control Properties

In this chapter, the mathematical models for PMSMs are derived. The key control properties of the PMSMs are discussed and they are compared.

PART II Sensorless Stable V/f Control of PMSMs

Chapter 3. Stability Characteristics of PMSMs Under Open-Loop V/f Control

Under open-loop V/f control the PMSMs stability behaviour is studied in detail in this chapter. The linearized PMSM model is described and the eigenvalues of the linearized system matrix are used to study the stability characteristics. The computer simulations and experimental results are provided to validate the stability characteristics of the PMSMs.

Chapter 4. Stabilization of Open-Loop V/f Controlled PMSMs

The methods for stabilizing the open-loop V/f controlled PMSMs are discussed in this chapter. A simplified linearized model is used to investigate the stabilizing methods. The implementation of the stabilizing methods are discussed and they are experimentally verified.

Chapter 5. Sensorless Stable PMSM Drive with V/f Control Approach

The complete V/f controlled PMSM drive system is discussed in this chapter. A voltage control method with stator resistance voltage drop compensation is discussed. In order

to provide the stability in the system, Chapter 4 discussed stabilizing technique is used. The performance of the complete drive system is given.

PART III Sensorless Field-Oriented Control of PMSMs

Chapter 6. Field-Oriented Control and Estimation of Rotor Position and Velocity

In this chapter, the rotor permanent-magnet flux oriented controlled PMSM drive system is introduced. The rotor position and velocity estimating techniques for this drive system are reviewed and their merits and demerits are discussed.

Chapter 7. Field-Oriented Controlled Drive System with and without Position Sensor

In this chapter, the control structure of the field-oriented controlled PMSM drive system is discussed in detail. The design of current and speed controller are discussed. The performance of the drive system with angular position sensor is examined. The rotor position and velocity estimation technique for the drive system is also investigated.

PART IV Conclusions

Chapter 8. Conclusion

The main conclusions are highlighted in this chapter with recommendations for future work.

PART V Appendices

A. Data for the IPMSM

Data for the IPMSM used in this project are given in this Appendix.

B. Various Relationship Derivations Related to Chapter 3 and Chapter 4

Some relationships, which are required in the discussion of Chapter 3 and Chapter 4, are derived in this Appendix.

C. Generation of PWM

The PWM generation in the drive systems is briefly described here.

D. The Laboratory Test System

In this Appendix, the laboratory test system used for experiments is described.

Bibliography

[1] Thomas M. Jahns, *Variable Frequency Permanent Magnet AC Machine Drives*, Chapter 6 in Power Electronics and Variable Frequency Drives, Technology and Applications, B. K. Bose, Ed., IEEE Press, 1997.

[2] Gordon R. Slemon, *Electrical Machines for Drives*, Chapter 2 in Power Electronics and Variable Frequency Drives, Technology and Applications, B. K. Bose, Ed., IEEE Press, 1997.

[3] Thomas M. Jahns, Gerald B. Kliman and Thomas W. Neumann, *Interior Permanent-Magnet Synchronous Motors for Adjustable-Speed Drives*, IEEE Transactions on Industry Applications, Vol. IA-22, No.4, pp. 738-747, July/August 1986.

[4] Peter Vas, *Vector and Direct Torque Control of Synchronous Machines*, Chapter 3 in Sensorless Vector and Direct Torque Control, pp. 87-257, Oxford University Press, 1998.

[5] Kaushik Rajashekara and Atsuo Kawamura, *Sensorless Control of Permanent Magnet AC Motors*, In proceedings of IEEE Industrial Electronics Society conference, pp. 1589-1594, 1994.

[6] Thomas M. Jahns, *Flux-Weakening Regime Operation of an Interior Permanent-Magnet Synchronous Motor Drive*, IEEE Transactions on Industry Applications, Vol. IA-23, No.4, pp. 681-689, July/August 1987.

[7] Werner Leonhard, *Variable Frequency Synchronous Motor Drives*, Chapter 14 in Control of Electrical Drives, Springer, 1997.

[8] Flemming Abrahamsen, *Energy Optimal Control of Induction Motor Drives*, Ph.D. Thesis, Institute of Energy Technology, Aalborg University, Denmark, 2000.

[9] Yaskawa Electric Corporation, *Super-Energy Saving Variable Speed Drive, VARISPEED-686SS5*, Product catalogue, October 1997.

[10] Toshihiro Sawa and Kaneyuki Hamada, *Introduction to the Permanent Magnet Motor Market*, In proceedings of the conference Energy Efficiency in Motor-Driven systems, pp. 81-94, 1999.

Chapter 2

Mathematical Models and Control Properties

2.1 Introduction

Development of the correct machine model through the understanding of physics of the machine is the key requirement for any type of electrical machine control. Since in this project an Interior type Permanent-Magnet Synchronous Motor (IPMSM) is used for the investigations, the mathematical models are developed for an IPMSM. However, to reduce the complexity, the development of those models is under some assumptions as used in many models developed for a wide variety of electrical machines.

The basic control properties of IPMSMs are also discussed and they are compared for the IPMSM used in this project.

2.2 Voltage equations in the stationary a,b,c reference frame

A conceptual diagram for two-pole IPMSM is shown in figure 2.1. It has 3-phase stator windings conceptually shown as aa', bb' and cc' with their current direction. These stator windings are identical windings and symmetrically displaced by 120^0. The axes as, bs and cs are magnetic axes of the stator phases a, b and c respectively. The rotor has buried magnets and, the rotor direct-axis (d^r-axis) and the rotor quadrature-axis (q^r-axis) are also shown in figure 2.1. No damper windings exist for the IPMSM used for the investigations for this project and therefore, the damper windings are not considered for modeling.

The following assumptions are made for the development of the IPMSM model.

1. The spatial stator phase winding distribution in the air gap is sinusoidal.

2. No thermal effect for stator resistance and the permanent-magnet flux.

3. No saturation effect for the inductances.

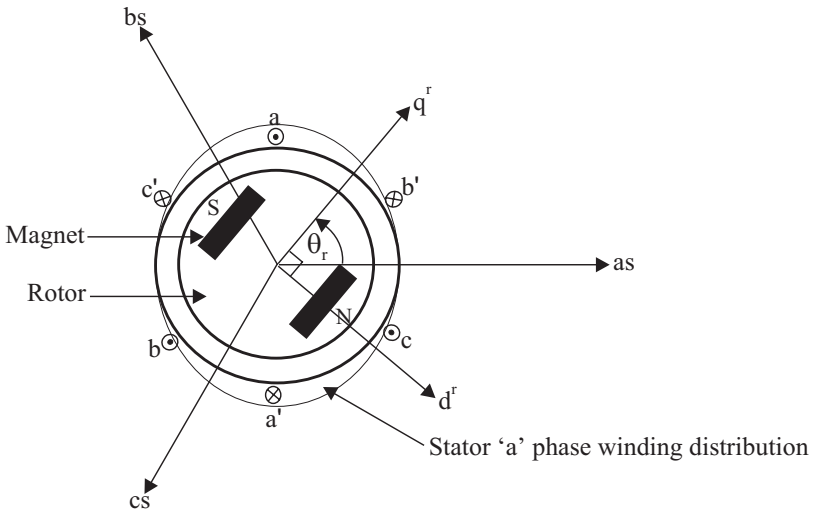

Figure 2.1: *Conceptual diagram for three phase, two pole IPMSM.*

4. No core losses in the machine.

The voltage equations for the stator windings can be written in the matrix form as

$$\boxed{\mathbf{v}_{abcs} = r_s \mathbf{i}_{abcs} + p\boldsymbol{\lambda}_{abcs}} \tag{2.2.1}$$

where, r_s is stator winding resistance per phase, p represents the operator $\frac{d}{dt}$ and $\mathbf{v}_{abcs}$ (Stator phase voltage matrix), $\mathbf{i}_{abcs}$ (Stator phase current matrix) and $\boldsymbol{\lambda}_{abcs}$ (Stator phase flux linkage matrix) are defined by

$$\mathbf{v}_{abcs} = \begin{bmatrix} v_{as} \\ v_{bs} \\ v_{cs} \end{bmatrix}; \quad \mathbf{i}_{abcs} = \begin{bmatrix} i_{as} \\ i_{bs} \\ i_{cs} \end{bmatrix}; \quad \boldsymbol{\lambda}_{abcs} = \begin{bmatrix} \lambda_{as} \\ \lambda_{bs} \\ \lambda_{cs} \end{bmatrix} \tag{2.2.2}$$

No rotor damper windings in the machine and therefore, no rotor circuit equations exist for the machine.

The stator windings' flux linkage matrix $\boldsymbol{\lambda}_{abcs}$ is related to the stator currents and rotor permanent-magnet flux by the following matrix equation.

$$\boldsymbol{\lambda}_{abcs} = \boldsymbol{\lambda}_{abcs(s)} + \boldsymbol{\lambda}_{abcs(r)} \tag{2.2.3}$$

where,

$$\boldsymbol{\lambda}_{abcs(s)} = \begin{bmatrix} L_{aas} & L_{abs} & L_{acs} \\ L_{bas} & L_{bbs} & L_{bcs} \\ L_{cas} & L_{cbs} & L_{ccs} \end{bmatrix} \mathbf{i}_{abcs} \tag{2.2.4}$$

$$\boldsymbol{\lambda}_{abcs(r)} = \lambda_m \begin{bmatrix} sin(\theta_r) \\ sin(\theta_r - \frac{2\pi}{3}) \\ sin(\theta_r + \frac{2\pi}{3}) \end{bmatrix} \tag{2.2.5}$$

In (2.2.4), L_{aas} is the self inductance of phase a winding, L_{abs} and L_{acs} are mutual inductances between a and b phases, a and c phases respectively. For self and mutual inductances of b and c phases the same notations are used. In (2.2.5), λ_m is the amplitude of the flux linkages established by the permanent-magnets on the rotor as viewed from the stator phase windings.

The inductances in (2.2.4) are described below.

Due to the rotor saliency in IPMSM the air gap is not uniform, and therefore, the self and mutual inductances of stator windings are a function of the rotor position. The derivation of these rotor position dependent inductances is available in details in [1]. The results are summarized here as following.

The stator winding self inductances are

$$L_{aas} = L_{ls} + L_A - L_B cos2\theta_r \tag{2.2.6}$$

$$L_{bbs} = L_{ls} + L_A - L_B cos(2\theta_r + \frac{2\pi}{3}) \tag{2.2.7}$$

$$L_{ccs} = L_{ls} + L_A - L_B cos(2\theta_r - \frac{2\pi}{3}) \tag{2.2.8}$$

where, L_{ls} is the leakage inductance and it is the same in all three phase windings since three phase windings are identical. L_A and L_B are given by

$$L_A = (\frac{N_s}{2})^2 \pi \mu_0 r l \varepsilon_1 \tag{2.2.9}$$

$$L_B = \frac{1}{2}(\frac{N_s}{2})^2 \pi \mu_0 r l \varepsilon_2 \tag{2.2.10}$$

where, N_s is number of turns of each phase winding, r is radius, which is from centre of machine to the inside circumference of the stator and l is the axial length of the air gap of the machine. μ_0 is permeability of the air. ε_1 and ε_2 are defined as

$$\varepsilon_1 = \frac{1}{2}(\frac{1}{g_{min}} + \frac{1}{g_{max}}) \tag{2.2.11}$$

$$\varepsilon_2 = \frac{1}{2}(\frac{1}{g_{min}} - \frac{1}{g_{max}}) \tag{2.2.12}$$

where, g_{min} is minimum air gap length and g_{max} is maximum air gap length.

The mutual inductances between stator phases are

$$L_{abs} = L_{bas} = -\frac{1}{2}L_A - L_B cos(2\theta_r - \frac{2\pi}{3}) \tag{2.2.13}$$

$$L_{acs} = L_{cas} = -\frac{1}{2}L_A - L_B cos(2\theta_r + \frac{2\pi}{3}) \tag{2.2.14}$$

$$L_{bcs} = L_{cbs} = -\frac{1}{2}L_A - L_B cos2\theta_r \tag{2.2.15}$$

Finally, the flux linkage matrix $\boldsymbol{\lambda}_{abcs}$ in (2.2.1) can be written in the following form

$$\begin{bmatrix} \lambda_{as} \\ \lambda_{bs} \\ \lambda_{cs} \end{bmatrix} = \boldsymbol{L} \begin{bmatrix} i_{as} \\ i_{bs} \\ i_{cs} \end{bmatrix} + \begin{bmatrix} sin(\theta_r) \\ sin(\theta_r - \frac{2\pi}{3}) \\ sin(\theta_r + \frac{2\pi}{3}) \end{bmatrix} \lambda_m \tag{2.2.16}$$

where,

$$\boldsymbol{L} = \begin{bmatrix} L_{ls} + L_A - L_B cos2\theta_r & -\frac{1}{2}L_A - L_B cos(2\theta_r - \frac{2\pi}{3}) & -\frac{1}{2}L_A - L_B cos(2\theta_r + \frac{2\pi}{3}) \\ -\frac{1}{2}L_A - L_B cos(2\theta_r - \frac{2\pi}{3}) & L_{ls} + L_A - L_B cos(2\theta_r + \frac{2\pi}{3}) & -\frac{1}{2}L_A - L_B cos2\theta_r \\ -\frac{1}{2}L_A - L_B cos(2\theta_r + \frac{2\pi}{3}) & -\frac{1}{2}L_A - L_B cos2\theta_r & L_{ls} + L_A - L_B cos(2\theta_r - \frac{2\pi}{3}) \end{bmatrix} \tag{2.2.17}$$

2.3 Voltage equations in space vector form

Another way to represent the machine voltage equations is space vector form. Space vector form of the machine equations has many advantages such as compact notation, easy algebraic manipulation, very simple graphical interpretation. Specially, this notation is very useful when analyzing the vector control based techniques of the machines. The space vector representation of AC machine equations has been discussed in detail in number of text books ([2], [3] and [4]).

The instantaneous value of the machine variable (current, voltage or flux linkage) can be represented along the phase axis as a vector and the space vector correspondent to this variable is defined as

$$\underline{f}_{abcs} = \frac{2}{3}[f_{as} + \underline{a} f_{bs} + \underline{a}^2 f_{cs}] \tag{2.3.1}$$

where, f_{as}, f_{bs} and f_{cs} are the instantaneous values of the machine variable in a, b and c phases respectively and

$$\underline{a} = e^{j\frac{2\pi}{3}} \tag{2.3.2}$$

$$\underline{a}^2 = e^{j\frac{4\pi}{3}} \tag{2.3.3}$$

With the above definition for space vector, the conjugate of it ($\underline{f}^{\star}_{abcs}$) becomes

$$\underline{f}^{\star}_{abcs} = \frac{2}{3}[f_{as} + \underline{a}^2 f_{bs} + \underline{a} f_{cs}] \tag{2.3.4}$$

The selection of constant $\frac{2}{3}$ in the definition given in (2.3.1) guarantees that for balanced sinusoidal phase waveforms the magnitude of the space vector is equal to the amplitude of that phase waveforms.

The IPMSM voltage equations in space vector form can be obtained using the definition in (2.3.1). Multiplying the second row of the stator voltage matrix equation

(2.2.1) by $\underline{a}$ and the third row by $\underline{a}^2$, adding the result to the first row and multiplying the entire result by $\frac{2}{3}$ it can be obtained the space vector form of the voltage equations as

$$\boxed{\underline{v}_{abcs} = r_s \underline{i}_{abcs} + p\underline{\lambda}_{abcs}} \tag{2.3.5}$$

where,

$$\underline{v}_{abcs} = \frac{2}{3}(v_{as} + \underline{a}v_{bs} + \underline{a}^2 v_{cs}), \tag{2.3.6}$$

$$\underline{i}_{abcs} = \frac{2}{3}(i_{as} + \underline{a}i_{bs} + \underline{a}^2 i_{cs}), \tag{2.3.7}$$

and

$$\underline{\lambda}_{abcs} = \frac{2}{3}(\lambda_{as} + \underline{a}\lambda_{bs} + \underline{a}^2 \lambda_{cs}), \tag{2.3.8}$$

The flux linkage space vector $\underline{\lambda}_{abcs}$ can be obtained from current space vector $\underline{i}_{abcs}$ and permanent-magnet flux λ_m as follows.

The flux linkage matrix which was given in (2.2.16) can be written in the following form.

$$\begin{bmatrix}\lambda_{as}\\ \lambda_{bs}\\ \lambda_{cs}\end{bmatrix} = \begin{bmatrix}L_{ls}+L_A & -\frac{1}{2}L_A & -\frac{1}{2}L_A\\ -\frac{1}{2}L_A & L_{ls}+L_A & -\frac{1}{2}L_A\\ -\frac{1}{2}L_A & -\frac{1}{2}L_A & L_{ls}+L_A\end{bmatrix}\begin{bmatrix}i_{as}\\ i_{bs}\\ i_{cs}\end{bmatrix} - \frac{L_B}{2}\begin{bmatrix}e^{j2\theta_r} & \underline{a}^2 e^{j2\theta_r} & \underline{a}e^{j2\theta_r}\\ \underline{a}^2 e^{j2\theta_r} & \underline{a}e^{j2\theta_r} & e^{j2\theta_r}\\ \underline{a}e^{j2\theta_r} & e^{j2\theta_r} & \underline{a}^2 e^{j2\theta_r}\end{bmatrix}\begin{bmatrix}i_{as}\\ i_{bs}\\ i_{cs}\end{bmatrix}$$
$$-\frac{L_B}{2}\begin{bmatrix}e^{-j2\theta_r} & \underline{a}e^{-j2\theta_r} & \underline{a}^2 e^{-j2\theta_r}\\ \underline{a}e^{-j2\theta_r} & \underline{a}^2 e^{-j2\theta_r} & e^{-j2\theta_r}\\ \underline{a}^2 e^{-j2\theta_r} & e^{-j2\theta_r} & \underline{a}e^{-j2\theta_r}\end{bmatrix}\begin{bmatrix}i_{as}\\ i_{bs}\\ i_{cs}\end{bmatrix} + \frac{\lambda_m}{2j}\begin{bmatrix}e^{j\theta_r}\\ \underline{a}^2 e^{j\theta_r}\\ \underline{a}e^{j\theta_r}\end{bmatrix} - \frac{\lambda_m}{2j}\begin{bmatrix}e^{-j\theta_r}\\ \underline{a}e^{-j\theta_r}\\ \underline{a}^2 e^{-j\theta_r}\end{bmatrix} \tag{2.3.9}$$

Multiplying the second row of this equation by $\underline{a}$ and the third row by $\underline{a}^2$, adding the result to the first row and multiplying the entire result by $\frac{2}{3}$, one obtains (after some simplification),

$$\begin{aligned}\underline{\lambda}_{abcs} &= \frac{2}{3}(\lambda_{as} + \underline{a}\lambda_{bs} + \underline{a}^2\lambda_{cs})\\ &= \frac{2}{3}(L_{ls} + \frac{3}{2}L_A)(i_{as} + \underline{a}i_{bs} + \underline{a}^2 i_{cs}) - L_B(i_{as} + \underline{a}^2 i_{bs} + \underline{a}i_{cs})e^{j2\theta_r} + \lambda_m e^{j(\theta_r - \frac{\pi}{2})}\end{aligned} \tag{2.3.10}$$

Using the basic definition for the space vector and its conjugate this expression becomes finally,

$$\boxed{\underline{\lambda}_{abcs} = (L_{ls} + \frac{3}{2}L_A)\underline{i}_{abcs} - \frac{3}{2}L_B \underline{i}^{\star}_{abcs} e^{j2\theta_r} + \lambda_m e^{j(\theta_r - \frac{\pi}{2})}} \tag{2.3.11}$$

Equations (2.3.5) and (2.3.11) represent the space vector model of the IPMSM.

2.4 d,q model

2.4.1 Transformation of machine variables to a general rotating reference frame

Even though the space vector form of machine equations becomes more compact, the rotor position dependent parameters still exist in that form of expressions (see (2.3.11) for the stator flux linkage vector). Therefore, the space vector approach discussed in the above section is still not a simple model, which can be used for the analysis. A simplification can be made if the space vector model referred to a suitably selected rotating reference frame. In the following, it is discussed how the space vector model transforms to a general rotating reference frame.

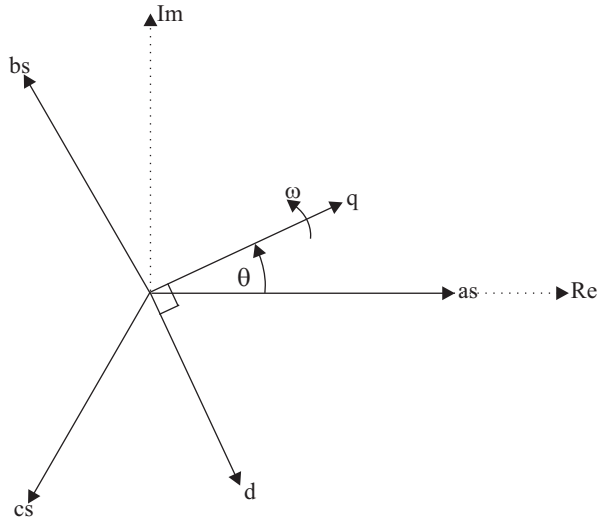

Figure 2.2: *Stator three phase axes (as,bs,cs) and general rotating reference frame (d,q).*

Figure 2.2 shows axes of reference for the three stator phases as, bs and cs. It also shows a rotating set of d,q axes, where the q-axis is located an angle θ from the stator a phase axis. Variables along the as, bs and cs stator axes can be referred to the q-and d-axes by the expressions

$$f_{qs} = \frac{2}{3}[f_{as}cos\theta + f_{bs}cos(\theta - \frac{2\pi}{3}) + f_{cs}cos(\theta + \frac{2\pi}{3})] \tag{2.4.1}$$

$$f_{ds} = \frac{2}{3}[f_{as}sin\theta + f_{bs}sin(\theta - \frac{2\pi}{3}) + f_{cs}sin(\theta + \frac{2\pi}{3})] \tag{2.4.2}$$

where, f represents any of the three phase stator variables such as voltage, current or flux linkage. The coefficient $\frac{2}{3}$ should be included in (2.4.1) and (2.4.2), since the space vector definition in (2.3.1) has the same coefficient. Since there are three phases, to obtain the full transformation to the d, q frame it is necessary to define the third new

variable which is called zero sequence component. The expression for the zero sequence component f_{0s} is

$$f_{0s} = \frac{1}{3}[f_{as} + f_{bs} + f_{cs}] \tag{2.4.3}$$

In general applications, machines are delta or wye connected without having a neutral return path. Therefore,

$$f_{as} + f_{bs} + f_{cs} = 0 \tag{2.4.4}$$

and zero sequence component does not exist.

Multiplying (2.4.2) by j and subtracting it from (2.4.1) one can obtain the space vector referred to the rotating d, q reference frame ($\underline{f}_{qds}$) as

$$\underline{f}_{qds} = f_{qs} - jf_{ds} = \frac{2}{3}[f_{as}e^{-j\theta} + f_{bs}e^{-j(\theta-\frac{2\pi}{3})} + f_{cs}e^{-j(\theta+\frac{2\pi}{3})}] \tag{2.4.5}$$

This expression for $\underline{f}_{qds}$ can be written as

$$\underline{f}_{qds} = \frac{2}{3}e^{-j\theta}[f_{as} + \underline{a}f_{bs} + \underline{a}^2 f_{cs}] \tag{2.4.6}$$

Finally, using the definition in (2.3.1) for space vectors, (2.4.6) can be written as

$$\boxed{\underline{f}_{qds} = e^{-j\theta}\underline{f}_{abcs}} \tag{2.4.7}$$

The expression (2.4.7) describes the transformation of a space vector to a general rotating reference frame.

2.4.2 Voltage equations in stationary d,q reference frame

Referring to figure 2.2, the stationary ($\omega = 0$) d,q reference frame is defined when $\theta = 0$. Therefore, from (2.4.7) the stationary reference frame vectors can be obtained as

$$\underline{f}^s_{qds} = \underline{f}_{abcs} = f^s_{qs} - jf^s_{ds} \tag{2.4.8}$$

where, superscript s denotes the stationary reference frame quantities. Applying the definition in (2.4.8) to (2.3.5), the stationary reference frame machine voltage equations can be obtained as

$$\underline{v}^s_{qds} = r_s\underline{i}^s_{qds} + p\underline{\lambda}^s_{qds} \tag{2.4.9}$$

where,

$$\underline{\lambda}^s_{qds} = (L_{ls} + \frac{3}{2}L_A)\underline{i}^s_{qds} - \frac{3}{2}L_B(\underline{i}^s_{qds})^\star e^{j2\theta_r} + \lambda_m e^{j(\theta_r - \frac{\pi}{2})} \tag{2.4.10}$$

Substituting the following expressions for complex vectors

$$\underline{v}^s_{qds} = v^s_{qs} - jv^s_{ds} \tag{2.4.11}$$

$$\underline{i}^s_{qds} = i^s_{qs} - ji^s_{ds} \tag{2.4.12}$$

$$\underline{\lambda}^s_{qds} = \lambda^s_{qs} - j\lambda^s_{ds} \tag{2.4.13}$$

and equating the real and imaginary parts in both sides of (2.4.9) and (2.4.10) one can obtain the scalar form of the machine equations in stationary reference frame as

$$v^s_{qs} = r_s i^s_{qs} + p\lambda^s_{qs} \tag{2.4.14}$$

$$v^s_{ds} = r_s i^s_{ds} + p\lambda^s_{ds} \tag{2.4.15}$$

and,

$$\lambda^s_{qs} = (L_{ls} + \frac{3}{2}L_A - \frac{3}{2}L_B cos(2\theta_r))i^s_{qs} + \frac{3}{2}L_B sin(2\theta_r)i^s_{ds} + \lambda_m sin(\theta_r) \tag{2.4.16}$$

$$\lambda^s_{ds} = \frac{3}{2}L_B sin(2\theta_r)i^s_{qs} + (L_{ls} + \frac{3}{2}L_A + \frac{3}{2}L_B cos(2\theta_r))i^s_{ds} + \lambda_m cos(\theta_r) \tag{2.4.17}$$

2.4.3 Voltage equations in rotor d,q reference frame

Since $\theta = \theta_r$ in rotor d,q reference frame, the voltage vector in that reference frame can be obtained multiplying the both sides of (2.3.5) by $e^{-j\theta_r}$ as,

$$\underline{v}_{abcs}e^{-j\theta_r} = r_s\underline{i}_{abcs}e^{-j\theta_r} + e^{-j\theta_r}p\underline{\lambda}_{abcs} \tag{2.4.18}$$

Using chain rule, (2.4.18) can be written as

$$\underline{v}_{abcs}e^{-j\theta_r} = r_s\underline{i}_{abcs}e^{-j\theta_r} + p\underline{\lambda}_{abcs}e^{-j\theta_r} + j\omega_r\underline{\lambda}_{abcs}e^{-j\theta_r} \tag{2.4.19}$$

and finally, the rotor reference frame voltage vector can be obtained from (2.4.19) as,

$$\boxed{\underline{v}^r_{qds} = r_s\underline{i}^r_{qds} + p\underline{\lambda}^r_{qds} + j\omega_r\underline{\lambda}^r_{qds}} \tag{2.4.20}$$

where, superscript r denotes the rotor reference frame quantities.

The flux linkage vector in rotor reference frame can be obtained as

$$\begin{aligned}
\underline{\lambda}^r_{qds} &= \underline{\lambda}_{abcs}e^{-j\theta_r} \\
&= (L_{ls} + \frac{3}{2}L_A)\underline{i}_{abcs}e^{-j\theta_r} - \frac{3}{2}L_B\underline{i}^\star_{abcs}e^{j2\theta_r}e^{-j\theta_r} + \lambda_m e^{j(\theta_r - \frac{\pi}{2})}e^{-j\theta_r} \\
&= (L_{ls} + \frac{3}{2}L_A)\underline{i}_{abcs}e^{-j\theta_r} - \frac{3}{2}L_B\underline{i}^\star_{abcs}e^{j\theta_r} + \lambda_m e^{-j\frac{\pi}{2}} \\
&= (L_{ls} + \frac{3}{2}L_A)\underline{i}^r_{qds} - \frac{3}{2}L_B(\underline{i}^r_{qds})^\star + \lambda_m e^{-j\frac{\pi}{2}}
\end{aligned} \tag{2.4.21}$$

It should be noted that when transforming the flux linkage vector to the rotor d,q reference frame the rotor position dependent terms disappear in the expression as it

can be seen from (2.4.21). The rotor position dependent inductances do not appear in rotor reference frame flux vector and this is the main advantage in rotor reference frame equations.

The expression for flux linkage vector (2.4.21) can also be written in magnetizing inductances.

The magnetizing inductances are defined as [1],

$$L_{md} = \frac{3}{2}(L_A + L_B) \tag{2.4.22}$$

$$L_{mq} = \frac{3}{2}(L_A - L_B) \tag{2.4.23}$$

Solving for L_A and L_B,

$$L_A = \frac{L_{md} + L_{mq}}{3} \tag{2.4.24}$$

$$L_B = \frac{L_{md} - L_{mq}}{3} \tag{2.4.25}$$

Using (2.4.24) and (2.4.25), the flux linkage vector given in (2.4.21) can be written from magnetizing inductances as

$$\underline{\lambda}^r_{qds} = (L_{ls} + \frac{L_{md} + L_{mq}}{2})\underline{i}^r_{qds} - (\frac{L_{md} - L_{mq}}{2})(\underline{i}^r_{qds})^\star + \lambda_m e^{-j\frac{\pi}{2}} \tag{2.4.26}$$

The more useful scalar form of (2.4.20) and (2.4.26) is derived below.

Substituting the following expressions for complex vectors

$$\underline{v}^r_{qds} = v^r_{qs} - jv^r_{ds} \tag{2.4.27}$$

$$\underline{i}^r_{qds} = i^r_{qs} - ji^r_{ds} \tag{2.4.28}$$

$$\underline{\lambda}^r_{qds} = \lambda^r_{qs} - j\lambda^r_{ds} \tag{2.4.29}$$

to (2.4.20) and (2.4.26), and equating the real parts and imaginary parts in both sides of the equations the scalar form of the machine equations in rotor reference frame can be obtained as

$$\boxed{\begin{aligned} v^r_{qs} &= r_s i^r_{qs} + p\lambda^r_{qs} + \omega_r \lambda^r_{ds} && (2.4.30)\\ v^r_{ds} &= r_s i^r_{ds} + p\lambda^r_{ds} - \omega_r \lambda^r_{qs} && (2.4.31)\end{aligned}}$$

where,

$$\boxed{\begin{aligned} \lambda^r_{qs} &= L_q i^r_{qs} && (2.4.32)\\ \lambda^r_{ds} &= L_d i^r_{ds} + \lambda_m && (2.4.33)\end{aligned}}$$

In (2.4.32) and (2.4.33), the L_q and L_d are defined as

$$L_q = L_{ls} + L_{mq} \tag{2.4.34}$$

$$L_d = L_{ls} + L_{md} \tag{2.4.35}$$

Substituting the relationships in (2.4.32) and (2.4.33) into (2.4.30) and (2.4.31), and also considering $p\lambda_m = 0$, the most common scalar form of the machine voltage equations in the rotor reference frame can be obtained as

$$\begin{aligned} v_{qs}^r &= r_s i_{qs}^r + pL_q i_{qs}^r + \omega_r L_d i_{ds}^r + \omega_r \lambda_m \quad (2.4.36) \\ v_{ds}^r &= r_s i_{ds}^r + pL_d i_{ds}^r - \omega_r L_q i_{qs}^r \quad (2.4.37) \end{aligned}$$

Equations (2.4.32), (2.4.33), (2.4.36) and (2.4.37) in the equivalent circuit form are shown in figure 2.3.

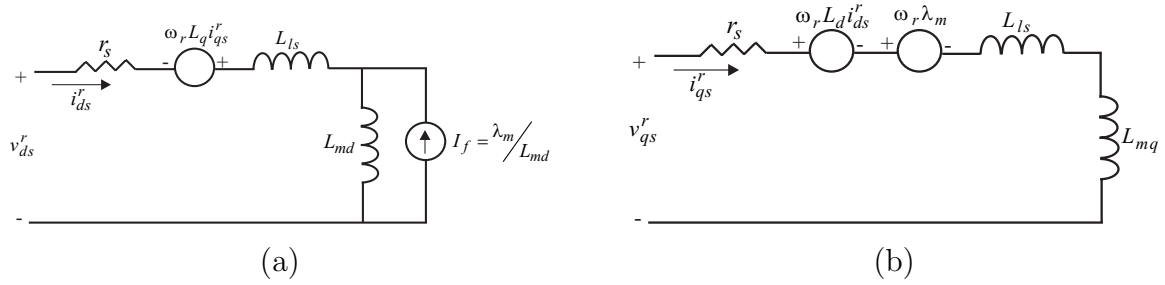

(a) (b)

Figure 2.3: *Equivalent circuit models of the IPMSM in the rotor reference frame. (a) Rotor d-axis equivalent circuit (b) Rotor q-axis equivalent circuit.*

Stationary d,q reference frame equations from L_d and L_q

The stationary d,q reference frame equations derived in § 2.4.2 can also be written in L_d and L_q. The equations in that form may also be useful for some analysis of the machine.

With the aid of (2.4.24), (2.4.25), (2.4.34) and (2.4.35), the stationary reference frame flux given in (2.4.16) and (2.4.17) can be written as

$$\lambda_{qs}^s = [L + \Delta L cos(2\theta_r)] i_{qs}^s - \Delta L sin(2\theta_r) i_{ds}^s + \lambda_m sin(\theta_r) \quad (2.4.38)$$

$$\lambda_{ds}^s = -\Delta L sin(2\theta_r) i_{qs}^s + [L - \Delta L cos(2\theta_r)] i_{ds}^s + \lambda_m cos(\theta_r) \quad (2.4.39)$$

where,

$$L = \frac{L_q + L_d}{2}, \quad \Delta L = \frac{L_q - L_d}{2} \quad (2.4.40)$$

The expressions given in (2.4.38) and (2.4.39) can also be written in matrix form as

$$\begin{bmatrix} \lambda_{qs}^s \\ \lambda_{ds}^s \end{bmatrix} = \begin{bmatrix} L + \Delta L cos(2\theta_r) & -\Delta L sin(2\theta_r) \\ -\Delta L sin(2\theta_r) & L - \Delta L cos(2\theta_r) \end{bmatrix} \begin{bmatrix} i_{qs}^s \\ i_{ds}^s \end{bmatrix} + \begin{bmatrix} \lambda_m sin(\theta_r) \\ \lambda_m cos(\theta_r) \end{bmatrix} \quad (2.4.41)$$

where, the inductance matrix is

$$\begin{bmatrix} L + \Delta L cos(2\theta_r) & -\Delta L sin(2\theta_r) \\ -\Delta L sin(2\theta_r) & L - \Delta L cos(2\theta_r) \end{bmatrix} \tag{2.4.42}$$

Substituting (2.4.38) and (2.4.39) to the (2.4.14) and (2.4.15), one can obtain the stationary reference frame voltage equations from L_d and L_q as

$$v_{qs}^s = r_s i_{qs}^s + p[(L + \Delta L cos(2\theta_r))i_{qs}^s - \Delta L sin(2\theta_r) i_{ds}^s] + \lambda_m \omega_r cos(\theta_r) \tag{2.4.43}$$

$$v_{ds}^s = r_s i_{ds}^s + p[-\Delta L sin(2\theta_r) i_{qs}^s + (L - \Delta L cos(2\theta_r))i_{ds}^s] - \lambda_m \omega_r sin(\theta_r) \tag{2.4.44}$$

2.5 The electromagnetic torque

The expression for the electromagnetic torque produced by the IPMSM can be derived using power balance equation of the machine.

The instantaneous power p_e flowing into the machine can be written from rotor d,q frame variables as

$$p_e = \frac{3}{2}(v_{ds}^r i_{ds}^r + v_{qs}^r i_{qs}^r) \tag{2.5.1}$$

After substituting the voltages v_{ds}^r and v_{qs}^r from (2.4.31) and (2.4.30), the equation (2.5.1) can be written separating the power quantities as in the following form.

$$p_e = \underbrace{\frac{3}{2}[r_s(i_{ds}^r)^2 + r_s(i_{qs}^r)^2]}_{Power\ \ loss\ \ in\ \ conductors} + \underbrace{\frac{3}{2}[pL_d\frac{(i_{ds}^r)^2}{2} + pL_q\frac{(i_{qs}^r)^2}{2}]}_{Rate\ \ of\ \ change\ \ of\ \ stored\ \ energy} + \underbrace{\frac{3}{2}[\omega_r\lambda_{ds}^r i_{qs}^r - \omega_r\lambda_{qs}^r i_{ds}^r]}_{For\ \ energy\ \ conversion} \tag{2.5.2}$$

In (2.5.2), the first term indicates the power loss in the conductors and the second term indicates the time rate of change of stored energy in the magnetic fields. The third term should be for energy conversion, that is, from electrical energy to mechanical energy. If this term (the electromechanical power) is denoted as p_{em}, then

$$p_{em} = \frac{3}{2}[\omega_r\lambda_{ds}^r i_{qs}^r - \omega_r\lambda_{qs}^r i_{ds}^r] \tag{2.5.3}$$

This electromechanical power output should be equal to the power output from the motor shaft, i.e., the multiplication of mechanical angular velocity of rotor shaft ω_{rm} and the machine produced torque T_e. Thus, (2.5.3) can be written as

$$\omega_{rm} T_e = \frac{3}{2}[\omega_r\lambda_{ds}^r i_{qs}^r - \omega_r\lambda_{qs}^r i_{ds}^r] \tag{2.5.4}$$

The relationship between mechanical angular velocity of the rotor and the electrical velocity is:

$$\omega_r = \frac{n}{2}\omega_{rm} \tag{2.5.5}$$

where, n is the number of poles of the machine.

Substituting ω_r from (2.5.5) to (2.5.4), one can obtain the electromagnetic torque expression for IPMSM in rotor d,q axes flux and current components as

$$T_e = \frac{3}{2}\frac{n}{2}[\lambda^r_{ds} i^r_{qs} - \lambda^r_{qs} i^r_{ds}] \tag{2.5.6}$$

Substituting λ^r_{qs} and λ^r_{ds} from (2.4.32) and (2.4.33), the torque expression in (2.5.6) becomes

$$\boxed{T_e = \frac{3}{2}\frac{n}{2}[\lambda_m i^r_{qs} + (L_d - L_q) i^r_{ds} i^r_{qs}]} \tag{2.5.7}$$

It can be seen from (2.5.7), the IPMSM produce torque consists of two parts, one is produced by the permanent-magnet flux (T_m) and the other is the reluctance torque (T_{re}), which is produced by the difference of the reluctance in rotor d- and q- axes. The expressions for those two torque components are

$$T_m = \frac{3}{2}\frac{n}{2}\lambda_m i^r_{qs} \tag{2.5.8}$$

$$T_{re} = \frac{3}{2}\frac{n}{2}(L_d - L_q) i^r_{ds} i^r_{qs} \tag{2.5.9}$$

It should be mentioned that for SPMSMs the reluctance torque component (T_{re}) does not exist due to the same reluctance paths in rotor d- and q-axes and only T_m exists.

The torque expression given in (2.5.7) can also be written using the current vector magnitude i_s and the torque angle α, i.e. angle between rotor q-axis and current vector. This way of expressing the torque is useful in a later section of this chapter and it is derived here.

The components of the current vector in the rotor reference frame and the torque angle are shown in figure 2.4.

Using torque angle α the current components i^r_{ds} and i^r_{qs} can be written as

$$i^r_{ds} = i_s cos\alpha \tag{2.5.10}$$

$$i^r_{qs} = i_s sin\alpha \tag{2.5.11}$$

Substituting i^r_{ds}, i^r_{qs} from (2.5.10) and (2.5.11) into (2.5.7), the torque expression from i_s and α can be obtained as

$$T_e = \frac{3}{2}\frac{n}{2}[\lambda_m i_s sin\alpha + \frac{1}{2}(L_d - L_q) i_s^2 sin2\alpha] \tag{2.5.12}$$

From (2.5.12), T_m and T_{re} components can be written as

$$T_m = \frac{3}{2}\frac{n}{2}\lambda_m i_s sin\alpha \tag{2.5.13}$$

$$T_{re} = \frac{3}{2}\frac{n}{2}\frac{1}{2}(L_d - L_q) i_s^2 sin2\alpha \tag{2.5.14}$$

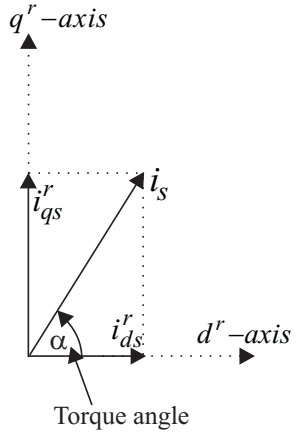

Figure 2.4: *Current vector components in rotor reference frame.*

For a given current magnitude, T_m and T_{re} varies according to the torque angle α, and therefore, the resultant torque of the IPMSM. For a given current magnitude, the variation of T_m and T_{re} and the resultant torque T_e with torque angle α is illustrated in figure 2.5. The IPMSM parameters used for this calculation are given in the Appendix A. The current magnitude is taken as the rated current magnitude of the machine.

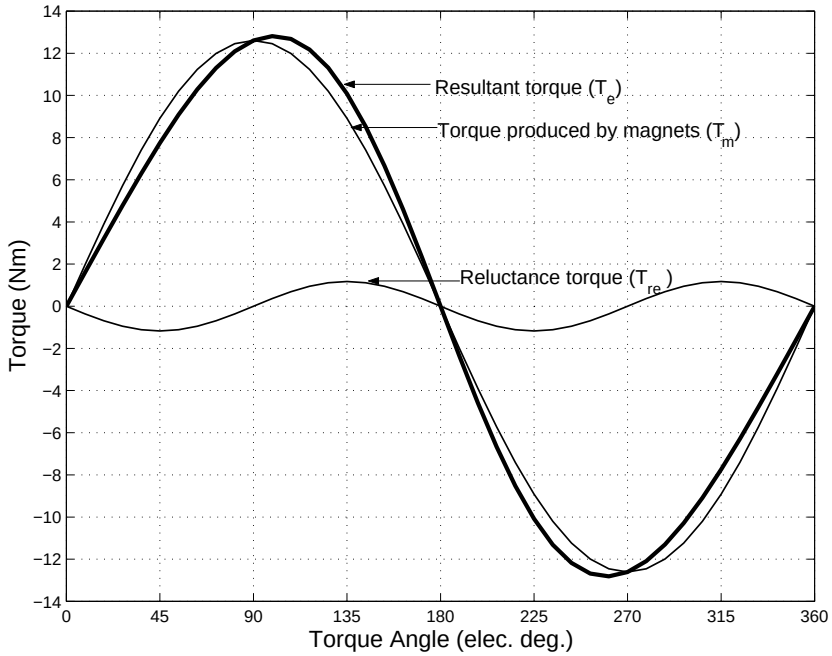

Figure 2.5: *For a given current magnitude, the variation of magnets produced torque (T_m) , reluctance torque (T_{re}) and resultant torque (T_e) as a function of torque angle (α).*

In torque expressions (2.5.7) and (2.5.12) currents are involved and, there is another useful torque expression, which describes from stator flux linkage λ_s and rotor permanent-magnet flux λ_m. Referring to figure 2.6, the stator flux components in rotor reference frame can be written as

$$\lambda_{qs}^r = \lambda_s sin(\psi) = L_q i_{qs}^r \tag{2.5.15}$$

$$\lambda_{ds}^r = \lambda_s cos(\psi) = L_d i_{ds}^r + \lambda_m \tag{2.5.16}$$

where, ψ is the angle between stator flux linkage vector and the rotor permanent-magnet flux vector.

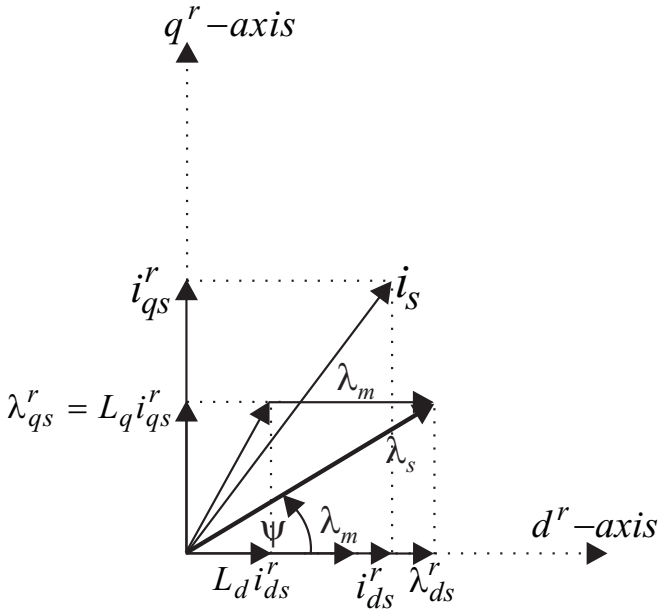

Figure 2.6: *Rotor permanent-magnet flux vector and stator flux linkage vector in rotor reference frame.*

From (2.5.15) and (2.5.16) the i_{qs}^r and i_{ds}^r can be obtained as

$$i_{qs}^r = \frac{\lambda_s sin(\psi)}{L_q} \tag{2.5.17}$$

$$i_{ds}^r = \frac{\lambda_s cos(\psi) - \lambda_m}{L_d} \tag{2.5.18}$$

Substituting λ_{qs}^r, λ_{ds}^r, i_{qs}^r and i_{ds}^r from (2.5.15), (2.5.16), (2.5.17) and (2.5.18) to the torque equation given in (2.5.6), one can obtain the torque expression in stator flux linkage and rotor permanent-magnet flux as

$$T_e = \frac{3}{2}\frac{n}{2}[\frac{\lambda_s \lambda_m sin(\psi)}{L_d} + \frac{\lambda_s^2 (L_d - L_q) sin(2\psi)}{2 L_d L_q}] \tag{2.5.19}$$

2.6 Mechanical equation of the machine

The relationship among the machine produced electromagnetic torque T_e, load torque T_l and the machine's electrical speed ω_r, gives the mechanical equation of the machine and it can be expressed as

$$T_e = J\frac{2}{n}p\omega_r + B_m\frac{2}{n}\omega_r + T_l \qquad (2.6.1)$$

where, J is the inertia of the rotor and the connected load, and B_m is the viscous friction coefficient.

2.7 Steady state model in rotor d,q reference frame

Steady state voltage equations in rotor d,q frame can be obtained directly from the dynamic voltage equations described in (2.4.36) and (2.4.37). In steady state, since currents in the rotor reference frame i^r_{qs} and i^r_{ds} become DC values (constants) the derivative terms in (2.4.36) and (2.4.37) become zero. Therefore, the steady state voltage equations in rotor reference frame can be expressed as

$$\begin{aligned} V^r_{qs} &= r_s I^r_{qs} + \omega_0 L_d I^r_{ds} + \omega_0 \lambda_m \qquad (2.7.1)\\ V^r_{ds} &= r_s I^r_{ds} - \omega_0 L_q I^r_{qs} \qquad (2.7.2) \end{aligned}$$

where,

V^r_{qs}, V^r_{ds} - Steady state rotor q- and d- axis voltages

I^r_{qs}, I^r_{ds} - Steady state rotor q- and d- axis currents

ω_0 - Steady state electrical speed of the rotor

From (2.7.1) and (2.7.2), the rotor reference frame steady state vector diagram of the IPMSM can be drawn as in figure 2.7.

The steady state torque expression can be written from (2.5.7) as

$$T_{e0} = \frac{3}{2}\frac{n}{2}[\lambda_m I^r_{qs} + (L_d - L_q) I^r_{ds} I^r_{qs}] \qquad (2.7.3)$$

where, T_{e0} is the steady state electromagnetic torque of the machine.

2.8 Control properties

In this section, basic steady state properties of the IPMSM under different control strategies will be studied. The key control strategies for the IPMSMs are as follows [5].

1. Constant torque angle ($\alpha = \frac{\pi}{2}$) control (CTAC)

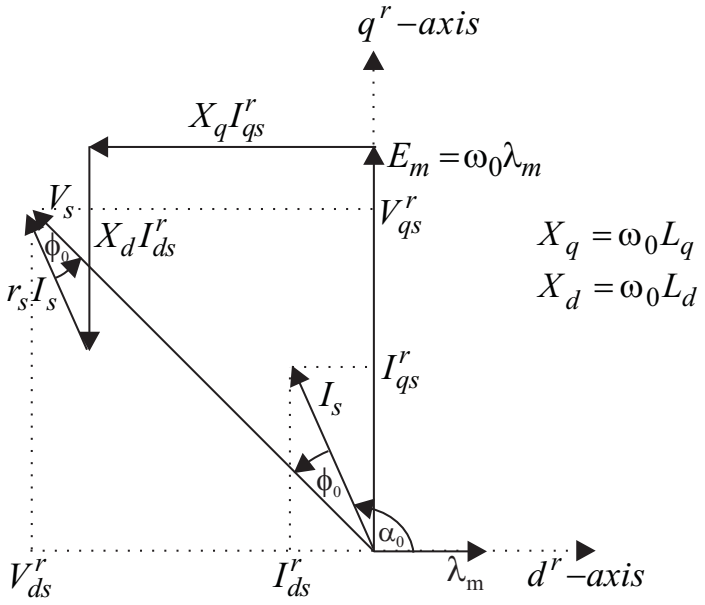

Figure 2.7: *Steady state vector diagram of the IPMSM in rotor reference frame. ϕ_0 and α_0 are steady state power factor angle and torque angle respectively.*

2. Maximum torque per ampere control (MTPAC)

3. Unity power factor control (UPFC)

4. Constant stator flux control (CSFC)

2.8.1 Normalization

In the following developments the normalized steady state machine equations are used to show the relationships among the machine variables. The base values for the normalization are selected as follows.

The base value for current (I_b) is selected as the amplitude of the rated phase current, i.e.

$$I_b = \sqrt{2} I_{rms(rated)} \tag{2.8.1}$$

The base voltage V_b is defined as

$$V_b = \omega_b \lambda_m \tag{2.8.2}$$

where,

$$\omega_b = 2\pi f_b \tag{2.8.3}$$

f_b is rated frequency of the machine.

The base value for torque (T_b) is

$$T_b = \frac{3}{2}\frac{n}{2}\lambda_m I_b \tag{2.8.4}$$

By definition, the base impedance Z_b is

$$Z_b = \frac{V_b}{I_b} \tag{2.8.5}$$

Then, the base inductance L_b is

$$L_b = \frac{Z_b}{\omega_b}. \tag{2.8.6}$$

2.8.2 Constant torque angle ($\alpha = \frac{\pi}{2}$) control

One of the easiest control strategy for IPMSMs is to control the torque angle in order to maintain it 90^0. This control can be achieved by controlling the rotor d-axis current component to zero leaving the current vector on the rotor q-axis. Therefore, this strategy is also referred to as $i^r_{ds} = 0$ control. However, it should be noted that from this control strategy the benefit of the IPMSM produced reluctance torque cannot be utilized, and therefore, this control strategy is not recommended for IPMSMs with high saliency ratio. For SPMSMs, this control strategy is the widely used and it will also become maximum torque per ampere control for SPMSMs as it will be shown later.

The relevant steady state performance equations for this control strategy is derived in the following.

Since $I^r_{ds} = 0$, from (2.7.3) the machine produced torque T_{e0} becomes

$$T_{e0} = \frac{3}{2}\frac{n}{2}\lambda_m I^r_{qs} = \frac{3}{2}\frac{n}{2}\lambda_m I_s \tag{2.8.7}$$

The normalized torque can be expressed as

$$T_{en} = \frac{T_{e0}}{T_b} = \frac{\frac{3}{2}\frac{n}{2}\lambda_m I_s}{\frac{3}{2}\frac{n}{2}\lambda_m I_b} = I_{sn} \tag{2.8.8}$$

From (2.7.1) and (2.7.2) the steady state voltage equations are

$$V^r_{qs} = r_s I^r_{qs} + \omega_0 \lambda_m = r_s I_s + \omega_0 \lambda_m \tag{2.8.9}$$

$$V^r_{ds} = -\omega_0 L_q I^r_{qs} = -\omega_0 L_q I_s \tag{2.8.10}$$

The magnitude of the voltage vector is given by,

$$V_s = \sqrt{(V^r_{qs})^2 + (V^r_{ds})^2} \tag{2.8.11}$$

The normalized voltage vector magnitude V_{sn} becomes,

$$V_{sn} = \frac{V_s}{V_b} = \frac{V_s}{\omega_b \lambda_m} = \sqrt{(r_{sn} I_{sn} + \omega_{0n})^2 + (\omega_{0n} L_{qn} I_{sn})^2} \tag{2.8.12}$$

The steady state vector diagram for this control strategy is depicted in figure 2.8.

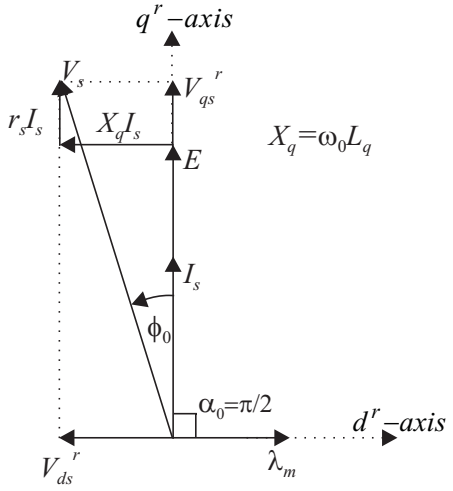

Figure 2.8: *Steady state vector diagram for constant torque angle* ($\alpha = \frac{\pi}{2}$) *control.*

2.8.3 Maximum torque per ampere control

From this control strategy, the minimum stator current magnitude can be impressed to the machine for a required electromagnetic torque [6]. Therefore, for a given operating point, the copper losses can be minimized in the machine. When the core losses are negligible, from this control method the maximum efficiency of the machine can also be obtained.

The steady state performance equations for maximum torque per ampere control are derived below.

The normalized steady state torque equation can be obtained from (2.5.12) as

$$T_{en} = \frac{T_{e0}}{T_b} = I_{sn}[sin\alpha + \frac{1}{2}(L_{dn} - L_{qn})I_{sn}sin2\alpha] \tag{2.8.13}$$

In figure 2.5, for a given current magnitude the variation of resultant torque with torque angle is shown. The torque angle, where the maximum torque is achieved for a given current, can be obtained by taking the derivative respect to torque angle of (2.8.13) and equating to zero, i.e.

$$\frac{d(T_{en})}{d\alpha} = I_{sn}[cos\alpha + (L_{dn} - L_{qn})I_{sn}cos2\alpha] = 0 \tag{2.8.14}$$

Solving for torque angle α

$$\alpha = cos^{-1}[\frac{-1}{4(L_{dn} - L_{qn})I_{sn}} \pm \sqrt{\frac{1}{2} + (\frac{1}{4(L_{dn} - L_{qn})I_{sn}})^2} \quad] \tag{2.8.15}$$

From figure 2.5, it can be seen that T_m is maximum at $\alpha = 90^0$ and the T_{re} is added to the resultant torque when $90^0 < \alpha < 180^0$. Therefore, the maximum resultant torque is

achieved always when $90^0 < \alpha < 180^0$. Because of this reason, in (2.8.15) only negative sign should be considered for the solution. Then, the expression for steady state torque angle in order to obtain maximum torque for a given current magnitude is

$$\boxed{\alpha_0 = cos^{-1}[\frac{-1}{4(L_{dn} - L_{qn})I_{sn}} - \sqrt{\frac{1}{2} + (\frac{1}{4(L_{dn} - L_{qn})I_{sn}})^2} \quad]} \tag{2.8.16}$$

The steady state voltage equations (2.7.1) and (2.7.2) can be written using the current vector magnitude I_s and the torque angle α_0 as

$$V_{qs}^r = r_s I_s sin\alpha_0 + \omega_0 L_d I_s cos\alpha_0 + \omega_0 \lambda_m \tag{2.8.17}$$

$$V_{ds}^r = r_s I_s cos\alpha_0 - \omega_0 L_q I_s sin\alpha_0 \tag{2.8.18}$$

The normalized voltage equations are

$$V_{qsn}^r = \omega_{0n}[\frac{r_{sn} I_{sn} sin\alpha_0}{\omega_{0n}} + L_{dn} I_{sn} cos\alpha_0 + 1] \tag{2.8.19}$$

$$V_{dsn}^r = \omega_{0n} I_{sn}[\frac{r_{sn} cos\alpha_0}{\omega_{0n}} - L_{qn} sin\alpha_0] \tag{2.8.20}$$

The normalized stator voltage magnitude is

$$V_{sn} = \sqrt{(V_{qsn}^r)^2 + (V_{dsn}^r)^2} \tag{2.8.21}$$

For a given current magnitude I_{sn} one can calculate α_0 from (2.8.16) and substituting those values to (2.8.13), (2.8.19) and (2.8.20) the torque and voltages can be calculated for this control strategy.

Since reluctance torque T_{re} does not exist in SPMSMs, from figure 2.5 one can observe that for a given current magnitude the maximum torque is always obtained at $\alpha = 90^0$. This means that for SPMSMs the maximum torque per ampere control is $\alpha = 90^0$ control.

Some insight into the maximum torque per ampere control technique can also get writing the normalized torque equation from I_{dsn}^r and I_{qsn}^r. From (2.5.7), the normalized torque equation can be written as

$$T_{en} = I_{qsn}^r + (L_{dn} - L_{qn}) I_{dsn}^r I_{qsn}^r \tag{2.8.22}$$

For a given torque there are infinite number of I_{dsn}^r and I_{qsn}^r values to fulfill the relationship in (2.8.22). Those values make a hyperbole in the rotor I_{dsn}^r, I_{qsn}^r plane. For different torque values, those constant torque loci in I_{dsn}^r, I_{qsn}^r plane are shown in figure 2.9. In each locus there is one point, where the current becomes minimum to obtain that torque. The locus, which those minimum current points are connected, is also shown in figure 2.9 and it is referred to as MTPA trajectory. Figure 2.9 is drawn for the IPMSM, where the parameters are given in Appendix A. The MTPA trajectory lies in the second quadrant, i.e. $90^0 < \alpha < 180^0$, as expected. For a SPMSM the MTPA trajectory should lie on $I_{dsn}^r = 0$ line.

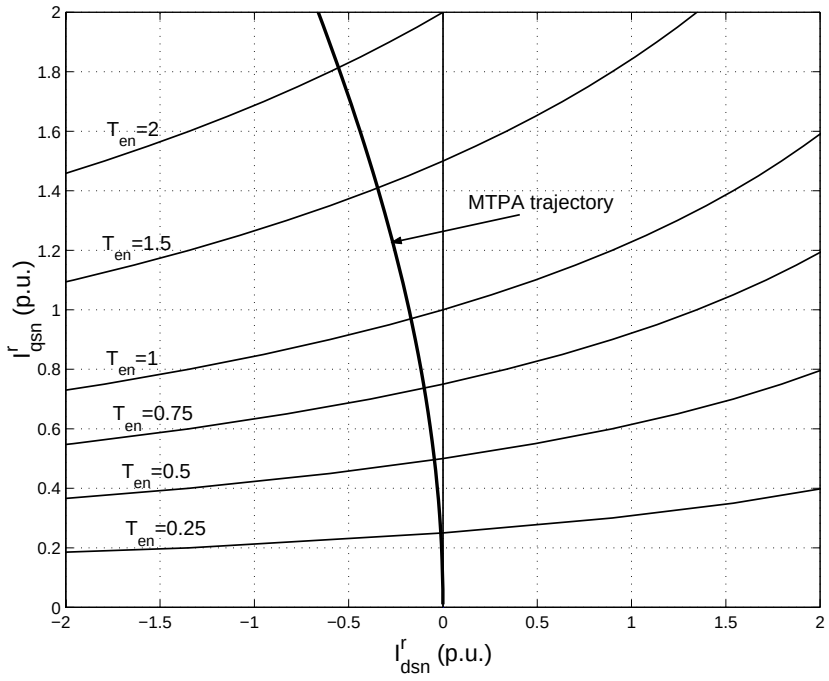

Figure 2.9: *Constant torque loci and maximum torque per ampere (MTPA) trajectory in I^r_{dsn}, I^r_{qsn} plane for the IPMSM.*

2.8.4 Unity power factor control

Since only active power is input to the machine under unity power factor control, the VA rating requirement of the inverter can be reduced.

Since power factor angle ϕ_0 becomes zero under this control strategy, there is no phase difference between the current vector and the voltage vector. This implies that the relationship

$$\frac{V^r_{qsn}}{V^r_{dsn}} = \frac{I^r_{qsn}}{I^r_{dsn}} = tan(\alpha_0) \tag{2.8.23}$$

is fulfilled. Substituting the voltages from (2.8.19) and (2.8.20), the equation (2.8.23) becomes

$$\frac{\frac{r_{sn}I_{sn}sin\alpha_0}{\omega_{0n}} + L_{dn}I_{sn}cos\alpha_0 + 1}{I_{sn}[\frac{r_{sn}cos\alpha_0}{\omega_{0n}} - L_{qn}sin\alpha_0]} = \frac{sin\alpha_0}{cos\alpha_0} \tag{2.8.24}$$

After simplifying, (2.8.24) becomes

$$I_{sn}(L_{qn}sin^2\alpha_0 + L_{dn}cos^2\alpha_0) = -cos\alpha_0 \tag{2.8.25}$$

Solving for torque angle α_0

$$\alpha_0 = cos^{-1}[\frac{-1 \pm \sqrt{1 - 4L_{qn}I^2_{sn}(L_{dn} - L_{qn})}}{2I_{sn}(L_{dn} - L_{qn})}] \tag{2.8.26}$$

In order to utilize the maximum torque for a given current magnitude of the IPMSM, $90^0 < \alpha_0 < 180^0$ (see figure 2.5). That is, $cos(\alpha_0) < 0$, and therefore, only positive sign must be considered in (2.8.26) (It should also be noted that $L_{dn} < L_{qn}$ for an IPMSM). Therefore,

$$\boxed{\alpha_0 = cos^{-1}[\frac{-1 + \sqrt{1 - 4L_{qn}I_{sn}^2(L_{dn} - L_{qn})}}{2I_{sn}(L_{dn} - L_{qn})}]} \tag{2.8.27}$$

After obtaining α_0 for a given current magnitude, the steady state normalized torque and voltages can be calculated for this control strategy from (2.8.13), (2.8.19), (2.8.20) and (2.8.21) respectively.

2.8.5 Constant stator flux control

Limiting the stator flux linkage magnitude λ_s, the stator voltage requirement can be kept comparably low. However, when limiting the stator flux linkage magnitude the torque producing capability of the machine is also limited.

As it can be seen from the torque expression (2.5.19), for a given stator flux magnitude λ_s the electromagnetic torque T_e is a function of ψ (the angle between stator flux linkage vector and the rotor permanent-magnet flux vector). This is depicted in figure 2.10 for different stator flux magnitudes (Machine parameters are given in Appendix A). As it can be seen from figure 2.10 when the magnitude of the stator flux is decreased the maximum torque, which can be produced by the machine is also decreased.

When controlling the flux for PMSMs, usually, the stator flux linkage magnitude λ_s is kept constant at a value equal to the rotor permanent-magnet flux magnitude λ_m, i.e. $\lambda_s = 1$ p.u.. With this selection, the stator voltage requirement to the machine can be kept comparably low and the torque producing capability of the machine is also not degraded.

In the following, the steady state performance equations are derived for the machine, when the stator flux linkage magnitude is equal to λ_m.

The magnitude of the stator flux linkage vector is

$$\lambda_s = \sqrt{(\lambda_{qs}^r)^2 + (\lambda_{ds}^r)^2} = \sqrt{(L_q I_{qs}^r)^2 + (L_d I_{ds}^r + \lambda_m)^2} \tag{2.8.28}$$

Equating

$$\lambda_s = \lambda_m \tag{2.8.29}$$

one can obtain the relationship for rotor frame currents as

$$(L_q I_{qs}^r)^2 + (L_d I_{ds}^r)^2 + 2L_d \lambda_m I_{ds}^r = 0 \tag{2.8.30}$$

Since $[(L_q I_{qs}^r)^2 + (L_d I_{ds}^r)^2] > 0$ and the machine parameters are positive values in (2.8.30), it can easily be seen that it should always $I_{ds}^r < 0$ for this control strategy.

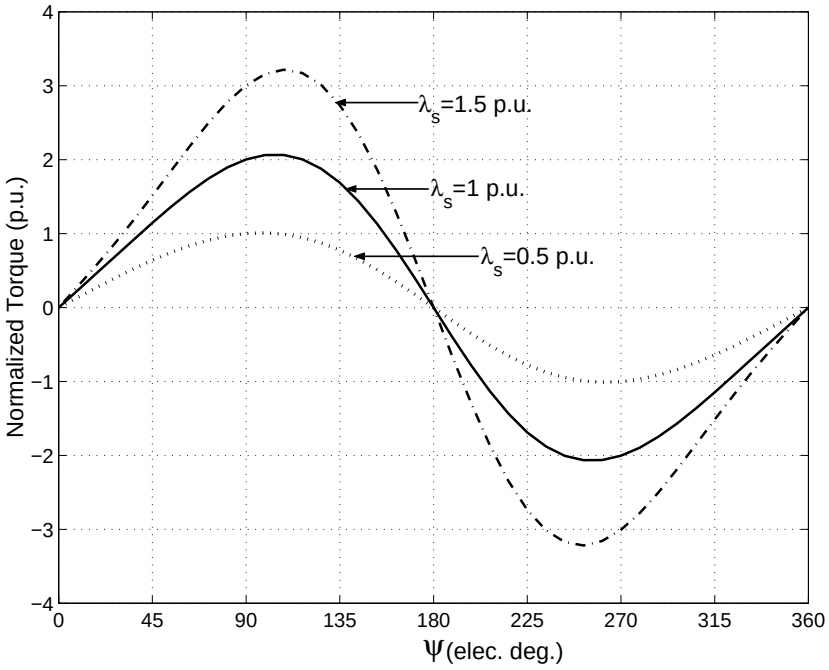

Figure 2.10: *For a given stator flux magnitude λ_s, the variation of the electromagnetic torque with ψ (the angle between stator flux linkage vector and the rotor permanent-magnet flux vector).*

If the rotor frame current components in (2.8.30) are substituted from the current vector magnitude and the torque angle using (2.5.10) and (2.5.11), the following expression can be obtained.

$$I_s = \frac{-2\lambda_m L_d cos\alpha_0}{L_q^2 sin^2\alpha_0 + L_d^2 cos^2\alpha_0} \tag{2.8.31}$$

After normalizing (2.8.31) one obtains

$$I_{sn} = \frac{-2cos\alpha_0}{L_{dn}(\sigma^2 sin^2\alpha_0 + cos^2\alpha_0)} \tag{2.8.32}$$

where,

$$\sigma = \frac{L_q}{L_d} = \frac{L_{qn}}{L_{dn}}. \tag{2.8.33}$$

Note $\sigma > 1$ for the IPMSMs.

The torque angle α_0 can be obtained from (2.8.32) as

$$\alpha_0 = cos^{-1}[\frac{-1}{I_{sn}L_{dn}(1-\sigma^2)} \pm \sqrt{(\frac{1}{I_{sn}L_{dn}(1-\sigma^2)})^2 - \frac{\sigma^2}{(1-\sigma^2)}} \quad] \tag{2.8.34}$$

Since $I_{ds}^r < 0$ for this control strategy, $90^0 < \alpha_0 < 180^0$,and therefore, only the negative sign should be considered in (2.8.34).

$$\boxed{\alpha_0 = cos^{-1}[\frac{-1}{I_{sn}L_{dn}(1-\sigma^2)} - \sqrt{(\frac{1}{I_{sn}L_{dn}(1-\sigma^2)})^2 - \frac{\sigma^2}{(1-\sigma^2)}} \quad]} \tag{2.8.35}$$

For a given stator current magnitude the α_0 can be calculated from (2.8.35) for this control strategy. The torque and voltages can be calculated using (2.8.13), (2.8.19), (2.8.20) and (2.8.21) respectively.

2.8.6 Comparison of control strategies

In order to compare the steady state performance characteristics of the above discussed control strategies, for each of the control strategy some important quantities of the machine are plotted as a function of the torque. The IPMSM parameters, which are used for the calculations are given in Appendix A.

The current requirement as a function of torque is illustrated in figure 2.11 for the different control strategies. It should be noted that for a given current the calculation of torque angle and torque is independent of the speed as it is seen when deriving the steady state performance equations for the control strategies (see (2.8.16),(2.8.27),(2.8.35) and (2.8.13)). Therefore, the relationships shown in figure 2.11 are independent of the speed of the machine.

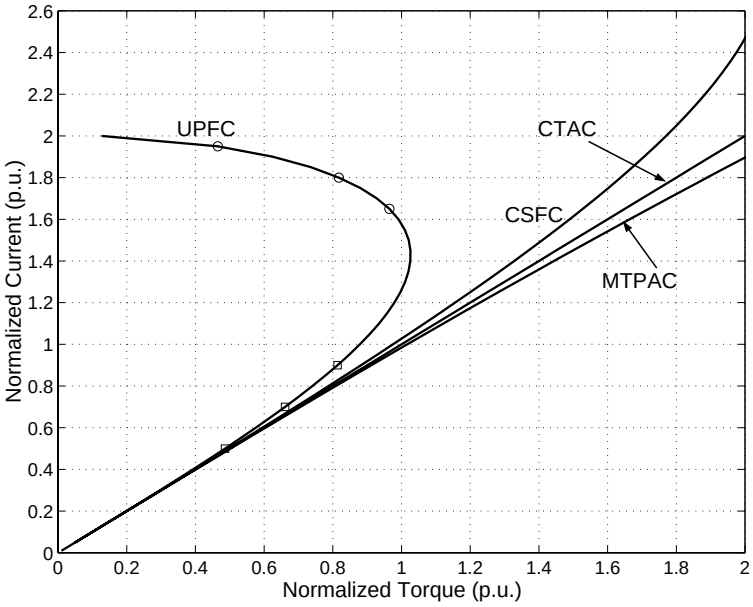

Figure 2.11: *Current requirement for different control strategies as a function of torque.*

It can be seen from figure 2.11, the MTPA requires the lowest current for a given torque as it is expected. However, up to 1 p.u. torque, there is no major difference for current requirements for CTAC, CSFC and MTPAC. From UPFC, the maximum torque, which can be produced in the machine is about 1 p.u.. Moreover, it can also be seen that there are two operating points in the machine for UPFC for each torque value up to that torque. However, it should be noted that the operating point with high current value cannot exist due to the current limitations to the machine. Even with lower current operating point UPFC requires somewhat higher current compared to the others when the torque is higher than about 0.6 p.u.. (Note that in every figure in this section, the two parts of the curve related to UPFC are marked with circles and squares in order to recognize the corresponding part of the curve in each figure. As it is mentioned, practically, the part with circles cannot exist for UPFC.)

The voltage requirements for the control strategies as a function of torque for two different speeds (1 p.u. speed and 0.1 p.u. speed) are shown in figure 2.12. Both high and low speeds the voltage requirement for UPFC is the lowest. For CTAC is the highest.

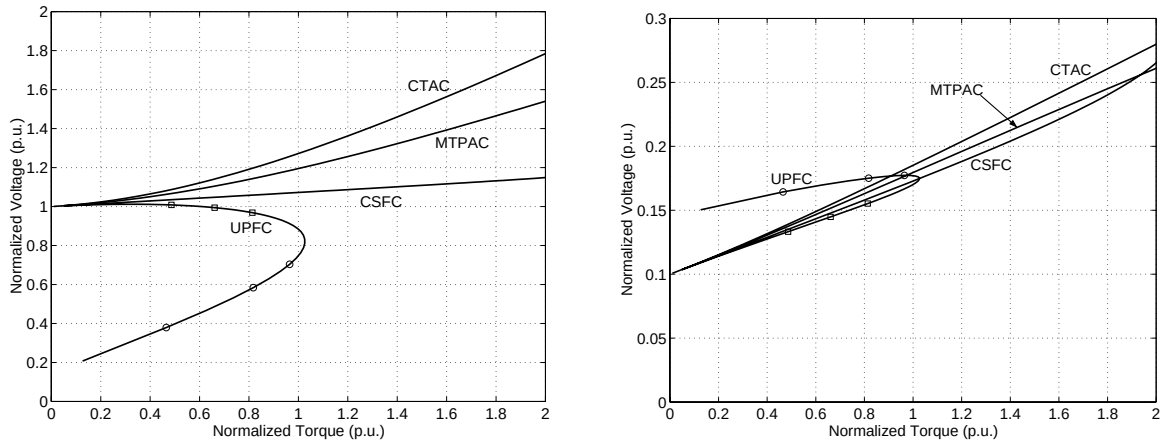

Figure 2.12: *Voltage requirement for different control strategies as a function of torque. (a) Rotor speed at 1 p.u. (b) Rotor speed at 0.1 p.u..*

VA rating requirement for different control strategies as a function of torque at 1 p.u. speed is shown in figure 2.13. VA rating comparison at high speed is the most important since the highest required VA rating for control strategies can be seen at high speeds. It can be seen from figure 2.13, both UPFC and CSFC have the lowest VA rating requirement. CTAC requires the highest VA rating.

The power factor variation as a function of torque for different control strategies is shown in figure 2.14. Both high and low speeds, the power factor decreases rapidly for CTAC compared to the others when the torque is increased. CSFC keeps the power

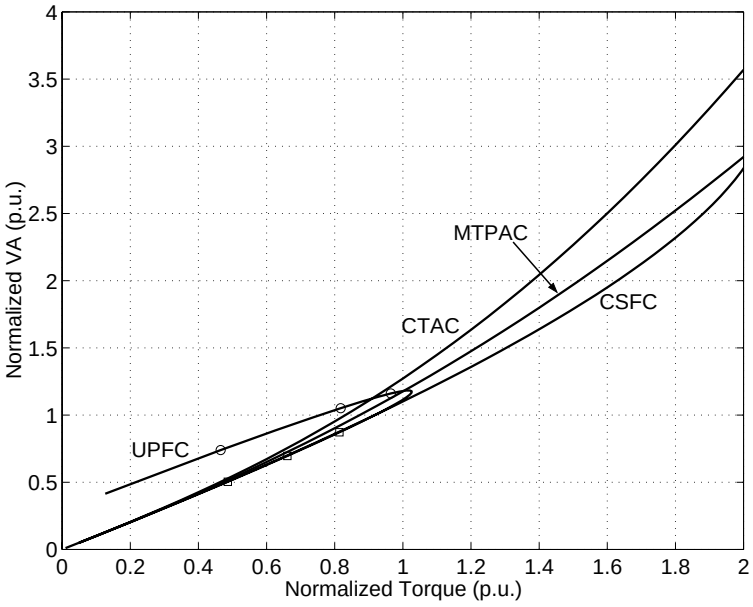

Figure 2.13: *VA rating requirement for different control strategies as a function of torque at 1 p.u. rotor speed.*

factor very close to unity until the torque reaches about 1 p.u..

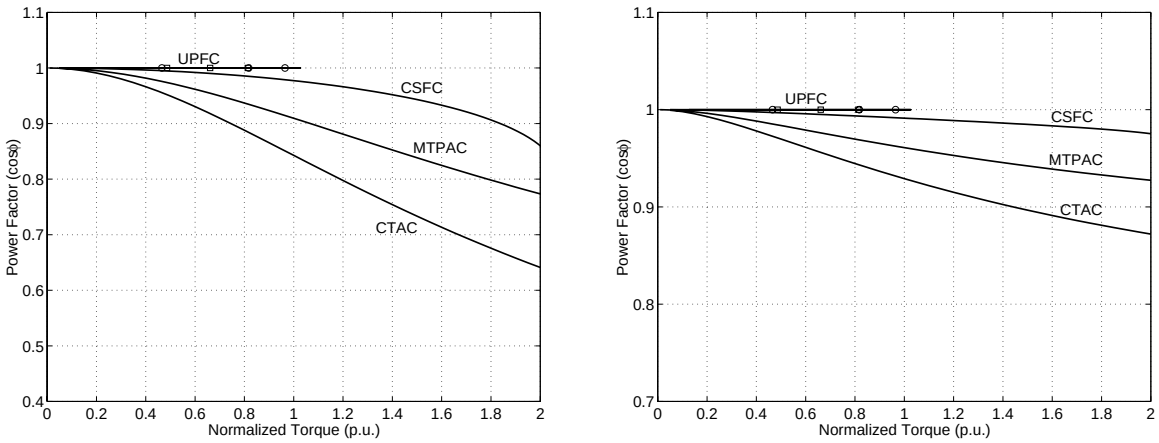

(a) (b)

Figure 2.14: *Variation of the power factor for different control strategies as a function of torque. (a) Rotor speed at 1 p.u. (b) Rotor speed at 0.1 p.u..*

The steady state performance characteristics comparison which was shown in figure 2.11, figure 2.12, figure 2.13 and figure 2.14 can be summarized based on the control strategies as below.

It can be seen that the voltage requirement is relatively high for CTAC. Even though

the current requirement is not very high, the high voltage requirement increases the VA rating. CTAC deteriorates the power factor when the load or the speed is increased in the machine.

The main advantage of MTPAC is the lowest current requirement to the machine. However, the voltage requirement is only second to CTAC. The high voltage requirement increases the VA rating. The power factor is only second to CTAC.

The benefit of the UPFC is the voltage requirement is relatively low to the machine. However, UPFC can only produce about 1 p.u. torque in the machine, which is the main drawback. When torque is increased, relatively high current is required to the machine from UPFC.

The voltage requirement for CSFC is only second to UPFC. However, CSFC can produce much higher torque in the machine compared to UPFC. Even though the current requirement is high at high torques, up to 1 p.u. torque there is no significant different between CSFC and MTPAC. CSFC also has the lowest VA rating requirement. The power factor is only second to UPFC and it is very close to unity up to 1 p.u. torque.

From this comparison study it can be concluded that the CSFC has better steady state performance characteristics compared to the others and it should be a good control strategy to consider.

2.9 Summary

The mathematical models for IPMSM have been derived in this chapter. Even though there are different forms to express the IPMSM voltage equations, the rotor d,q reference frame voltage equations are the most convenient. The simplification in rotor d,q reference frame voltage equations is due to the disappearance of position dependent inductances in those equations.

The electromagnetic torque of the IPMSM is not only produced by the permanent-magnet flux but also by the reluctance difference in rotor d- and q-axes. This is different from SPMSMs where the electromagnetic torque is only produced by the permanent-magnet flux.

The steady state performance characteristic equations for key control strategies of IPMSM have also been derived in this chapter. The comparison of steady state performance characteristics of the key control strategies reveals that the overall performance of the constant stator flux linkage control strategy is better compared to other control strategies.

Bibliography

[1] Paul C. Krause, Oleg Wasynczuk and Scott D. Sudhoff, *Analysis of Electric Machinery*, IEEE Press, 1995.

[2] Marian P. Kazmierkowski and Henryk Tunia, *Automatic Control of Converter-Fed Drives*, Elsevier Science Publishers B.V., 1994.

[3] D. W. Novotny and T. A. Lipo, *Vector Control and Dynamics of AC Drives*, Oxford University Press, 1998.

[4] Peter Vas, *Sensorless Vector and Direct Torque Control*, Oxford University Press, 1998.

[5] R. Krishnan, *Electric Motor Drives: Modeling, Analysis, and Control*, Prentice Hall, First Edition, 2001.

[6] Thomas M. Jahns, Gerald B. Kliman and Thomas W. Neumann, *Interior Permanent-Magnet Synchronous Motors for Adjustable-Speed Drives*, IEEE Transactions on Industry Applications, Vol. IA-22, No.4, pp. 738-747, July/August 1986.

Part II

Sensorless Stable V/f Control of PMSMs

Chapter 3

Stability Characteristics of PMSMs Under Open-Loop V/f Control

3.1 Introduction

When PMSM drives are used for applications like pumps and fans, where high dynamic performance is not a demand, V/f control of them may be sufficient to achieve the required control performance. However, as described in § 1.2 of Chapter 1, the V/f control of PMSMs can only be achieved in closed-loop manner, in order to assure the self synchronization. This makes the design of V/f control for PMSMs somewhat difficult. In order to obtain the background knowledge for designing the V/f control of PMSMs in closed-loop manner, it is important to understand the stability characteristics of PMSMs under open-loop V/f control. The open-loop V/f control is referred to as, the V/f control without incorporating any feedback for self synchronization as shown in figure 3.1.

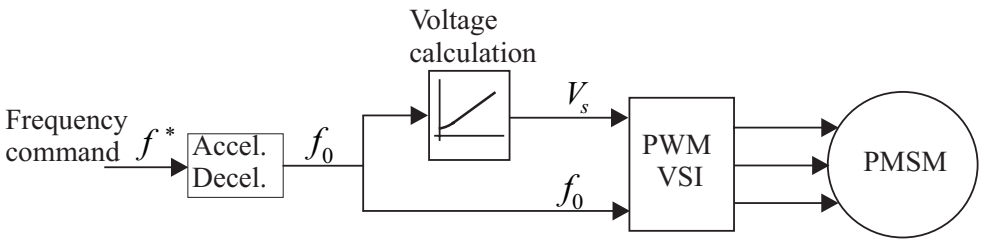

Figure 3.1: *Open-loop V/f control of PMSMs.*

The objective of this chapter is to study the stability characteristics of PMSMs under open-loop V/f control. For this purpose, to use linear system theory for analysis, the nonlinear PMSM equations derived in Chapter 2 are linearized. This linearized PMSM model is the tool for studying the stability behaviour of the PMSMs under open-loop V/f control. Computer simulations and experimental results are provided to validate the results obtained from the linearized PMSM model analysis.

3.2 Linearized PMSM model

3.2.1 PMSM equations in state variable form

The PMSM's rotor d^r, q^r frame voltage equations, torque expression and the mechanical equation, which are derived in Chapter 2, are used here to develop the linearized machine model of the PMSM. Here, another machine variable is defined, that is, the load angle δ, which is useful for the analysis.

The load angle δ is defined as

$$\delta = \theta_e - \theta_r \tag{3.2.1}$$

where, θ_e and θ_r are electrical angular position of applied stator voltage vector and electrical rotor angular position respectively. Figure 3.2 illustrates the load angle δ defined in (3.2.1).

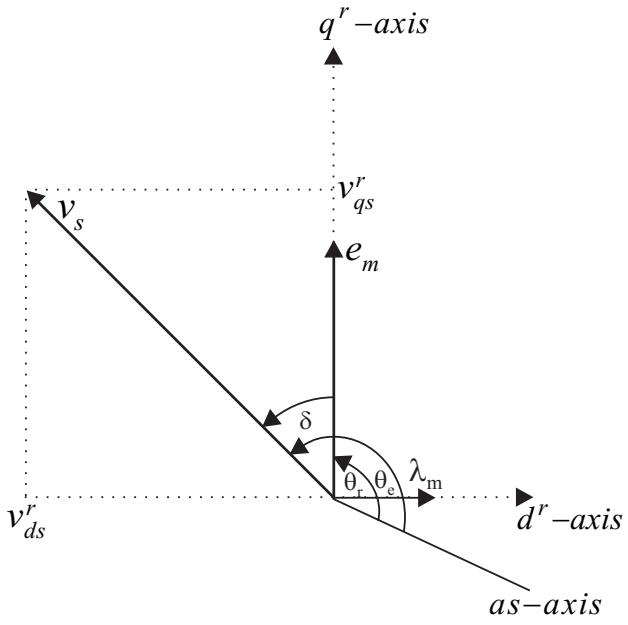

Figure 3.2: *Rotor reference frame vector diagram showing the load angle δ.*

Differentiating (3.2.1) one can obtain

$$p\delta = \omega_e - \omega_r \tag{3.2.2}$$

where, ω_e and ω_r are the electrical angular speed of applied voltage vector and the rotor respectively.

Using δ, the rotor frame voltage components v_{qs}^r and v_{ds}^r can be obtained as

$$v_{qs}^r = v_s cos(\delta) \tag{3.2.3}$$

$$v_{ds}^r = -v_s sin(\delta) \tag{3.2.4}$$

where, v_s is the magnitude of the applied voltage vector.

Substituting v_{qs}^r and v_{ds}^r from (3.2.3) and (3.2.4) to (2.4.36) and (2.4.37) derived in Chapter 2, the following equations can be obtained.

$$v_s cos(\delta) = r_s i_{qs}^r + pL_q i_{qs}^r + \omega_r L_d i_{ds}^r + \omega_r \lambda_m \tag{3.2.5}$$

$$-v_s sin(\delta) = r_s i_{ds}^r + pL_d i_{ds}^r - \omega_r L_q i_{qs}^r \tag{3.2.6}$$

Substituting the torque expression (2.5.7) to the mechanical equation (2.6.1) one obtains

$$\frac{3}{2}\frac{n}{2}[\lambda_m i_{qs}^r + (L_d - L_q) i_{ds}^r i_{qs}^r] = J\frac{2}{n}p\omega_r + B_m\frac{2}{n}\omega_r + T_l \tag{3.2.7}$$

The four equations (3.2.5), (3.2.6), (3.2.7) and (3.2.2) can be rearranged to obtain the four system equations in state variable form as

$$\begin{aligned}
pi_{qs}^r &= \frac{-i_{qs}^r}{\sigma\tau_s} - \frac{\omega_r}{\sigma}\left(\frac{\lambda_m}{L_d} + i_{ds}^r\right) + \frac{v_s cos(\delta)}{\sigma L_d} && (3.2.8)\\
pi_{ds}^r &= \frac{-i_{ds}^r}{\tau_s} + \sigma\omega_r i_{qs}^r - \frac{v_s sin(\delta)}{L_d} && (3.2.9)\\
p\omega_r &= \frac{3}{2J}\left(\frac{n}{2}\right)^2[\lambda_m i_{qs}^r + L_d(1-\sigma) i_{qs}^r i_{ds}^r] - \frac{1}{J}B_m\omega_r - \frac{n}{2J}T_l && (3.2.10)\\
p\delta &= \omega_e - \omega_r && (3.2.11)
\end{aligned}$$

In these equations

$$\tau_s = \frac{L_d}{r_s} \tag{3.2.12}$$

$$\sigma = \frac{L_q}{L_d} \tag{3.2.13}$$

3.2.2 Linearization

The above obtained machine state equations (3.2.8)-(3.2.11) have the form

$$\dot{x} = \mathbf{f}(x, u) \tag{3.2.14}$$

where, x is the vector of the machine state variables and $\mathbf{f}$ is the nonlinear function of the state x and the inputs u.

The linearized form of the nonlinear system given in (3.2.14) can be written as

$$\dot{\Delta x} = A(X)\Delta x + B(X)\Delta u \tag{3.2.15}$$

where, Δx is perturbation matrix for state variables x, $A(X)$ is state transition matrix, Δu is input perturbation matrix and $B(X)$ is input matrix [1], [2].

The linearized state equations in (3.2.15) can be obtained from the nonlinear state equations in (3.2.14) as described below.

It should be considered the each machine state variables in (3.2.14) is composed of a steady state component X and a small perturbation (Δx_i) as

$$x_i = X + \Delta x_i \tag{3.2.16}$$

In (3.2.16), x_i is the i th state variable.

Substituting (3.2.16) for the corresponding state variable in (3.2.14), and cancelling steady state terms and neglecting second order perturbations the linearized equations in (3.2.15) are obtained [1], [2], [3], [4].

Applying this linearizing method to the nonlinear PMSM state equations described in (3.2.8)-(3.2.11), the obtained linearized PMSM equations can be written in matrix form as

$$p\begin{bmatrix}\Delta i_{qs}^r\\ \Delta i_{ds}^r\\ \Delta\omega_r\\ \Delta\delta\end{bmatrix} = \begin{bmatrix}\frac{-1}{\sigma\tau_s} & \frac{-\omega_0}{\sigma} & \frac{-1}{\sigma}(\frac{\lambda_m}{L_d}+I_{ds}^r) & \frac{-V_s}{\sigma L_d}sin(\delta_0)\\ \sigma\omega_0 & \frac{-1}{\tau_s} & \sigma I_{qs}^r & \frac{-V_s}{L_d}cos(\delta_0)\\ \frac{3}{2}(\frac{n}{2})^2\frac{1}{J}[\lambda_m+L_d(1-\sigma)I_{ds}^r] & \frac{3}{2}(\frac{n}{2})^2\frac{1}{J}L_d(1-\sigma)I_{qs}^r & \frac{-B_m}{J} & 0\\ 0 & 0 & -1 & 0\end{bmatrix}\begin{bmatrix}\Delta i_{qs}^r\\ \Delta i_{ds}^r\\ \Delta\omega_r\\ \Delta\delta\end{bmatrix} + \begin{bmatrix}\frac{cos(\delta_0)}{\sigma L_d} & 0 & 0\\ \frac{-sin(\delta_0)}{L_d} & 0 & 0\\ 0 & 0 & \frac{-n}{2J}\\ 0 & 1 & 0\end{bmatrix}\begin{bmatrix}\Delta v_s\\ \Delta\omega_e\\ \Delta T_l\end{bmatrix} \tag{3.2.17}$$

In the linearized system given in (3.2.17), the state transition matrix (the system matrix)

$$A(X) = \begin{bmatrix}\frac{-1}{\sigma\tau_s} & \frac{-\omega_0}{\sigma} & \frac{-1}{\sigma}(\frac{\lambda_m}{L_d}+I_{ds}^r) & \frac{-V_s}{\sigma L_d}sin(\delta_0)\\ \sigma\omega_0 & \frac{-1}{\tau_s} & \sigma I_{qs}^r & \frac{-V_s}{L_d}cos(\delta_0)\\ \frac{3}{2}(\frac{n}{2})^2\frac{1}{J}[\lambda_m+L_d(1-\sigma)I_{ds}^r] & \frac{3}{2}(\frac{n}{2})^2\frac{1}{J}L_d(1-\sigma)I_{qs}^r & \frac{-B_m}{J} & 0\\ 0 & 0 & -1 & 0\end{bmatrix} \tag{3.2.18}$$

where

I^r_{qs}, I^r_{ds}	-	Magnitude of the steady state rotor q^r- and d^r- axis currents
V_s	-	Magnitude of the steady state stator applied voltage
ω_0	-	Steady state electrical speed of the rotor
δ_0	-	Steady state load angle

The PMSM's voltages and currents in the rotor fixed reference frame become constant values in a steady state operating point, and therefore, the state transition matrix $A(X)$ also becomes a constant matrix (time invariant) in the linearized model described in (3.2.17) for that operating point. This makes the analysis of the system more convenient and this advantage is due to the selection of the PMSM equations in the rotor fixed reference frame [5].

The above obtained matrix form of the linearized machine model can also be illustrated in block diagram form as shown in figure 3.3.

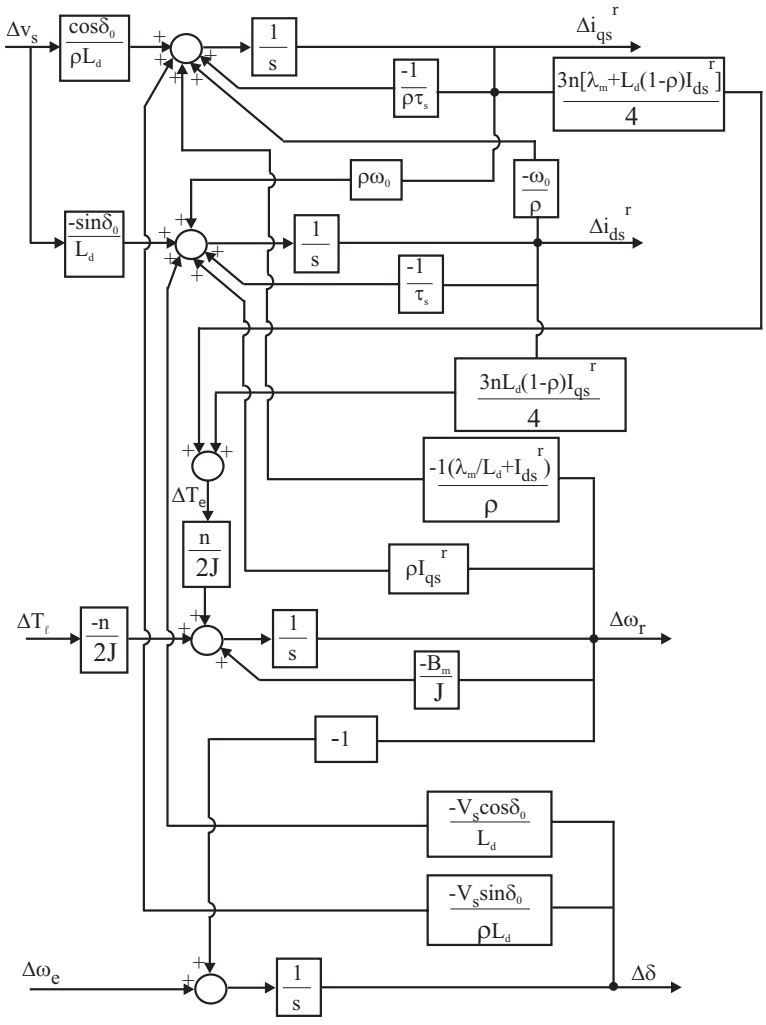

Figure 3.3: *Block diagram form of the linearized PMSM model.*

3.3 Linearized PMSM model under open-loop V/f control

Under open-loop V/f control the commanded voltage magnitude and the frequency are directly applied to the PMSM. No adjustments are made for them measuring other signals. This means that there are no perturbation components in the applied voltage magnitude and the frequency, i.e. the conditions

$$\Delta v_s = 0 \tag{3.3.1}$$

$$\Delta \omega_e = 0 \tag{3.3.2}$$

are fulfilled.

Applying these two conditions to the linearized PMSM model in matrix equation (3.2.17), the PMSM model under open-loop V/f control can be obtained as

$$p \begin{bmatrix} \Delta i_{qs}^r \\ \Delta i_{ds}^r \\ \Delta \omega_r \\ \Delta \delta \end{bmatrix} = \begin{bmatrix} \frac{-1}{\sigma \tau_s} & \frac{-\omega_0}{\sigma} & \frac{-1}{\sigma}(\frac{\lambda_m}{L_d} + I_{ds}^r) & \frac{-V_s}{\sigma L_d} sin(\delta_0) \\ \sigma \omega_0 & \frac{-1}{\tau_s} & \sigma I_{qs}^r & \frac{-V_s}{L_d} cos(\delta_0) \\ \frac{3}{2}(\frac{n}{2})^2 \frac{1}{J}[\lambda_m + L_d(1-\sigma) I_{ds}^r] & \frac{3}{2}(\frac{n}{2})^2 \frac{1}{J} L_d (1-\sigma) I_{qs}^r & \frac{-B_m}{J} & 0 \\ 0 & 0 & -1 & 0 \end{bmatrix} \begin{bmatrix} \Delta i_{qs}^r \\ \Delta i_{ds}^r \\ \Delta \omega_r \\ \Delta \delta \end{bmatrix} + \begin{bmatrix} 0 \\ 0 \\ \frac{-n}{2J} \\ 0 \end{bmatrix} \Delta T_l \tag{3.3.3}$$

Now, the state transition matrix of the system $A_1(X)$ is

$$A_1(X) = \begin{bmatrix} \frac{-1}{\sigma \tau_s} & \frac{-\omega_0}{\sigma} & \frac{-1}{\sigma}(\frac{\lambda_m}{L_d} + I_{ds}^r) & \frac{-V_s}{\sigma L_d} sin(\delta_0) \\ \sigma \omega_0 & \frac{-1}{\tau_s} & \sigma I_{qs}^r & \frac{-V_s}{L_d} cos(\delta_0) \\ \frac{3}{2}(\frac{n}{2})^2 \frac{1}{J}[\lambda_m + L_d(1-\sigma) I_{ds}^r] & \frac{3}{2}(\frac{n}{2})^2 \frac{1}{J} L_d (1-\sigma) I_{qs}^r & \frac{-B_m}{J} & 0 \\ 0 & 0 & -1 & 0 \end{bmatrix} \tag{3.3.4}$$

and it is same as $A(X)$ given in (3.2.18).

Taking into account the two relationships

$$V_s cos(\delta_0) = V_{qs}^r \tag{3.3.5}$$

$$-V_s sin(\delta_0) = V_{ds}^r \tag{3.3.6}$$

the $A_1(X)$ can also be written without involving δ_0 as follows.

$$A_1(X) = \begin{bmatrix} \frac{-1}{\sigma\tau_s} & \frac{-\omega_0}{\sigma} & \frac{-1}{\sigma}(\frac{\lambda_m}{L_d} + I_{ds}^r) & \frac{V_{ds}^r}{\sigma L_d} \\ \sigma\omega_0 & \frac{-1}{\tau_s} & \sigma I_{qs}^r & \frac{-V_{qs}^r}{L_d} \\ \frac{3}{2}(\frac{n}{2})^2\frac{1}{J}[\lambda_m + L_d(1-\sigma)I_{ds}^r] & \frac{3}{2}(\frac{n}{2})^2\frac{1}{J}L_d(1-\sigma)I_{qs}^r & \frac{-B_m}{J} & 0 \\ 0 & 0 & -1 & 0 \end{bmatrix} \tag{3.3.7}$$

Under open-loop V/f control, the small signal dynamics (or linearized system dynamics) of the system can also be visualized in terms of the block diagram form as shown in figure 3.4. One can obtain this block diagram taking into account the relationships given in (3.3.1) and (3.3.2) to the full small signal dynamics model given in the block diagram form in figure 3.3.

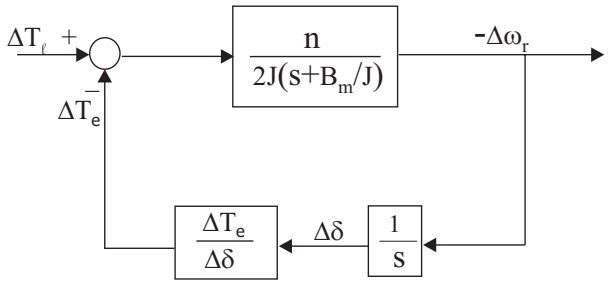

Figure 3.4: *Block diagram form of the linearized PMSM model under open-loop V/f control.*

The block diagram in figure 3.4 shows that the torque perturbations produce rotor speed perturbations (through the rotor mechanical dynamics), which in turn create load angle and torque perturbations which are feedback in a closed-loop system. The characteristic equation for this system is

$$1 + \frac{n}{2Js(s + \frac{B_m}{J})}(\frac{\Delta T_e}{\Delta\delta}) = 0 \tag{3.3.8}$$

One can find the transfer function for $\frac{\Delta T_e}{\Delta \delta}$ in (3.3.8), by linearizing the torque equation (2.5.7) and considering the first, second and fourth equations in the matrix equation (3.3.3). The derivation of this transfer function is given in Appendix B.1.

3.4 Investigation of stability characteristics under open-loop V/f control

After obtaining the linearized model of the system under open-loop V/f control, the system can be analyzed using the linear system theory. According to the linear system theory, the eigenvalues of the state transition matrix $A_1(X)$ express the poles of the system. Therefore, the location of the eigenvalues of $A_1(X)$ in the s-plane indicates the system's stability characteristics for the conditions under consideration. The eigenvalues of $A_1(X)$ (system poles) are determined by the solution to the determinant equation

$$det(s\mathbf{I} - A_1(X)) = 0 \tag{3.4.1}$$

where, $\mathbf{I}$ is the unit matrix.

The system poles can also be found from the solutions to the characteristic equation (3.3.8). However, in this section the eigenvalues of the state transition matrix $A_1(X)$ are used to investigate the stability characteristics of PMSMs under open loop V/f control. The eigenvalue plots of $A_1(X)$, which are drawn as a function of a appropriate parameter, will be the key to understand any instability and the damping of the system for the conditions under consideration. The IPMSM parameters, which are given in Appendix A, are used for the following calculations.

3.4.1 The machine under no-load

Under no-load, the ideal condition is assumed, i.e. the machine does not produce a torque, and therefore, $I^r_{qs} = 0$. In order to reduce the losses I^r_{ds} does not need to flow in the machine under no-load. Therefore, under no-load the voltage is applied to the machine only to compensate the back EMF (E_m) produced by the rotor PM flux. This implies that the conditions for no-load are, $V_s = E_m = \omega_0 \lambda_m = V^r_{qs}$, $I^r_{qs} = 0$ and $V^r_{ds} = 0$, $I^r_{ds} = 0$. Applying these conditions to the matrix $A_1(X)$ given in (3.3.7), the drawn eigenvalue plot of it, as a function of the applied frequency is shown in figure 3.5. This plot is symmetric on the real axis and the four parts correspond to the four eigenvalues of matrix $A_1(X)$ for each operating point.

From figure 3.5, it can be seen that, when the applied frequency is increased, one set of poles is moving away from the imaginary axis in the left half of the s-plane. For high frequencies the real part of the eigenvalues is almost a constant for this set. The damping of the other set decreases with increasing frequency and above a certain frequency the eigenvalues migrate into the right half of the s-plane making the system

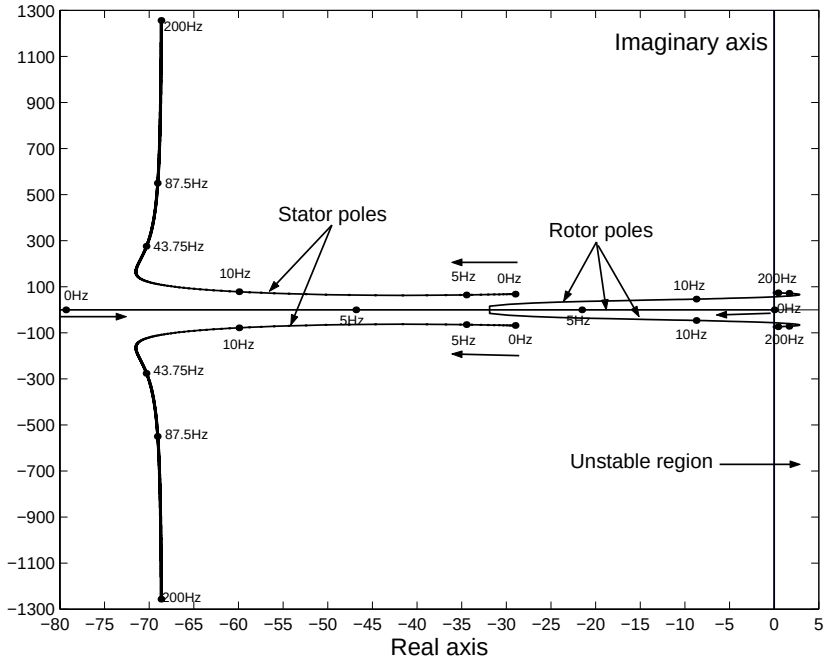

Figure 3.5: *Eigenvalue plot for the machine under no-load, as a function of the applied frequency.*

unstable. After this crossing frequency this set of poles remain in the unstable region when the applied frequency is increased.

It should be noted that the set of poles, which is comparably fast in figure 3.5 represents the fast acting electrical dynamics in the stator of the machine. These poles are referred to as "stator" poles of the machine. The remaining set of poles, which is comparably slow, represents the mechanical dynamics of the machine. This set of poles is referred to as "rotor" poles of the machine [2]. From figure 3.5, it can be seen that the rotor poles of the machine become dominant poles since they mainly impact on the stability characteristics of the machine. An enlarged view of these rotor poles in the s-plane is shown in figure 3.6. From figure 3.6 it can be seen that the machine becomes unstable after about 15 Hz.

Figure 3.7 illustrates the loci of the rotor poles with different inertia of the system, under no-load, as a function of the applied frequency. When the inertia of the system is increased the mechanical dynamics of the machine become slow. This can clearly be seen from figure 3.7, where the rotor poles become slow when the inertia is increased. It can also be seen in figure 3.7, the oscillation frequency decreases in the machine when increasing the inertia of the system, also as expected. However, the instability in the machine still exists with increased inertia.

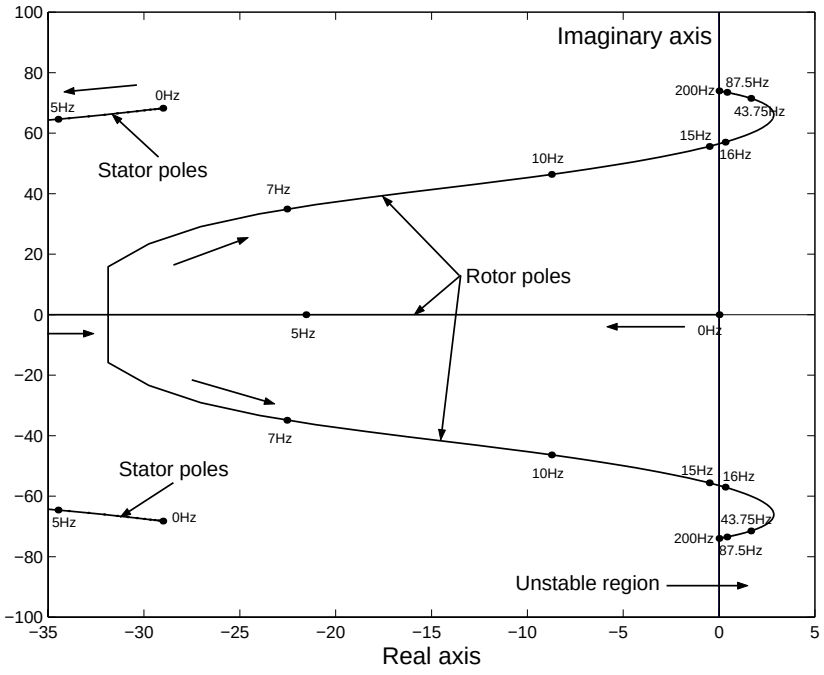

Figure 3.6: *Enlarged view of rotor poles of the machine, under no load, as a function of the applied frequency.*

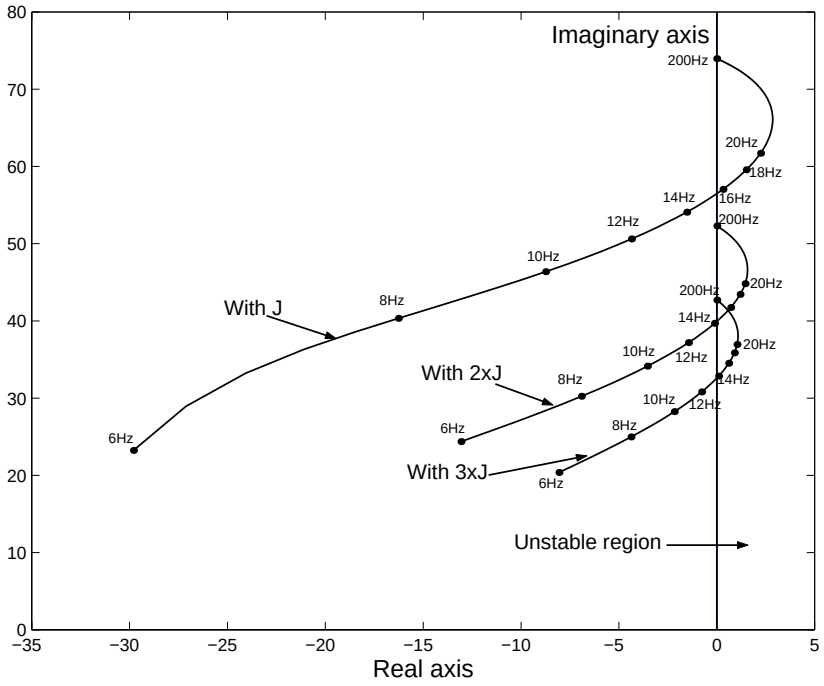

Figure 3.7: *The loci of the rotor poles with different inertia of the system, under no-load, as a function of the applied frequency.*

3.4.2 The machine under load

When the machine under load, the stability characteristics are investigated under the different control strategies discussed in §2.8 of Chapter 2. Under load, the steady state values of the machine variables (i.e. $I^r_{qs}, I^r_{ds}, V^r_{qs}, V^r_{ds}$), which require to determine the elements of state transition matrix $A_1(X)$, are calculated under those different control strategies.

Figure 3.8 shows the eigenvalue plot of matrix $A_1(X)$, machine under full-load, with constant stator flux linkage control strategy, as a function of the applied frequency. The shape of this eigenvalue plot is very similar to the eigenvalue plot, which is drawn for the no-load condition of the machine in figure 3.5. The eigenvalue plots drawn under full-load with other control strategies reveal that there is no significant change in the shape of the complete eigenvalue plot.

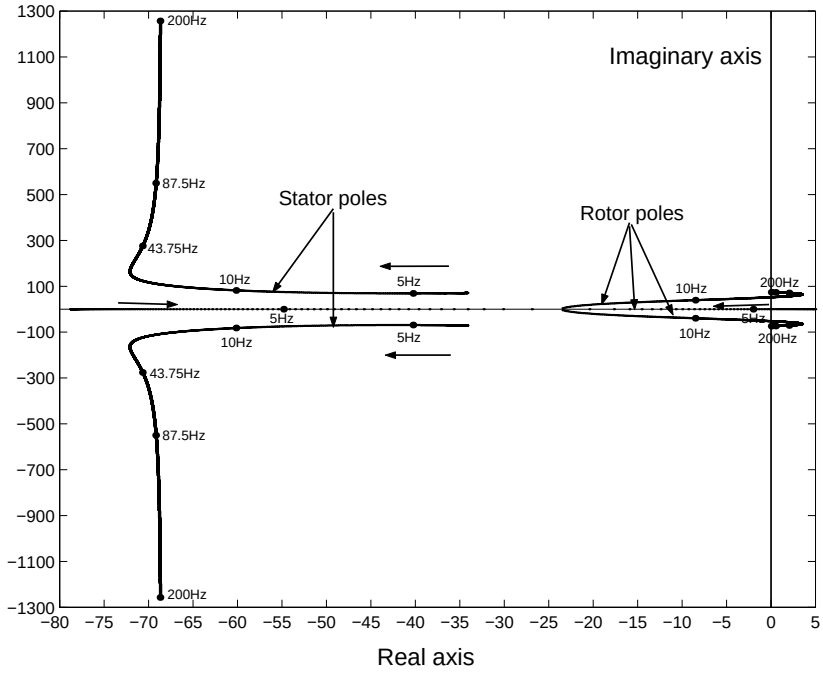

Figure 3.8: *Eigenvalue plot for the machine under full-load, constant stator flux linkage control, as a function of the applied frequency.*

In figure 3.9- figure 3.12, the eigenvalue plots are shown with different control strategies, under different load conditions in the machine. For clarity, only the dominant poles (rotor poles) are shown in those figures. The no-load condition is also shown for comparison. It can be seen that the eigenvalues of the machine migrate into the right half of the s-plane, i.e. the machine becomes unstable, after exceeding a certain applied frequency (about 15 Hz) regardless of the control strategy and the load condition of the machine. Under open-loop V/f control, this type of stability behaviour of PMSMs was also observed in [6] and [7], and it was referred to as mid-frequency instability of

PMSMs.

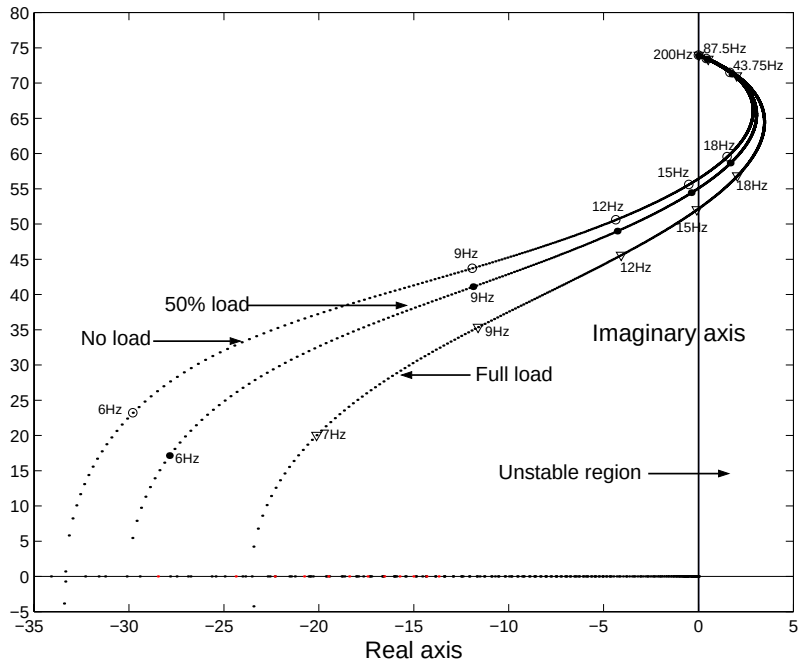

Figure 3.9: *The loci of dominant poles under different load conditions, constant stator flux linkage control, as a function of the applied frequency.*

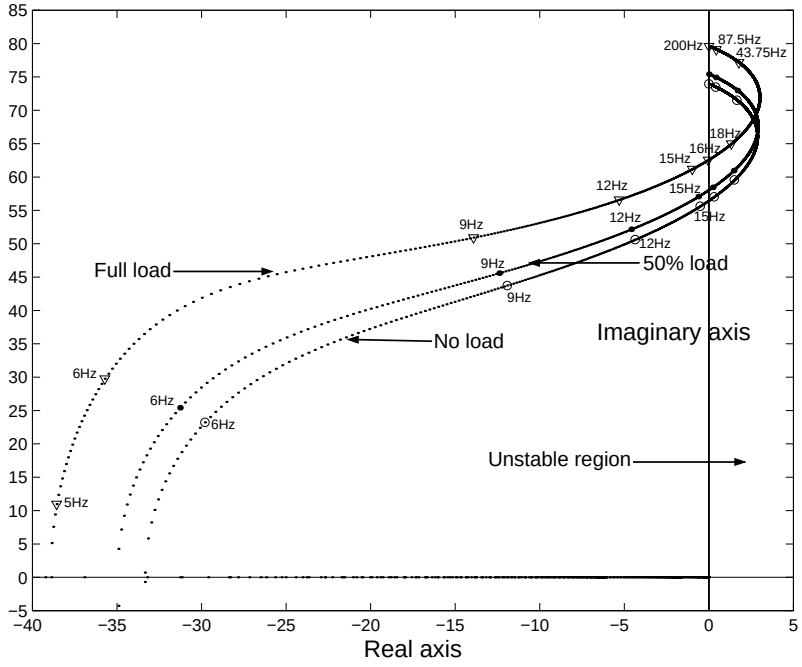

Figure 3.10: *The loci of dominant poles under different load conditions, $i_{ds}^r = 0$ control, as a function of the applied frequency.*

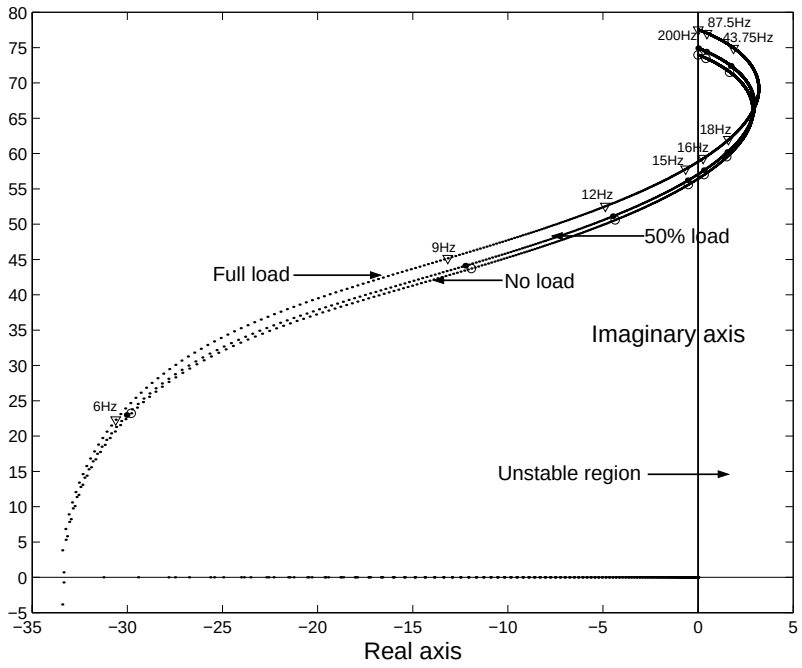

Figure 3.11: *The loci of dominant poles under different load conditions, maximum torque per ampere control, as a function of the applied frequency.*

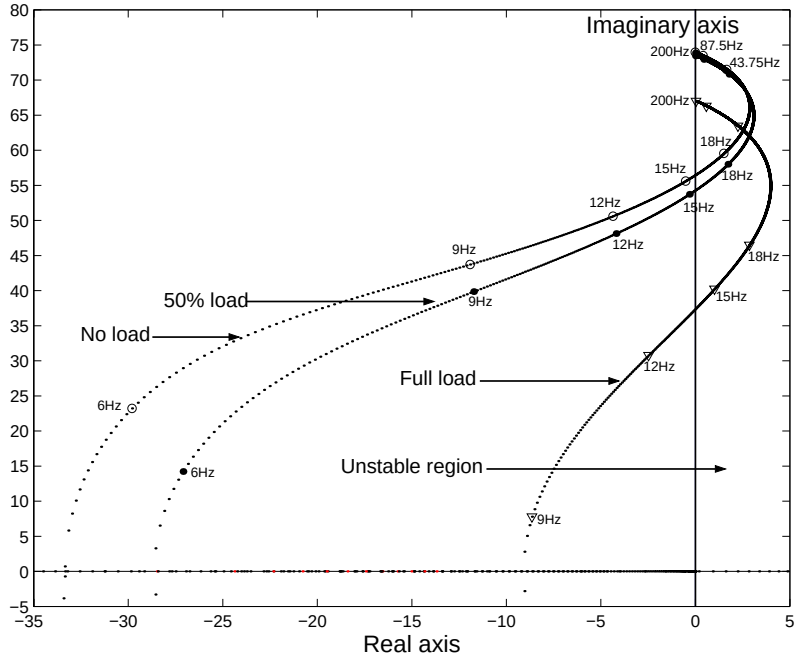

Figure 3.12: *The loci of dominant poles under different load conditions, unity power factor control, as a function of the applied frequency.*

3.4.3 Simulations and experimental results

In order to verify the stability behaviour of the machine, which was demonstrated using the eigenvalue plots obtained from the linearized model of the machine, first, the computer simulations were carried out for different operating points using the full non-linear model of the machine.

The machine was modeled using the equations (3.2.8)-(3.2.11) and, the rotor speed and the load condition of the machine were initialized to the required steady state operating point value. Then, the machine was simulated exciting the frequency and the voltage correspondent to that steady state operating point, using a voltage source inverter with space vector modulation (see figure 3.1). A constant DC-link voltage (560 V) was used for the voltage source inverter. The machine parameters were same as used for the eigenvalue plot calculations. They are given in Appendix A.

Figure 3.13 shows the simulated rotor speed responses at different frequencies under no-load, i.e. $V_s = E_m$. It can be seen from this rotor speed responses the system is stable at low frequencies (at 5 Hz and 10 Hz) and at high frequencies (at 43.75 Hz and 87.5 Hz) the system is unstable as expected from the eigenvalue plots drawn under no-load (see figure 3.5 and figure 3.6).

Figure 3.14 shows the simulated rotor speed responses at different frequencies, machine under full-load, with the excitation voltage according to the constant stator flux linkage control strategy. Again, the results in figure 3.14 agree with the stability analysis of the machine, which was demonstrated in the eigenvalue plots drawn under full-load with this control strategy (see figure 3.8 and figure 3.9).

To see the stability behaviour of the machine experimentally, the following laboratory tests were carried out in a prototype drive system, under no-load. The drive system consists of a voltage source inverter with space vector modulation (see Appendix C) and the IPMSM, which is used for the analysis. More details of this laboratory drive system can be found in Appendix D.

The machine was ramped up to the different frequencies, under no-load, applying the voltage $V_s = E_m = 2\pi f_0 \lambda_m$. For all measurements the machine was started from a same initial rotor position. The plots of measured rotor speeds are shown in figure 3.15. It can be seen from this measurements, the stable operation at low frequencies and the unstable operation at high frequencies of the machine, as expected from the previous analysis. Moreover, the oscillations at high frequencies have a good agreement with the eigenvalue plot, which was drawn for the no-load case in figure 3.6.

In order to see whether any effect from ramp up time to the instability seen at high frequencies, the rotor speed at 43.75 Hz was measured with different ramp up times. The results are shown in figure 3.16(a). As it can be seen, changing the ramp up time the stable operation of the machine cannot be achieved. Another measurement was carried out applying a higher than the no-load voltage to the machine at the same frequency. The measured rotor speed is shown in figure 3.16(b). The stable operation

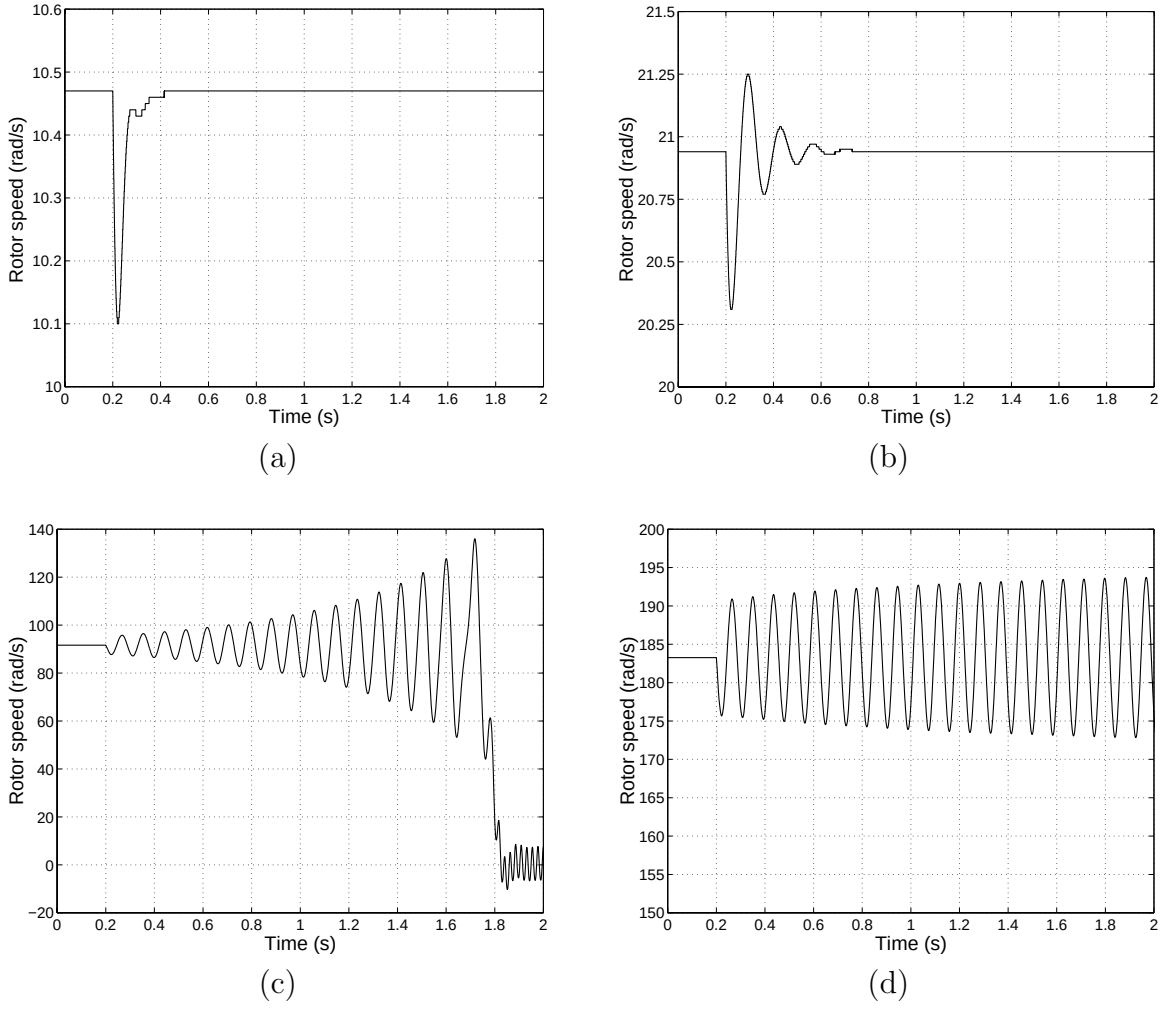

Figure 3.13: *Simulated rotor speed responses, machine under no-load. The excitation voltage $V_s = E_m$. (a) At 5 Hz (b) At 10 Hz (c) At 43.75 Hz (50% of the rated frequency) (d) At 87.5 Hz (rated frequency).*

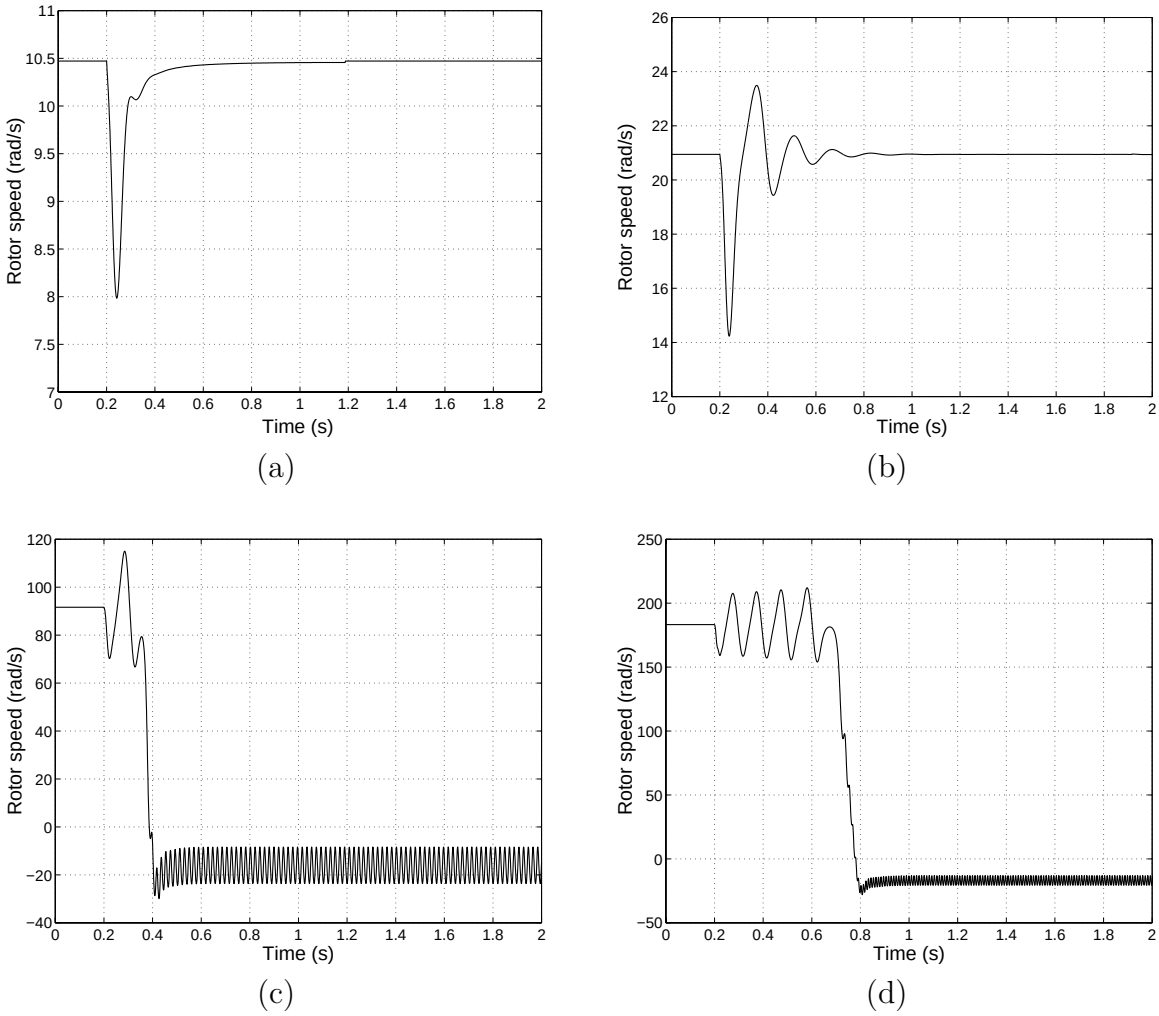

Figure 3.14: *Simulated rotor speed responses, machine under full-load. The excitation voltage is according to constant stator flux linkage control. (a) At 5 Hz (b) At 10 Hz (c) At 43.75 Hz (50% of the rated frequency) (d) At 87.5 Hz (rated frequency).*

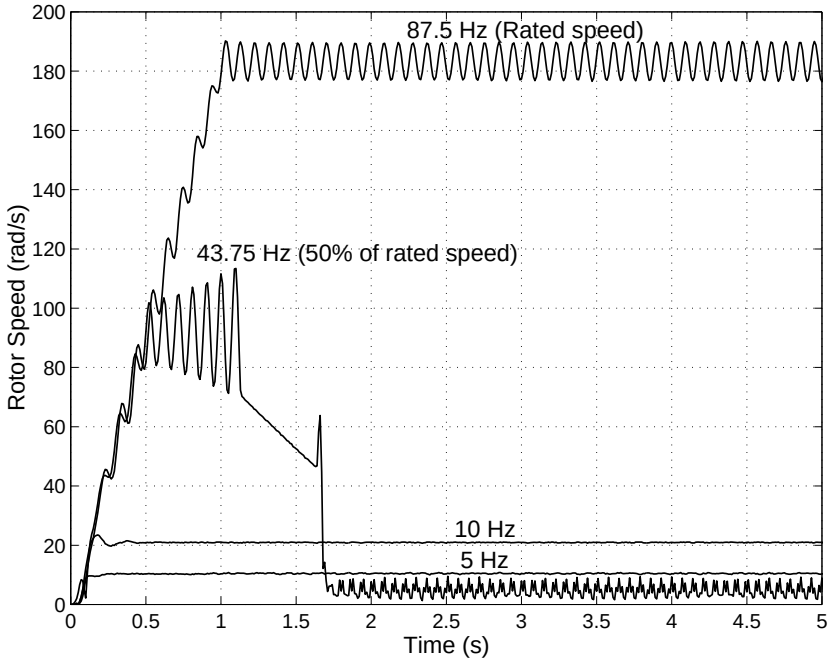

Figure 3.15: *Measured rotor speeds at different frequencies, under no-load.*

of the machine can also not be achieved applying a higher voltage to the machine, as it can be seen from the rotor speed measurement shown in figure 3.16(b).

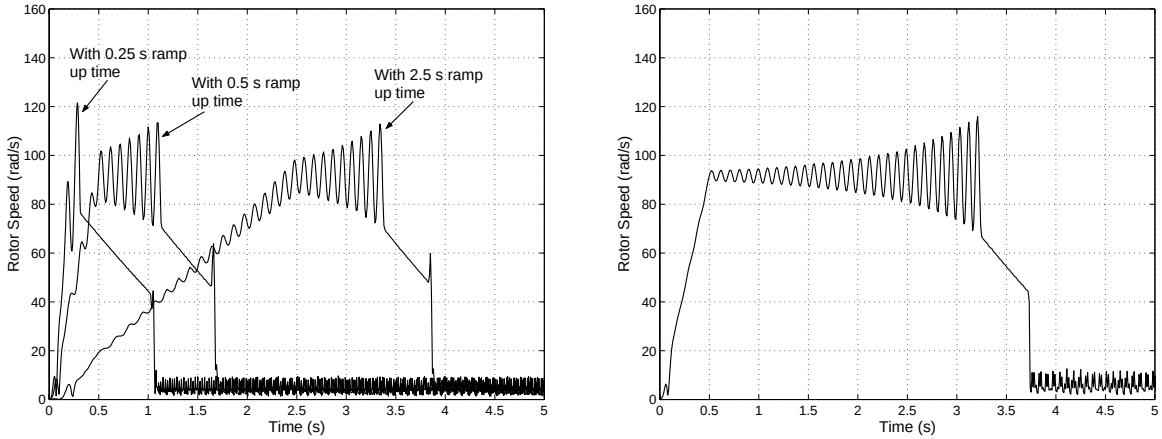

Figure 3.16: *Measured rotor speeds at 43.75 Hz, under no-load. (a) With different ramp up times (b) Applying a half of the rated voltage to the machine.*

3.5 Summary

This chapter has been investigated the stability characteristics of the PMSMs under open-loop V/f control. First, the linearized PMSM model has been derived when the machine is under open-loop V/f control. The eigenvalues of the state transition matrix of this linearized PMSM model have been used to investigate the stability characteristics of the machine. The drawn eigenvalue plots for the machine under no-load and under load conditions, as a function of the applied frequency, have revealed that the machine becomes unstable after exceeding a certain applied frequency (mid-frequency instability) under open-loop V/f control. Computer simulations and experimental results have verified that stability behaviour of the machine.

Since the machine has been operated under open-loop, it does not assure the synchronization of machine's stator excitation and motion of the rotor. Without this synchronization the electrical and the mechanical modes of the machine do not have proper coupling and this leads to the instability of the machine, after exceeding a certain applied frequency, as it is seen in the investigation. However, at low frequencies the electrical and the mechanical modes of the machine have coupling, which makes the stable operation of the machine.

Bibliography

[1] William L. Brogan, *Nonlinear Equations and Perturbation Theory*, Chapter 13 in Modern Control Theory, Second Edition, Prentice-Hall, Inc., 1985.

[2] Paul C. Krause, Oleg Wasynczuk and Scott D. Sudhoff, *Linearized Equations of Induction and Synchronous Machines*, Chapter 7 in Analysis of Electric Machinery, IEEE Press, 1995.

[3] Thomas A. Lipo and Paul C. Krause, *Stability Analysis for Variable Frequency Operation of Synchronous Machines*, IEEE Transactions on Power Apparatus and Systems, Vol. PAS-87, No.1, pp. 227-234, January 1968.

[4] Edward P. Cornell and Donald W. Novotny, *Theoretical and Experimental Analysis of Operating Point Stability of Synchronous Machines*, IEEE Transactions on Power Apparatus and Systems, Vol. PAS-91, No.1, pp. 241-248, Jan.-Feb. 1972.

[5] George C. Verghese, Jeffrey H. Lang and Leo F. Casey, *Analysis of Instability in Electrical Machines*, IEEE Transactions on Industry Applications, Vol. IA-22, No.5, pp. 853-864, Sept./Oct. 1986.

[6] R. S. Colby, *Efficient High Speed Permanent Magnet Synchronous Motor Drives*, Ph.D. Thesis, University of Wisconsin-Madison,1987.

[7] P. H. Mellor, M. A. Al-Taee and K. J. Binns, *Open-loop Stability Characteristics of Synchronous Drive Incorporating High Field Permanent Magnet Motor*, IEE Proceedings-B, Vol. 138, No. 4, pp. 175-184, July 1991.

Chapter 4

Stabilization of Open-Loop V/f Controlled PMSMs

4.1 Introduction

As it is shown in Chapter 3, the PMSM becomes unstable after exceeding a certain applied frequency under open-loop V/f control. Under open-loop V/f control, there is no assurance for synchronization of PMSM's stator excitation and the motion of the rotor. This leads to that observed instability behaviour of the PMSM. In order to achieve stable operation for a wide frequency range, the open-loop V/f controlled PMSMs require some means of synchronization of the stator excitation and the motion of the rotor. This chapter investigates how this can be achieved for open-loop V/f controlled PMSMs.

First, in this chapter, the small signal dynamics model, which is derived in §3.2 of Chapter 3 is simplified, so that it can mainly provide the behaviour of the principal system roots of the system. This simplified small signal dynamics model is an easy tool to understand how the system is stabilized. It will be shown in detail that the applied frequency modulation proportional to the perturbations in the input power of the machine should be a suitable solution to achieve stable operation of open-loop V/f controlled PMSMs for a wide frequency range. Then, two ways to implement this frequency modulated stabilizing loop in the drive system will be discussed. One method uses calculated input power of the machine and the other method uses measured DC-link current in the DC-link of the drive. Small signal analysis, computer simulations and experimental results are presented to validate those stabilizing techniques.

4.2 Simplified small signal dynamics model

The small signal dynamics model (the linearized machine model) of the PMSM, which is shown in figure 3.3 of Chapter 3 is a very complex one. From that model it is not easy to see how the system is stabilized under open-loop V/f control. Therefore, a simplification is necessary for that small signal dynamics model, so that it can be used

to see how the system is stabilized.

In this section, a simplified small signal dynamics model is developed based on the model derived in § 3.2 of Chapter 3. The key approximation for the simplification is discussed. Moreover, the validity of the obtained simplified small signal dynamics model is studied under open-loop V/f control of PMSMs.

4.2.1 Approximation for the simplification

A simplification can be achieved to the small signal dynamics model of the PMSM shown in figure 3.3 of Chapter 3, considering an approximation for the electromagnetic torque perturbation production in the machine. In the approximation, it is considered the electromagnetic torque perturbation in the machine is produced only due to the perturbation in the load angle and proportionally to it [1]. This can be written mathematically as

$$\Delta T_e = k_e(\Delta\delta) \tag{4.2.1}$$

The k_e in (4.2.1) is electromechanical spring constant and it is equal to the slope of the torque-load angle curve at the steady state operating point, i.e.

$$k_e = \frac{\partial T_{e0}}{\partial \delta_0}|_{\delta_0 \text{ at steady state operating point.}} \tag{4.2.2}$$

The steady state electromagnetic torque T_{e0} is a function of V_s, ω_0 and δ_0. One can obtain this relationship considering the steady state voltage equations in the rotor frame and the electromagnetic torque equation. The derivation of this relationship is given in Appendix B.2. For a given steady state voltage V_s and frequency ω_0 the relationship between T_{e0} and δ_0 can be drawn as in figure 4.1. Figure 4.1 is drawn at rated frequency and voltages are calculated for different load conditions using constant stator flux linkage control strategy. The IPMSM parameters given in Appendix A are used for the calculation. According to (4.2.2), k_e is the slope of one of the curves shown in figure 4.1 at the steady state operating point.

When the T_{e0} is known as a function of V_s, ω_0 and δ_0, one can easily derive the expression for k_e using (4.2.2). This derivation is given in Appendix B.3. k_e is also a function of V_s, ω_0 and δ_0. One particular interest is to see the variation of k_e with frequency for different load conditions. This is useful in later analysis and it is shown in figure 4.2 for the IPMSM parameters given in Appendix A. For calculations, the constant stator flux linkage control strategy is used. From figure 4.2 it can be seen that the k_e is not much affected from the load and at high frequencies it becomes almost a constant value.

4.2.2 Block diagram for simplified small signal dynamics model

Representing the rotor velocity (ω_r), electrical angular velocity (ω_e) and load angle (δ) as the sum of the steady state component and the perturbation component, one may

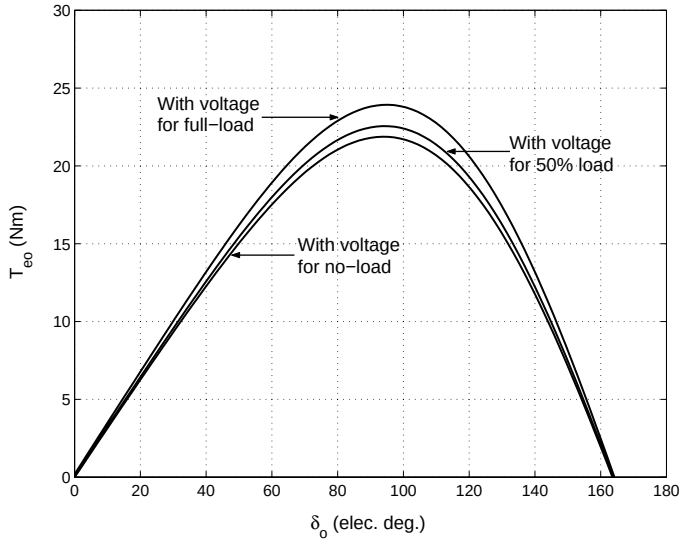

Figure 4.1: *Relationship between T_{e0} and δ_0 at rated frequency, for different applied voltages to the machine. The required applied voltages for different load conditions are calculated according to the constant stator flux linkage control strategy.*

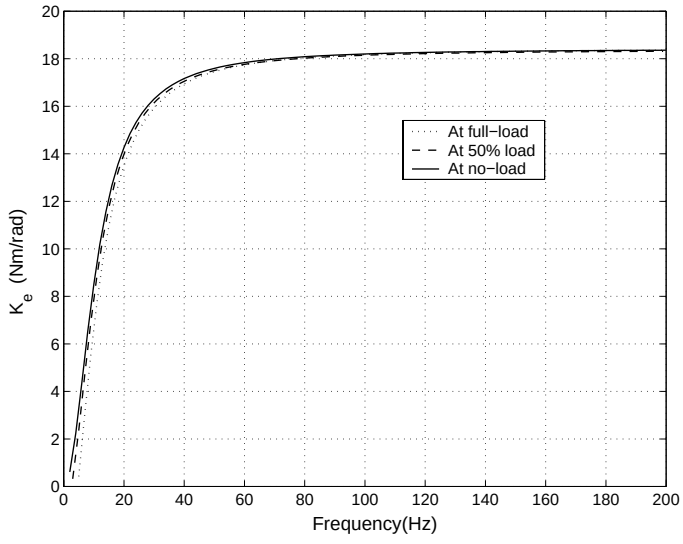

Figure 4.2: *The variation of k_e with frequency under different load conditions, constant stator flux linkage control.*

write

$$\omega_r = \omega_0 + \Delta\omega_r \tag{4.2.3}$$

$$\omega_e = \omega_0 + \Delta\omega_e \tag{4.2.4}$$

$$\delta = \delta_0 + \Delta\delta \tag{4.2.5}$$

Substituting these relationships to (3.2.2) of Chapter 3, the following relationship for the perturbation components can be obtained.

$$\Delta\delta = \int (\Delta\omega_e - \Delta\omega_r)dt \tag{4.2.6}$$

The mechanical equation for the system is (see (2.6.1) of Chapter 2)

$$p\omega_r = \frac{n}{2J}T_e - \frac{1}{J}B_m\omega_r - \frac{n}{2J}T_l \tag{4.2.7}$$

Linearizing (4.2.7) one obtains,

$$p\Delta\omega_r = \frac{n}{2J}\Delta T_e - \frac{1}{J}B_m\Delta\omega_r - \frac{n}{2J}\Delta T_l \tag{4.2.8}$$

Rearranging and substituting s for p, the equation (4.2.8) can be written as

$$-(\Delta\omega_r)(s + \frac{B_m}{J}) = \frac{n}{2J}(\Delta T_l - \Delta T_e) \tag{4.2.9}$$

Using (4.2.6), (4.2.9) and the approximation for ΔT_e given in (4.2.1), the block diagram for the simplified small signal dynamics model can be drawn as in figure 4.3.

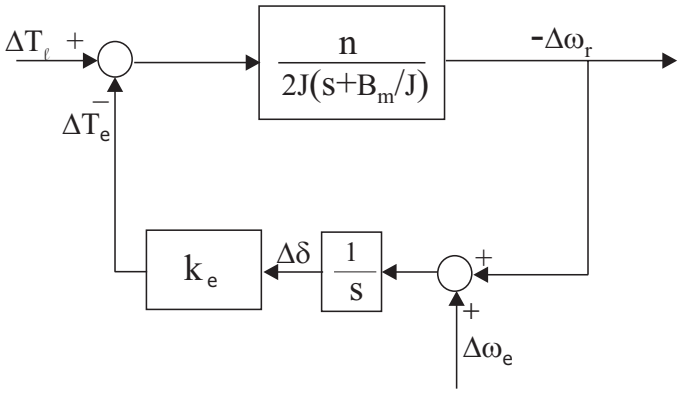

Figure 4.3: *Simplified small signal dynamics model of the PMSM.*

Comparing figure 3.3 in Chapter 3 and figure 4.3 one can see the simplification in figure 4.3 is due to the approximation made for ΔT_e generation. In figure 4.3 the ΔT_e is generated only from $\Delta\delta$ incorporating the gain k_e.

4.2.3 Simplified small signal dynamics model under open-loop V/f control

Under open-loop V/f control, it can be considered the PMSM is excited from a voltage with constant amplitude and frequency, where the conditions $\Delta v_s = 0$ and $\Delta\omega_e = 0$ are fulfilled (see § 3.3 of Chapter 3). Due to the approximation made to obtain the simplified small signal dynamics model the Δv_s does not exist as an input to that model. Therefore, using the condition $\Delta\omega_e = 0$, the above obtained simplified small signal dynamics model in figure 4.3 can be drawn for open-loop V/f control as in figure 4.4.

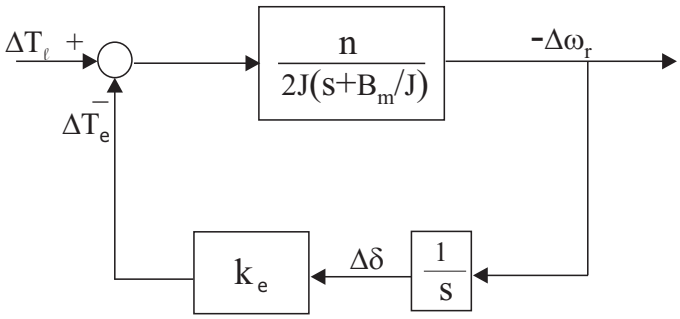

Figure 4.4: *Simplified small signal dynamics model of the PMSM, under open-loop V/f control.*

The characteristic equation for this system is

$$1 + \frac{n}{2J(s + \frac{B_m}{J})}(\frac{k_e}{s}) = 0 \tag{4.2.10}$$

$$\therefore 2Js^2 + 2B_m s + nk_e = 0 \tag{4.2.11}$$

The solution to this equation (the location of the system poles in the s-plane) is

$$s = \frac{-B_m}{2J} \pm j\frac{\sqrt{2Jnk_e - B_m^2}}{2J} \tag{4.2.12}$$

In (4.2.12), the k_e varies according to the steady state operating point of the machine. When the applied frequency is changed at no-load and full-load the location of the system poles in the s-plane is shown in figure 4.5.

When the full small signal dynamics model was used in § 3.3 of Chapter 3, the system became a fourth order system. It can be seen that when the simplified small signal dynamics model is used the system is reduced to almost an undamped second order system.

The natural frequency of oscillation (ω_d) of the poles in figure 4.5 are given by (from (4.2.12))

$$\omega_d = \frac{\sqrt{2Jnk_e - B_m^2}}{2J} \tag{4.2.13}$$

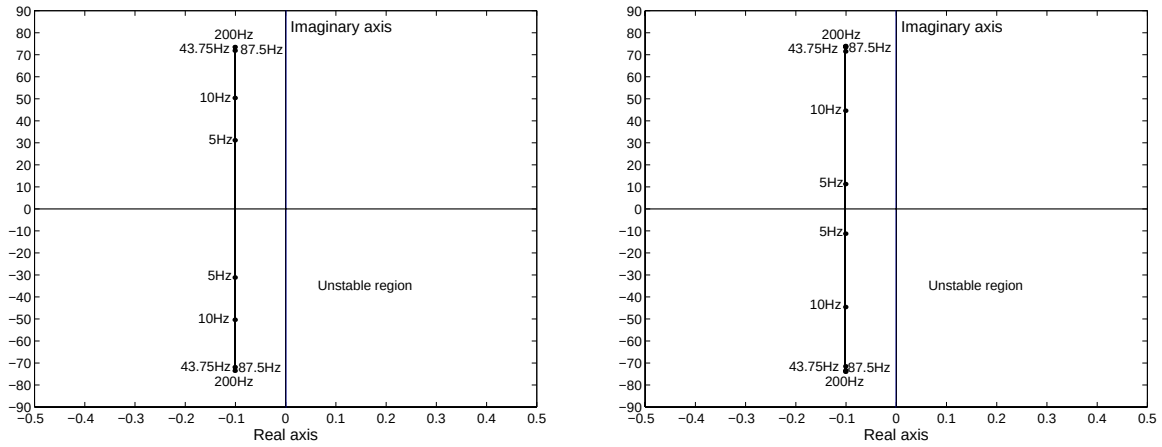

Figure 4.5: *The location of system poles from simplified small signal dynamics model, as a function of the applied frequency. (a) Under no load (b) Under full load, constant stator flux linkage control.*

Figure 4.6 compares the natural frequency of the dominant poles of the full small signal dynamics model and natural frequency of the poles of the simplified small signal dynamics model under open-loop V/f control. It can be seen from the plots drawn in figure 4.6 the natural frequencies from both models have a good agreement, except some deviations at low frequencies.

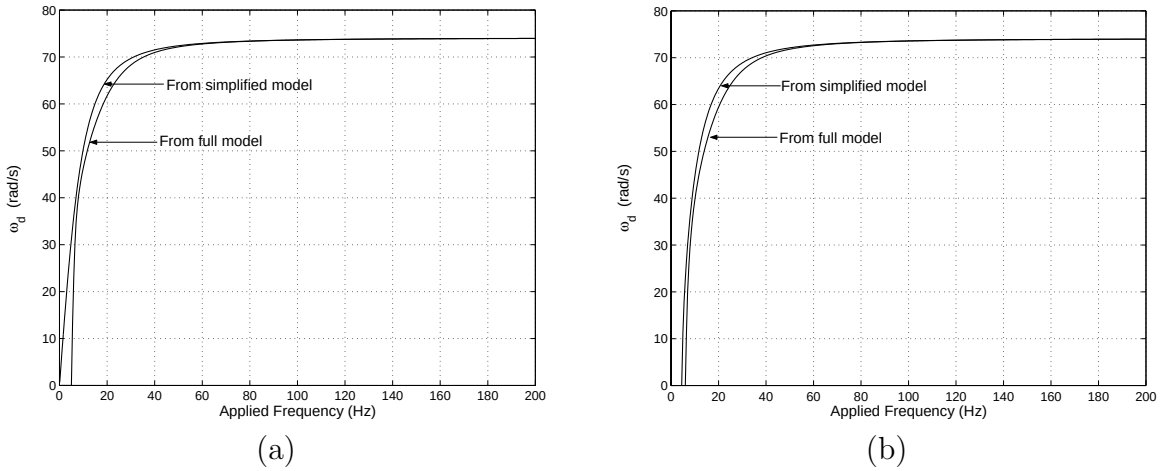

Figure 4.6: *Comparison of natural frequencies (ω_d) from the dominant poles of the full small signal dynamics model and from the poles of the simplified small signal dynamics model. (a) Under no load (b) Under full load, constant stator flux linkage control.*

It can be concluded that the characteristics of the poles of the simplified small signal dynamics model express the characteristics of the dominant poles (rotor poles) of the full small signal dynamics model. When the frequency is increased the similarity in the characteristics is also increased.

4.3 Stabilization by frequency modulation-*Simplified small signal model analysis*

The simplified small signal dynamics model, which is derived in § 4.2 can be used to show how to stabilize the open-loop V/f controlled PMSMs by modulating the applied frequency. In the following, using the simplified small signal dynamics model, different methods to modulate the applied frequency to achieve stabilization of the system are discussed.

4.3.1 Frequency modulation using rotor velocity perturbations

The rotor velocity perturbations ($\Delta\omega_r$) can be used to modulate the applied frequency to add damping and stabilize the system.

If the applied frequency is modulated using the rotor velocity perturbations as in the following relationship,

$$\Delta\omega_e = -k_v \frac{d(\Delta\omega_r)}{dt} \tag{4.3.1}$$

then, the simplified small signal dynamics model in figure 4.3 can be drawn as shown in figure 4.7. In (4.3.1), k_v is the gain for the frequency modulation component.

From the block diagram shown in figure 4.7 the characteristic equation of the system can be obtained as

$$s^2 + \frac{(2B_m + nk_ek_v)}{2J}s + \frac{n}{2J}k_e = 0 \tag{4.3.2}$$

This characteristic equation indicates that the damping of the system can be controlled by properly selecting the gain k_v.

However, to implement this method a rotor position sensor is required to obtain the rotor velocity perturbations. This is of course not desirable in sensorless control and this technique will not be investigated further in this chapter.

4.3.2 Frequency modulation using power perturbations

The perturbations in the power of the system can also be used to modulate the supply frequency in order to stabilize the system. This can also be shown using the simplified small signal dynamics model.

The motor power balance equation can be written as

$$p_e = p_{ml} + \frac{dw_{em}}{dt} + \frac{2}{n}\omega_r T_e \tag{4.3.3}$$

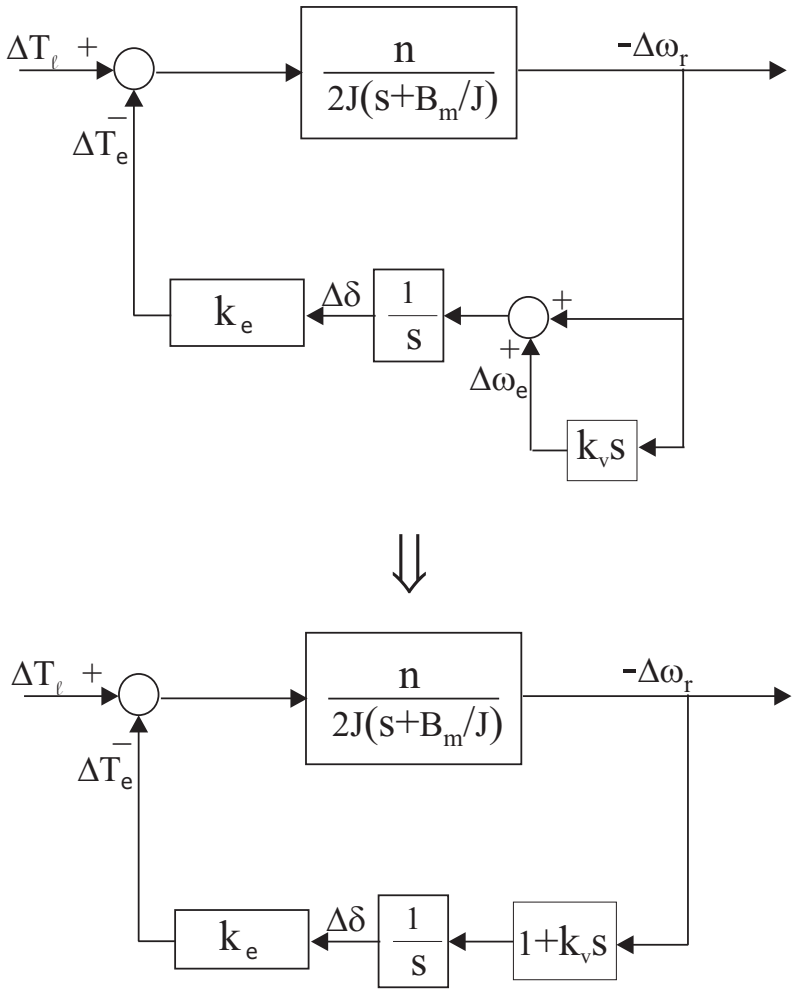

Figure 4.7: *Block diagram representation of the PMSM simplified small signal dynamics, when the applied frequency is modulated as* $\Delta\omega_e = -k_v \frac{d(\Delta\omega_r)}{dt}$.

The input power p_e is distributed among the motor losses P_{ml}, the change in electromagnetic energy storage w_{em} and the mechanical output power of the machine.

Using the mechanical equation of the machine (see (2.6.1) of Chapter 2) the equation (4.3.3) can be written as

$$p_e = P_e + \Delta p_e = p_{ml} + \frac{dw_{em}}{dt} + (\frac{2}{n})^2 \frac{J}{2}\frac{d}{dt}\omega_r^2 + (\frac{2}{n})^2 B_m \omega_r^2 + \frac{2}{n}\omega_r T_l \tag{4.3.4}$$

where, P_e is the steady state power and Δp_e is the perturbation component.

It is assumed that for a given operating point the first two terms in right side of (4.3.4) are almost constant and the perturbations in the power are only due to the last three terms of (4.3.4). With this assumption the perturbations in the power can be written as

$$\Delta p_e = (\frac{2}{n})^2 J\omega_0 \frac{d}{dt}\Delta\omega_r + 2(\frac{2}{n})^2 B_m \omega_0 \Delta\omega_r + \frac{2}{n}T_{l0}\Delta\omega_r \tag{4.3.5}$$

where, T_{l0} is the steady state load torque.

If the supply frequency is modulated proportionally to the perturbations in the power, then $\Delta\omega_e$ can be written as

$$\Delta\omega_e = -k_p \Delta p_e = k_p[(\frac{2}{n})^2 J\omega_0 \frac{d}{dt}(-\Delta\omega_r) + 2(\frac{2}{n})^2 B_m\omega_0(-\Delta\omega_r) + \frac{2}{n}T_{l0}(-\Delta\omega_r)] \tag{4.3.6}$$

where, k_p is the proportional gain.

With this type of modulation for the applied frequency, the simplified small signal dynamics model given in figure 4.3 can be drawn as shown in figure 4.8.

The block diagram shown in figure 4.8 gives the characteristic equation for the system as

$$s^2 + (\frac{B_m}{J} + \frac{2k_e\omega_0 k_p}{n})s + \frac{k_e}{2J}[n + 4(\frac{2}{n})B_m k_p \omega_0 + 2T_{l0}k_p] = 0 \tag{4.3.7}$$

The roots of this equation, i.e. the poles of the system in the s-plane, are

$$s_{1,2} = -(\frac{B_m}{2J} + \frac{k_e\omega_0 k_p}{n}) \pm \sqrt{(\frac{B_m}{2J} + \frac{k_e\omega_0 k_p}{n})^2 - \frac{k_e}{2J}[n + 4(\frac{2}{n})B_m k_p\omega_0 + 2T_{l0}k_p]} \tag{4.3.8}$$

Since B_m, J, n are constants for the machine and k_e, ω_0, T_{l0} are also constants for a given operating point, the damping of the system for an operating point can be controlled by properly selecting the gain k_p as it can be seen from (4.3.8). Figure 4.9 and figure 4.10 show the location of the system poles when the gain k_p is increased under no load and full load at rated frequency, respectively. It can be seen from figure 4.9 and figure 4.10 how the gain k_p affects to the system's damping at the operating points considered.

As it can be seen from (4.3.8), using a constant value for the gain k_p it is not possible to fix the location of the poles, since the location of the poles is also vary according to ω_0, k_e and T_{l0}. However, there is a possibility to approximately fix the location of the poles if $\omega_0 k_p$ term is kept constant (i.e. varying k_p inversely proportional to ω_0). The

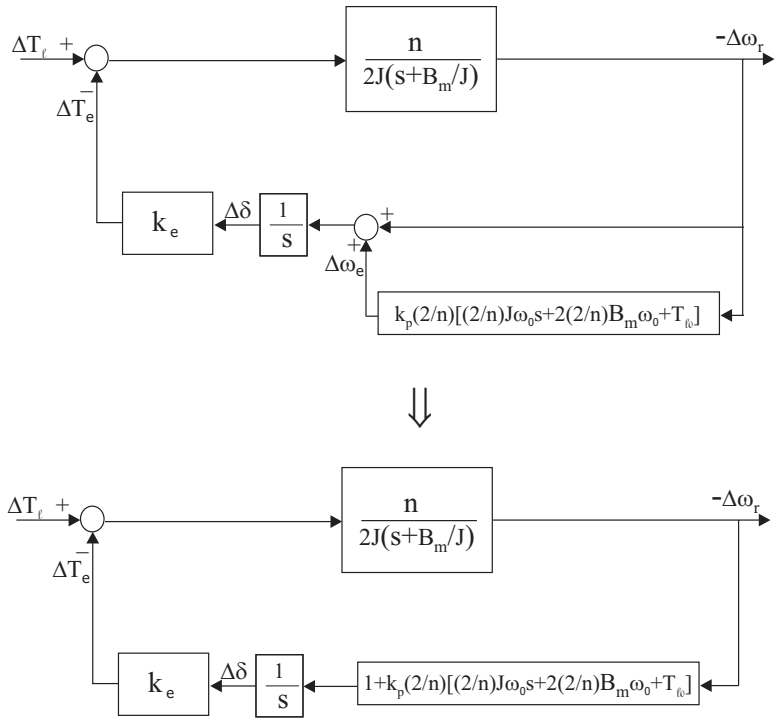

Figure 4.8: *Block diagram representation of the PMSM simplified small signal dynamics when the applied frequency is modulated proportionally to the power perturbations, i.e* $\Delta\omega_e = -k_p \Delta p_e$.

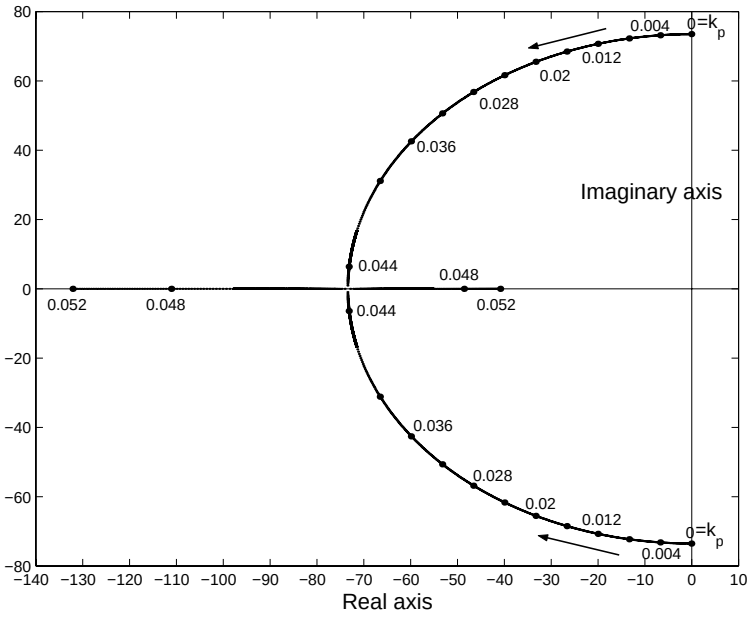

Figure 4.9: *Location of the system poles from the simplified small signal dynamics model when the applied frequency is modulated proportionally to the power perturbations, at no load, rated frequency (87.5 Hz), as a function of the gain k_p.*

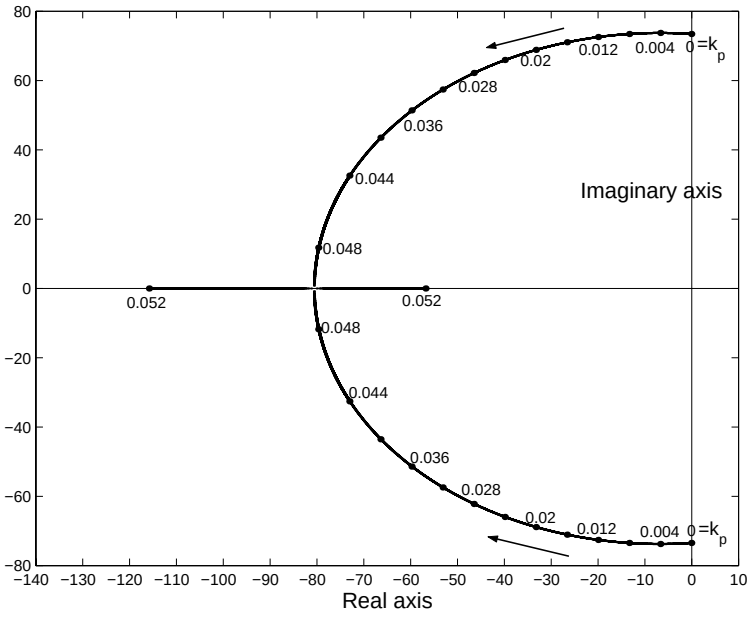

Figure 4.10: *Location of the system poles from the simplified small signal dynamics model when the applied frequency is modulated proportionally to the power perturbations, at full load, rated frequency (87.5 Hz), as a function of the gain k_p.*

variation of k_e and T_{l0} can still somewhat affect to the location of the poles with that way of selecting the gain k_p. However, at high frequencies since k_e is also a constant (see figure 4.2) it can be expected that the location of the poles can almost be fixed, at least in high frequencies, when varying k_p inversely proportional to ω_0.

The location of the poles as a function of the applied frequency is shown in figure 4.11 and figure 4.12 for no-load and full-load cases respectively. For these plots the gain k_p was selected such that $\omega_0 k_p = 8$ (i.e. $k_p = \frac{8}{\omega_0}, \omega_0 \neq 0$). This gives $k_p = 0.015$ at rated frequency. From figure 4.11 and figure 4.12, it can be seen that when the applied frequency is high the location of the poles is almost constant (i.e. poles have almost a constant damping factor) as expected.

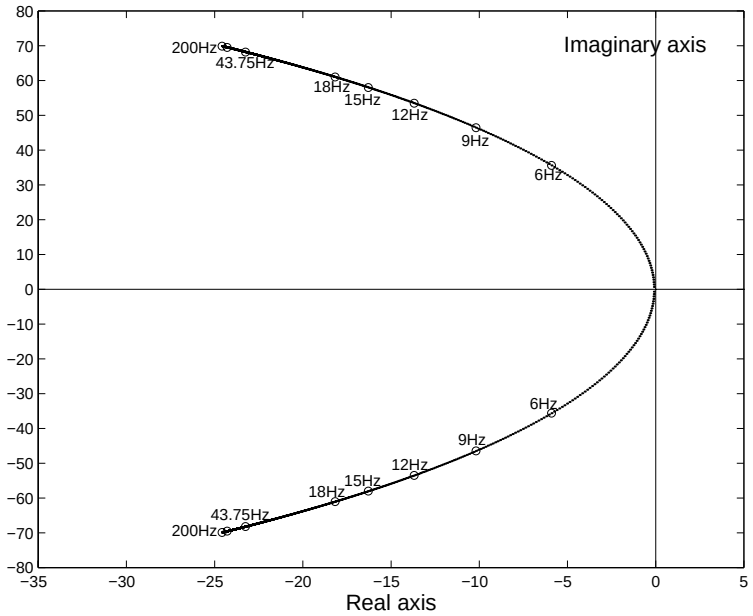

Figure 4.11: *Location of the system poles from the simplified small signal dynamics model when the applied frequency is modulated proportionally to the power perturbations, at no load, as a function of the applied frequency. The product $k_p\omega_0 = 8$.*

4.3.3 Frequency modulation using DC-link current perturbations

Modulation of the applied frequency according to the perturbations in the DC-link current is also a method to stabilize open-loop V/f controlled PMSMs [2], [3], [4], [5], [6].

For voltage source inverter driven drives, the DC-link current perturbations can be considered as proportional to the power perturbations in the system, since the DC-link bus voltage is almost a constant. Using the same analysis method as in § 4.3.2, it can

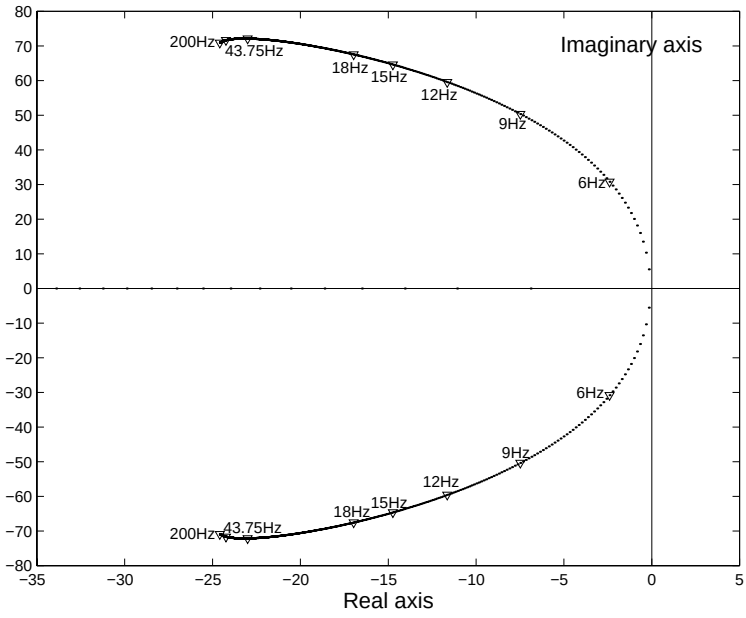

Figure 4.12: *Location of the system poles from the simplified small signal dynamics model when the applied frequency is modulated proportionally to the power perturbations, at full load, constant stator flux linkage control, as a function of the applied frequency. The product* $k_p\omega_0 = 8$.

be shown that how the system can be stabilized by modulating the applied frequency using the DC-link current perturbations.

Expressing the DC-link current i_{dc} as the addition of the steady state value I_{dc} and the perturbation component Δi_{dc} the DC-link power balance equation can be written as

$$V_{dc}(I_{dc} + \Delta i_{dc}) = p_{il} + p_{ml} + \frac{dw_{em}}{dt} + (\frac{2}{n})^2 \frac{J}{2}\frac{d}{dt}\omega_r^2 + (\frac{2}{n})^2 B_m \omega_r^2 + \frac{2}{n}\omega_r T_l \qquad (4.3.9)$$

where, V_{dc} is constant DC-link voltage and p_{il} is the inverter losses.

The difference in (4.3.9) compared to the (4.3.4) is the inclusion of the inverter losses p_{il}. Due to the same reasons mentioned in the previous § 4.3.2, the DC-link power perturbations can be approximated due to the last three terms of (4.3.9). With this approximation, the perturbations in the DC-link power can be written as

$$V_{dc}\Delta i_{dc} = (\frac{2}{n})^2 J\omega_0 \frac{d}{dt}\Delta\omega_r + 2(\frac{2}{n})^2 B_m \omega_0 \Delta\omega_r + \frac{2}{n}T_{l0}\Delta\omega_r \qquad (4.3.10)$$

and the perturbations in the DC-link current can be derived as

$$\Delta i_{dc} = \frac{1}{V_{dc}}[(\frac{2}{n})^2 J\omega_0 \frac{d}{dt}\Delta\omega_r + 2(\frac{2}{n})^2 B_m \omega_0 \Delta\omega_r + \frac{2}{n}T_{l0}\Delta\omega_r] \qquad (4.3.11)$$

Using the simplified small signal dynamics model, it can be shown that these perturbations in the DC-link current can be used to modulate the applied frequency to add necessary damping to the system.

If the applied frequency is modulated proportionally to the perturbations in the DC-link current, then

$$\Delta\omega_e = -k_i\Delta i_{dc} = \frac{k_i}{V_{dc}}[(\frac{2}{n})^2 J\omega_0\frac{d}{dt}(-\Delta\omega_r) + 2(\frac{2}{n})^2 B_m\omega_0(-\Delta\omega_r) + \frac{2}{n}T_{l0}(-\Delta\omega_r)] \tag{4.3.12}$$

where, k_i is the proportional gain.

With this relationship for $\Delta\omega_e$, the block diagram in figure 4.3 can be drawn as shown in figure 4.13.

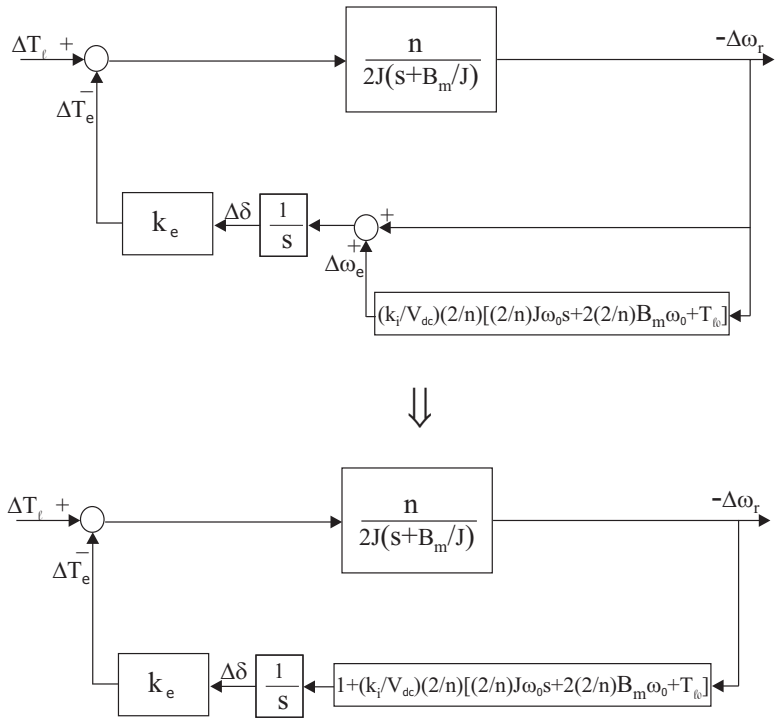

Figure 4.13: *Block diagram of PMSM simplified small signal dynamics when the applied frequency is modulated proportionally to the DC-link current perturbations, i.e.* $\Delta\omega_e = -k_i\Delta i_{dc}$.

The block diagram shown in figure 4.13 gives the characteristic equation of the system as follows.

$$s^2 + (\frac{B_m}{J} + \frac{2k_e\omega_0 k_i}{nV_{dc}})s + \frac{k_e}{2J}[n + 4(\frac{2}{n})\frac{B_m k_i\omega_0}{V_{dc}} + \frac{2T_{l0}k_i}{V_{dc}}] = 0 \tag{4.3.13}$$

The roots of this equation, i.e. the poles of the system are

$$s_{1,2} = -(\frac{B_m}{2J} + \frac{k_e\omega_0 k_i}{nV_{dc}}) \pm \sqrt{(\frac{B_m}{2J} + \frac{k_e\omega_0 k_i}{nV_{dc}})^2 - \frac{k_e}{2J}[n + 4(\frac{2}{n})\frac{B_m k_i\omega_0}{V_{dc}} + \frac{2T_{l0}k_i}{V_{dc}}]} \tag{4.3.14}$$

If the expression (4.3.14) is compared with the expression (4.3.8), one can see that the difference in (4.3.14) is the appearance of constant V_{dc} in denominator of some terms.

Therefore, due to the similar explanations given for (4.3.8), almost a fixed location for the poles of this system (i.e. almost a constant damping factor) can be achieved at high applied frequencies by selecting the gain k_i, such that $\omega_0 k_i$ is a constant value.

Referring to (4.3.6) and (4.3.12), if one selects the gain k_p for frequency modulation, which incorporates the power perturbations, then using the relationship

$$k_i = k_p V_{dc} \tag{4.3.15}$$

it can be found that the gain for the frequency modulation, which incorporates the DC-link current perturbations, in order to have the same pole locations for both systems.

4.4 Stability verification for frequency modulation

In the previous § 4.3, the simplified small signal dynamics model was used to show how damping can be added to the system by modulating the applied frequency. The simplified model was an easy tool to predict how the applied frequency should be modulated to add damping to the system. The suitable selection of the gains for applied frequency modulation to add damping to the system was also seen from the simplified model analysis. However, the simplified model analysis is with some approximations to the system. The true effect to the system from the applied frequency modulation can be seen from the analysis made with the full small signal dynamics model incorporating the knowledge obtained from the simplified model analysis.

4.4.1 Frequency modulation using power perturbations-*Full small signal model analysis*

In this section, the analysis is made using the full linearized system equations, to see the true effect to the system by modulating the applied frequency proportional to the power perturbations of the system, which is discussed in § 4.3.2 using simplified small signal model analysis.

Under the condition of the applied frequency modulation, the system equations (3.2.8)-(3.2.11), which are given in Chapter 3, remain valid. However, because of the frequency modulation, ω_e in (3.2.11) is now a state variable, i.e. ω_e has a relation with other state variables. In order to describe the system fully, now, there should be an another state equation (fifth state equation) for the state variable ω_e. This state equation, which describes the relation between ω_e and other state variables, can be obtained considering how the applied frequency is modulated.

As described in § 4.3.2, to add damping to the system the applied frequency should be modulated using power perturbations as follows.

$$\Delta\omega_e = -k_p \Delta p_e \tag{4.4.1}$$

The perturbation component of the power Δp_e can be extracted by passing the system power p_e through a first order high-pass filter. Therefore, Δp_e can be written as

$$\Delta p_e = \frac{s}{s + \frac{1}{\tau_h}} p_e \tag{4.4.2}$$

where, τ_h is the high-pass filter time constant.

Substituting Δp_e from (4.4.2) to (4.4.1) and rearranging it the following relationship is obtained.

$$p\Delta\omega_e + \frac{\Delta\omega_e}{\tau_h} = -k_p p(p_e) \tag{4.4.3}$$

The derivative of the power $p(p_e)$ in (4.4.3) can be obtained considering the power balance equation of the system.

The power balance equation can be written as

$$p_e = \frac{3}{2}[v^r_{qs} i^r_{qs} + v^r_{ds} i^r_{ds}] \tag{4.4.4}$$

Substituting v^r_{qs} and v^r_{ds} from (3.2.3) and (3.2.4) of Chapter 3, the equation (4.4.4) can be written as

$$p_e = \frac{3}{2} v_s [i^r_{qs} cos(\delta) - i^r_{ds} sin(\delta)] \tag{4.4.5}$$

Taking the derivative for both sides of the (4.4.5), one obtains

$$p(p_e) = \frac{3}{2} V_s [cos(\delta) p i^r_{qs} - sin(\delta) p i^r_{ds} - (i^r_{qs} sin(\delta) + i^r_{ds} cos(\delta)) p\delta] \tag{4.4.6}$$

When obtaining (4.4.6), it is considered the applied voltage is a constant, since no perturbations are incorporated with it (i.e. $\Delta v_s = 0$).

After substituting the expression for the derivative of the power given in (4.4.6), the equation (4.4.3) can be written as

$$p\Delta\omega_e + \frac{\Delta\omega_e}{\tau_h} = -k_p \frac{3}{2} V_s [p i^r_{qs} cos(\delta) - p i^r_{ds} sin(\delta) - (i^r_{qs} sin(\delta) + i^r_{ds} cos(\delta)) p\delta] \tag{4.4.7}$$

Substituting the derivative terms $p i^r_{qs}$, $p i^r_{ds}$ and $p\delta$ from (3.2.8), (3.2.9) and (3.2.11) of Chapter 3 to the (4.4.7), one can obtain the required fifth state equation as

$$\begin{aligned} p\Delta\omega_e = k_p \frac{3}{2} V_s \{ & [\frac{cos(\delta)}{\sigma\tau_s} + \omega_r \sigma sin(\delta) + (\omega_e - \omega_r) sin(\delta)] i^r_{qs} \\ & + [\frac{\omega_r cos(\delta)}{\sigma} - \frac{sin(\delta)}{\tau_s} + (\omega_e - \omega_r) cos(\delta)] i^r_{ds} \\ & + \frac{\omega_r \lambda_m cos(\delta)}{\sigma L_d} - (\frac{V_s}{L_d})(\frac{cos^2(\delta)}{\sigma} + sin^2(\delta)) \} - \frac{\Delta\omega_e}{\tau_h} \end{aligned} \tag{4.4.8}$$

The linearized form of the five nonlinear equations (i.e. equations (3.2.8)-(3.2.11) of Chapter 3 and (4.4.8)) of the system under applied frequency modulation proportional to the power perturbations can be written as

$$p\Delta x = A_2(X)\Delta x + B_2(X)\Delta T_l \tag{4.4.9}$$

where,

$$\Delta x = \begin{bmatrix} \Delta i_{qs}^r & \Delta i_{ds}^r & \Delta\omega_r & \Delta\delta & \Delta\omega_e \end{bmatrix}^T \tag{4.4.10}$$

and

$$B_2(X) = \begin{bmatrix} 0 & 0 & \frac{-n}{2J} & 0 & 0 \end{bmatrix}^T \tag{4.4.11}$$

The elements of the system's state transition matrix $A_2(X)$ are given in Appendix B.4.

Now, the system becomes a fifth order system and the eigenvalues of the state transition matrix $A_2(X)$ can be used to investigate the effectiveness of the applied frequency modulation to the system.

Figure 4.14 and figure 4.15 illustrate the effect from the variation of gain k_p to the stator and rotor poles of the system at rated frequency, no-load and full-load, respectively. The IPMSM parameters given in Appendix A were used to draw these plots. The cut-off frequency of the high pass filter, which was needed to obtain the power perturbation Δp_e, was selected to 2.5 Hz, i.e. the time constant $\tau_h = 0.0637s$. This time constant affects mainly to the fifth pole of the system, which lies always on the negative real axis of the s-plane. It was observed that the above selected value gave a reasonably good dynamics to the system locating the fifth pole at around $s = -20$. It can be observed in figure 4.14 and figure 4.15, when the gain k_p is increased the locus of the rotor poles has a similar shape as it is seen in root loci in figure 4.9 and figure 4.10 in § 4.3.2, where the analysis is made using the simplified small signal dynamics model. This indicates the dynamics of the rotor poles are dominant in the simplified small signal dynamics model. It can also be observed in figure 4.14 and figure 4.15, the stator poles move towards to the right half of the s-plane when the gain k_p is increased and they migrate into the right half of the s-plane at a certain gain. This indicates that there is an upper limit when selecting the gain k_p for the stabilizing loop, which modulates the applied frequency of the system.

The effectiveness of the stabilizing loop to the system rotor poles at no-load and full-load, as a function of the applied frequency, is shown in figure 4.16 and figure 4.17, respectively. In both figures the locus of rotor poles without stabilizing loop (without applied frequency modulation) in the system is also shown for the comparison. For the stabilizing loop the gain k_p was selected such that the product $k_p\omega_0 = 8$ (i.e. $k_p = \frac{8}{\omega_0}, \omega_0 \neq 0$). This gives $k_p = 0.015$ at rated frequency. The added damping to the rotor poles from the stabilizing loop can be seen in these two figures.

It can also be seen from figure 4.16 and figure 4.17, at high applied frequencies with stabilizing loop in the system the rotor poles have almost a constant damping factor. This matches with the prediction made using simplified small signal dynamics model in § 4.3.2. At high frequencies, the location of the rotor poles with the stabilizing loop in the system, has a very close agreement with the location of poles at high frequencies in figure 4.11 and figure 4.12 in § 4.3.2. However, at low frequencies, there is a deviation

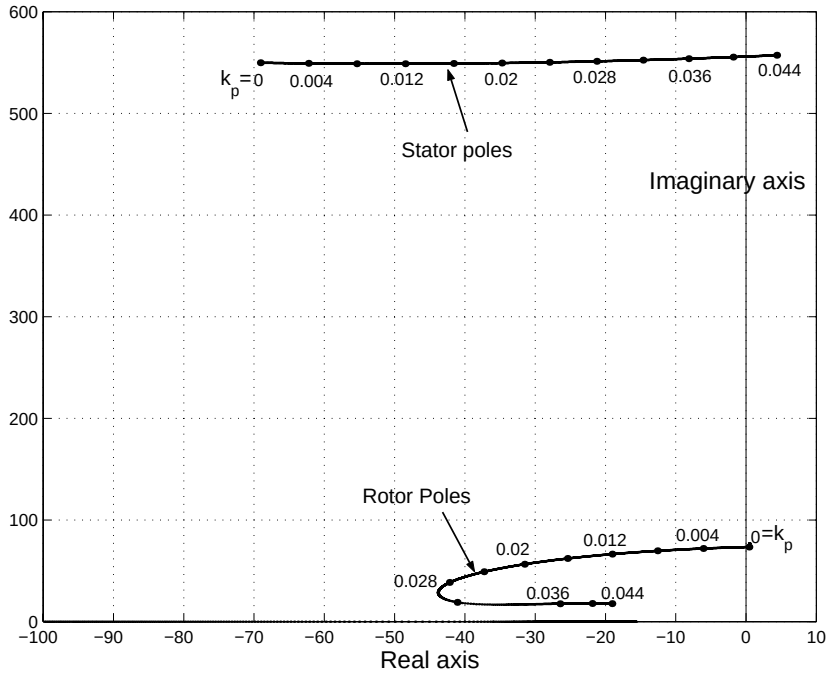

Figure 4.14: *The locus of stator and rotor poles at no-load, rated frequency, as a function of the stabilizing loop gain k_p.*

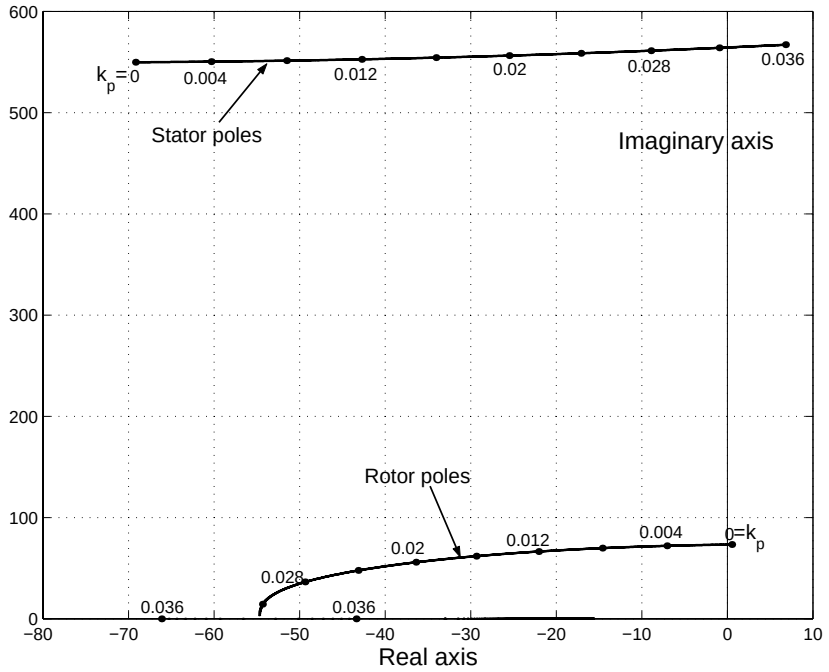

Figure 4.15: *The locus of stator and rotor poles at full-load, rated frequency, constant stator flux linkage control, as a function of the stabilizing loop gain k_p.*

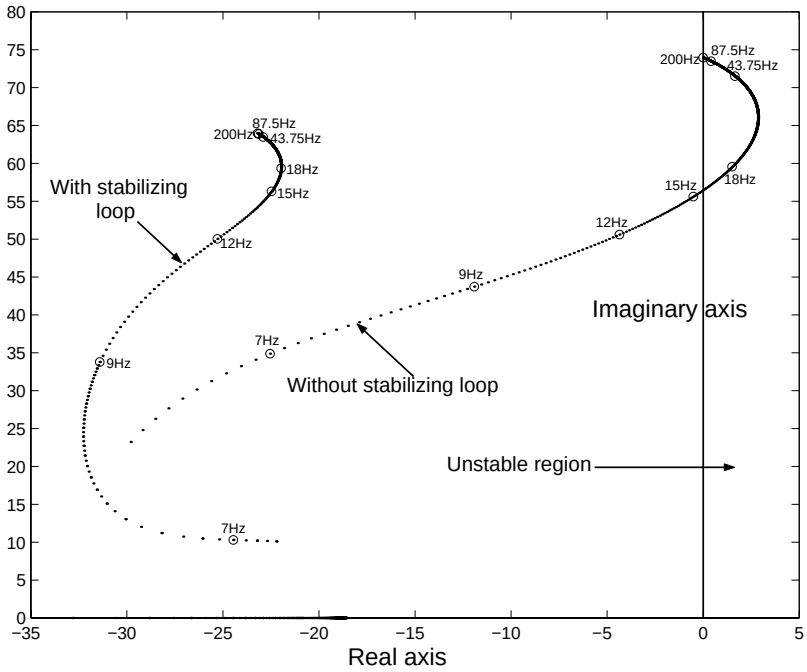

Figure 4.16: *The loci of rotor poles, with and without stabilizing loop at no load, as a function of the applied frequency. For the stabilizing loop, the product* $k_p\omega_0 = 8$.

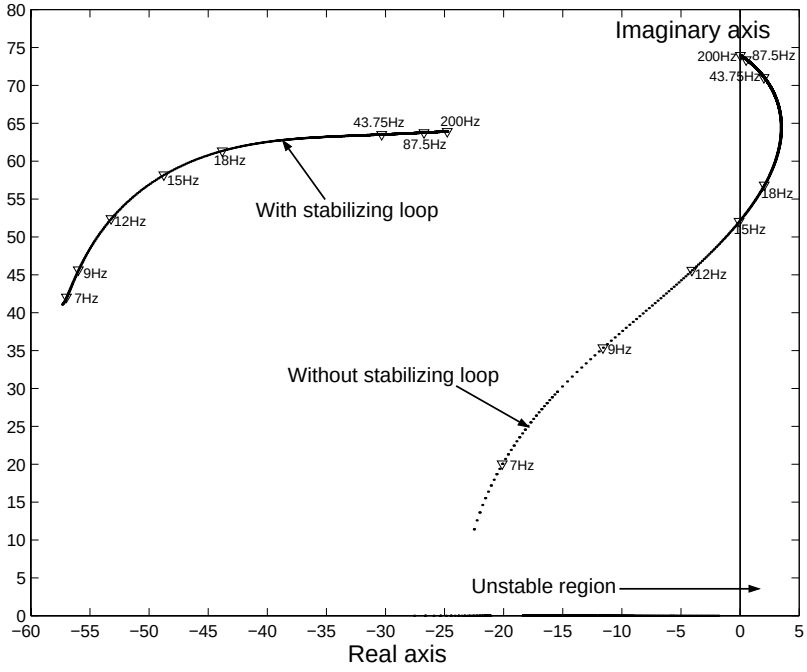

Figure 4.17: *The loci of rotor poles, with and without stabilizing loop at full load, constant stator flux linkage control, as a function of the applied frequency. For the stabilizing loop, the product* $k_p\omega_0 = 8$.

in location of the poles in the simplified small signal dynamics model's prediction. This is due to the approximation made to simplify the model. However, the prediction at high frequencies is the most important, since the instability occurs in the system at relatively high frequencies as it is shown in § 3.4 of Chapter 3.

Figure 4.18 shows the loci of rotor poles with stabilizing loop in the system, under different load conditions, as a function of the applied frequency. It can be seen that how the system damping is affected from the stabilizing loop under different load conditions of the machine.

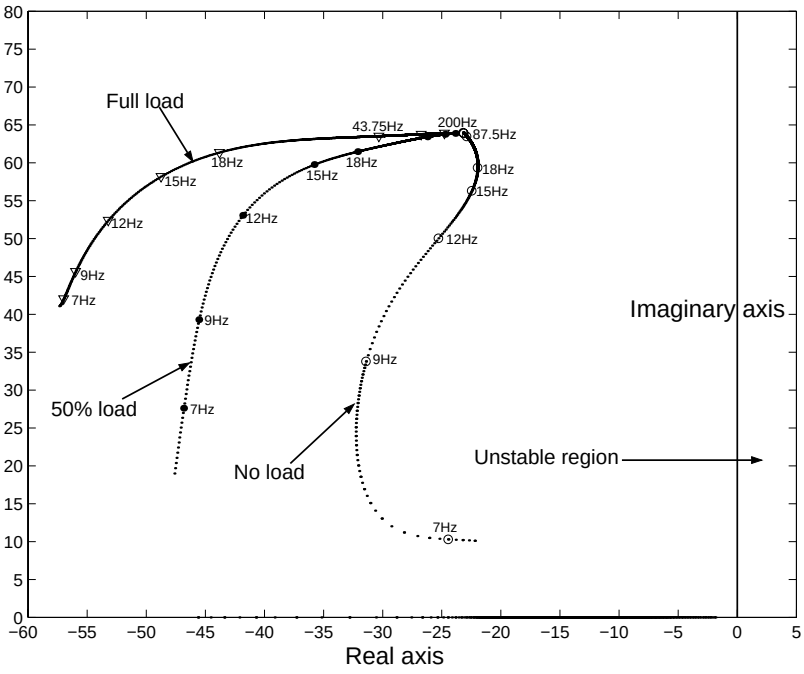

Figure 4.18: *The loci of rotor poles with stabilizing loop, under different load conditions, constant stator flux linkage control, as a function of the applied frequency. For the stabilizing loop, the product* $k_p\omega_0 = 8$.

4.4.2 Implementation of the stabilizing loop

According to the discussion in § 4.3.2 and in § 4.4.1, to stabilize the system, the applied frequency should be modulated using power perturbations as

$$\Delta\omega_e = -k_p \Delta p_e \tag{4.4.12}$$

The perturbation component of the input power Δp_e can be extracted by passing the input power p_e through a first order high-pass filter. The input power p_e can be calculated using the expression

$$p_e = \frac{3}{2} v_s i_s cos(\phi) \tag{4.4.13}$$

where, i_s is the magnitude of the stator current vector and ϕ is the power factor angle.

One can obtain the expression (4.4.13) for the input power, considering the expression given in (4.4.5). Taking the rotor frame current components along the voltage vector one can obtain (see figure 4.19)

$$i^r_{qs}cos(\delta) - i^r_{ds}sin(\delta) = i_s cos(\phi) \tag{4.4.14}$$

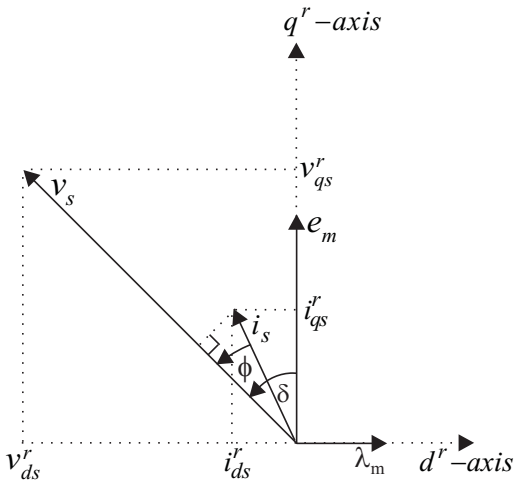

Figure 4.19: *Voltage and current vector in the rotor reference frame.*

Substituting (4.4.14) into the (4.4.5) one obtains the expression (4.4.13) for the input power.

The commanded magnitude of the stator voltage vector can be used for v_s in (4.4.13). The $i_s cos(\phi)$ term in (4.4.13) is the stator current vector component along with the stator voltage vector. This term can directly be calculated if the stator current vector is seen in the stator voltage vector fixed reference frame as shown in figure 4.20. Referring to figure 4.20 and equation (2.4.1) of Chapter 2, the $i_s cos(\phi)$ term can directly be calculated measuring the two phase currents as

$$i^v_{qs} = i_s cos\phi = \frac{2}{3}[i_{as}cos(\theta_e) + i_{bs}cos(\theta_e - \frac{2\pi}{3}) - (i_{as} + i_{bs})cos(\theta_e + \frac{2\pi}{3})] \tag{4.4.15}$$

The commanded position of the stator voltage vector can be used for θ_e in (4.4.15).

With this knowledge, the implementation of the stabilizing loop, which uses input power perturbations to modulate the applied frequency, is shown in figure 4.21.

If the DC-link current perturbations are used to stabilize the system, the applied frequency should be modulated as (see § 4.3.3)

$$\Delta\omega_e = -k_i \Delta i_{dc} \tag{4.4.16}$$

Measuring the DC-link current the perturbation component Δi_{dc} can be extracted. The implementation of the stabilizing loop using DC-link current perturbations is shown in

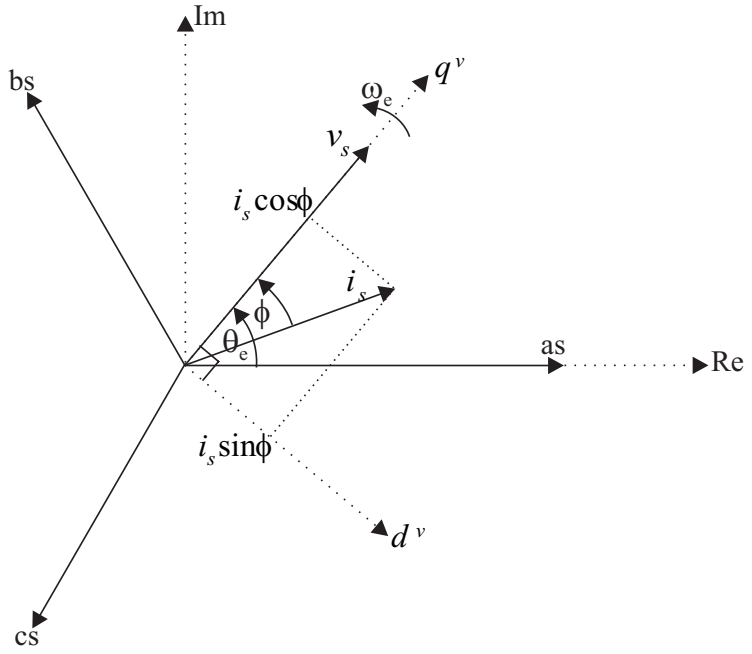

Figure 4.20: *Stator current vector in stator voltage vector fixed reference frame.*

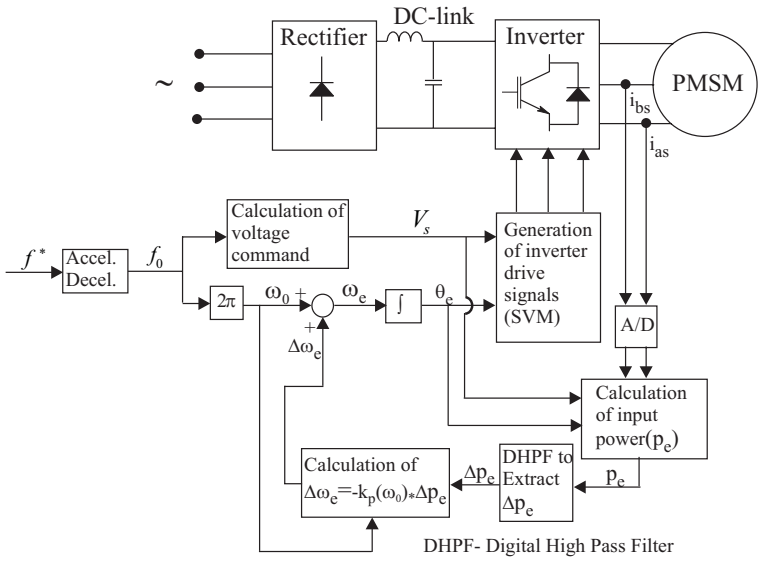

Figure 4.21: *Block diagram showing the implementation of the stabilizing loop, which uses input power perturbations to modulate the applied frequency.*

figure 4.22. The DC-link current can be measured using a current sensor in the DC-link. Before sampling, the DC-link current should be passed through an analogue low-pass filter as shown in figure 4.22, to filter out the high frequency current components due to the switchings in the inverter. Similar to the method used to obtain the input power perturbations Δp_e, the sampled DC-link current can be passed through a digital high-pass filter to extract the perturbation component Δi_{dc}.

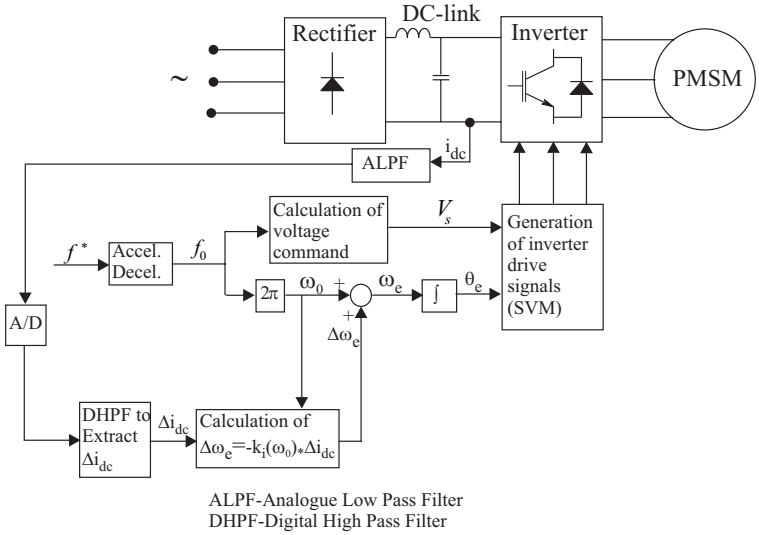

Figure 4.22: *Block diagram showing the implementation of the stabilizing loop, which uses DC-link current perturbations to modulate the applied frequency.*

4.4.3 Simulations and experimental results

To demonstrate the effectiveness of the frequency modulation, the computer simulations were carried out for the system with frequency modulated stabilizing loop using both input power perturbations and DC-link current perturbations.

The stabilizing loop, which uses the input power perturbations was modeled in the system as shown in figure 4.21. A voltage source inverter with a constant DC-link voltage (560 V) was used and, the switching frequency and the sampling frequency of the system was 5 kHz. The parameters, which were used for the simulations were the same as the parameters used to draw the eigenvalue plots with the stabilizing loop in figure 4.16 and figure 4.17. In order to see the operating point stability with the stabilizing loop, the simulation method used here is exactly the same as the method used in § 3.4.3 of Chapter 3. The rotor speed and the load condition of the machine were initialized to the required steady state operating point value, and then, the machine was simulated exciting the frequency and the voltage correspondent to that steady state operating point. The simulated rotor speed responses with input power perturbation

stabilizing loop, machine under no-load and full-load are shown in figure 4.23 and figure 4.24 respectively. Each figure shows the rotor speed responses at 43.75 Hz (50% of rated frequency) and at 87.5 Hz (Rated frequency). Comparing these simulated rotor speed responses with the simulation results, which were given in figures 3.13(c),(d) and figures 3.14(c),(d) in Chapter 3, it can be seen that the effectiveness of the frequency modulated stabilizing loop in the system.

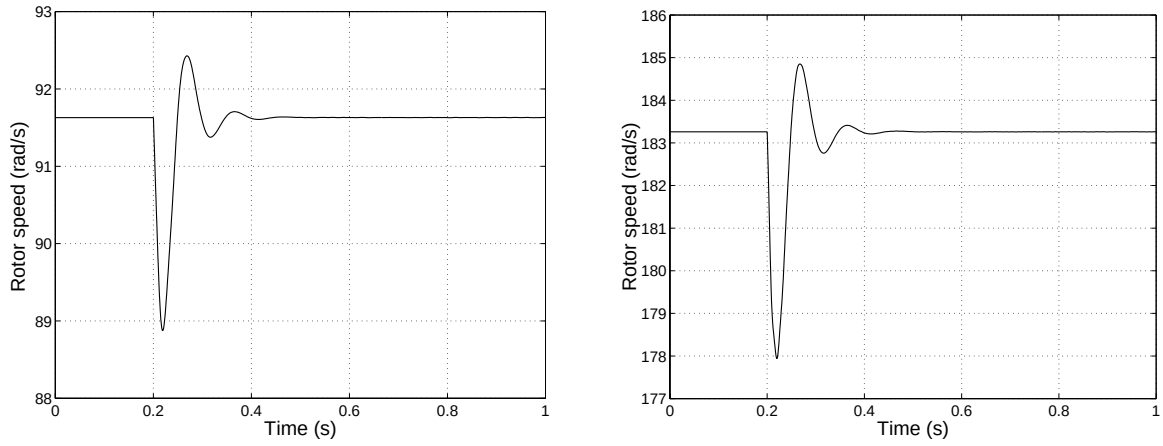

(a) (b)

Figure 4.23: *Simulated rotor speed responses, machine under no-load, with input power perturbation stabilizing loop. The excitation voltage $V_s = E_m$. (a) At 43.75 Hz (50% of the rated frequency) (b) At 87.5 Hz (rated frequency).*

The same simulations were carried out for the system with the stabilizing loop, which uses DC-link current perturbations. The stabilizing loop was modeled as shown in figure 4.22. A second-order Butterworth type analogue low-pass filter with 1 kHz cut-off frequency was used to filter out the high frequency current components in the measured DC-link current, before sampling it. In order to have a higher bandwidth (i.e. higher cut-off frequency) in the filter, a second-order filter was selected rather than a first order one. Since the sampling frequency of the system is 5 kHz, the cut-off frequency of the second-order filter was able to select as high as 1 kHz to obtain the DC-link current in average sense. The gain k_i for this stabilizing loop was calculated according to (4.3.15), using the gain k_p which was used for the previous simulation, in order to have same system poles as in the stabilizing loop with power perturbations. Other parameters for the system were the same as for the previous simulation with power perturbation stabilizing loop. The simulated rotor speed responses are shown in figure 4.25 and figure 4.26 for no-load and full-load cases respectively. These simulation results also show the effectiveness of this stabilizing loop in the system.

The variation of other variables with rotor speed is shown in figure 4.27 and figure

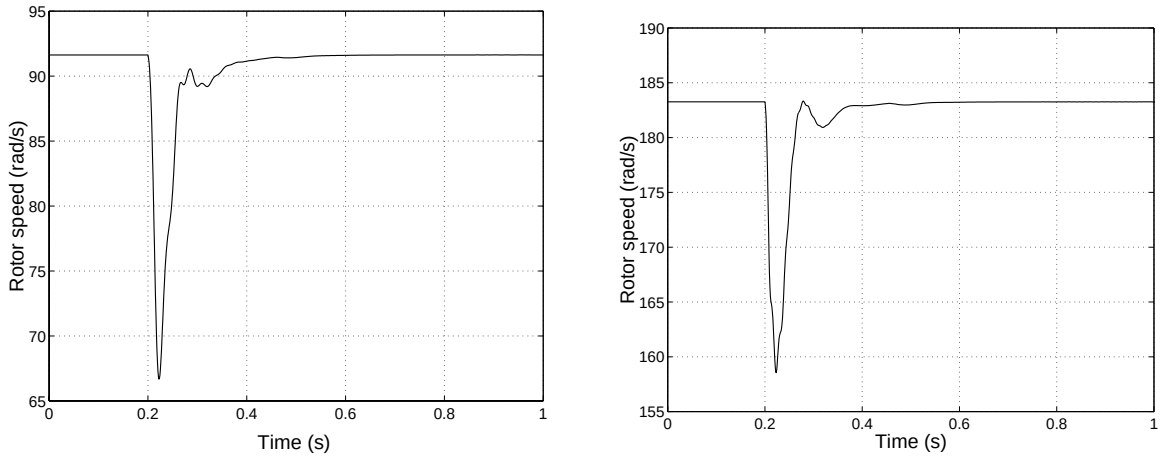

(a) (b)

Figure 4.24: *Simulated rotor speed responses, machine under full-load, with input power perturbation stabilizing loop. The excitation voltage is according to constant stator flux linkage control. (a) At 43.75 Hz (50% of the rated frequency) (b) At 87.5 Hz (rated frequency).*

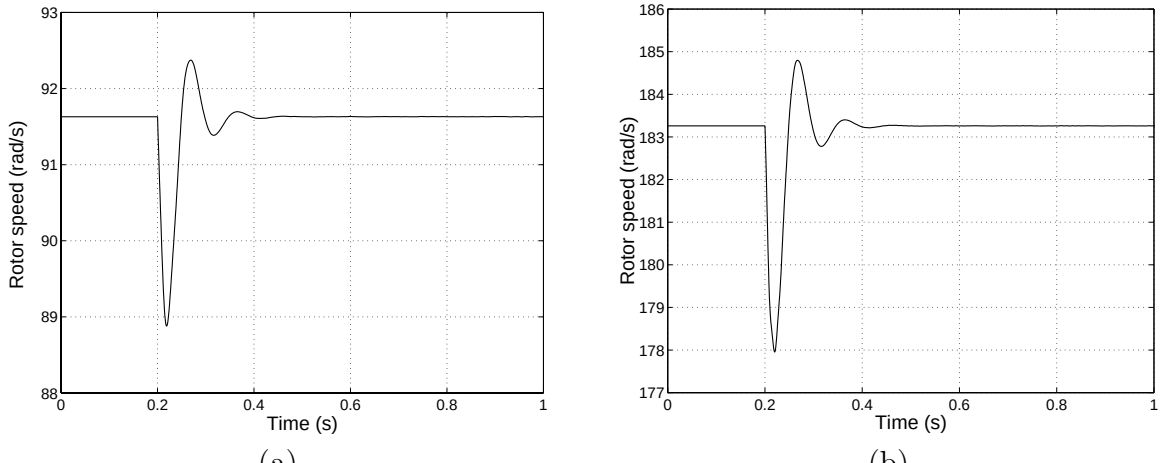

(a) (b)

Figure 4.25: *Simulated rotor speed responses, machine under no-load, with DC-link current perturbation stabilizing loop. The excitation voltage $V_s = E_m$. (a) At 43.75 Hz (50% of the rated frequency) (b) At 87.5 Hz (rated frequency).*

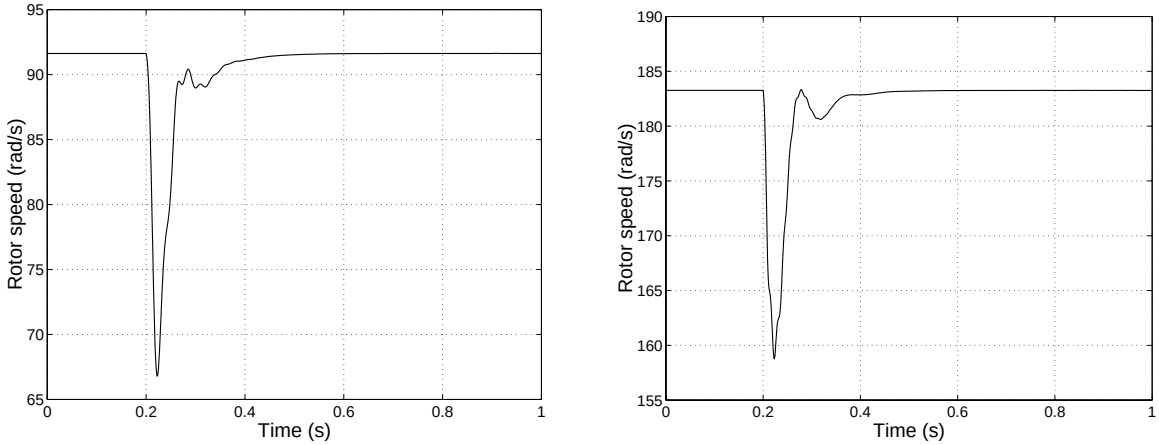

Figure 4.26: *Simulated rotor speed responses, machine under full-load, with DC-link current perturbation stabilizing loop. The excitation voltage is according to constant stator flux linkage control. (a) At 43.75 Hz (50% of the rated frequency) (b) At 87.5 Hz (rated frequency).*

4.28 for power perturbation stabilizing loop and DC-link current perturbation stabilizing loop respectively. For these simulation results, the machine was under full-load and at rated frequency.

The power perturbation stabilizing loop and the DC-link current perturbation stabilizing loop were also implemented in the laboratory prototype drive system as shown in figure 4.21 and figure 4.22 respectively. The parameters for the stabilizing loops (The time constants of the filters and the gains k_p, k_i) were selected as same as for the simulations. The switching frequency and the sampling frequency of the DSP-microcontroller based prototype drive system (see Appendix D) is 5 kHz.

The measured rotor speeds, when the machine is ramped up to different frequencies, under no-load (i.e. applying the voltage $V_s = E_m = 2\pi f_0 \lambda_m$) with stabilizing loops in the system are shown in figure 4.29. Comparing these measurements with the measured speeds in figure 3.15 of Chapter 3, where the stabilizing loop was not in effect, it can be seen the effectiveness of the stabilizing loop in the system at high frequencies.

The measured rotor speed and the stabilizing loop variables when the machine is ramped up to 50% of rated frequency under no-load are shown in figure 4.30 and in figure 4.31 with power perturbation stabilizing loop and with DC-link current perturbation stabilizing loop in the system respectively. After the initial transients during ramping the system's stable operation can be seen with each stabilizing loop in the system, in contrast to the situation under open-loop V/f control at this frequency shown in figure 3.15 of Chapter 3.

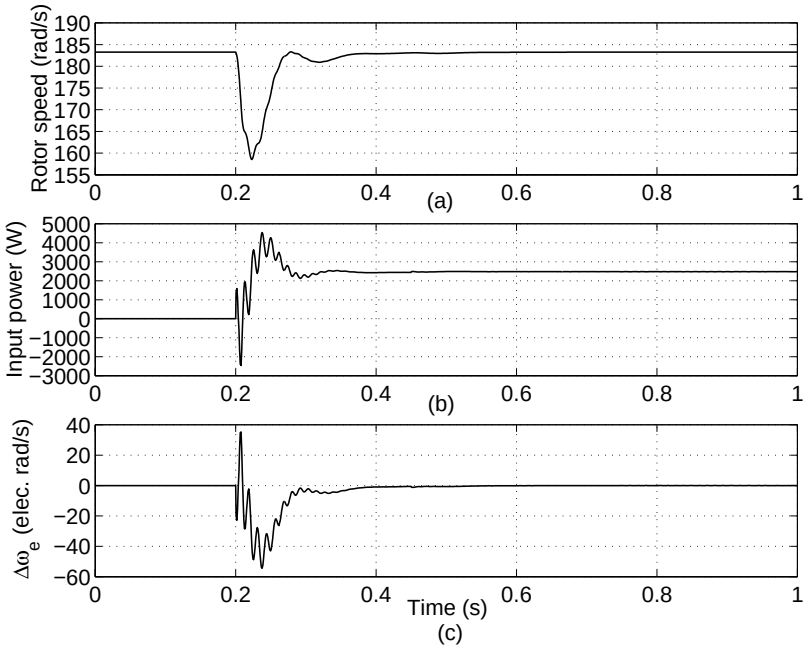

Figure 4.27: *Simulated variables, machine under full-load, at rated frequency (87.5 Hz), with input power perturbation stabilizing loop. The excitation voltage is according to constant stator flux linkage control. (a) Rotor speed (b) Input power (c) Frequency modulation signal ($\Delta\omega_e$).*

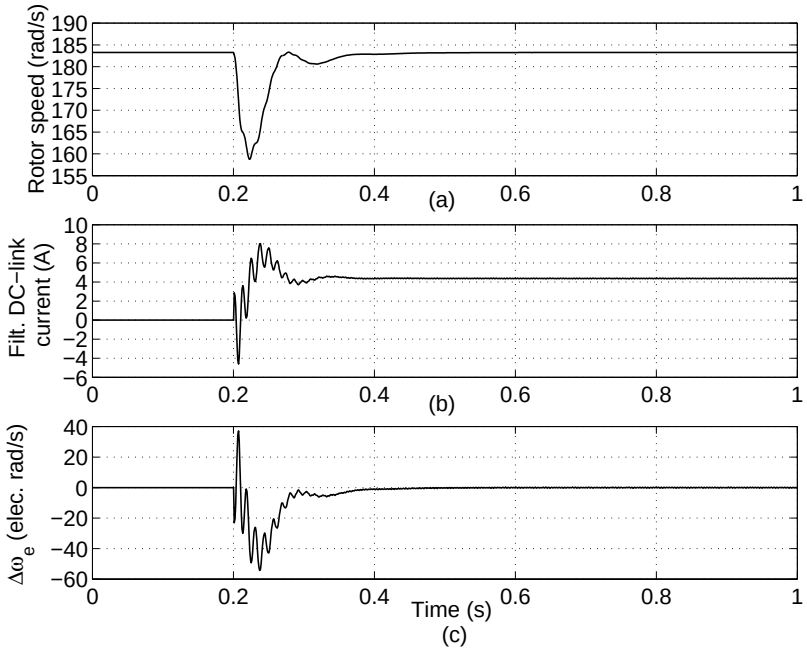

Figure 4.28: *Simulated variables, machine under full-load, at rated frequency (87.5 Hz), with DC-link current perturbation stabilizing loop. The excitation voltage is according to constant stator flux linkage control. (a) Rotor speed (b) Filtered DC-link current (c) Frequency modulation signal ($\Delta\omega_e$).*

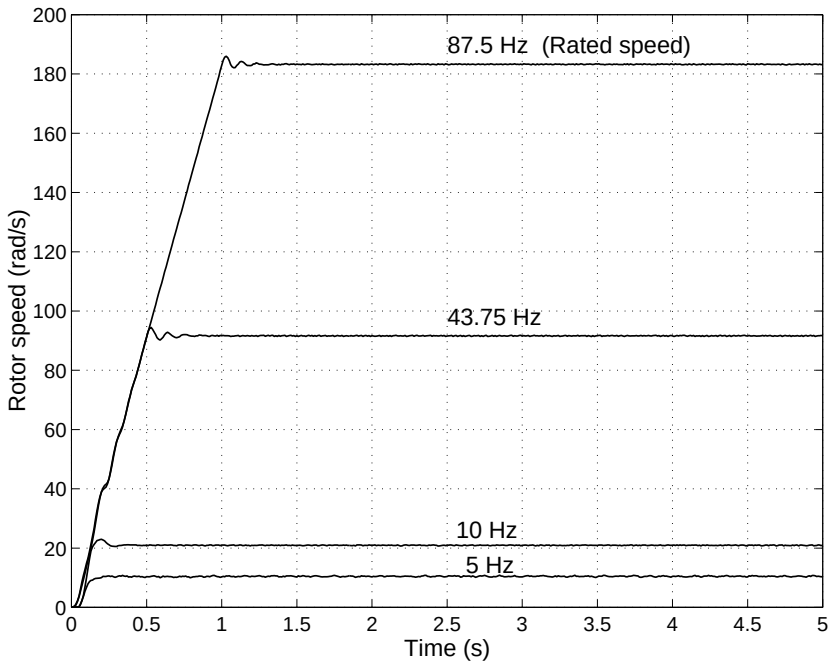

(a)

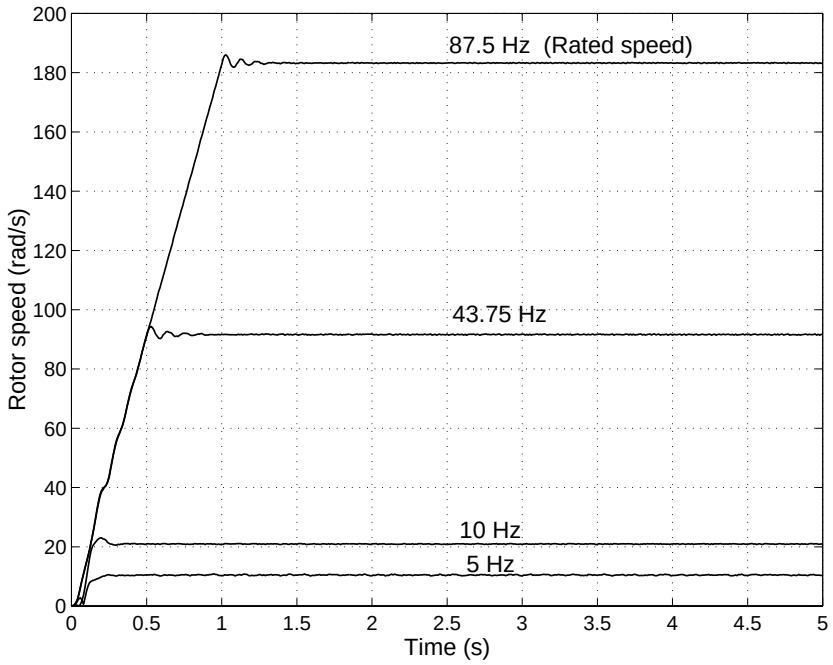

(b)

Figure 4.29: *Measured rotor speeds at different frequencies, under no-load with frequency modulated stabilizing loops. (a) With power perturbation stabilizing loop (b) With DC-link current perturbation stabilizing loop.*

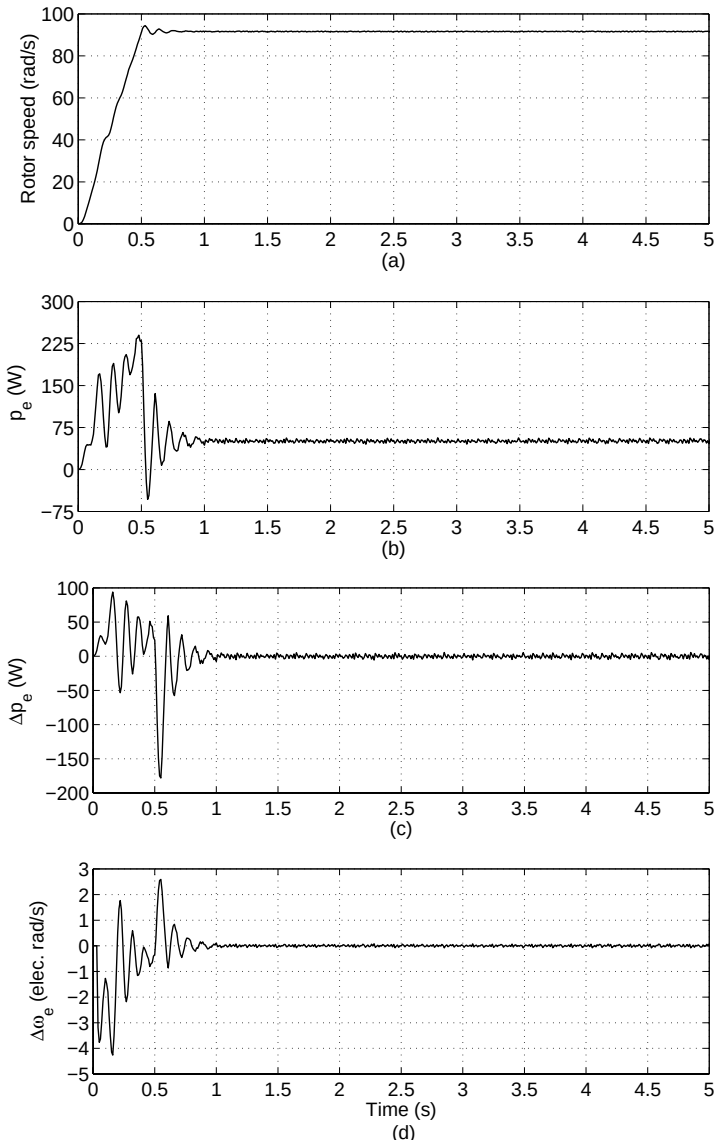

Figure 4.30: *Measured variables when the machine is ramped up to 50% of rated frequency under no-load with power perturbation stabilizing loop. (a) Rotor speed (b) Input power p_e (c) Input power perturbation Δp_e (d) Frequency modulation signal $\Delta\omega_e$.*

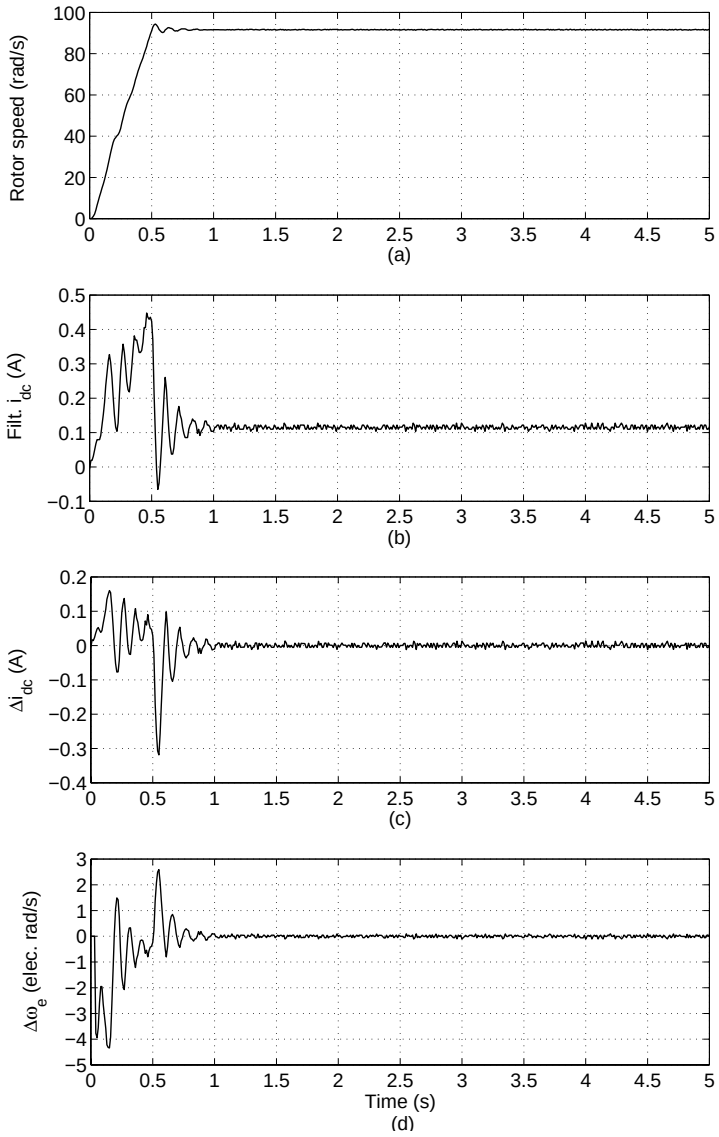

Figure 4.31: *Measured variables when the machine is ramped up to 50% of rated frequency under no-load with DC-link current perturbation stabilizing loop. (a) Rotor speed (b) Filtered DC-link current (c) DC-link current perturbation Δi_{dc} (d) Frequency modulation signal $\Delta\omega_e$.*

4.5 Summary

The solutions for mid-frequency instability of the open-loop V/f controlled PMSMs have been investigated in this chapter. The simplified small signal dynamics model presented in this chapter has helped to think how to stabilize the system by frequency modulation. The machine's power balance equation incorporated with this small signal dynamics model has shown that by modulating the applied frequency proportional to the perturbations in the input power the stable operation of the PMSM is possible for a wide frequency range. For voltage source inverter driven drives the perturbations in the DC-link current can also be used for that purpose. The simplified small signal dynamics model has also helped to select the gains for those stabilizing loops. To implement those stabilizing loops either calculated input power of the system or measured DC-link current can be used and no rotor position sensor is required. The full small signal dynamics analysis, computer simulations and laboratory test results have verified the effectiveness of those stabilizing loops.

After adding the stabilizing loop to the open-loop V/f controlled PMSM, the system is operated in closed-loop manner providing the synchronization between the stator excitation and the motion of the rotor. The physical meaning of the stabilizing loop can be seen as that way and it enables the stable operation of the PMSM for a wide frequency range as expected.

Bibliography

[1] R. S. Colby, *Efficient High Speed Permanent Magnet Synchronous Motor Drives*, Ph.D. Thesis, University of Wisconsin-Madison, USA, 1987.

[2] R. S. Colby and D. W. Novotny, *An Efficiency-Optimizing Permanent-Magnet Synchronous Motor Drive*, IEEE Transactions on Industry Applications, Vol. 24, No.3, pp. 462-469, May/June 1988.

[3] J. Birk, P. S. Frederiksen and F. Blaabjerg, *Digital Implemented Sensorless Power Factor Control of Permanent Magnet AC-Machine with a Minimum Number of Transducers*, Proceedings of power electronics, motion control conference (PEMC), pp. 337-342, 1994.

[4] P. S. Frederiksen, J. Birk and F. Blaabjerg, *Comparison of Two Energy Optimizing Techniques for PM-machines*, Proceedings of IECON'94, Vol. 1, pp. 32-37, 1994.

[5] Yoshinobu Nakamura, Toshiaki Kudo, Fuminori Ishibashi and Sadayoshi Hibino, *High-Efficiency Drive Due to Power Factor Control of a Permanent Magnet Synchronous Motor*, IEEE Transactions on Power Electronics, Vol. 10, No.2, pp. 247-253, March 1995.

[6] P. D. Chandana Perera, Frede Blaabjerg, John K. Pedersen and Paul Thogersen, *Open Loop Stability and Stabilization of Permanenr Magnet Synchronous Motor Drives Using DC-Link Current*, Proceedings of IEEE Nordic Workshop on Power and Industrial Electronics, pp. 47-53, June 2000.

Chapter 5

Sensorless Stable PMSM Drive with V/f Control Approach

5.1 Introduction

In Chapter 4, methods for stabilizing open-loop V/f controlled PMSM drives were discussed. With that knowledge, the stable V/f controlled PMSM drive can be shown as in figure 5.1.

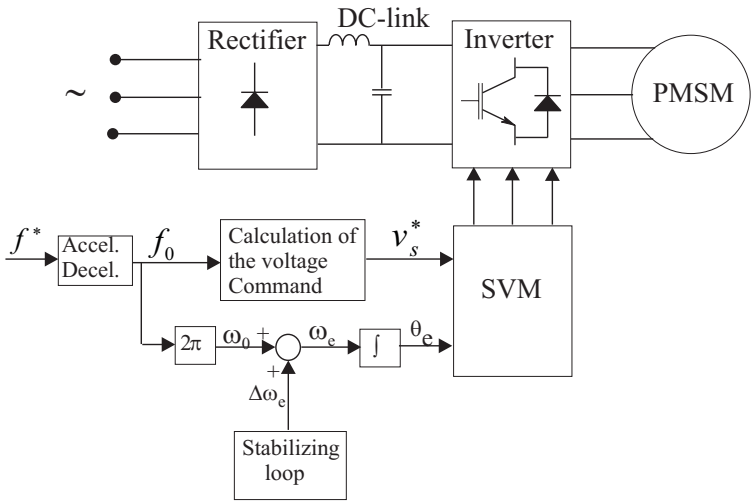

Figure 5.1: *Block diagram of the stable V/f controlled PMSM drive.*

In the analysis in Chapter 4, it was also considered, during operation, a constant stator flux linkage is maintained in the machine of the drive system. If the stator resistance voltage drop is neglected, using constant V/f ratio control, the machine's stator flux linkage can be maintained approximately a constant value. However, especially, during low speed operation, the constant V/f ratio control makes problems, since the stator resistance voltage drop is not negligible at low speeds. Overcoming that problem, the magnitude of the stator voltage control method of the machine, is discussed in this

chapter. Moreover, the performance of the total drive scheme, which includes the proposed voltage control method and the stabilizing loop, is studied through simulations and experimental results.

5.2 Voltage magnitude control method

In the V/f controlled PMSM drive the voltage magnitude should be controlled properly, in order to maintain the required stator flux level in the machine and obtain the satisfactory performance from the drive (the properties of constant stator flux linkage control of PMSMs are discussed in detail in § 2.8.5 of Chapter 2).

For V/f controlled induction motor drives, the voltage magnitude control methods, in order to maintain the required stator flux level in the machine were widely discussed in the literature [1], [2], [3], [4], [5], [6]. For PMSM drives, it has not been widely discussed, but, some concept used for induction motor drives may applicable to PMSM drives. In subsequent sections, a voltage magnitude control method is studied for the PMSM drive system shown in figure 5.1.

5.2.1 Constant V/f ratio control

From § 2.7 of Chapter 2, the steady state voltage equations for the IPMSM are

$$V_{qs}^r = r_s I_{qs}^r + \omega_0 L_d I_{ds}^r + \omega_0 \lambda_m = r_s I_{qs}^r + \omega_0 \lambda_{ds}^r \tag{5.2.1}$$

$$V_{ds}^r = r_s I_{ds}^r - \omega_0 L_q I_{qs}^r = r_s I_{ds}^r - \omega_0 \lambda_{qs}^r \tag{5.2.2}$$

where $\omega_0 = 2\pi f_0$ and f_0 is the applied frequency to the machine. If the stator resistance voltage drop is neglected, the steady state voltage equations can be approximated as

$$V_{qs}^r \approx \omega_0 \lambda_{ds}^r \tag{5.2.3}$$

$$V_{ds}^r \approx -\omega_0 \lambda_{qs}^r \tag{5.2.4}$$

and the magnitude of the stator voltage vector is

$$V_s = \sqrt{(V_{qs}^r)^2 + (V_{ds}^r)^2} \approx \omega_0 \sqrt{(\lambda_{ds}^r)^2 + (\lambda_{qs}^r)^2} = \omega_0 \lambda_s \tag{5.2.5}$$

Therefore,

$$\frac{V_s}{\omega_0} \approx \lambda_s \tag{5.2.6}$$

It can be seen that when the stator resistance voltage drop is neglected, the ratio $\frac{V_s}{\omega_0}$ is equal to the magnitude of the stator flux linkage vector λ_s. Controlling the $\frac{V_s}{\omega_0}$ ratio equals to the required stator flux magnitude, one can maintain the required stator flux to the machine, if the stator resistance voltage drop is negligible. However, when

the machine operates under load with high current, the stator resistance voltage drop is high and it cannot be neglected (This is very important at low speeds). Therefore, controlling the $\frac{V_s}{\omega_0}$ ratio to a constant value, the magnitude of the stator flux cannot be maintained a constant value when the machine is operated under load. This implies that in order to maintain the required flux in the machine, the magnitude of the stator voltage should be compensated for stator resistance voltage drop, when the machine is operated under load. How this can be achieved will be discussed in the following §5.2.2.

5.2.2 Calculation of voltage magnitude with stator resistance voltage drop compensation

Using IPMSM's steady state vector diagram the calculation of the voltage magnitude with vector compensation of the stator resistance voltage drop will be discussed in this section.

The IPMSM's steady state vector diagram, which is described in § 2.7 of Chapter 2 is drawn in the figure 5.2 (a). This vector diagram can be simplified to obtain the stator voltage vector as an addition of stator resistance voltage drop and stator flux induced voltage (E_s). This is shown in the triangle OAB of the vector diagram in figure 5.2 (b).

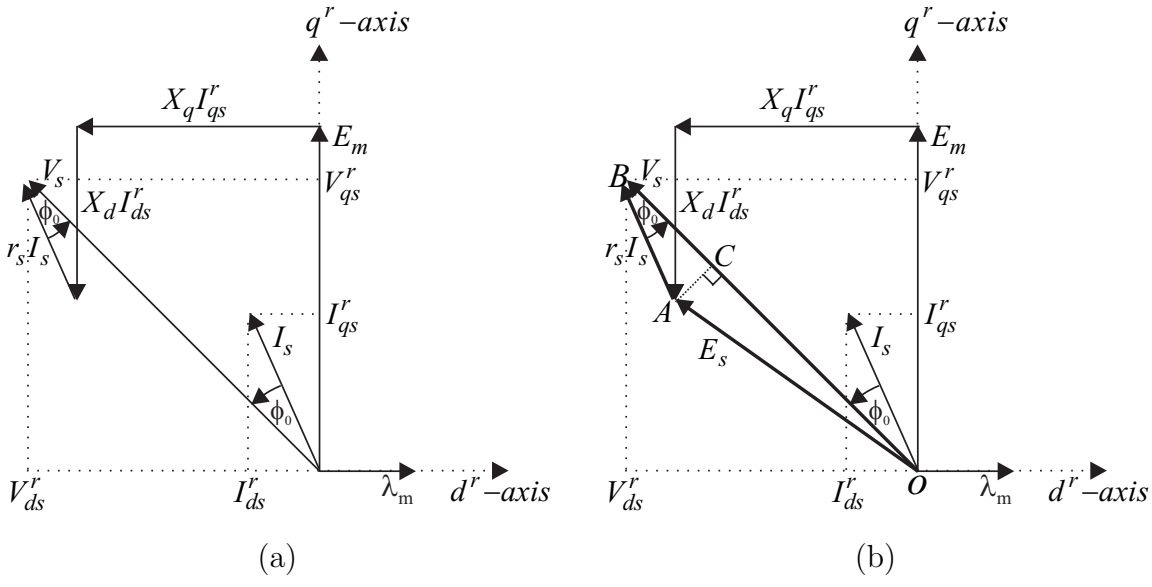

Figure 5.2: *(a) Steady state vector diagram of the IPMSM. (b) Steady state vector diagram of the IPMSM showing the stator voltage vector as vector addition of stator resistance voltage drop and induced voltage from the stator flux (In the triangle OAB).*

In the triangle OAB the AC is drawn perpendicular to the OB. From OAB triangle the magnitude of the stator voltage V_s can be obtained as

$$V_s = BC + CO = I_s r_s cos\phi_0 + \sqrt{E_s^2 - I_s^2 r_s^2 sin^2\phi_0} \tag{5.2.7}$$

where, ϕ_0 is the steady state power factor angle.

Using the trigonometric relationship $sin^2\phi_0 + cos^2\phi_0 = 1$, the magnitude of the stator voltage vector given in (5.2.7) can also be written as

$$V_s = I_s r_s cos\phi_0 + \sqrt{E_s^2 + I_s^2 r_s^2 cos^2\phi_0 - I_s^2 r_s^2} \tag{5.2.8}$$

Even though in (5.2.8) contains the steady state quantities, this expression can be used to command the voltage to the machine using instantaneously measured quantities, so that the machine's stator flux is as the required value in steady state. Using instantaneously measured quantities and required value for stator flux, the implementation of (5.2.8) is discussed below.

In (5.2.8), the stator flux induced voltage E_s can be calculated from the required steady state constant stator flux. Due to the reasons mentioned in § 2.8.5 of Chapter 2, the required magnitude of the stator flux is selected as λ_m. Therefore, the E_s can be calculated as

$$E_s = 2\pi f_0 \lambda_m \tag{5.2.9}$$

The term $I_s cos\phi_0$ in (5.2.8) is the stator current vector component along with the stator voltage vector (active current component). This is the same current component, which is used for power calculation in § 4.4.2 of Chapter 4, for the power perturbation stabilizing loop. Measuring two phase currents this term can be calculated instantaneously as described in § 4.4.2 of Chapter 4 and the equation for it as follows.

$$i_s cos\phi = \frac{2}{3}[i_{as} cos(\theta_e) + i_{bs} cos(\theta_e - \frac{2\pi}{3}) - (i_{as} + i_{bs}) cos(\theta_e + \frac{2\pi}{3})] \tag{5.2.10}$$

In (5.2.10), θ_e is the position of the voltage vector in the stationary reference frame (This is known in the system).

I_s (the magnitude of the stator current vector) in (5.2.8), can also be obtained instantaneously measuring two phase currents and calculating the stationary d^s, q^s reference frame current components as

$$i_s = \sqrt{(i_{ds}^s)^2 + (i_{qs}^s)^2} = \sqrt{\frac{1}{3}(i_{as} + 2i_{bs})^2 + (i_{as})^2} \tag{5.2.11}$$

Using the instantaneously calculated values and the commanded value for E_s the final expression for calculation of magnitude of the voltage command v_s^* can be written as

$$v_s^* = (i_s cos\phi) r_s + \sqrt{(2\pi f_0 \lambda_m)^2 + (i_s cos\phi)^2 r_s^2 - i_s^2 r_s^2} \tag{5.2.12}$$

It should be mentioned that (5.2.12) expresses the magnitude of the stator voltage command, with vector addition of the stator resistance voltage drop to the induced voltage from the required stator flux.

Measuring the instantaneous currents the implementation of (5.2.12) in the digital drive system is shown in figure 5.3. The previous sampling period calculated value of the position of the voltage vector, i.e. $\theta_e(k-1)$, is used to calculate the active current component ($i_s cos\phi$) given in (5.2.10). In order to eliminate the high frequency ripples in calculated currents i_s and $i_s cos\phi$, two digital low-pass filters (DLPF) are used as shown in figure 5.3. Without those two filters the calculated voltage command can be distorted by the ripples in the currents and it affects the stable operation of the system. During low speed operation, since the voltage is low, the elimination of distortion in voltage command is particularly important by filtering the currents. It was found that the cut-off frequency of the filters used for the currents should be selected as low as 5 Hz, in order to obtain the satisfactory performance from the system for the whole operating frequency range.

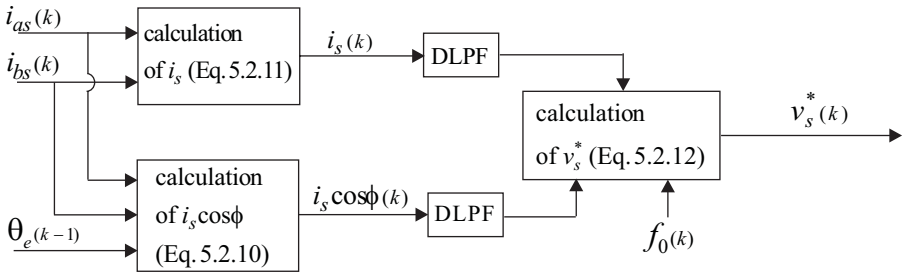

Figure 5.3: *Derivation of the voltage command in the drive with vector compensation of the stator resistance voltage drop.*

5.3 The complete drive scheme

If the voltage control method described in §5.2.2 is used in the drive system, refer to the discussion in §4.4.2 of Chapter 4, it is obvious that the stabilizing loop which uses direct input power perturbations should be the best stabilizing technique to incorporate with the drive. If DC-link current perturbation stabilizing loop is used, the system will require an extra current sensor to measure the DC-link current and an analogue low-pass filter (see figure 4.22 of Chapter 4). When the voltage control method described in §5.2.2 is used in the drive, the input power calculation can easily be done and the derivation of the frequency modulation signal is straightforward. This is shown in figure 5.4 and this method is used in the drive.

The complete drive scheme with voltage control and the stabilizing loop is shown in figure 5.5.

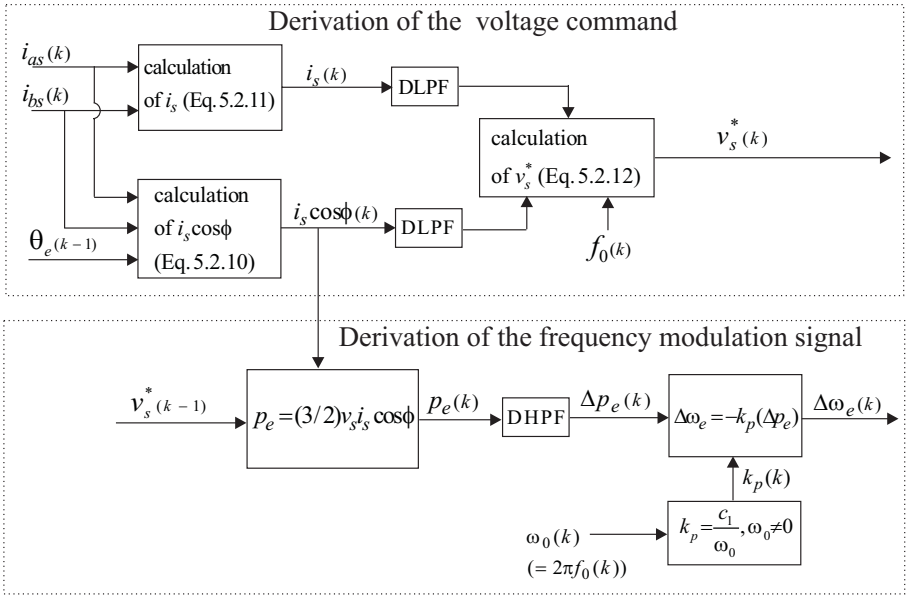

Figure 5.4: *Derivation of the voltage command and the frequency modulation signal in the drive system.*

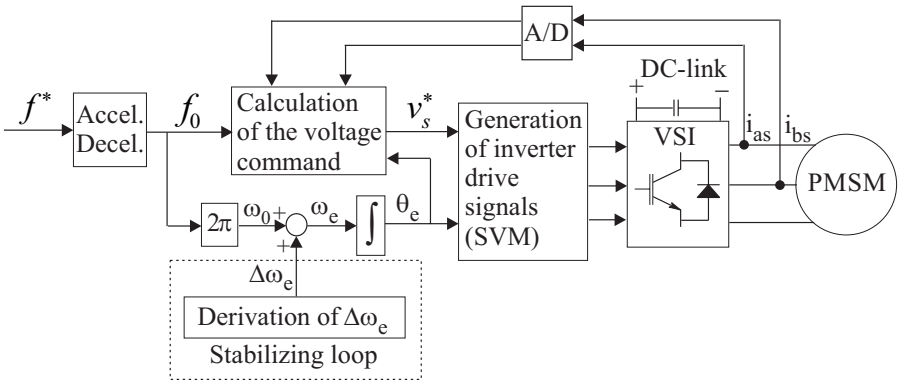

Figure 5.5: *The complete drive scheme with voltage control and stabilizing loop.*

5.3.1 Inverter nonlinearity compensation

In order to obtain the commanded voltage accurately to the machine, the compensation of the inverter nonlinearities, i.e. ripple in the DC-link voltage, dead-time and voltage drop across the power devices, is also considered in the drive system shown in figure 5.5. The details about inverter nonlinearity compensation are given in Appendix C.

5.3.2 Starting of the drive

Before starting the drive system, a DC voltage is applied to the machine so that the rotor can be aligned to a known initial position. Maintaining the θ_e to zero the DC voltage is applied to the machine from the modulator. In this way, the rotor d-axis is aligned with stator a-phase axis [7], [8]. In order to obtain a slow motion of the rotor during this process, the DC voltage is applied to the machine as shown in figure 5.6, rather than directly applying a constant value from the beginning. The voltage is ramped up slowly (t_1 =200 ms) and applied it to the machine for a while (v =10 V, t_2 =500 ms) and it is ramped down to zero slowly. After applying the voltage in that way, the starting of the drive is delayed for another 100 ms in order to give time to decay the currents. After this process, which lasts within 1 s, the drive is started applying the initial voltage vector along the rotor q-axis, assuring a positive starting torque from the machine.

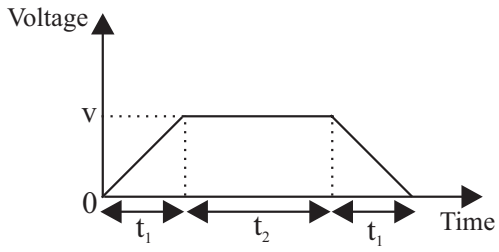

Figure 5.6: *The DC voltage applied to the machine before starting so that the rotor can be aligned to a known position.*

Without knowing the initial rotor position arbitrary applying the initial voltage vector to the machine, in some situations, the rotor may cause to rotate opposite direction and the smooth start of the machine may not be possible.

5.4 Performance of the drive

In order to investigate the performance of the drive scheme shown in figure 5.5, it was implemented in the laboratory test system. The voltage control algorithm and the stabilizing loop were implemented in the digital system with 5 kHz sampling rate. The

details about the laboratory test system is given in Appendix D. The motor parameter values (r_s and λ_m) required for voltage control algorithm were used from the motor name-plate. The stabilizing loop parameters were selected as the values used for the analysis in §4.4.1 of Chapter 4. They are

$$\tau_h(\text{High-pass filter time constant}) = 0.0637s \tag{5.4.1}$$

$$k_p(\text{Stabilizing loop gain}) = \frac{8}{\omega_0}, \omega_0 \neq 0 \tag{5.4.2}$$

The stabilizing loop was added to the system after exceeding the applied frequency 3 Hz.

5.4.1 Effect of the stabilizing loop

Using the drive configuration shown in figure 5.5, the machine was ramped up to the rated speed under no-load and put into continuous operation. The measured variables are shown in figure 5.7 and the stable operation of the system can be seen from these measurements. In the second test, the drive was started in the same way, but, after 6 s the stabilizing loop was removed from the control algorithm, forcing the stabilizing loop gain k_p to zero. The measured variables for this test are shown in figure 5.8. After removing the stabilizing loop from the control algorithm, the system became unstable as it can be seen from the measurements in figure 5.8. The requirement of the stabilizing loop in the control algorithm is evident from these two experiments.

5.4.2 Load disturbance rejection

For the drive system shown in figure 5.5, a 12 Nm load step (100% load step) was added at 43.75 Hz, where there were severe problems observed under open-loop V/f control (see figure 3.15 of Chapter 3). The computer simulations are shown in figure 5.9 and the laboratory measurements are shown in figure 5.10 (Measured variables are shown after starting the drive, i.e. applying of the DC voltage before starting of the drive is not shown). From these results it can be seen that the drive's capability of stable operation overcoming sudden load change in the system. Moreover, it can also be seen that there is a good agreement between computer simulation results and laboratory measurements.

The effect of the stabilizing loop gain to the system can be seen from the measurements shown in figure 5.11. Figure 5.11(a) shows the speed response when adding a 100% load step to the drive at 87.5 Hz (rated speed) with nominal gain, i.e. $k_p = \frac{8}{\omega_0}$. Figure 5.11(b) shows the results with half of the nominal gain, i.e. $k_p = \frac{4}{\omega_0}$. The less damping in the system with reduced gain in the stabilizing loop can be seen as expected from the analysis shown in figure 4.15 of Chapter 4.

To verify the importance of the r_s voltage drop compensation (especially at low frequencies) in the voltage control of the machine, two tests were carried out. For the

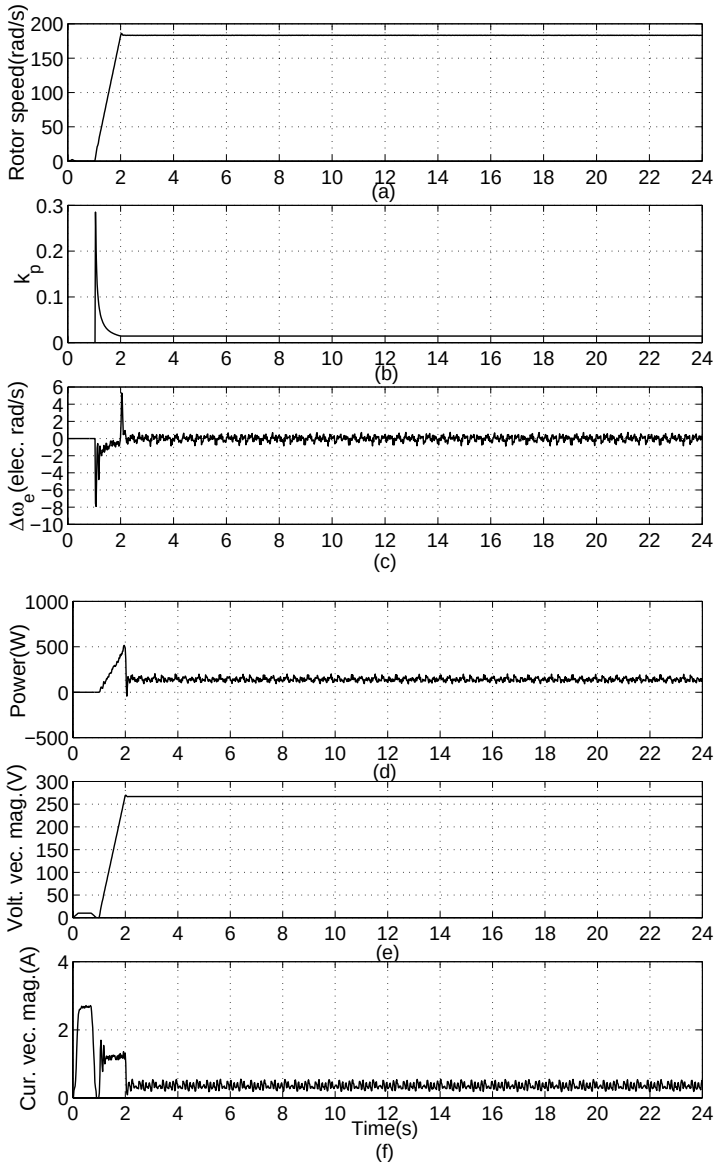

Figure 5.7: *Measured variables from the complete drive system for the rated speed (87.5 Hz), under no-load. (a) Rotor speed (b) Stabilizing loop gain k_p (c) Frequency modulation signal $\Delta\omega_e$ (d) Calculated input power in the stabilizing loop (e) Commanded magnitude of the voltage vector (f) Magnitude of the current vector.*

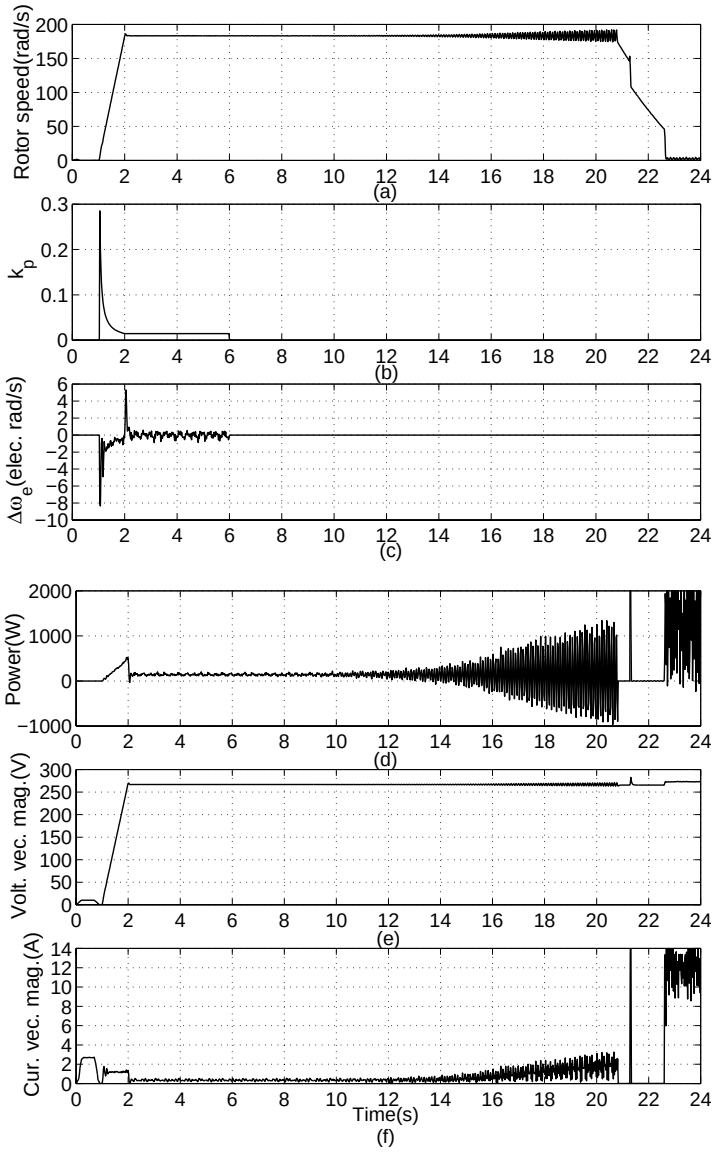

Figure 5.8: *Measured variables, removing the stabilizing loop from the system, at rated speed (87.5 Hz), under no-load. (a) Rotor speed (b) Stabilizing loop gain k_p (c) Frequency modulation signal $\Delta\omega_e$ (d) Calculated input power in the stabilizing loop (e) Commanded magnitude of the voltage vector (f) Magnitude of the current vector.*

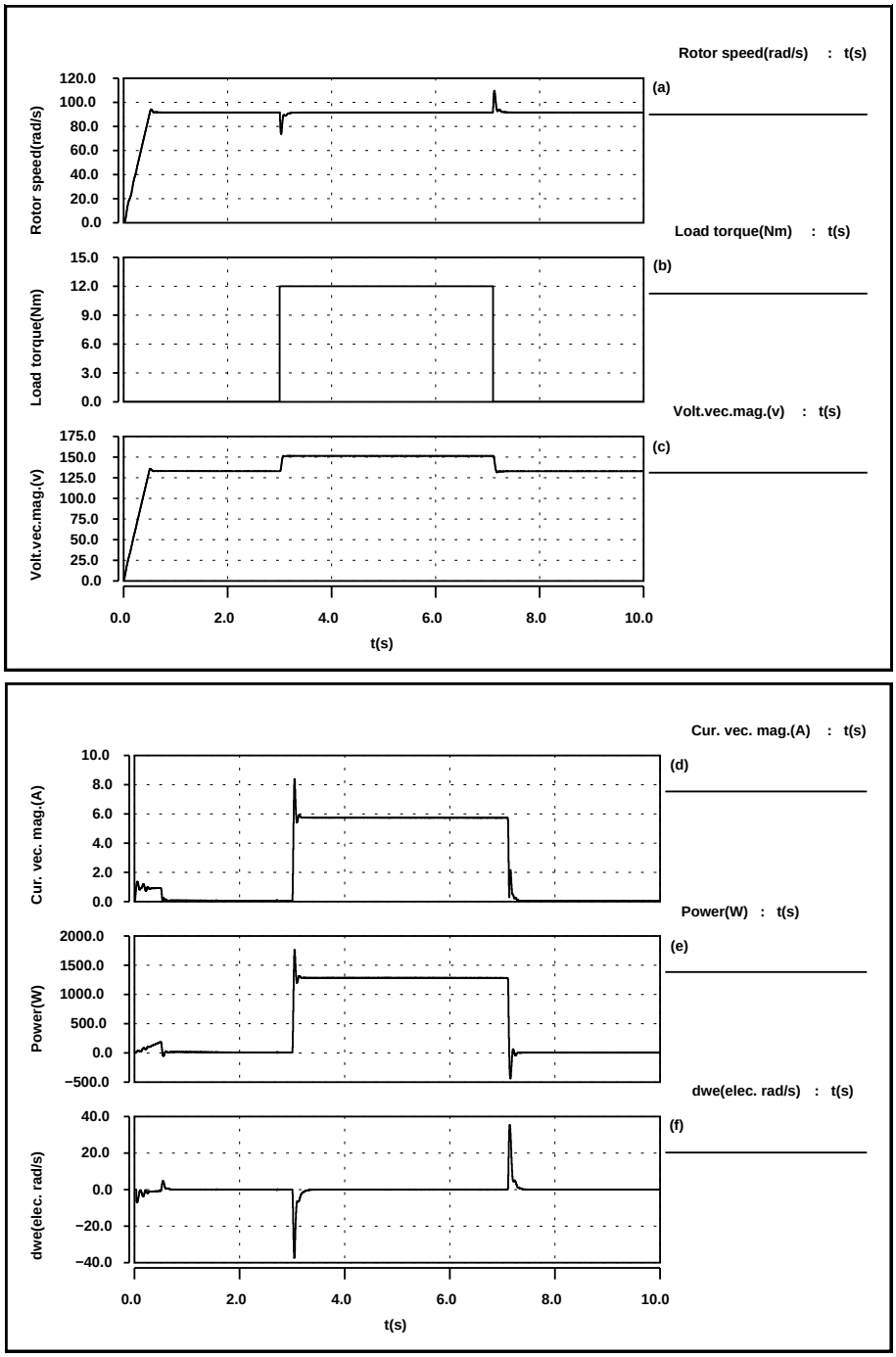

Figure 5.9: *Simulated variables with a 100% load step to the drive at 43.75 Hz. (a) Rotor speed (b) Applied load torque to the machine (c) Commanded magnitude of the voltage vector (d) Magnitude of the current vector (e) Input power (f) Frequency modulation signal* $\Delta\omega_e$.

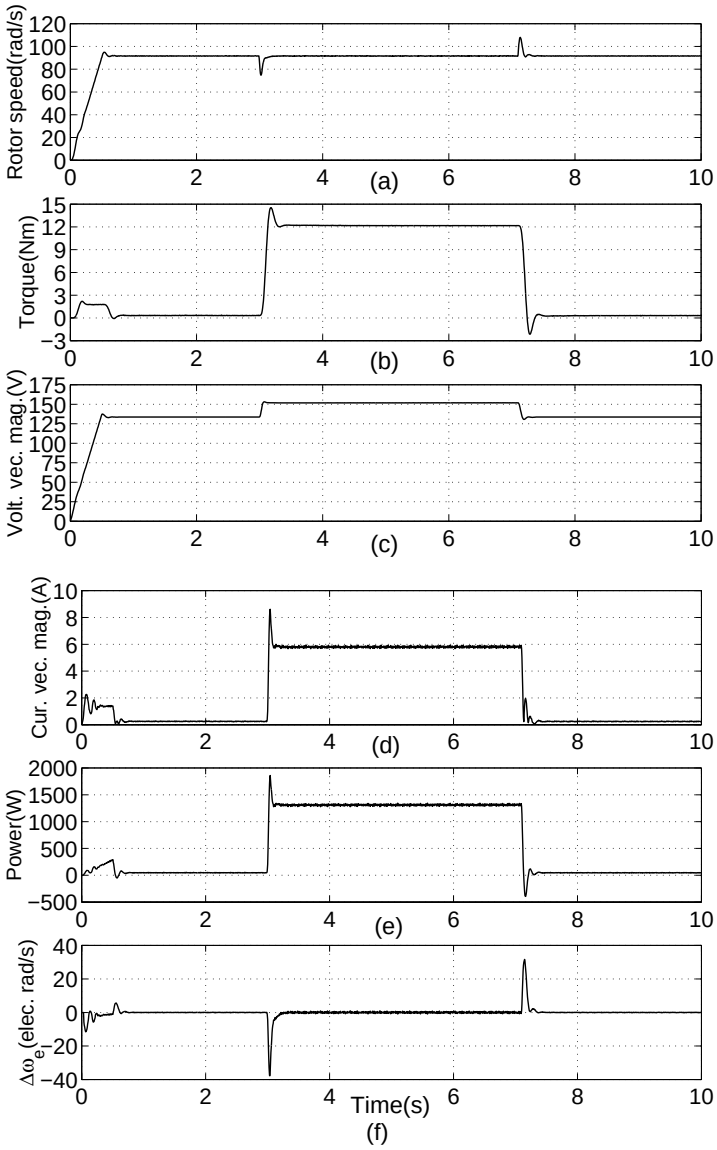

Figure 5.10: *Measured variables with a 100% load step to the drive at 43.75 Hz. (a) Rotor speed (b) Measured torque on the rotor shaft (From the torque transducer) (c) Commanded magnitude of the voltage vector (d) Magnitude of the current vector (e) Input power (f) Frequency modulation signal* $\Delta\omega_e$.

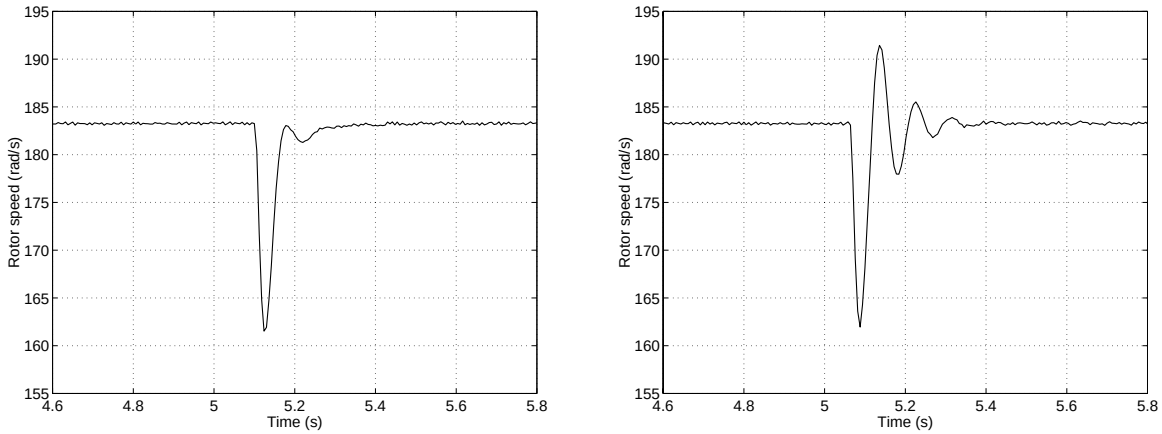

Figure 5.11: *Measurements of the speed responses, when adding a 100% load step to the drive at rated speed, with different gains to the stabilizing loop. (a) With nominal gain (b) With half of the nominal gain.*

first test, the complete drive configuration shown in figure 5.5 was used, whereas for the second test only the voltage control of the drive was changed to the relationship given in (5.2.9), i.e. voltage control without r_s voltage drop compensation using constant V/f ratio control ($\frac{v_s^*}{f_0} = 2\pi\lambda_m$). Both tests were done at 4.4 Hz (5% of the rated frequency) with 50% load step. The measurements are shown in figure 5.12 and figure 5.13, respectively. It can be seen from figure 5.13 the drive cannot overcome the load change due to the lack of voltage to the machine.

5.4.3 Performance with quadratic load

For pumps and fans applications, the load on the machine has a quadratic profile with rotor speed. The performance of the drive system with that type of load (quadratic load) is investigated through simulations. The load on the machine is modeled as

$$T_l = \mathcal{A}\omega_{rm}^2 \tag{5.4.3}$$

where, $\mathcal{A}$ is a constant and ω_{rm} is mechanical rotor speed of the machine. The constant $\mathcal{A}$ is calculated so that at rated speed the rated load torque is applied to the machine. This gives $\mathcal{A} = 3.6 \times 10^{-4}\ Nm\ rad^{-2}\ s^2$ for the machine used for analyzing here.

The simulation results with quadratic load in the system are shown in figure 5.14. This simulation results show that the drive can operate satisfactorily with quadratic load in the system.

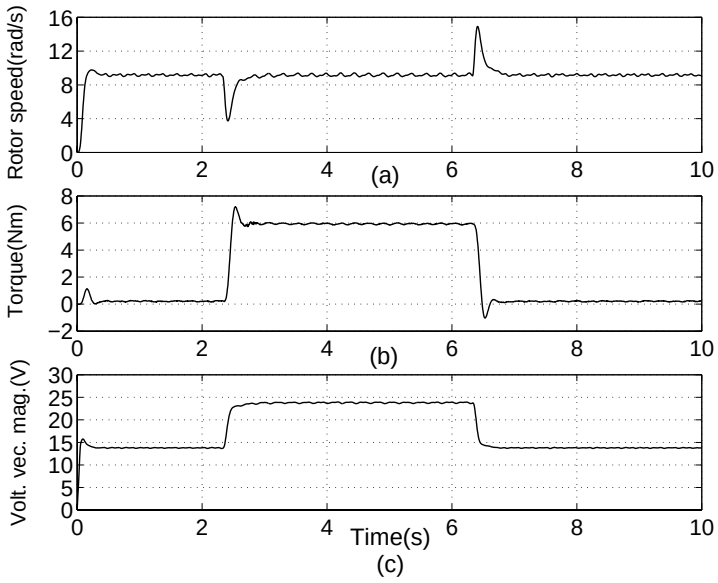

Figure 5.12: *Measured variables with a 50% load step to the drive at 5% rated speed. (a) Rotor speed (b) Measured torque on the rotor shaft (c) Commanded magnitude of the voltage vector.*

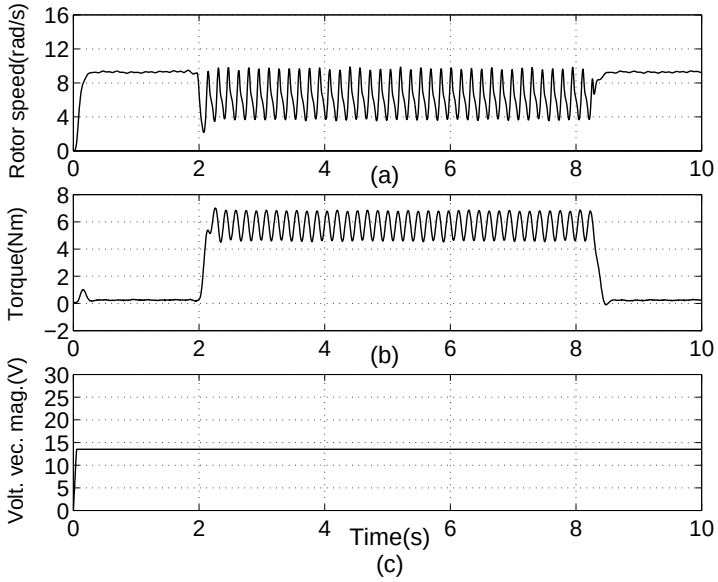

Figure 5.13: *Measured variables with a 50% load step at 5% rated speed, without r_s voltage drop compensation in the voltage control of the drive. (a) Rotor speed (b) Measured torque on the rotor shaft (c) Commanded magnitude of the voltage vector.*

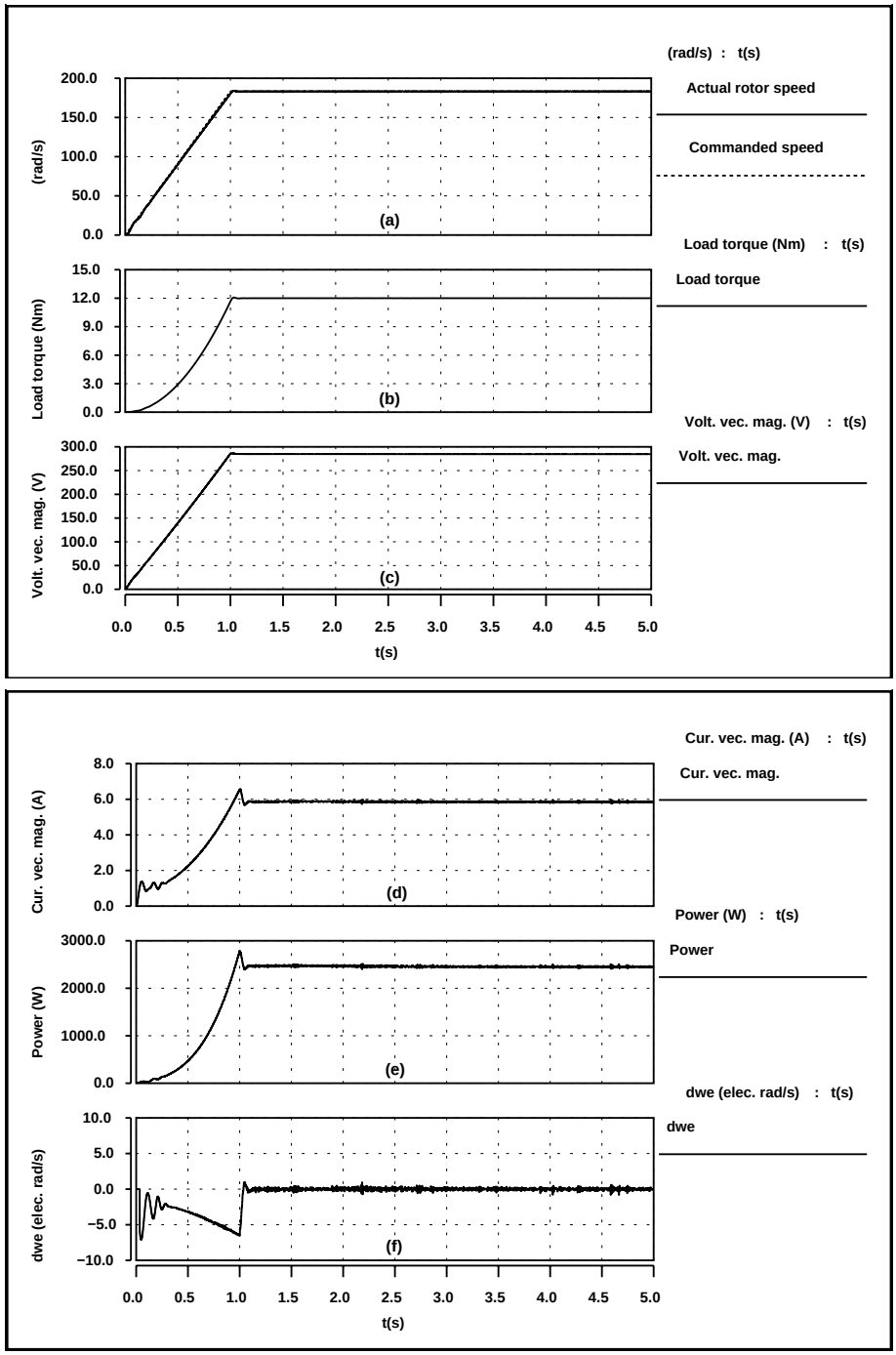

Figure 5.14: *Simulation results, when ramping up the drive to the rated speed with quadratic load. (a) Actual and commanded rotor speed (b) Applied load torque to the machine (c) Commanded magnitude of the voltage vector (d) Magnitude of the current vector (e) Input power (f) Frequency modulation signal* $\Delta\omega_e$.

5.5 Summary

In this chapter, the complete stable V/f controlled PMSM drive has been presented. In order to improve the performance, especially at low speeds, the machine's voltage has been controlled with vector addition of the stator resistance voltage drop to the stator flux induced voltage. The stability in the drive system has been assured from the input power perturbation stabilizing loop, which is discussed in Chapter 4. Only phase current measurements are required to implement the complete control algorithm and no rotor position sensor is required.

The performance of the complete drive system has been studied through computer simulations and laboratory experiments. The results have shown that the proposed sensorless stable V/f controlled PMSM drive can operate 5%-100% of rated speed with satisfactory performance for pumps and fans applications.

It is believed that the proposed V/f control approach in this chapter is novel for PMSM drives (Note that this drive scheme is also described in [9] by the author). Especially, it is capable of providing stable operation of the drive for wide frequency range with improved low speed performance.

Bibliography

[1] A. Abbondanti, *Method of Flux Control in Induction Motors Driven by Variable Frequency, Variable Voltage Supplies*, Proceedings of IEEE/IAS International Semiconductor Power Converter Conference, pp. 177-184, 1977.

[2] Kunio Koga, Ryuzo Ueda and Toshikatsu Sonoda, *Evaluations on Operating Performances of Three Typical v/f Control Schemes in PWM Inverter Drive Induction Motor System*, Proceedings of IEEE Industrial Electronics Society Conference (IECON), pp. 701-706, 1991.

[3] T. Kataoka, Y. Sato and A. Bendiabdellah, *A Novel Volts/Hertz Control Method for an Induction Motor to Improve the Torque Characteristics in the Low Speed Range*, Proceedings of European Power Electronics Conference (EPE), pp. 485-488, 1993.

[4] Werner Leonhard, *Control of Induction Motor Drives*, Chapter 12 in Control of Electrical Drives, Springer, 1997.

[5] Alfredo Munoz-Garcia, Thomas A. Lipo and Donald W. Novotny, *A New Induction Motor v/f Control Method Capable of High-Performance Regulation at Low Speeds*, IEEE Transactions on Industry Applications, Vol. 34, No.4, pp. 813-821, July/August 1998.

[6] Flemming Abrahamsen, *Energy Optimal Control of Induction Motor Drives*, Ph.D. Thesis, Institute of Energy Technology, Aalborg University, Denmark, 2000.

[7] T. Takeshita and N. Matsui, *Starting of Sensorless Brushless DC Motor*, Proceedings of ISPE'92, pp. 398-403, 1992.

[8] Nobuyuki Matsui, *Sensorless PM Brushless DC Motor Drives*, IEEE Transactions on Industrial Electronics, Vol. 43, No.2, pp. 300-308, April 1996.

[9] P. D. Chandana Perera, Frede Blaabjerg, John K. Pedersen and Paul Thøgersen, *A Sensorless, Stable V/f Control Method for Permanent-Magnet Synchronous Motor Drives*, Proceedings of IEEE Applied Power Electronics Conference (APEC), pp. 83-89, 2002 (also accepted for publishing in IEEE Transactions on Industry Appplications).

Part III

Sensorless Field-Oriented Control of PMSMs

Chapter 6

Field-Oriented Control and Estimation of Rotor Position and Velocity

6.1 Introduction

Except V/f control approach, the other method of controlling an IPMSM is the incorporation of a torque controller in the control system as explained in §1.2.1 of Chapter 1. The torque control of the IPMSM can be understood from the torque expression derived in §2.5 of Chapter 2.

The instantaneous torque developed by an IPMSM is given by (see (2.5.7) of Chapter 2)

$$T_e = \frac{3}{2}\frac{n}{2}[\lambda_m i^r_{qs} + (L_d - L_q) i^r_{ds} i^r_{qs}] \tag{6.1.1}$$

It can be seen from (6.1.1), the IPMSM developed torque can be controlled by properly controlling the currents i^r_{qs} and i^r_{ds}, i.e. controlling the stator currents in the reference frame fixed to the rotor permanent-magnet flux vector [1], [2], [3]. This can be referred to as rotor permanent-magnet flux oriented control.

In this chapter, first, the rotor permanent-magnet flux oriented controlled drive system will be described giving emphasis to the main control sections of it. The rotor position and velocity information are essential for this drive system and the state of the art approaches to rotor position and velocity estimation are discussed next, reviewing the past work of various authors.

6.2 Rotor permanent-magnet flux oriented controlled drive system

The closed-loop control approach described in §1.2.1 of Chapter 1 incorporates a torque and a speed controller in the control system (see figure 1.6 of Chapter 1). As it is seen from (6.1.1), the torque control of the machine can be achieved by controlling the stator currents in the reference frame fixed to the rotor permanent-magnet flux (i.e. rotor

reference frame). The drive system, which incorporates this concept to achieve torque control is shown in figure 6.1.

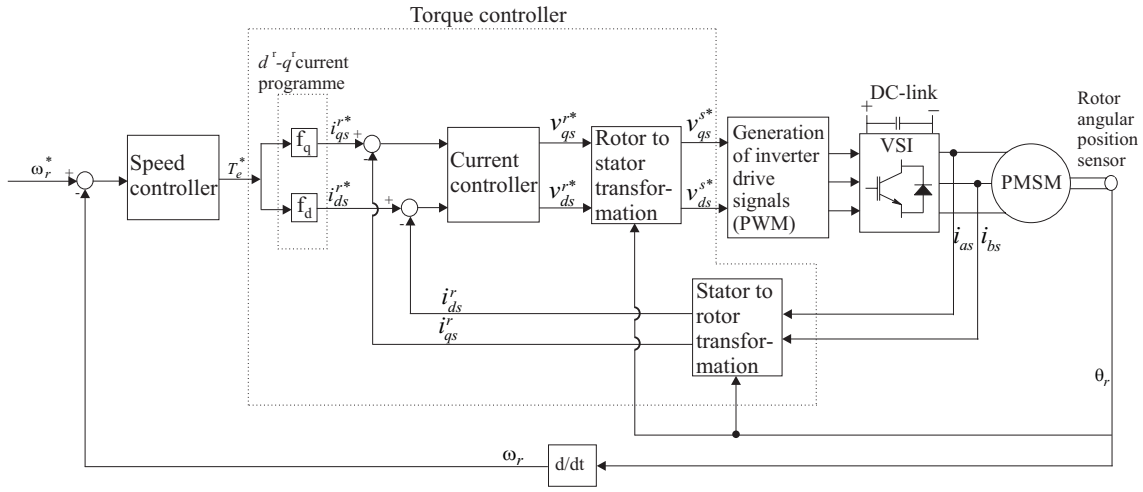

Figure 6.1: *Block diagram for rotor permanent-magnet flux oriented controlled drive system.*

The speed controller generates the torque command (T_e^*) and this torque command is mapped into commands for rotor reference frame (d^r, q^r reference frame) current components i_{qs}^{r*} and i_{ds}^{r*} using function generators f_q and f_d respectively, as shown in figure 6.1. These two function generators can be extracted in order to operate the machine under any of the strategies discussed in §2.8 of Chapter 2. The commanded rotor reference frame current components, which are DC quantities for a constant torque command, are compared with actual rotor reference frame currents i_{qs}^r and i_{ds}^r, which are obtained from measuring the stator currents and stator to rotor transformation using rotor position. The current errors are input to the current controller and it generates the rotor reference frame voltage commands v_{qs}^{r*} and v_{ds}^{r*}. The current controller consists of two PI controllers, each for q^r- and d^r-axis current errors, and it will be discussed in detail in Chapter 7. The rotor reference frame voltage commands are transformed to the stator reference frame voltage commands v_{qs}^{s*} and v_{ds}^{s*} using the rotor position feedback. These voltage commands generate the drive signals for voltage source inverter from PWM.

The design of all controllers in this drive system will be discussed in detail in Chapter 7.

6.3 Rotor position and velocity estimation techniques

For the previous §6.2 discussed PMSM control scheme, the information of the PMSM's rotor position and the velocity is an essential requirement. The rotor position is required

to the torque controller in order to perform reference frame transformations for currents and voltages (i.e. for self-synchronization), whereas the actual velocity of the rotor is required in the control system in order to control the speed in closed-loop manner. The direct approach to obtain this position and speed feedback signals to the control system is, the use of a rotor angular position sensor mechanically coupled to the rotor as shown in figure 6.1. However, as described in §1.2.2 of Chapter 1, this rotor angular position sensor is not desirable in the system. The rotor angular position sensor can be eliminated from the system, if the rotor position and velocity are estimated accurately, using other measurable quantities of the machine. In this section, such rotor position and velocity estimation techniques are reviewed for the PMSM drive scheme shown in figure 6.1.

6.3.1 Back-EMF calculation based methods

Since the rotor permanent-magnet flux is aligned with the rotor d-axis in the PMSM, the permanent-magnet flux induced voltage (i.e. back-EMF) always lies on the rotor q-axis. Therefore, in the stationary reference frame, the position of the back-EMF vector indicates the rotor position angle θ_r. This is shown in figure 6.2.

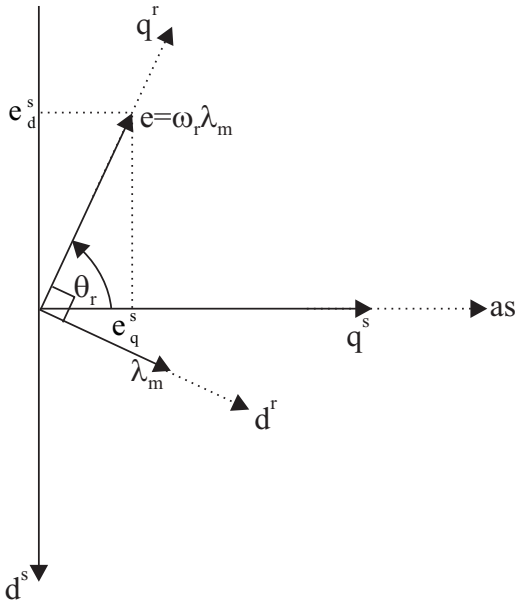

Figure 6.2: *Back-EMF vector in the stationary reference frame.*

If it is possible to calculate the position of the back-EMF vector in the stationary reference frame, the rotor position is known in the system. For SPMSMs and IPMSMs, using the electrical equations of the machine, the possibility of calculating the position of the back-EMF vector in the stationary reference frame is investigated below.

According to figure 6.2 the position of the back-EMF vector, i.e. the rotor position,

$$\theta_r = tan^{-1}(\frac{e_d^s}{e_q^s}) \tag{6.3.1}$$

where,

$$e_q^s = \omega_r \lambda_m cos(\theta_r) \tag{6.3.2}$$

$$e_d^s = \omega_r \lambda_m sin(\theta_r) \tag{6.3.3}$$

The stationary frame voltage equations, which are derived for IPMSMs in Chapter 2 (see (2.4.43) and (2.4.44)), are written here again for convenience.

$$v_{qs}^s = r_s i_{qs}^s + p[(L + \Delta L cos(2\theta_r))i_{qs}^s - \Delta L sin(2\theta_r) i_{ds}^s] + \omega_r \lambda_m cos(\theta_r) \tag{6.3.4}$$

$$v_{ds}^s = r_s i_{ds}^s + p[-\Delta L sin(2\theta_r) i_{qs}^s + (L - \Delta L cos(2\theta_r))i_{ds}^s] - \omega_r \lambda_m sin(\theta_r) \tag{6.3.5}$$

For SPMSMs, since $L_d = L_q = L$ and $\Delta L = 0$, (6.3.4) and (6.3.5) become

$$v_{qs}^s = r_s i_{qs}^s + L p i_{qs}^s + \omega_r \lambda_m cos(\theta_r) \tag{6.3.6}$$

$$v_{ds}^s = r_s i_{ds}^s + L p i_{ds}^s - \omega_r \lambda_m sin(\theta_r) \tag{6.3.7}$$

For SPMSMs, e_q^s and e_d^s can be obtained from (6.3.6) and (6.3.7) as

$$e_q^s = \omega_r \lambda_m cos(\theta_r) = v_{qs}^s - r_s i_{qs}^s - L p i_{qs}^s \tag{6.3.8}$$

$$e_d^s = \omega_r \lambda_m sin(\theta_r) = -v_{ds}^s + r_s i_{ds}^s + L p i_{ds}^s \tag{6.3.9}$$

It is possible to calculate the e_q^s and e_d^s from (6.3.8) and (6.3.9) for a SPMSM and obtain the rotor position from (6.3.1) [4], [5]. To calculate e_q^s and e_d^s, the stator voltages can be measured or estimated (using switching states of the inverter and the DC-link voltage [3]). The stator currents can be measured and the derivative term of the currents can be calculated as

$$p i_{xs}^s(k) = \frac{i_{xs}^s(k) - i_{xs}^s(k-1)}{T} \tag{6.3.10}$$

where subscript x denotes q or d, k is sampling number and T is sampling period.

The main problem with this technique is the estimation of rotor position at zero speed and at low speeds. As it can be seen from the (6.3.8) and (6.3.9) at zero speed the back-EMF components become zero and it is not possible to obtain the rotor position at zero speed. At low speeds, since the back-EMF is small the noise in the estimated back-EMF signals becomes a greater portion leading to a large error in the estimated rotor position. Large errors can also be introduced by the differentiation term of the phase currents in the back-EMF estimation. Moreover, as it can be seen from (6.3.8) and (6.3.9), this technique is sensitive to the variation of parameters r_s and L.

From (6.3.4) and (6.3.5), the back-EMF components for an IPMSM should be written as

$$e_q^s = \lambda_m \omega_r cos(\theta_r) = v_{qs}^s - r_s i_{qs}^s - (L + \Delta L cos(2\theta_r)) p i_{qs}^s + 2\omega_r \Delta L sin(2\theta_r) i_{qs}^s + \Delta L sin(2\theta_r) p i_{ds}^s + 2\omega_r \Delta L cos(2\theta_r) i_{ds}^s \quad (6.3.11)$$

$$e_d^s = \lambda_m \omega_r sin(\theta_r) = -v_{ds}^s + r_s i_{ds}^s + (L - \Delta L cos(2\theta_r)) p i_{ds}^s + 2\omega_r \Delta L sin(2\theta_r) i_{ds}^s - \Delta L sin(2\theta_r) p i_{qs}^s - 2\omega_r \Delta L cos(2\theta_r) i_{qs}^s \quad (6.3.12)$$

It can be seen from the most right side of the (6.3.11) and (6.3.12), the calculation of e_q^s and e_d^s is not feasible for an IPMSM. Unlike the SPMSM, the IPMSM inductances are rotor position dependent in the stationary reference frame equations and this makes the difficulty to calculate the back-EMF components e_q^s and e_d^s from (6.3.11) and (6.3.12). Eliminating that problem, recently, an advanced observer based technique was proposed to calculate the back-EMF components of an IPMSM [6]. However, zero and low speed performance is still a problem as it is mentioned for SPMSMs.

6.3.2 Stator flux linkage based methods

Some approaches were proposed to estimate the rotor position, knowing the stator flux linkage vector. The stator flux linkage vector can be estimated using the stationary reference frame voltage equations (see (2.4.14) and (2.4.15) of Chapter 2) as

$$\lambda_{qs}^s = \int (v_{qs}^s - r_s i_{qs}^s) dt \quad (6.3.13)$$

$$\lambda_{ds}^s = \int (v_{ds}^s - r_s i_{ds}^s) dt \quad (6.3.14)$$

The stator phase voltages, currents and stator resistance should be known to estimate the flux components from (6.3.13) and (6.3.14). Integration drift is a problem when using (6.3.13) and (6.3.14) for flux estimation and it should be avoided using proper integration techniques [7], [8].

In [9] and [10], the estimated stator flux is used to calculate the 3-phase stator currents with an assumed rotor position. The difference between those calculated currents and the actual currents of the machine, i.e. current errors, are used to correct the assumed rotor position. The concept is possible to use for both SPMSMs and IPMSMs. In order to avoid the integrator drift during flux estimation, the estimated flux is corrected in the algorithm using the corrected rotor position and the measured stator currents. The same rotor position estimation concept is used in [11] for sensorless operation of a SPMSM drive above zero speed. Instead of using 3-phase current errors, the assumed rotor position is corrected using the rotor q-axis current error in [11].

The machine parameters are used in these rotor position estimation algorithms, and therefore, they are sensitive to parameter variations. Moreover, the initial rotor position is not detectable from these techniques, and therefore, the starting performance can degrade unless another technique is used to detect the initial rotor position.

6.3.3 Rotor position estimation based on stator phase inductance calculation

As it can be seen from (2.2.16) and (2.4.41) of Chapter 2, the stator phase inductances of an IPMSM are a function of the rotor position. Some techniques are proposed in the literature to obtain the rotor position information from on-line calculation of the stator phase inductances.

In [12], the phase inductances are calculated for an IPMSM, assuming that during one switching period the inductances are not changed due to the rotor position, i.e. assuming the switching frequency of the current controlled PWM inverter is high. In order to obtain the rotor position, the calculated inductances are compared with a pre-calculated look-up table, which contains the relationship between inductances and the rotor position. To calculate the inductances the parameters r_s and λ_m are used, and therefore, the variation of these parameters can affect the accuracy of inductance calculation. Moreover, a high switching frequency (>10 kHz) is required for accurate calculation of the inductances. At zero speed the inductance calculation is not possible from the proposed method, since current, voltage and back-EMF of the machine are zero at zero speed.

Using harmonic components of the voltage and current, which are generated from the PWM voltage source inverter, the calculation of the inductance matrix given in (2.4.42) (see Chapter 2) and extraction of the rotor position from the elements of that matrix is proposed in [13],[14],[15]. Special PWM patterns are used and the harmonic voltage components are calculated from that PWM patterns. The harmonic components of the current are calculated from the measured currents. Using those harmonic components of voltage and current the inductance matrix is calculated from (2.4.43) and (2.4.44) (see Chapter 2). During the calculations, the resistor drop and the back-EMF can be neglected in (2.4.43) and (2.4.44), since only harmonic components of voltage and current are used. The main advantage of this technique is no motor parameters are required to extract the rotor position. Therefore, it is not sensitive to motor parameter variation. Moreover, since the machine is excited at zero speed with special PWM pattern, the inductance calculation is possible, and therefore, the rotor position. However, special PWM patterns and special current sampling technique (in order to obtain the harmonic components of the current) are required to implement this technique.

6.3.4 Rotor position estimation based on hypothetical rotor position

In this technique, a rotor position is assumed and assuming that position is correct, the machine variables (voltages or currents) in the rotor reference frame are calculated from the rotor reference frame machine model, using the knowledge of previous values of variables. Then, the measured 3-phase variables (voltages or currents) of the machine are transformed to the rotor reference frame values using the assumed rotor position. The error between those transformed values and the values obtained from previous model calculation are used to calculate the error in the assumed rotor position. The assumed rotor position is corrected accordingly. This technique was proposed in [16] for sensorless operation of a SPMSM drive. It proposed two methods to correct the assumed rotor position. In the first method, the voltage error was used, whereas in the second method the current error was used. It was also concluded that the current error based method was better than the voltage error based method. The initial rotor position is not directly detectable from this technique. Therefore, in [16], it was proposed to apply special pilot voltages to the machine before starting, and look into the current profiles of the machine to detect the initial rotor position.

The technique, which used current errors to calculate the position error, was also used in [17] for an IPMSM with low saliency ratio. However, for IPMSMs with high saliency ratio, this technique may cause problems, since the rotor position error calculation is not very accurate for those machines from this technique.

6.3.5 Observer based methods

The use of a state observer is another way to extract the rotor position and velocity information of the PMSM. In the state observer, the dynamics of the machine are modeled and drive these dynamics with the same input as it is used to drive the real machine, and ensure the states of the modeled machine, such as rotor position, velocity, follow the states of the real machine. The error between the output of the real machine (which is measurable) and the output of the modeled machine is used in the observer in order to correct any errors in the estimated states, such as rotor position, velocity.

Since the PMSM model is nonlinear, the designing of a state observer is more complex compared with a system having a linear model such as a DC motor.

The PMSM model in stationary reference frame or in rotor fixed reference frame has the form

$$\dot{x} = f(x, u) \tag{6.3.15}$$

$$y = h(x) \tag{6.3.16}$$

where, x, u and y are, states, inputs and output of the system respectively. f is a nonlinear function of x and u, and h is a linear function of x. The full state observer

for this system has the form

$$\hat{\dot{x}} = f(\hat{x}, u) + G(\hat{x})[y - h(\hat{x})] \tag{6.3.17}$$

$$\hat{y} = h(\hat{x}) \tag{6.3.18}$$

where G is the observer gain matrix, which is a function of estimated states $\hat{x}$. Unlike linear observers the gain matrix is not a constant in this case. The gain matrix $G(\hat{x})$ should be designed in order to guarantee the satisfactory convergence performance of the estimated states.

Interesting analysis for designing a state observer for a PMSM can be found in [18]. As it can be seen from the analysis in [18], due to the existence of the saliency, the complexity of the state observer is increased for an IPMSM compared to a SPMSM. Observers are model based, and therefore, it can be expected the parameter variation in the system can affect the performance of the observer. However, not all the parameters, but some parameter variation can give a considerable effect for the observer performance as it can be seen in simulation studies in [18] and [19]. A solution to this problem is the inclusion of an on-line parameter estimator in the control system as described in [20].

Since the estimation of rotor position and velocity is the main concern, the other states, such as currents, which can be measured easily, may not be required to estimate in the system. This helps to reduce the order of the observer reducing the computational power needed for the observer algorithm. This reduced order observer design for a SPMSM is discussed in [21] and [22].

An extension to the above discussed observer approach is the extended Kalman filter algorithm. The extended Kalman filter algorithm to estimate the rotor position and velocity of a SPMSM is discussed in [3], [23], [24]. This algorithm may robust against parameter variations and measurement noise, however, it is computationally intensive.

Initial rotor position is not detectable with these observer techniques. Therefore, the starting performance of the drive is an issue to consider when these techniques are used.

6.3.6 Position and velocity estimation using high frequency signal injection

Continuous high frequency carrier signal injection is one of the technique, which can be used to extract the position and velocity information in an AC machine with saliency [25]. The basis for the technique is, the injection of a high frequency carrier signal, either voltage or current, on top of the fundamental excitation of the machine. This carrier signal excitation induces current or voltage signals (Depend on voltage or current carrier signal injection) that contains information relating to the rotor position of the

machine. Using suitable signal processing techniques, it is possible to extract this position information in induced current or voltage, in order to provide continuous estimates of rotor position and velocity to the control system.

Due to the saliency in the IPMSMs they are very good candidate for this technique. The application of high frequency carrier voltage signal injection to extract the rotor position of an IPMSM can be found in [26] and [27]. Since the high frequency carrier voltage signal is injected continuously and the induced current signal in the machine exists regardless of the speed of the machine, using this technique the extraction of the rotor position is possible at zero and very low speeds. This becomes main advantage of this technique. In order to extract the rotor position from the induced current, filters and a tracking observer is required. The accuracy of designing the filters and the tracking observer affects the performance of the position estimation using this technique.

6.4 Summary

In this chapter, first, the rotor permanent-magnet flux oriented controlled PMSM drive system, which incorporates the current control in rotor permanent-magnet flux fixed reference frame to achieve torque control, has been discussed. It has been shown that the rotor position and velocity information is essential requirement for the control system of this drive. Literature review reveals that last decade or so there has been a considerable attention for eliminating the rotor position sensor, which is conventionally used to obtain position and velocity information for the control system of this drive. In this chapter, attempts have been made to categorize those proposed techniques based on the concept used to estimate the rotor position and velocity. Moreover, their merits and demerits have been discussed.

From machine type point of view, it is apparent that the saliency in IPMSMs provide some different approaches, like induction calculation based methods and high frequency signal injection methods, to estimate the rotor position and velocity. It is also apparent that the saliency in IPMSMs increases the complexity in the algorithms compared to the SPMSMs when most of the other position and velocity estimation techniques are used.

Bibliography

[1] Thomas M. Jahns, Gerald B. Kliman and Thomas W. Neumann, *Interior Permanent-Magnet Synchronous Motors for Adjustable-Speed Drives*, IEEE Transactions on Industry Applications, Vol. IA-22, No.4, pp. 738-747, July-August 1986.

[2] Toshihiro Sawa and Kaneyuki Hamada, *Introduction to the Permanent Magnet Motor Market*, In proceedings of the conference Energy Efficiency in Motor-Driven systems, pp. 81-94, 1999.

[3] Peter Vas, *Vector and Direct Torque Control of Synchronous Machines*, Chapter 3 in Sensorless Vector and Direct Torque Control, pp. 87-257, Oxford University Press, 1998.

[4] Marcel Jufer and Razack Osseni, *Back EMF Indirect Detection for Self-Commutation of Synchronous Motors*, Proceedings of European Conference on Power Electronics and Applications, pp. 1125-1129, 1987.

[5] M. Schroedl, *An Improved Position Estimator for Sensorless Controlled Permanent Magnet Sysnchronous Motors*, Proceedings of European Conference on Power Electronics and Applications, Vol.3, pp. 418-423, 1991.

[6] Zhiqian Chen, Mutuwo Tomita, Shinji Ichikawa, Shinji Doki and Shigeru Okuma *Sensorless Control of Interior Permanent Magnet Synchronous Motor by Estimation of an Extended Electromotive Force*, Proceedings of IEEE/IAS Annual Meeting, Vol.3, pp. 1814 -1819, 2000.

[7] Jun Hu and Bin Wu, *New Integration Algorithms for Estimating Motor Flux over a Wide Speed Range*, IEEE Transactions on Power Electronics, Vol. 13, No.5, pp. 969-977, September 1998.

[8] Markku Niemela, Juha Pyrhonen, Olli Pyrhonen and Julius Luukko, *Drift Correction Methods of the Stator Flux Linkage in DTC Synchronous Motor Drives*, Proceedings of European Conference on Power Electronics and Applications, 1999.

[9] Nesimi Ertugrul and P.P. Acarnley, *A New Algorithm for Sensorless Operation of Permanent Magnet Motors*, IEEE Transactions on Industry Applications, Vol. 30, No.1, pp. 126-133, January-February 1994.

[10] Chris French and Paul Acarnley, *Control of Permanent Magnet Motor Drives Using a New Position Estimation Technique*, IEEE Transactions on Industry Applications, Vol. 32, No.5, pp. 1089-1097, September-Ocober 1996.

[11] Stefan Ostlund and Michael Brokemper, *Sensorless Rotor-Position Detection from Zero to Rated Speed for an Integrated PM Synchronous Motor Drive*, IEEE Transactions on Industry Applications, Vol. 32, No.5, pp. 1158-1165, September-Ocober 1996.

[12] Ashok B. Kulkarni and Mehrdad Ehsani, *A Novel Position Sensor Elimination Technique for the Interior Permanent-Magnet Synchronous Motor Drive*,

IEEE Transactions on Industry Applications, Vol. 28, No.1, pp. 144-150, January-February 1992.

[13] Satoshi Ogasawara and Hirofumi Akagi, *An Approach to Real-Time Position Estimation at Zero and Low Speed for a PM Motor Based on Saliency*, IEEE Transactions on Industry Applications, Vol. 34, No.1, pp. 163-168, January-February 1998.

[14] Satoshi Ogasawara and Hirofumi Akagi, *Implementation and Position Control Performance of a Position-Sensorless IPM Motor Drive System Based on Magnetic Saliency*, IEEE Transactions on Industry Applications, Vol. 34, No.4, pp. 806-812, July-Aug. 1998.

[15] Yu Kazunori, Satoshi Ogasawara and Hirofumi Akagi, *Performance Evaluations of a Position-Sensorless IPM Motor Drive System Based on Detection of Current Switching Ripples*, Proceedings of Power Electronics Specialist Conference, 2000.

[16] Nobuyuki Matsui, *Sensorless PM Brushless DC Motor Drives*, IEEE Transactions on Industrial Electronics, Vol. 43, No.2, pp. 300-308, April 1996.

[17] Takaharu Takeshita and Nobuyuki Matsui, *Sensorless Control and Initial Position Estimation of Salient-Pole Brushless DC Motor*, Proceedings of the 4th International Workshop on Advanced Motion Control, Vol. 1, pp. 18-23, 1996.

[18] Lawrence A. Jones and Jeffrey H. Lang, *A State Observer for the Permanent-Magnet Synchronous Motor*, IEEE Transactions on Industrial Electronics, Vol. 36, No.3, pp. 374-382, August 1989.

[19] Teck-Seng Low, Tong-Heng Lee and Kuan-Teck Chang, *A Nonlinear Speed Observer for Permanent-Magnet Synchronous Motors*, IEEE Transactions on Industrial Electronics, Vol. 40, No.3, pp. 307-316, June 1993.

[20] Raymond B. Sepe and Jeffrey H. Lang, *Real-Time Observer-Based (Adaptive) Control of a Permanent-Magnet Synchronous Motor without Mechanical Sensors*, IEEE Transactions on Industry Applications, Vol. 28, No.6, pp. 1345-1352, November-December 1992.

[21] Joohn-Sheok Kim and Seung-Ki Sul, *High Performance PMSM Drives without Rotational Position Sensors Using Reduced Order Observer*, Proceedings of IEEE/IAS Annual Meeting, pp. 75-82, 1995.

[22] Jorge Solsona, Maria I. Valla and Carlos Muravchik, *A Nonlinear Reduced Order Observer for Permanent Magnet Synchronous Motors*, IEEE Transactions on Industrial Electronics, Vol. 43, No.4, pp. 492-497, August 1996.

[23] Rached Dhaouadi, Ned Mohan and Lars Norum, *Design and Implementation of an Extended Kalman Filter for the State Estimation of a Permanent Magnet Synchronous Motor*, IEEE Transactions on Power Electronics, Vol. 6, No.3, pp. 491-497, July 1991.

[24] S. Bolognani, R. Oboe and M. Zigliotto, *Sensorless Full-Digital PMSM Drive with EKF Estimation of Speed and Rotor Position*, IEEE Transactions on Industrial Electronics, Vol. 46, No.1, pp. 184 -191, February 1999.

[25] Michael W. Degner, *Flux, Position and Velocity Estimation In AC Machines Using Carrier Signal Injection*, Ph.D. Thesis, University of Wisconsin-Madison,1998.

[26] M.J. Corley and R.D. Lorenz, *Rotor Position and Velocity Estimation for a Salient-Pole Permanent Magnet Synchronous Machine at Standstill and High Speeds*, IEEE Transactions on Industry Applications, Vol. 34, No.4, pp. 784-789, July-Aug. 1998.

[27] Limei Wang and R.D. Lorenz, *Rotor Position Estimation for Permanent Magnet Synchronous Motor Using Saliency-Tracking Self-Sensing Method*, Proceedings of IEEE/IAS Annual Meeting, Vol. 1, pp. 445-450, 2000.

Chapter 7

Field-Oriented Controlled Drive System with and without Position Sensor

7.1 Introduction

The rotor permanent-magnet flux oriented controlled drive system is introduced in §6.2 of Chapter 6. In this chapter, first, the control structure of that drive system is described in detail. The design of the current and speed controller is also discussed. The performance of the controller is examined with a position sensor in the drive system.

For sensorless operation, a rotor position and velocity estimating technique is described for the drive system. Only motor terminal current measurements are required for position and velocity estimating algorithm. The estimating algorithm is analyzed in detail and the performance of the sensorless drive system is studied through simulations.

7.2 The control structure of the drive system

Figure 7.1 shows the detailed control structure of the drive system. The speed controller generates the torque command and the torque control is achieved by controlling the current in the rotor reference frame. The torque command is mapped into rotor reference frame current commands using function generators f_q and f_d. The rotor reference frame current commands (i_{qs}^{r*} and i_{ds}^{r*}) are commanded to the machine through the current controller in order to achieve the torque request to the machine. The current controller consists of two PI controllers as shown in figure 7.1. The actual rotor reference frame currents (i_{qs}^{r} and i_{ds}^{r}), which are needed for current control, are obtained by measuring two phase currents (see figure 6.1 of Chapter 6) and transforming them from stator coordinates to rotor coordinates using the relationships

$$i_{qs}^{r} = \frac{2}{3}[i_{as}cos(\theta_r) + i_{bs}cos(\theta_r - \frac{2\pi}{3}) - (i_{as} + i_{bs})cos(\theta_r + \frac{2\pi}{3})] \tag{7.2.1}$$

$$i_{ds}^{r} = \frac{2}{3}[i_{as}sin(\theta_r) + i_{bs}sin(\theta_r - \frac{2\pi}{3}) - (i_{as} + i_{bs})sin(\theta_r + \frac{2\pi}{3})] \tag{7.2.2}$$

where, θ_r is the rotor position.

The rotor reference frame voltage commands (v_{qs}^{r*} and v_{ds}^{r*}), which are the outputs of the current controller, are transformed to the stationary reference frame voltage commands v_{qs}^{s*} and v_{ds}^{s*}. Those voltage commands are used in PWM generator, which generates the duty cycles (D_a, D_b, D_c) for the inverter drive signals.

In the following, each section of this control structure and the design procedure for the controllers are discussed in detail.

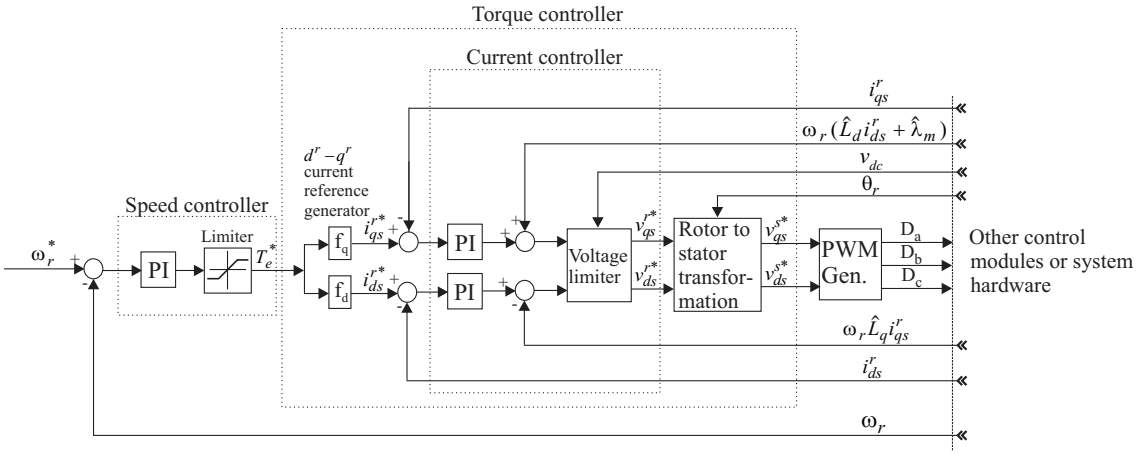

Figure 7.1: *Control structure of the drive system.*

7.2.1 Current controller

Coupling in rotor d,q frame voltage equations

The rotor reference frame voltage equations, which are derived in Chapter 2 (equation (2.4.30) and (2.4.31)) are as follows.

$$v_{qs}^r = r_s i_{qs}^r + p\lambda_{qs}^r + \omega_r \lambda_{ds}^r \tag{7.2.3}$$

$$v_{ds}^r = r_s i_{ds}^r + p\lambda_{ds}^r - \omega_r \lambda_{qs}^r \tag{7.2.4}$$

where,

$$\lambda_{qs}^r = L_q i_{qs}^r \tag{7.2.5}$$

$$\lambda_{ds}^r = L_d i_{ds}^r + \lambda_m \tag{7.2.6}$$

Substituting λ_{qs}^r and λ_{ds}^r to the derivative terms in (7.2.3) and (7.2.4) one can obtain the following two equations.

$$v_{qs}^r = r_s i_{qs}^r + L_q p i_{qs}^r + \omega_r \lambda_{ds}^r \tag{7.2.7}$$

$$v_{ds}^r = r_s i_{ds}^r + L_d p i_{ds}^r - \omega_r \lambda_{qs}^r \tag{7.2.8}$$

These two rotor fixed reference frame voltage equations can be illustrated in block diagram form as shown in figure 7.2. In this block diagram, the voltages are taken as inputs and the existing input cross coupling terms can be seen in this model.

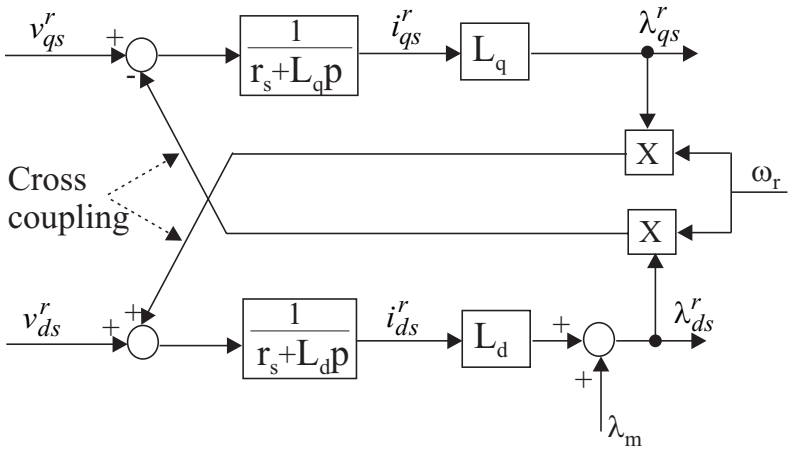

Figure 7.2: *Block diagram representation of the rotor fixed reference frame voltage equations of the PMSM, showing the cross coupling terms.*

Design of current controllers

The rotor fixed reference frame currents become DC values in steady state. Therefore, PI controllers can be used to control these currents with zero steady state error, because input to the controllers become constant values (DC values) in steady state [1], [2].

The rotor d,q currents cannot be controlled independently, due to the cross coupling in rotor d,q circuits as shown in figure 7.2. In order to control i^r_{ds} when v^r_{ds} is changed the i^r_{ds} is changed as desired, but this causes to change the v^r_{qs}, and therefore the i^r_{qs}, which is not desirable. This degrades the control performance of the current control. To obtain better performance in current control the i^r_{ds} and the i^r_{qs} should be able to control independently. This can be achieved by decoupling the cross couplings in rotor d,q circuits [1],[2],[3],[4]. The PI controllers with this decoupling control are shown in figure 7.3. The speed (measured or estimated), measured stator currents and machine parameters can be used to add the decoupling terms, i.e. $\omega_r\hat{\lambda}^r_{ds}$ and $\omega_r\hat{\lambda}^r_{qs}$, to the PI controllers' output as shown in figure 7.3.

The design procedure for the q-axis and the d-axis current controllers shown in figure 7.3 is the same. In the following, only the q-axis current controller design procedure is discussed in detail.

Assuming the cross couplings in the system are fully decoupled due to the decoupling terms, the discrete model for designing the rotor q-axis current controller can be drawn as shown in figure 7.4.

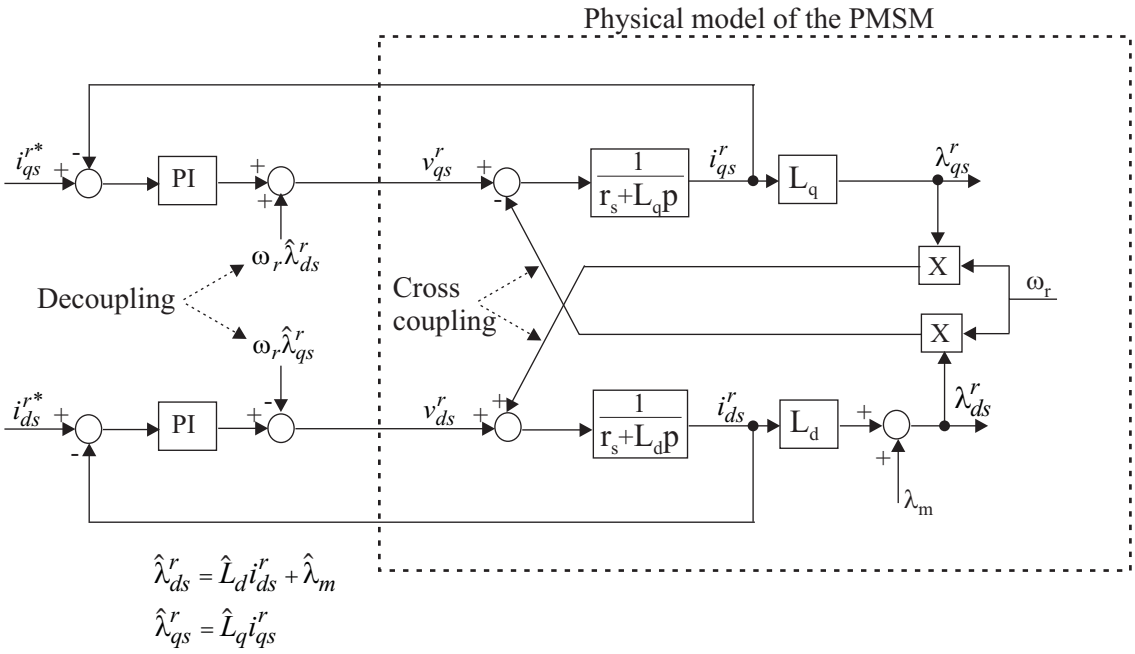

Figure 7.3: *Rotor reference frame current PI controllers with decoupling control.*

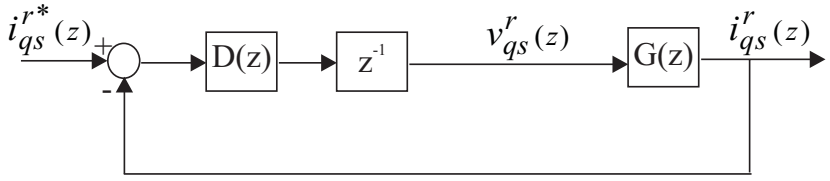

Figure 7.4: *The discrete model for designing the rotor q-axis current controller.*

In figure 7.4, $D(z)$ is the discrete transfer function for the PI controller and it has the form

$$\begin{aligned} D(z) &= k_{pq} + \frac{k_{iq}}{1 - z^{-1}} \\ &= \frac{(k_{pq} + k_{iq})(z - \frac{k_{pq}}{k_{pq}+k_{iq}})}{(z-1)} \end{aligned} \tag{7.2.9}$$

where, k_{pq} and k_{iq} are proportional and integral gain respectively.

The one sampling time delay, which is represented by z^{-1} in figure 7.4, is due to the data conversion and computation time delay in the digital system.

The $G(z)$ represents the discrete transfer function for the machine with zero order hold effect. The $G(z)$ can be obtained as [5], [6],

$$G(z) = (1 - z^{-1}) Z_{trans}(\frac{G(s)}{s}) \tag{7.2.10}$$

where, $G(s)$ is s-domain transfer function for the machine and

$$G(s) = \frac{1}{r_s + sL_q} \tag{7.2.11}$$

Substituting (7.2.11) into (7.2.10) one obtains

$$G(z) = (1 - z^{-1}) Z_{trans}(\frac{1}{s(r_s + sL_q)}) \tag{7.2.12}$$

After obtaining the Z-transformation, (7.2.12) can be written as

$$\begin{aligned} G(z) &= \frac{(1 - z^{-1}) z (1 - e^{\frac{-T}{\tau_q}})}{r_s (z-1)(z - e^{\frac{-T}{\tau_q}})} \\ &= \frac{(1 - e^{\frac{-T}{\tau_q}})}{r_s (z - e^{\frac{-T}{\tau_q}})} \\ &= \frac{a}{z - b} \end{aligned} \tag{7.2.13}$$

where,
T is the sampling time of the digital system,

$$\tau_q = \frac{L_q}{r_s}, \quad a = \frac{(1 - e^{\frac{-T}{\tau_q}})}{r_s}, \quad b = e^{\frac{-T}{\tau_q}}$$

These parameter values for the laboratory test system are,
T=0.0002 s (Both switching frequency and sampling frequency of the drive system are 5 kHz), τ_q=0.0173 s, a=0.0035, b=0.9885.

The motor phase currents are sampled in the beginning of the each PWM switching period, i.e. when zero voltage vector is applied to the machine, avoiding the inverter

switching noise in the current measurements. Therefore, a filter is not used in the current feedback path in the current controller.

The root locus method [6] is used to design the current controllers of the drive system.

The discrete transfer function for the system shown in figure 7.4 is

$$\frac{i_{qs}^{r}(z)}{i_{qs}^{r*}(z)} = \frac{D(z)G(z)z^{-1}}{1 + D(z)G(z)z^{-1}} \tag{7.2.14}$$

After substituting $D(z)$ and $G(z)$ this becomes

$$\frac{i_{qs}^{r}(z)}{i_{qs}^{r*}(z)} = \frac{a(k_{pq} + k_{iq})(z - \frac{k_{pq}}{k_{pq}+k_{iq}})}{z(z-1)(z-b) + a(k_{pq} + k_{iq})(z - \frac{k_{pq}}{k_{pq}+k_{iq}})} \tag{7.2.15}$$

The characteristic equation of the system is

$$1 + D(z)G(z)z^{-1} = 0 \tag{7.2.16}$$

Substituting $D(z)$ and $G(z)$ to (7.2.16) one obtains

$$1 + \frac{a(k_{pq} + k_{iq})(z - \frac{k_{pq}}{k_{pq}+k_{iq}})}{z(z-1)(z-b)} = 0 \tag{7.2.17}$$

The equation (7.2.17) has the form

$$1 + k'H(z) = 0 \tag{7.2.18}$$

where,

$$k' = a(k_{pq} + k_{iq}) \tag{7.2.19}$$

$$H(z) = \frac{(z - \frac{k_{pq}}{k_{pq}+k_{iq}})}{z(z-1)(z-b)} \tag{7.2.20}$$

In order to draw the root locus for the characteristic equation (7.2.18) the zero of H(z) at

$$z = z_{oi} = \frac{k_{pq}}{k_{pq} + k_{iq}} \tag{7.2.21}$$

must be known (This zero is from the PI controller). After drawing the root loci for different locations of that zero, it was found that it should be selected in order to cancel out the pole at $z = b$ to obtain the satisfactory performance from the controller (This way of selecting the zero cancelling the pole at $z = b$ is also described in [7], [8]).

After selecting the location of the zero one can draw the root locus and select the desired closed-loop poles on it. The gain k' correspondent to the selected closed-loop

poles can also be obtained. Knowing z_{oi} and k' the PI controller gains can be obtained by solving (7.2.19) and (7.2.21). The expressions for them are

$$k_{pq} = \frac{k'}{a} z_{oi} \tag{7.2.22}$$

$$k_{iq} = \frac{k'}{a}(1 - z_{oi}) \tag{7.2.23}$$

Figure 7.5 shows the z-plane root locus and the selected closed-loop poles for the q-axis current controller, which the characteristic equation is given by (7.2.18). The closed-loop poles are selected in order to have the characteristics as given in table 7.1. The natural frequency (ω_n) 3480 rad/s gives the bandwidth of the current controller 554 Hz, which is about 0.11 times the sampling frequency of the system. The calculated PI controller gains are given in table 7.2.

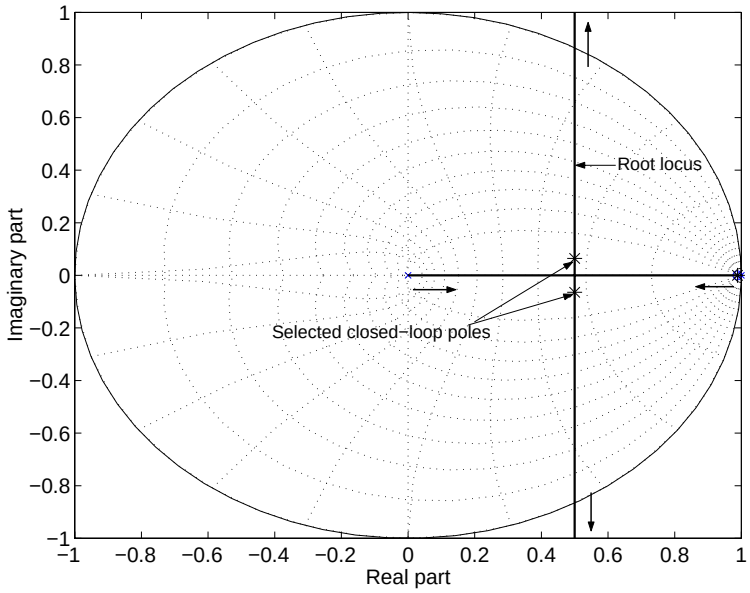

Figure 7.5: *The root locus and the selected closed-loop poles for the rotor q-axis current controller.*

The design procedure for rotor d-axis current controller is exactly the same as the procedure discussed for rotor q-axis current controller. The results are given in figure 7.6, table 7.3 and table 7.4.

Integrator antiwindup

There are limits for the output of the PI controllers in the drive system. For example, the speed PI controller output is the commanded torque to the machine and due to the limitation in the current to the machine there is a limit for this torque. The output of the current PI controllers is the voltage command to the machine and the voltage command is limited by the maximum available voltage from the inverter.

Closed-loop poles (In Z-plane)	Equivalent damping factor (ξ) in S-plane	Equivalent natural frequency (ω_n) in S-plane (rad/s)
0.50+0.06i	0.98	3480
0.50-0.06i	0.98	3480

Table 7.1: Characteristics of selected closed-loop poles for rotor q-axis current controller.

k_{pq}	k_{iq}
72.1	0.84

Table 7.2: PI controller gains for rotor q-axis current controller.

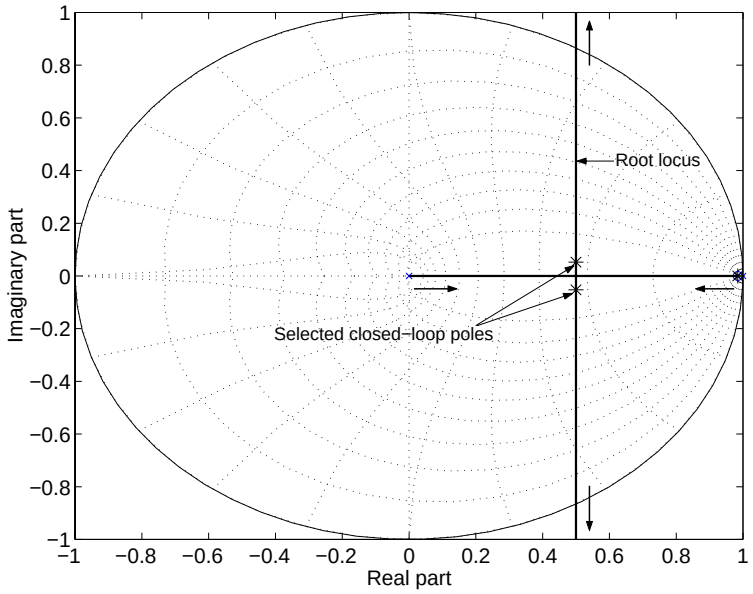

Figure 7.6: *The root locus and the selected closed-loop poles for the rotor d-axis current controller.*

Closed-loop poles (In Z-plane)	Equivalent damping factor (ξ) in S-plane	Equivalent natural frequency (ω_n) in S-plane (rad/s)
0.50+0.06i	0.98	3480
0.50-0.06i	0.98	3480

Table 7.3: Characteristics of selected closed-loop poles for rotor d-axis current controller.

k_{pd}	k_{id}
52.2	0.83

Table 7.4: PI controller gains for rotor d-axis current controller.

The discrete PI controller with limits to the output is shown in figure 7.7. If the unconstrained output u_{uc} of the PI controller exceeds the limit in the limiter and the integrator keeps on integrating the error e, the integral term y will become a very large value (i.e., integrator "winds up"). The consequence of this is the u_{uc} becomes a very large value, which should be decreased later resulting in substantial overshoot in the system.

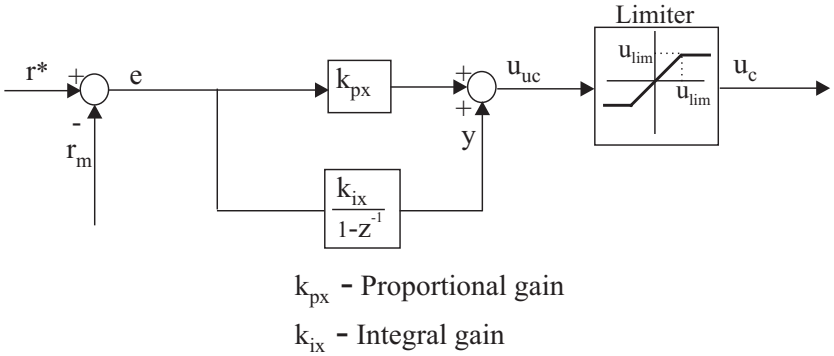

Figure 7.7: *Discrete PI controller with limits to the output.*

The solution to this problem is integrator antiwindup, which "turns off" the integral action as soon as u_{uc} exceeds the limit. Several integrator antiwindup methods have been proposed in the literature [9], [10]. The implemented method for the PI controllers of the drive system is shown in figure 7.8. As it can be seen that there is an extra feedback path, which is generated by knowing u_{uc} and u_c and forming an error signal e_s. The e_s is fed to the input of the integrator through the gain $\frac{1}{k_{aw}}$. When u_{uc} exceeds the limit, this extra feedback path around the integrator moves rapidly to decrease the input to the integrator, avoiding windup.

For implementation k_{aw} is selected as

$$k_{aw} = k_{px}. \tag{7.2.24}$$

Referring to the analysis in [10], this choice results in better performance for a PI controller.

Voltage limiter in the controller's output

The rotor reference frame voltage commands to the machine is obtained by adding the decoupling terms to the current PI controller's output (see figure 7.3). To assure the magnitude of the stator voltage command does not exceed the maximum available voltage from the inverter, the limits should be considered to the rotor reference frame voltage commands.

The magnitude of the voltage is limited to the largest circle that fits in the voltage hexagon during SVM (see Appendix C for more details) and, with this limit the

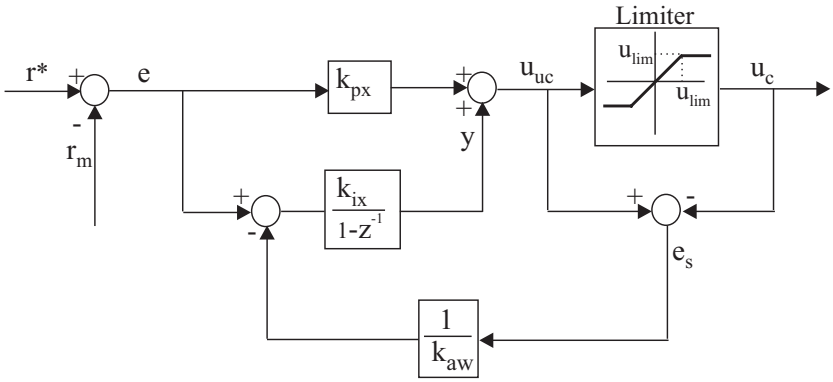

Figure 7.8: *Discrete PI controller with integrator antiwindup.*

magnitude of the maximum voltage v_{max} becomes

$$v_{max} = \frac{v_{dc}}{\sqrt{3}} \tag{7.2.25}$$

where, v_{dc} is the DC-link voltage of the inverter.

The implementation of current controller with voltage limiter is shown in figure 7.9.

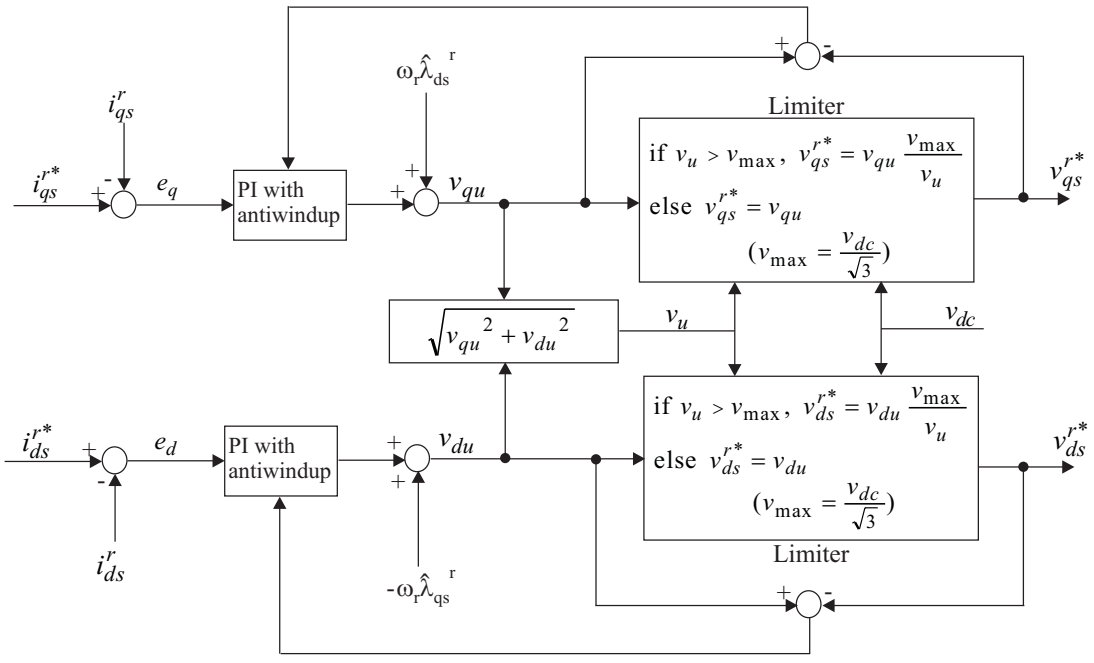

Figure 7.9: *Block diagram showing the implementation of current controller with voltage limiter.*

Referring to figure 7.9, the unconstrained voltage vector magnitude v_u from the q-

and d-axis current controllers is

$$v_u = \sqrt{v_{qu}^2 + v_{du}^2} \tag{7.2.26}$$

where, v_{qu} and v_{du} are unconstrained voltage outputs from q- and d-axis current controllers respectively.

When v_u exceeds the maximum voltage v_{max}, i.e. $v_u > v_{max}$, the corresponding constrained q- and d-axis voltages are calculated without changing the unconstrained voltage vector angle, but only the magnitude of it. With this consideration, when $v_u > v_{max}$ the magnitude of the constrained q- and d- axis voltages (i.e., final command values of q- and d- axis voltages) are calculated as follows.

$$v_{qs}^{r*} = v_{qu}\frac{v_{max}}{v_u} \tag{7.2.27}$$

$$v_{ds}^{r*} = v_{du}\frac{v_{max}}{v_u} \tag{7.2.28}$$

The v_{dc} is measured for this implementation.

7.2.2 Speed controller

The mechanical system equation of the machine is given by (see (2.6.1) of Chapter 2)

$$T_e - T_l = J\frac{2}{n}p\omega_r + B_m\frac{2}{n}\omega_r \tag{7.2.29}$$

Considering the relationship in (7.2.29) the model used to design the speed controller is shown in figure 7.10.

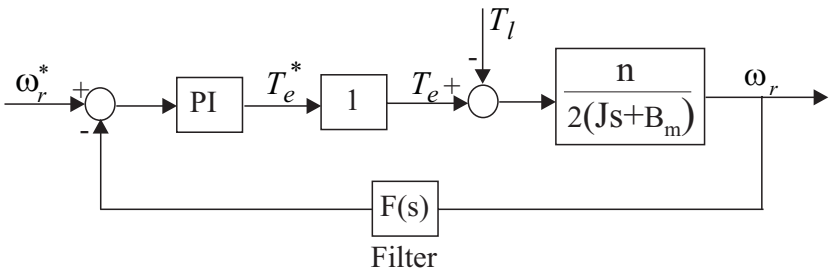

Figure 7.10: *The model used to design the speed controller.*

A PI controller is used in the speed loop. Since the inner current loop, which commands torque to the machine, has a much higher bandwidth compared to the speed loop, it is modeled using the gain 1 as shown in figure 7.10. Since the speed feedback is filtered using a first order low-pass filter, this filter is included in the feedback path.

The discrete model for designing the speed controller is shown in figure 7.11.

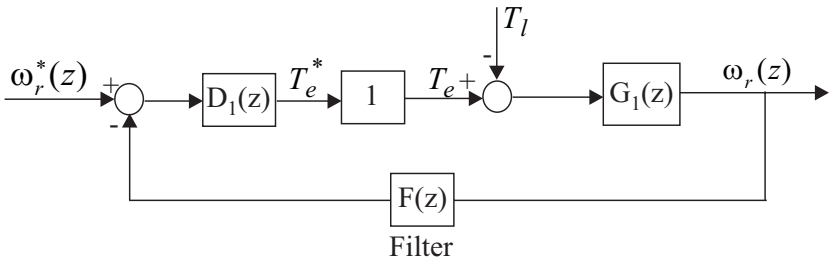

Figure 7.11: *The discrete model for designing the speed controller.*

The $D_1(z)$ is the discrete transfer function for the PI controller and

$$\begin{aligned} D_1(z) &= k_{ps} + \frac{k_{is}}{1 - z^{-1}} \\ &= \frac{(k_{ps} + k_{is})(z - \frac{k_{ps}}{k_{ps}+k_{is}})}{(z-1)} \end{aligned} \tag{7.2.30}$$

where, k_{ps} and k_{is} are proportional and integral gain respectively.

The $G_1(z)$ is the discrete transfer function for the mechanical model of the machine with zero order hold effect. The $G_1(z)$ can be obtained as

$$G_1(z) = (1 - z^{-1}) Z_{trans}(\frac{G_1(s)}{s}) \tag{7.2.31}$$

where, $G_1(s)$ is s-domain transfer function

$$G_1(s) = \frac{n}{2(Js + B_m)}. \tag{7.2.32}$$

Substituting (7.2.32) into (7.2.31) one obtains

$$G_1(z) = (1 - z^{-1}) Z_{trans}(\frac{n}{2s(Js + B_m)}) \tag{7.2.33}$$

After obtaining the Z-transformation, (7.2.33) can be written as

$$\begin{aligned} G_1(z) &= \frac{n(1 - z^{-1})z(1 - e^{\frac{-T}{\tau_m}})}{2B_m(z-1)(z - e^{\frac{-T}{\tau_m}})} \\ &= \frac{n(1 - e^{\frac{-T}{\tau_m}})}{2B_m(z - e^{\frac{-T}{\tau_m}})} \\ &= \frac{a_1}{z - b_1} \end{aligned} \tag{7.2.34}$$

where,

$$\tau_m = \frac{J}{B_m}, \quad a_1 = \frac{n(1 - e^{\frac{-T}{\tau_m}})}{2B_m}, \quad b_1 = e^{\frac{-T}{\tau_m}}$$

The $F(z)$ is the discrete transfer function for the first order low-pass filter. The s-domain transfer function for this filter is

$$F(s) = \frac{\omega_c}{s + \omega_c} \tag{7.2.35}$$

where,

$$\omega_c = 2\pi f_c \tag{7.2.36}$$

and f_c is the cut-off frequency of the filter. Using bilinear transform [11], i.e. substituting

$$s = \frac{2}{T}(\frac{z-1}{z+1}), \tag{7.2.37}$$

one can obtain the discrete transfer function $F(z)$ as

$$F(z) = k_1 \frac{z+1}{z-b_2} \tag{7.2.38}$$

where,

$$k_1 = \frac{T\omega_c}{2 + T\omega_c} \quad \text{and} \quad b_2 = \frac{2 - T\omega_c}{2 + T\omega_c}$$

In the laboratory test system f_c=100 Hz filter is used.

To design the speed PI controller the root locus method is used as for the current controllers.

The discrete transfer function ($\omega_r^*(z)$ as the input and $\omega_r(z)$ as the output) for the system shown in figure 7.11 is

$$\frac{\omega_r(z)}{\omega_r^*(z)} = \frac{D_1(z)G_1(z)}{1 + D_1(z)G_1(z)F(z)} \tag{7.2.39}$$

After substituting $D_1(z)$, $G_1(z)$ and $F(z)$, (7.2.39) becomes

$$\frac{\omega_r(z)}{\omega_r^*(z)} = \frac{a_1(k_{ps} + k_{is})(z - \frac{k_{ps}}{k_{ps}+k_{is}})(z - b_2)}{(z-1)(z-b_1)(z-b_2) + a_1k_1(k_{ps} + k_{is})(z - \frac{k_{ps}}{k_{ps}+k_{is}})(z+1)} \tag{7.2.40}$$

The characteristic equation of the system is

$$1 + D_1(z)G_1(z)F(z) = 0 \tag{7.2.41}$$

Substituting $D_1(z)$, $G_1(z)$ and $F(z)$ to (7.2.41) one obtains

$$1 + \frac{k_1a_1(k_{ps} + k_{is})(z - \frac{k_{ps}}{k_{ps}+k_{is}})(z+1)}{(z-1)(z-b_1)(z-b_2)} = 0 \tag{7.2.42}$$

The equation (7.2.42) has the form

$$1 + k'' H_1(z) = 0 \tag{7.2.43}$$

where,

$$k^{''} = k_1 a_1 (k_{ps} + k_{is}) \tag{7.2.44}$$

$$H_1(z) = \frac{(z - \frac{k_{ps}}{k_{ps}+k_{is}})(z+1)}{(z-1)(z-b_1)(z-b_2)} \tag{7.2.45}$$

Figure 7.12 shows the z-plane root locus and the selected closed-loop poles for the speed controller, which the characteristic equation is given by (7.2.43). For this root locus the zero from the PI controller ($z = z_{os} = \frac{k_{ps}}{k_{ps}+k_{is}}$) is selected at $z = b_1$, in order to cancel out the slow pole from the machine. Knowing the z_{os} and the root locus gain $k^{''}$ for the selected closed-loop poles, the PI controller gains can be calculated as

$$k_{ps} = \frac{k^{''}}{k_1 a_1} z_{os} \tag{7.2.46}$$

$$k_{is} = \frac{k^{''}}{k_1 a_1} (1 - z_{os}) \tag{7.2.47}$$

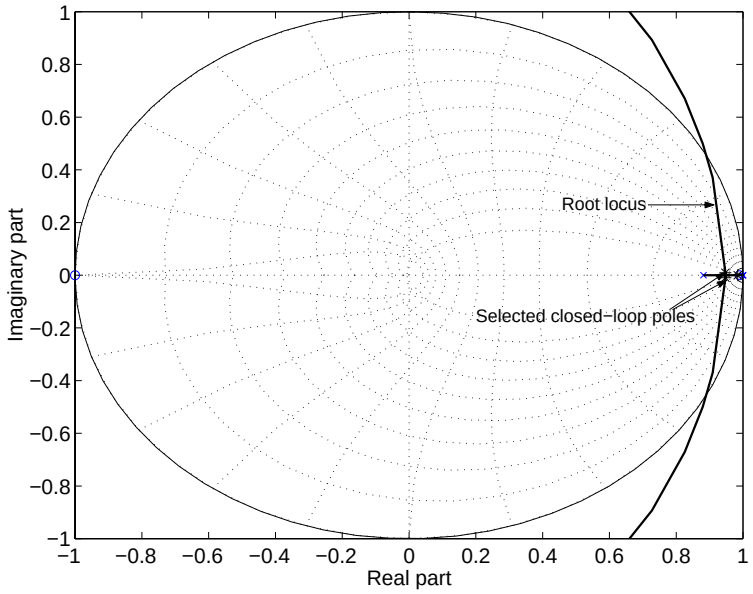

Figure 7.12: *The root locus and the selected closed-loop poles for the speed controller.*

The characteristics of the selected closed-loop poles and the calculated PI controller gains are given in table 7.5 and table 7.6 respectively. The selected closed-loop poles' ω_n=274 rad/s, which gives the bandwidth of the speed controller 44 Hz. This is about 12 times less than the bandwidth of the current controller.

The speed PI controller also includes integrator antiwindup function as described for current controllers. The speed PI controller output is torque command to the machine and it is limited to 150% of rated torque of the machine (i.e. 18 Nm). The maximum

Closed loop poles (In Z-plane)	Equivalent damping factor (ξ) in S-plane	Equivalent natural frequency (ω_n) in S-plane (rad/s)
0.95+0.01i	0.98	274
0.95-0.01i	0.98	274

Table 7.5: Characteristics of selected closed-loop poles for the speed controller.

k_{ps}	k_{is}
0.63	0.01

Table 7.6: PI controller gains for the speed controller.

torque can be produced by the machine is 150% of rated torque, and therefore, the torque command is limited to that value.

7.2.3 Current reference generator

The speed controller output is the torque command, which requires to move the rotor of the machine towards to the desired velocity. This torque command is mapped into the rotor d- and q-axis current commands from the current reference generator (see figure 7.1). The analysis made in §2.8 of Chapter 2 reveal that the overall performance of the constant stator flux linkage control strategy, which maintains the magnitude of the stator flux linkage to λ_m, is better compared to the others. Therefore, the constant stator flux linkage control strategy is used to map the torque command to the rotor d- and q-axis current commands. The rotor d- and q-axis currents as a function of the torque, in order to achieve the constant stator flux linkage λ_m, is shown in figure 7.13. The detailed discussion and the derivation of steady state equations for the constant stator flux linkage control strategy is given in §2.8.5 of Chapter 2.

The two relationships shown in figure 7.13 is programmed in the current reference generator so that the torque command is mapped into the rotor d- and q-axis current commands.

7.2.4 Voltage transformation and PWM

The current controller outputs are the desired voltage to the machine in the rotor fixed reference frame. The inverter of the drive should be controlled so that this voltage to be applied on the phases of the machine.

First, the rotor fixed reference frame voltage commands, which are the outputs of the current controller, are transformed to the stationary reference frame voltage

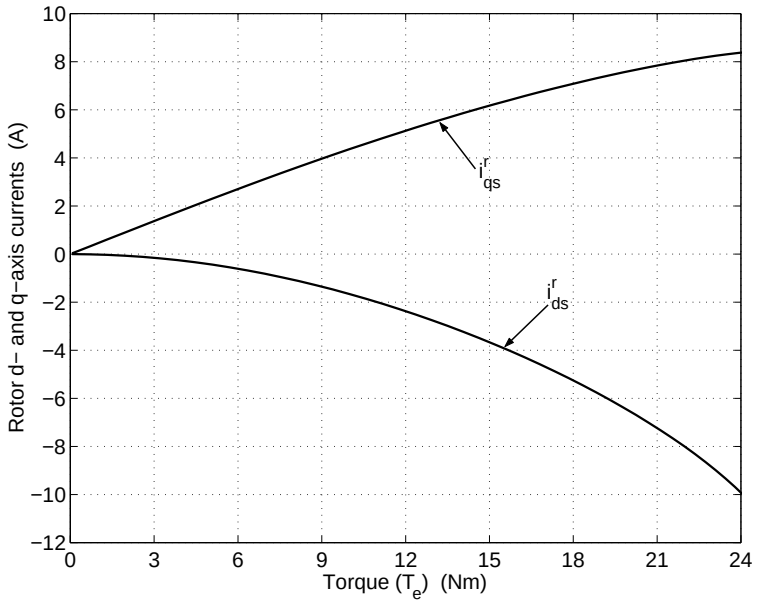

Figure 7.13: *The rotor d- and q-axis currents (i^r_{ds}, i^r_{qs}) as a function of the torque (T_e), in order to achieve constant stator flux linkage λ_m.*

commands (see figure 7.1) using the rotor position as follows.

$$v^{s*}_{qs} = v^{r*}_{qs} cos(\theta_r) + v^{r*}_{ds} sin(\theta_r) \tag{7.2.48}$$

$$v^{s*}_{ds} = v^{r*}_{qs} sin(\theta_r) - v^{r*}_{ds} cos(\theta_r) \tag{7.2.49}$$

These stationary reference frame voltage commands are used to generate the inverter control signals (see Appendix C), so that the voltage command is applied to the phases of the machine.

7.3 The drive system with position sensor

The field-oriented controlled drive system with position sensor is studied in this section. The block diagram of the drive system with position sensor is shown in figure 7.14. The controller uses the position and velocity information from the rotor mounted position sensor.

All control functions of the drive system are implemented in a laboratory test system and the details of the laboratory test system can be found in Appendix D. For the drive system, the current and the speed controller gains are as given in table 7.2, table 7.4 and table 7.6. For all simulations and experimental results presented in this section the drive is started from a known initial rotor position.

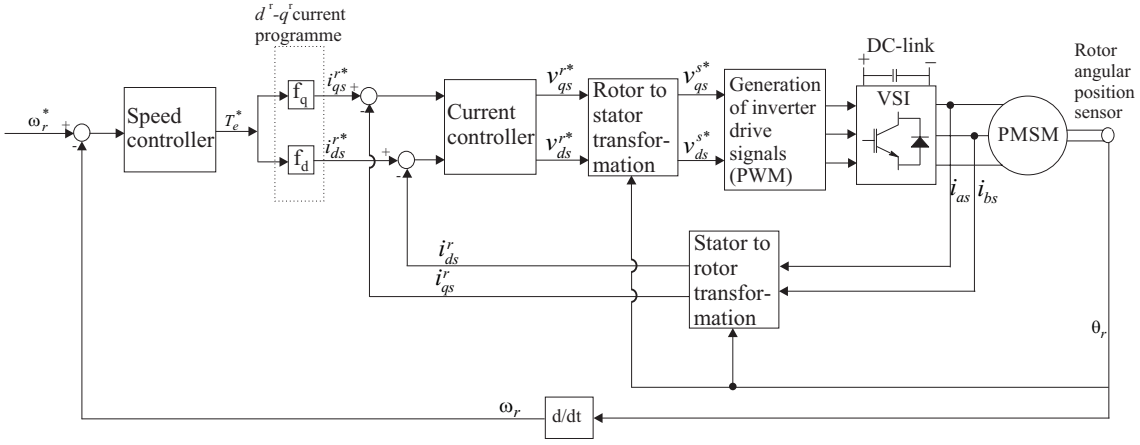

Figure 7.14: *Block diagram of rotor permanent-magnet flux oriented controlled drive system with position sensor.*

7.3.1 Validation of current and speed controller design

In order to validate the design of the current controller, the step responses of the rotor d- and q-axis currents are measured in the drive system. For these tests, the outer speed loop is disabled and the controller is operated only with the current loop. The rotor speed is measured and the desired current step references are given to the controller at required rotor frequencies. The measured current responses at low and high frequencies are shown in figure 7.15. In order to see the i^r_{qs} step responses, the i^r_{qs} reference is stepped from 1 A to 2 A with i^r_{ds} reference is fixed at zero. For i^r_{ds} step responses, the i^r_{ds} reference is stepped from 0 A to -1 A with i^r_{qs} reference is fixed at 1 A.

The current controllers are designed with ω_n =3480 rad/s and ξ ≈1 (see table 7.1 and table 7.3). The rise time (t_r), i.e. the time required for the step response to reach from 10% to 90% of the final value, can approximately be calculated as $t_r \approx \frac{1.8}{\omega_n}$, when ξ ≈0.5 [6]. With this relationship, when ω_n =3480 rad/s, the rise time can be calculated as t_r =0.52 ms, which is about 2.5 sampling periods. However, when ξ =1, somewhat longer rise time can be expected. As it can be seen from the measurements in figure 7.15 the rise time for the current step responses is about 4 sampling periods (i.e. t_r ≈0.8 ms), which agree with the design.

In order to see the effectiveness of the decoupling in the current controller, the measured current step responses at high speed (60 Hz), with and without decoupling in the current controller, are compared in figure 7.16. As it can be seen from the current responses, without decoupling the current controller becomes sluggish as expected.

The measured step response of the speed with inner current loop is shown in figure 7.17. The speed reference is stepped from 100 rad/s to 105 rad/s, under no-load, as shown in figure 7.17. The rise time for this response is about 10 ms, which gives the

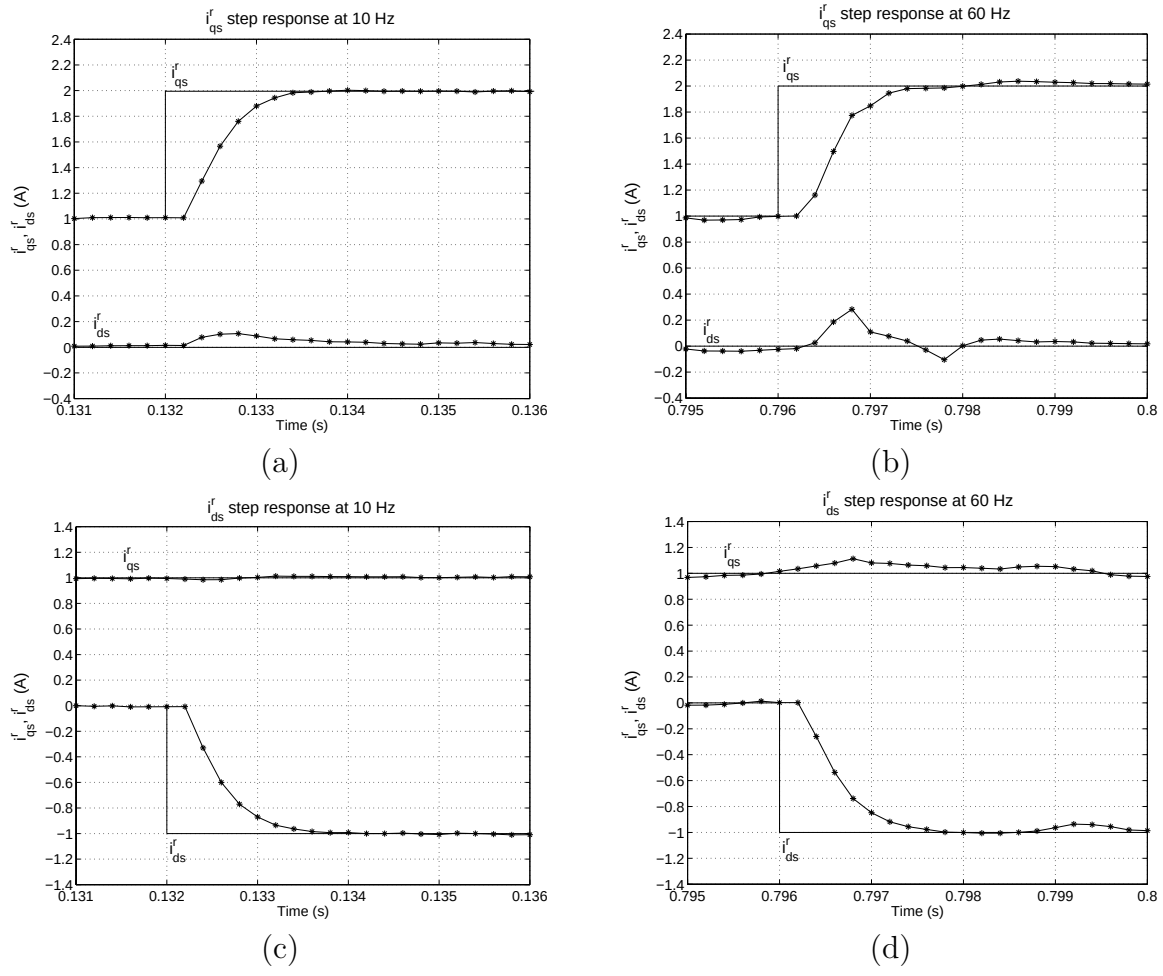

Figure 7.15: *Measured current step responses at different frequencies. (a), (b) i^r_{qs} step responses. i^r_{ds} reference is fixed at zero. (c), (d) i^r_{ds} step responses. i^r_{qs} reference is fixed at 1 A.*

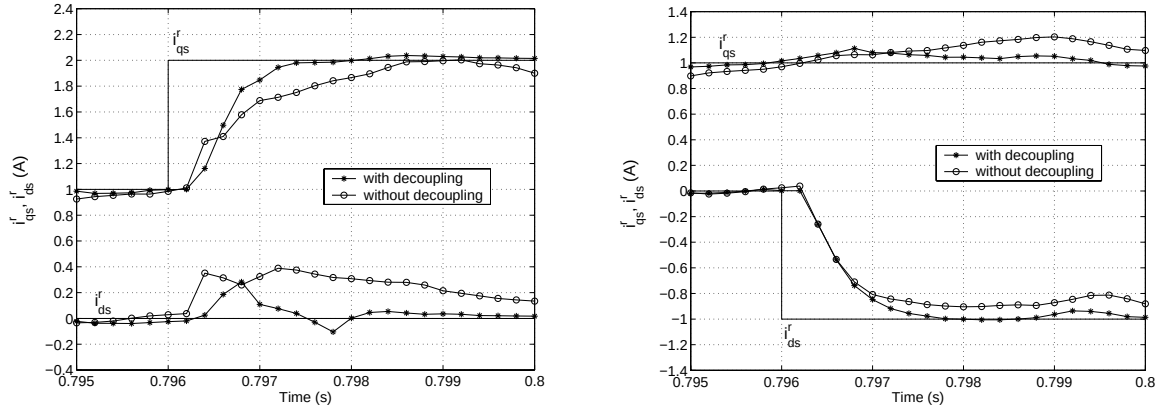

Figure 7.16: *Measured current step responses with and without decoupling in the current controller. The measurements are taken at 60 Hz. (a) i^r_{qs} step responses. i^r_{ds} reference is fixed at zero. (b) i^r_{ds} step responses. i^r_{qs} reference is fixed at 1 A.*

bandwidth of the speed loop about 12 times less than the current loop as expected from the design. Even though the speed loop is designed with $\xi \approx 1$ (see table 7.5) an overshoot can be seen in the response shown in figure 7.17. This is due to the fact that the existence of a zero in the speed loop closed loop transfer function given in (7.2.40). Even though the zero from the PI controller is cancelled out during the design, a zero still exists at $z = b_2$ due to the filter in the feedback path. Therefore, an overshoot can be expected in the speed response.

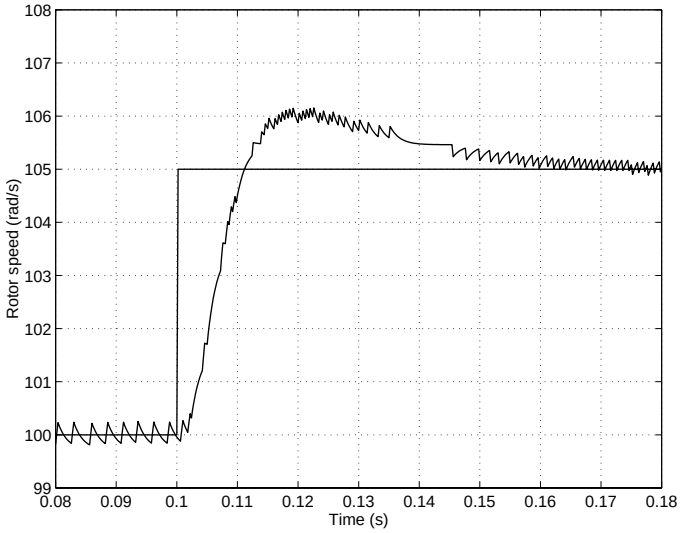

Figure 7.17: *Measured step response of the speed.*

The effect of the integrator antiwindup in the PI controller can be seen from the measurements shown in figure 7.18. In order to saturate the speed controller, a large speed step (50 rad/s) was commanded and the speed response is measured with and without integrator antiwindup in the speed PI controller. As it can be seen from the measurements shown in figure 7.18 without integrator antiwindup the overshoot is increased substantially in the response.

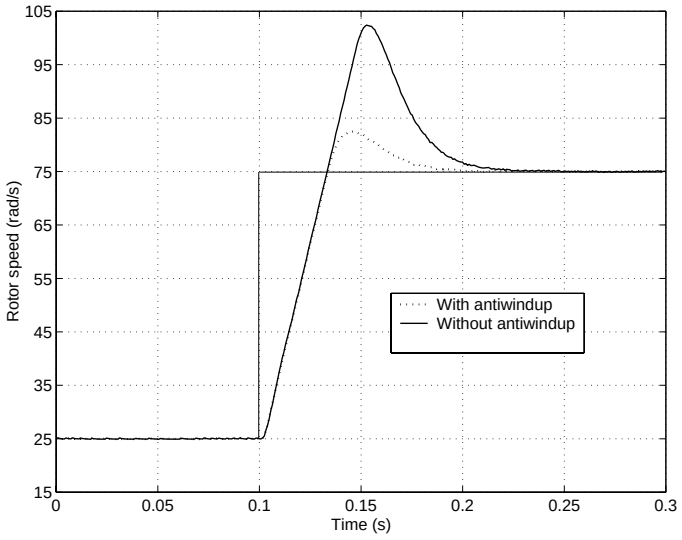

Figure 7.18: *Measured speed step responses with and without integrator antiwindup in the speed PI controller.*

7.3.2 The performance of the complete drive system

The field-oriented controller performance with a load disturbance to the drive was tested at 50% of rated speed. The simulations are shown in figure 7.19 and figure 7.20. For simulations, a constant DC-link voltage was assumed for the VSI and the actual rotor position of the machine was used in the controller. The drive system was simulated in the Saber simulation programme. The laboratory measurements of the drive system under the same conditions as simulations are shown in figure 7.21 and figure 7.22. Both simulations and laboratory measurements verify the satisfactory performance of the speed and current controller.

The currents are controlled in the drive in order to achieve constant stator flux linkage($\lambda_s = \lambda_m$) in the machine. Figure 7.20(e) shows the simulated magnitude of the actual stator flux in the machine. It can be seen that the magnitude of the stator flux is kept constant in the machine as expected. It can also be seen that the constant flux value is almost equal to λ_m(=0.4832 V s/rad).

The performance of the drive during low-speed operation can be seen from the measurements shown in figure 7.23. At 5% of rated speed a 50% load step is added

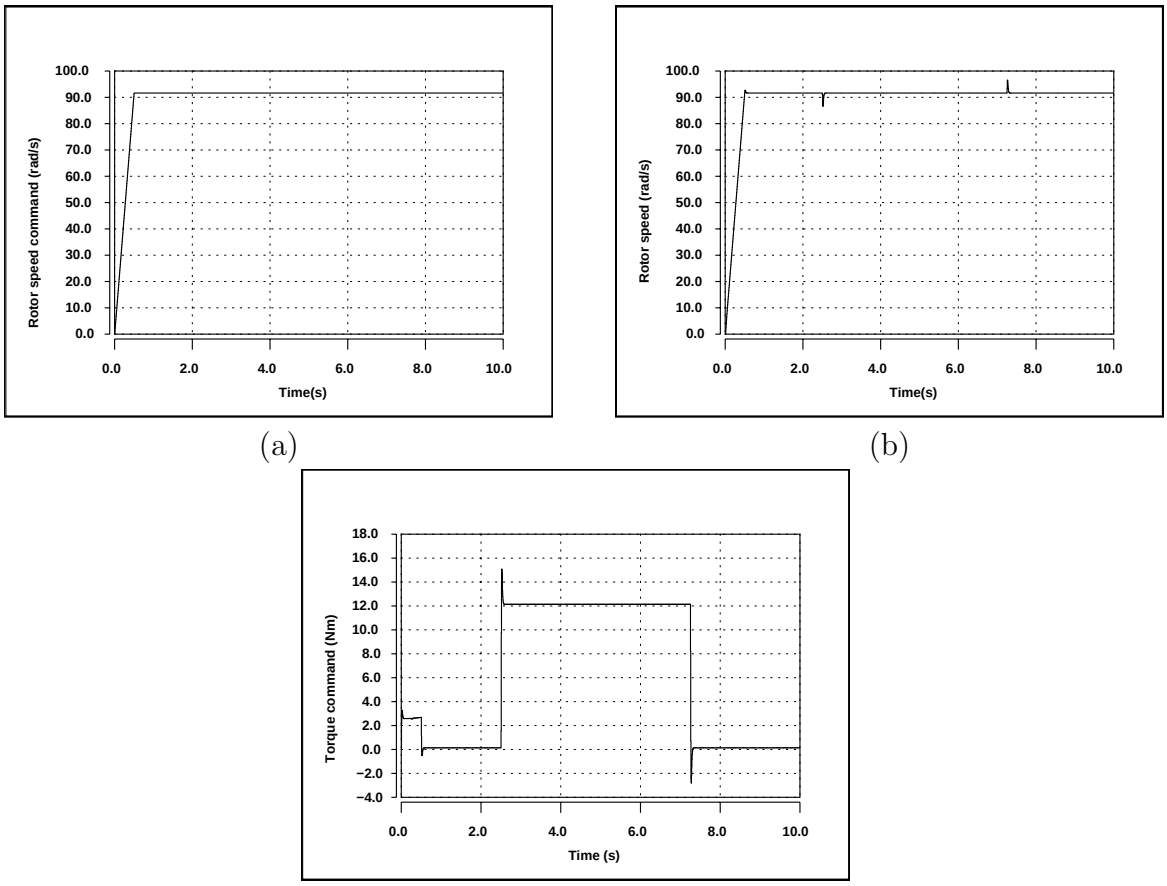

Figure 7.19: *Simulated variables, when adding a 100% load step to the drive at 50% of rated speed. (a) Rotor speed command (b) Actual rotor speed (c) Torque command (T_e^*) in the controller.*

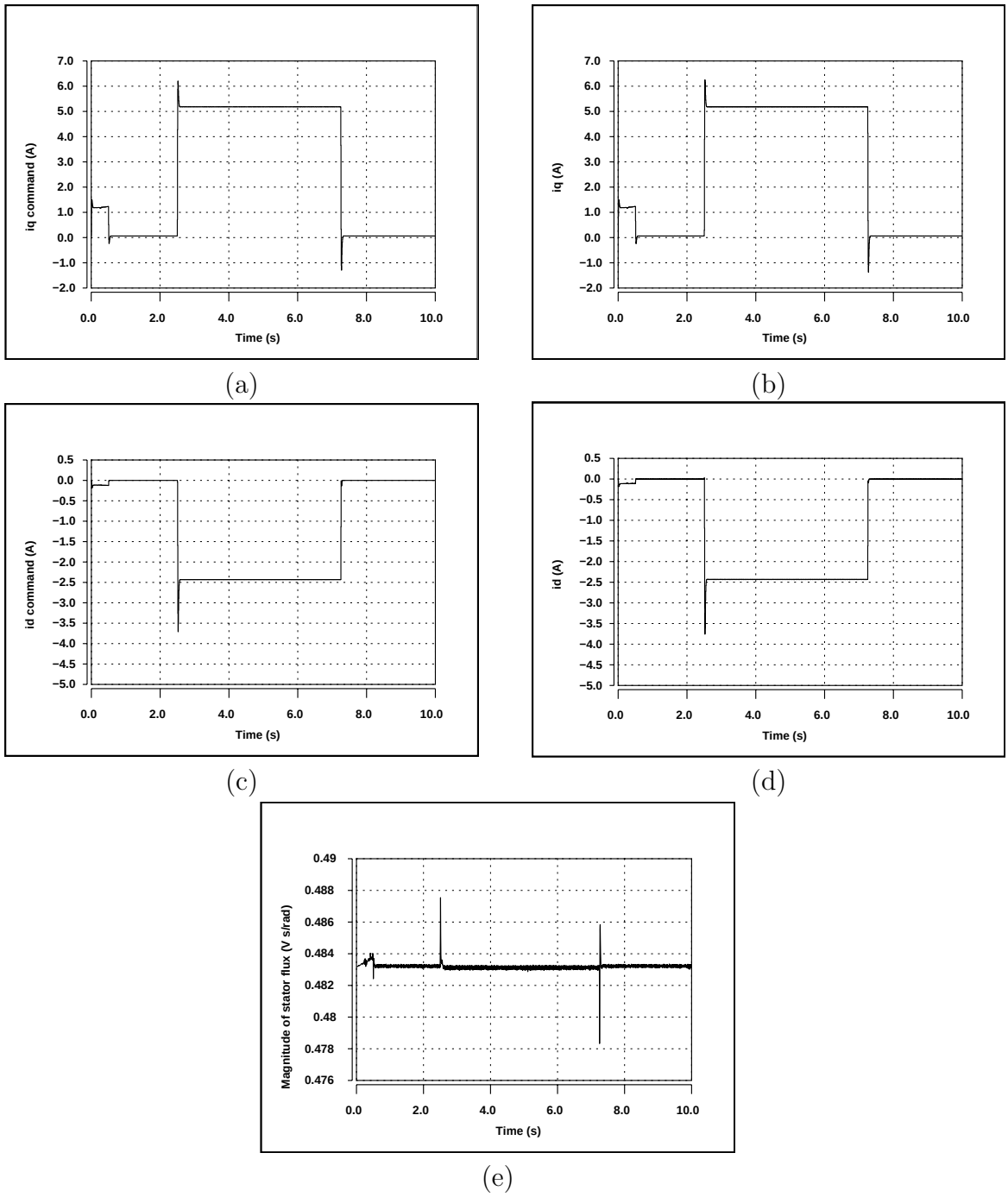

Figure 7.20: *Simulated variables, when adding a 100% load step to the drive at 50% of rated speed. (a) q-axis current command (i^{r*}_{qs}) (b) Actual q-axis current (i^{r}_{qs}) (c) d-axis current command (i^{r*}_{ds}) (d) Actual d-axis current (i^{r}_{ds}) (e) Magnitude of the stator flux (λ_s).*

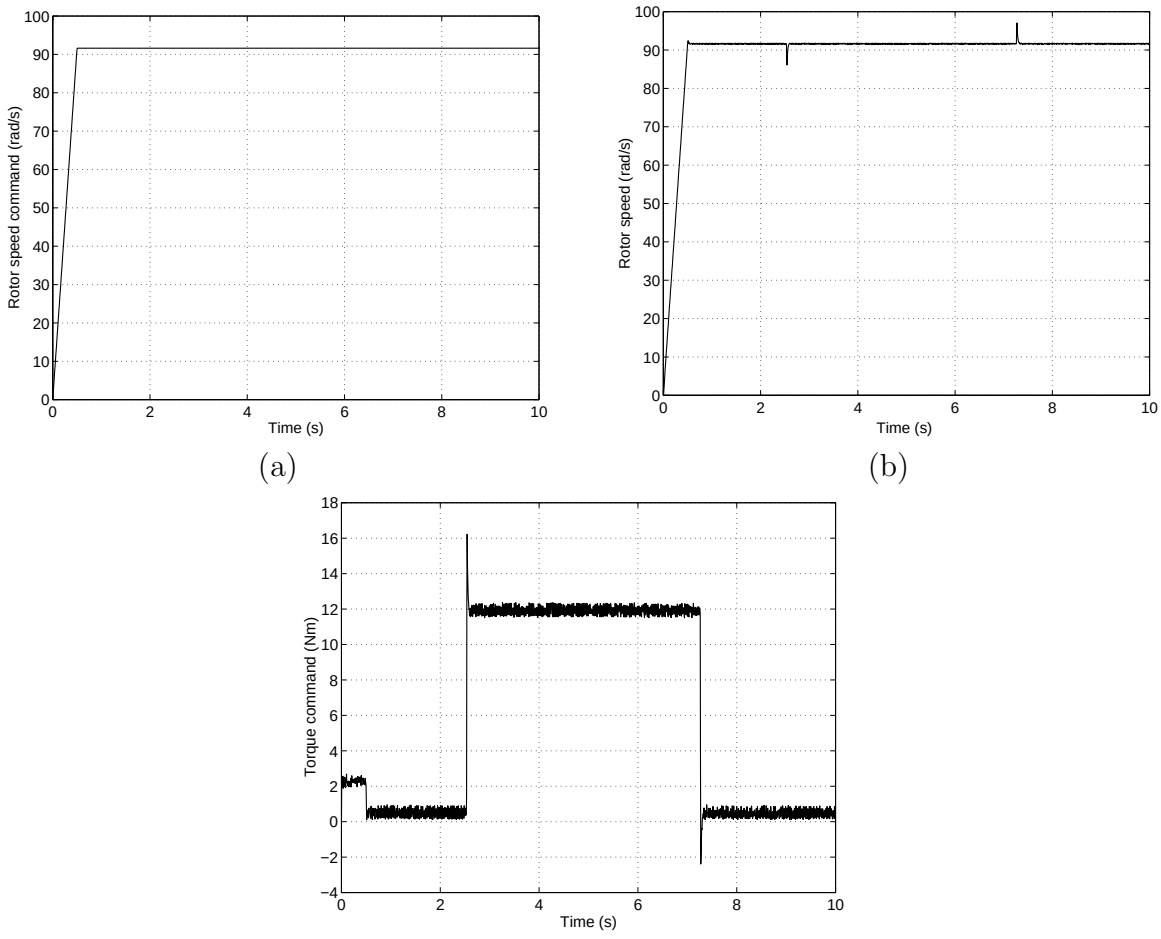

Figure 7.21: *Measured variables, when adding a 100% load step to the drive at 50% of rated speed. (a) Rotor speed command (b) Actual rotor speed (c) Torque command (T_e^*) in the controller.*

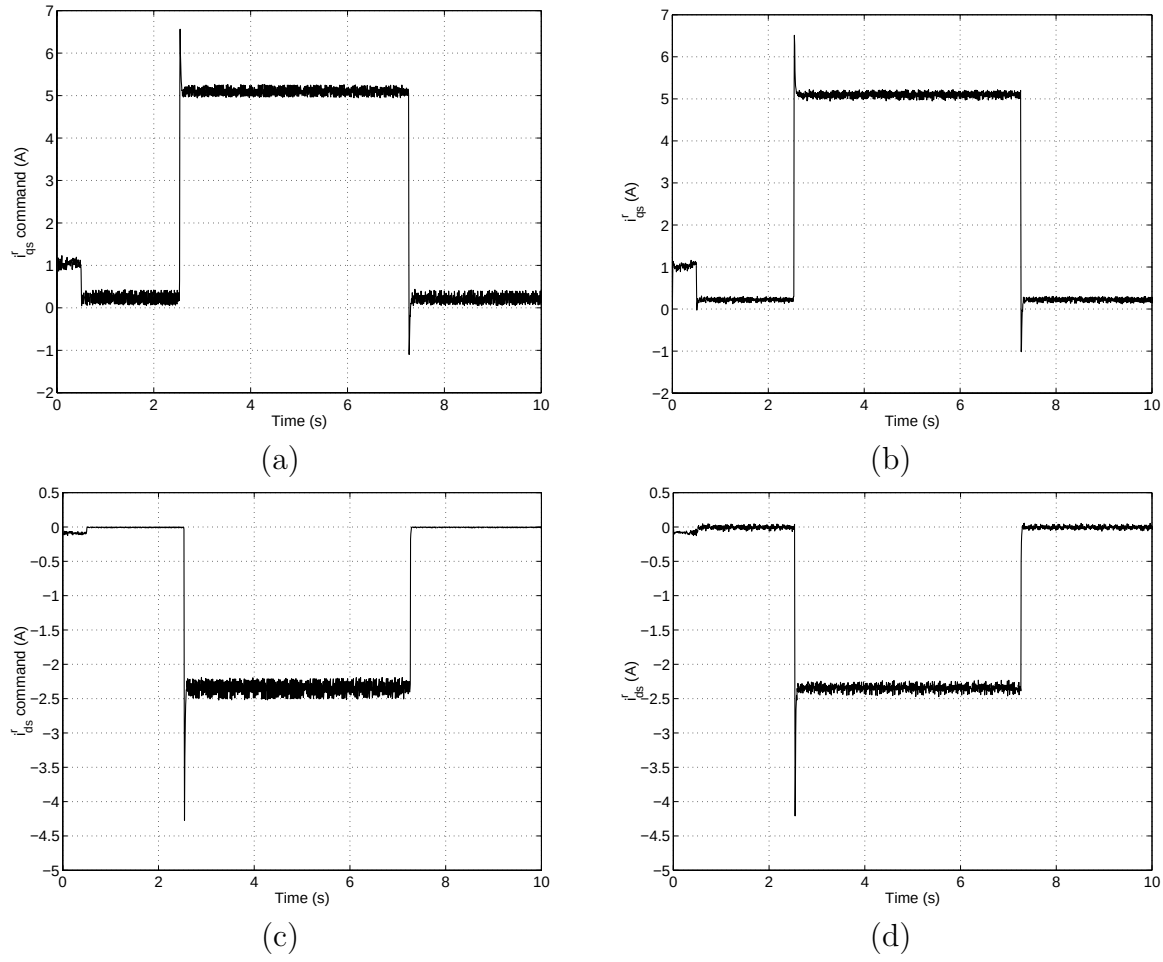

Figure 7.22: *Measured variables, when adding a 100% load step to the drive at 50% of rated speed. (a) q-axis current command (i^{r*}_{qs}) (b) Actual q-axis current (i^{r}_{qs}) (c) d-axis current command (i^{r*}_{ds}) (d) Actual d-axis current (i^{r}_{ds}).*

to the machine and, as it can be seen from the measurements the drive can operate successfully overcoming the load step at this speed.

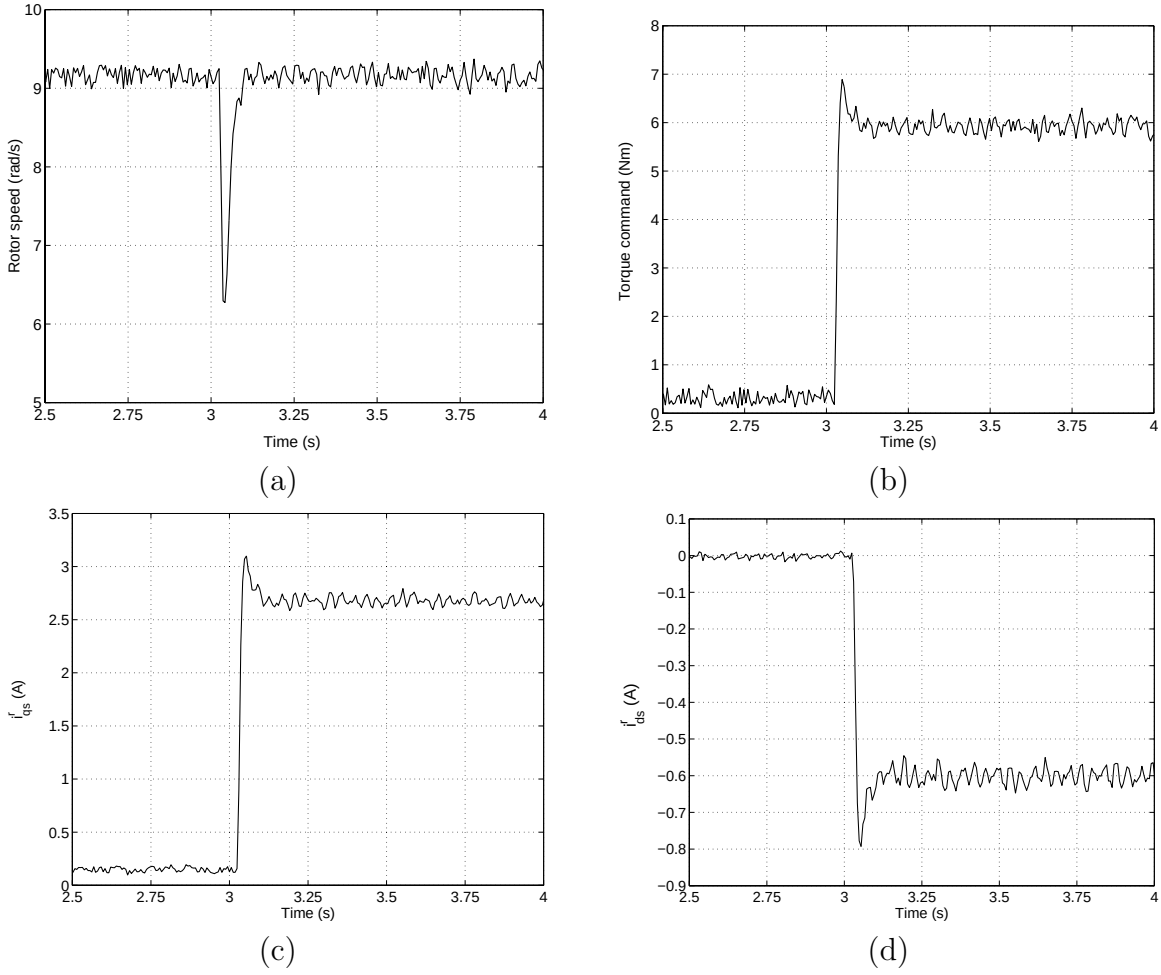

Figure 7.23: *Measured variables, when adding a 50% load step to the drive at 5% of rated speed. (a) Rotor speed (b) Torque command (T_e^*) in the controller (c) q-axis current (i^r_{qs}) (d) d-axis current (i^r_{ds}).*

The performance of the drive with quadratic load is investigated through simulations. Figure 7.24 shows the results. The quadratic load on the machine is modeled as described in §5.4.3 of Chapter 5. As it can be seen from the results in figure 7.24 the drive can operate satisfactorily with a quadratic load.

Figure 7.25 compares the dynamic response of the field-oriented controlled (FOC) drive system and the V/f controlled drive system discussed in Chapter 5. For both drive systems the measurements are at 50% of rated speed with 100% load step. It can be seen that the fast dynamic response in the field-oriented controlled drive system as expected.

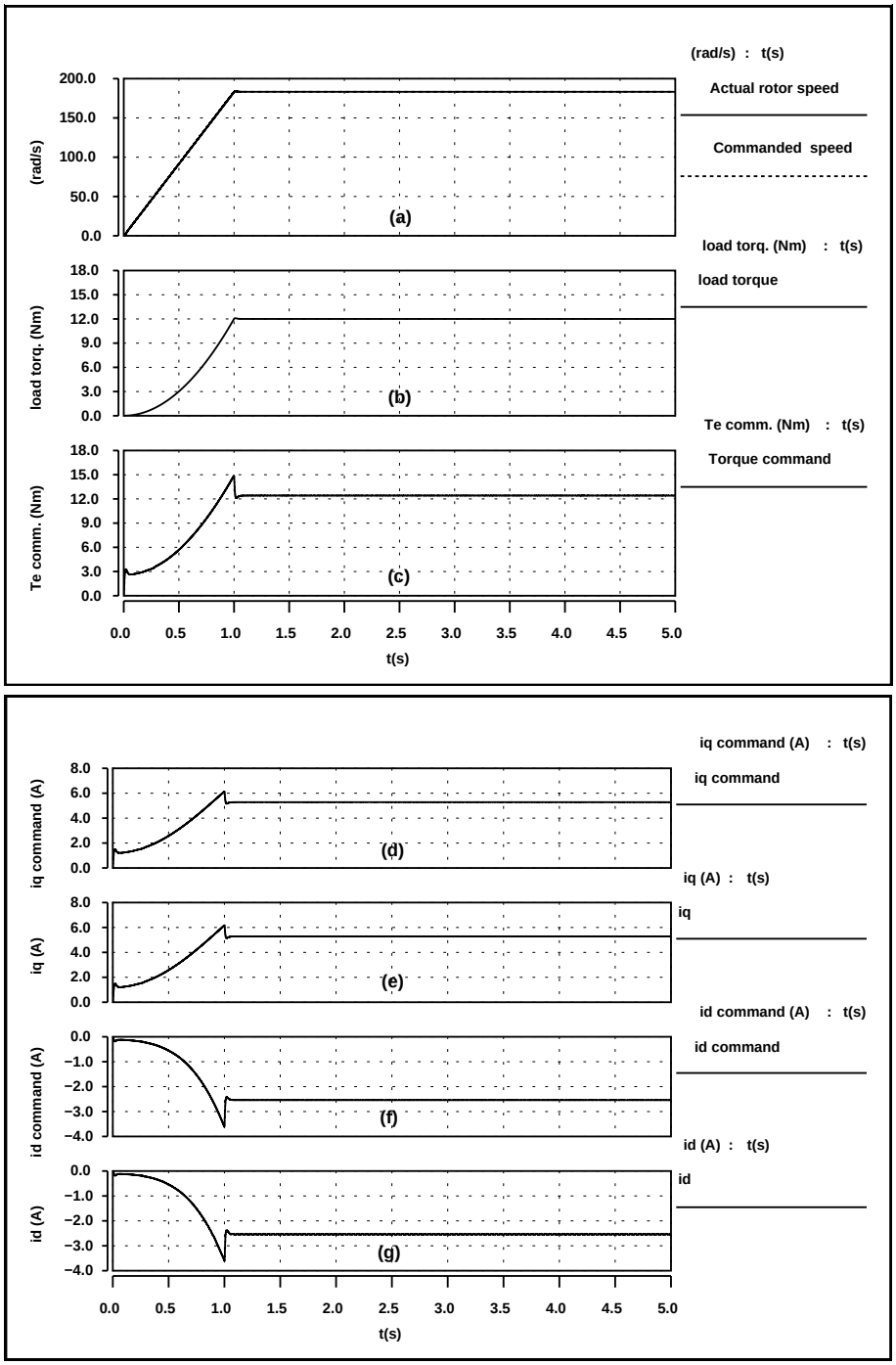

Figure 7.24: *Simulation results, when ramping up the drive to the rated speed with quadratic load. (a) Actual and commanded rotor speed (b) Applied load torque to the machine (c) Torque command (T_e^*) in the controller (d) q-axis current command (i_{qs}^{r*}) (e) Actual q-axis current(i_{qs}^{r}) (f) d-axis current command (i_{ds}^{r*}) (g) Actual d-axis current(i_{ds}^{r}).*

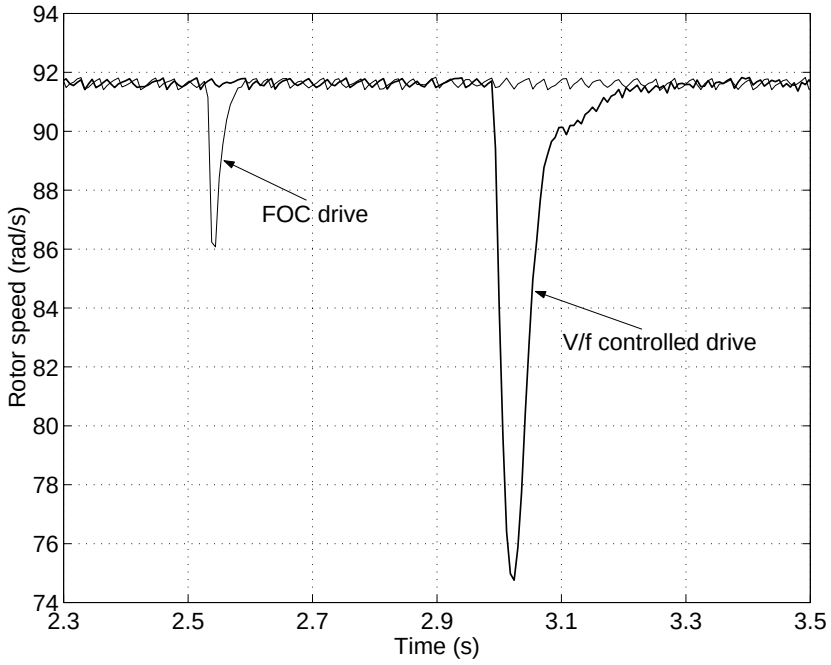

Figure 7.25: *Measured speed responses from the field-oriented controlled drive system and the V/f controlled drive system, when 100% load step is added at 50% rated speed.*

7.4 Sensorless Control

In order to eliminate the rotor position sensor in the rotor permanent-magnet flux oriented controlled drive system, a rotor position and velocity estimation technique is studied in this section. Only motor phase currents are measured for position and velocity estimation. The overall block diagram of the sensorless drive system (i.e. with rotor position and velocity estimator) is shown in figure 7.26.

7.4.1 Rotor position and velocity estimation

The rotor position and velocity estimation algorithm requires the estimation of the stator flux linkage. Using the estimated stator flux, the stator currents are estimated at a predicted rotor position. The difference between the estimated stator currents and the measured currents, i.e. current errors, are used to correct the error in the predicted rotor position. The block diagram of the algorithm is shown in figure 7.27. The number in the each block of figure 7.27 indicates the execution order of the estimation algorithm. The principle is similar to the one used in [12],[13] and [14]. In subsequent sections, each step of this algorithm is discussed in detail.

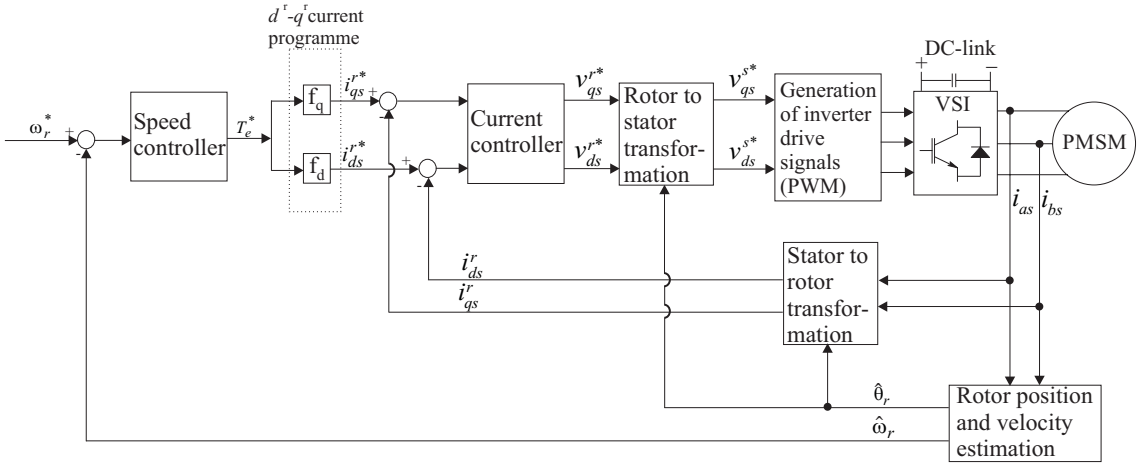

Figure 7.26: *Block diagram of the sensorless rotor permanent-magnet flux oriented controlled drive system.*

Stator flux linkage estimation

In the first step, the stator flux linkage is estimated integrating the difference between the stator voltage and the ohmic voltage drop. For discrete implementation, the rectangular rule is used for the integration. Therefore, the stator flux linkages are obtained as

$$\hat{\lambda}^s_{qs}(k) = T[v^{s*}_{qs}(k-1) - r_s i^s_{qs}(k)] + \lambda^s_{qs}(k-1) \tag{7.4.1}$$

$$\hat{\lambda}^s_{ds}(k) = T[v^{s*}_{ds}(k-1) - r_s i^s_{ds}(k)] + \lambda^s_{ds}(k-1) \tag{7.4.2}$$

where, T is sampling time and k is sampling number. The i^s_{qs} and i^s_{ds} are obtained by transforming the measured phase currents to the 2-phase stationary reference frame currents as shown in figure 7.27. The phase voltages are not measured and the controller commanded voltages to the machine in the previous sampling period, i.e. $v^{s*}_{qs}(k-1)$ and $v^{s*}_{ds}(k-1)$, are used in (7.4.1) and (7.4.2).

In order to avoid integrator drift problems the stator flux is updated in step 4 of the algorithm using corrected rotor position and measured currents (This will be discussed in detail later). Those updated flux values (λ^s_{qs} and λ^s_{ds}) in the previous sampling period are used in (7.4.1) and (7.4.2) to calculate the stator flux values in the present sampling period.

Stator current estimation

In step 2 of the algorithm the stator currents are estimated using the estimated flux in step 1 and the predicted rotor position. The equations for stator currents estimation are obtained from the solutions to the currents in (2.4.38) and (2.4.39) of Chapter 2.

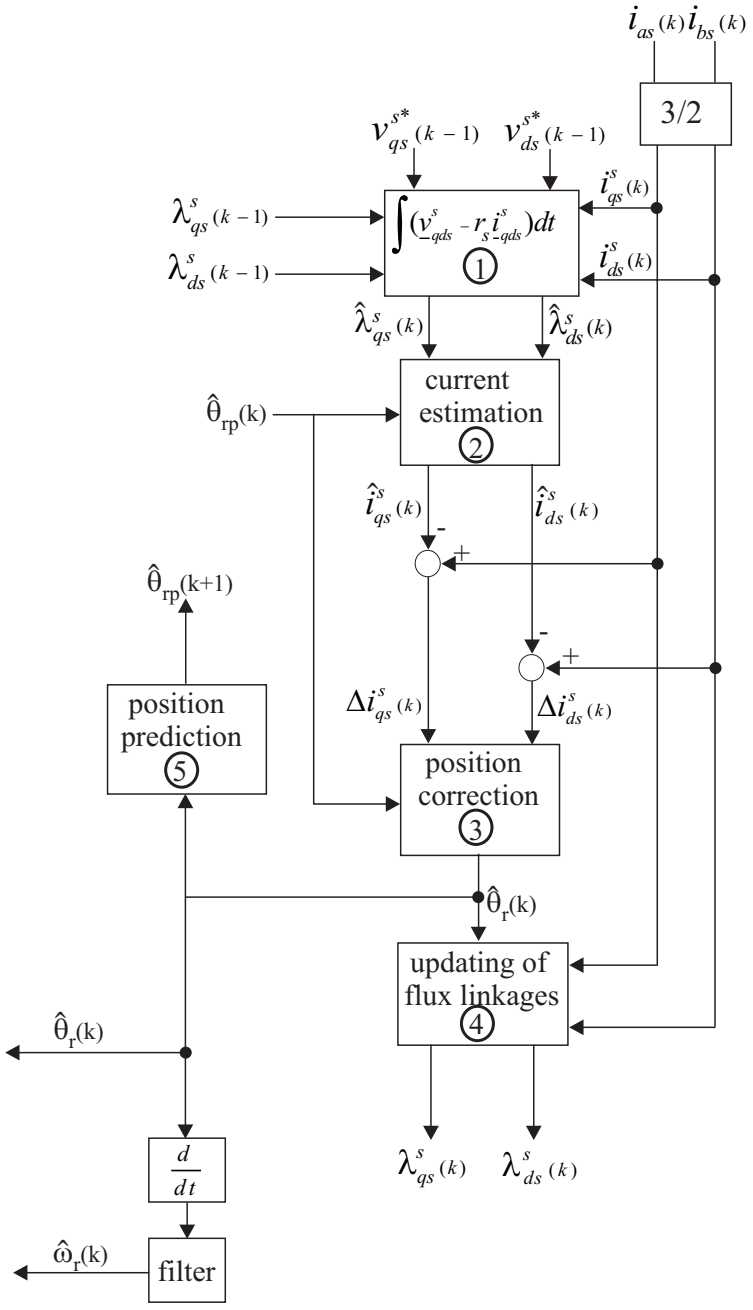

Figure 7.27: *Block diagram of the rotor position and velocity estimation algorithm.*

Those equations for stator currents estimation are

$$\hat{i}^s_{qs}(k) = \frac{[L - \Delta L cos(2\hat{\theta}_{rp}(k))]\hat{\lambda}^s_{qs}(k) + \Delta L sin(2\hat{\theta}_{rp}(k))\hat{\lambda}^s_{ds}(k) - (L + \Delta L)\lambda_m sin(\hat{\theta}_{rp}(k))}{L^2 - \Delta L^2} \tag{7.4.3}$$

$$\hat{i}^s_{ds}(k) = \frac{[L + \Delta L cos(2\hat{\theta}_{rp}(k))]\hat{\lambda}^s_{ds}(k) + \Delta L sin(2\hat{\theta}_{rp}(k))\hat{\lambda}^s_{qs}(k) - (L + \Delta L)\lambda_m cos(\hat{\theta}_{rp}(k))}{L^2 - \Delta L^2} \tag{7.4.4}$$

where, $L = \frac{L_q + L_d}{2}$ and $\Delta L = \frac{L_q - L_d}{2}$.

Position correction

The most important part of the algorithm is the correction of the predicted rotor position. For this purpose, the difference between the measured (actual) current and the estimated current, i.e. current errors

$$\Delta i^s_{qs}(k) = i^s_{qs}(k) - \hat{i}^s_{qs}(k) \tag{7.4.5}$$

$$\Delta i^s_{ds}(k) = i^s_{ds}(k) - \hat{i}^s_{ds}(k) \tag{7.4.6}$$

are used. Different methods exist to correct the position using current errors and they are analyzed in detail in §7.4.2.

Updating of flux linkages

In step 4, the flux is recalculated using the corrected rotor position and the measured stator currents. The stationary reference frame flux equations (2.4.38) and (2.4.39) of Chapter 2 are used for this purpose. Those equations are

$$\lambda^s_{qs}(k) = [L + \Delta L cos(2\hat{\theta}_r(k))]i^s_{qs}(k) - \Delta L sin(2\hat{\theta}_r(k))i^s_{ds}(k) + \lambda_m sin(\hat{\theta}_r(k)) \tag{7.4.7}$$

$$\lambda^s_{ds}(k) = [L - \Delta L cos(2\hat{\theta}_r(k))]i^s_{ds}(k) - \Delta L sin(2\hat{\theta}_r(k))i^s_{qs}(k) + \lambda_m cos(\hat{\theta}_r(k)) \tag{7.4.8}$$

These updated flux values are used in step 1 of the algorithm in the next sampling interval to estimate the flux. In this way, the integrator drift problems can be avoided in the flux estimation in step 1.

Prediction of rotor position

The position is predicted assuming the position varies with time as a second-order polynomial

$$\theta_r = At^2 + Bt + C. \tag{7.4.9}$$

Using three estimated previous positions the position at $(k + 1)$ sampling instant is predicted using second-order polynomial curve fitting. Figure 7.28 illustrates the principle and it is described below.

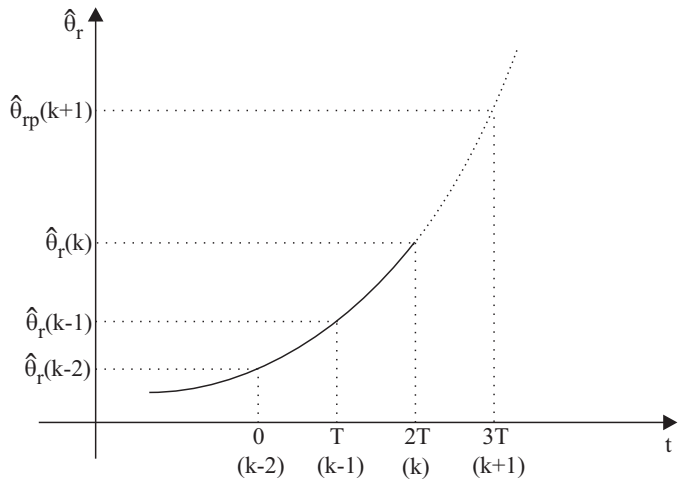

Figure 7.28: *Rotor position prediction using polynomial curve fitting.*

Assuming $t = 0$ at $(k-2)$ sampling instant, the rotor position can be obtained from (7.4.9) as

$$\hat{\theta}_r(k-2) = C. \tag{7.4.10}$$

At $(k-1)$ sampling instant

$$\hat{\theta}_r(k-1) = AT^2 + BT + C. \tag{7.4.11}$$

At (k) sampling instant

$$\hat{\theta}_r(k) = A(2T)^2 + B(2T) + C. \tag{7.4.12}$$

At $(k+1)$ sampling instant the predicted position is

$$\hat{\theta}_{rp}(k+1) = A(3T)^2 + B(3T) + C. \tag{7.4.13}$$

Solving (7.4.10), (7.4.11) and (7.4.12) for A,B and C, and substituting A,B and C values to (7.4.13) one can obtain the predicted rotor position at $(k+1)$ sampling instant as

$$\hat{\theta}_{rp}(k+1) = 3\hat{\theta}_r(k) - 3\hat{\theta}_r(k-1) + \hat{\theta}_r(k-2) \tag{7.4.14}$$

In step 5 of the algorithm, using three previously estimated positions, the position in next sampling instant is predicted using (7.4.14).

7.4.2 Analysis of position correction methods for the position estimation algorithm

Method 1:

A rotor position correction term from the stationary frame current errors can be obtained from the linearized stationary frame flux equations [12],[13]. Since the stationary

frame flux is a function of i^s_{qs},i^s_{ds} and θ_r (see (2.4.38) and (2.4.39) of Chapter 2) the linearized forms of the flux equations can be written as

$$\Delta\lambda^s_{qs} = \frac{\partial\lambda^s_{qs}}{\partial i^s_{qs}}\Delta i^s_{qs} + \frac{\partial\lambda^s_{qs}}{\partial i^s_{ds}}\Delta i^s_{ds} + \frac{\partial\lambda^s_{qs}}{\partial\theta_r}\Delta\theta_r \tag{7.4.15}$$

$$\Delta\lambda^s_{ds} = \frac{\partial\lambda^s_{ds}}{\partial i^s_{qs}}\Delta i^s_{qs} + \frac{\partial\lambda^s_{ds}}{\partial i^s_{ds}}\Delta i^s_{ds} + \frac{\partial\lambda^s_{ds}}{\partial\theta_r}\Delta\theta_r \tag{7.4.16}$$

It is assumed that the flux estimation in step 1 of the algorithm is accurate and the current errors are due to the error in the predicted position. Therefore, substituting $\Delta\lambda^s_{qs} = 0$ and $\Delta\lambda^s_{ds} = 0$ into (7.4.15) and (7.4.16), the position errors can be calculated from current errors as

$$\Delta\theta^s_q = \frac{-(\frac{\partial\lambda^s_{qs}}{\partial i^s_{qs}}\Delta i^s_{qs} + \frac{\partial\lambda^s_{qs}}{\partial i^s_{ds}}\Delta i^s_{ds})}{\frac{\partial\lambda^s_{qs}}{\partial\theta_r}} \tag{7.4.17}$$

$$\Delta\theta^s_d = \frac{-(\frac{\partial\lambda^s_{ds}}{\partial i^s_{qs}}\Delta i^s_{qs} + \frac{\partial\lambda^s_{ds}}{\partial i^s_{ds}}\Delta i^s_{ds})}{\frac{\partial\lambda^s_{ds}}{\partial\theta_r}} \tag{7.4.18}$$

Substituting partial derivative terms to (7.4.17) and (7.4.18), the expressions for calculating $\Delta\theta^s_q$ and $\Delta\theta^s_d$ can be written as

$$\Delta\theta^s_q = \frac{-[L + \Delta L cos(2\hat{\theta}_{rp})]\Delta i^s_{qs} + \Delta L sin(2\hat{\theta}_{rp})\Delta i^s_{ds}}{-2\Delta L i^s_{qs} sin(2\hat{\theta}_{rp}) - 2\Delta L i^s_{ds} cos(2\hat{\theta}_{rp}) + \lambda_m cos(\hat{\theta}_{rp})} \tag{7.4.19}$$

$$\Delta\theta^s_d = \frac{\Delta L sin(2\hat{\theta}_{rp})\Delta i^s_{qs} - [L - \Delta L cos(2\hat{\theta}_{rp})]\Delta i^s_{ds}}{-2\Delta L i^s_{qs} cos(2\hat{\theta}_{rp}) + 2\Delta L i^s_{ds} sin(2\hat{\theta}_{rp}) - \lambda_m sin(\hat{\theta}_{rp})} \tag{7.4.20}$$

A single position error term ($\Delta\theta$) can be obtained by taking the average of two position errors,

$$\Delta\theta(k) = \frac{\Delta\theta^s_q(k) + \Delta\theta^s_d(k)}{2} \tag{7.4.21}$$

The corrected rotor position is obtained as

$$\hat{\theta}_r(k) = \hat{\theta}_{rp}(k) + \Delta\theta(k) \tag{7.4.22}$$

The difficulty of correcting rotor position using this method appears when calculating error terms $\Delta\theta^s_q$ and $\Delta\theta^s_d$. The denominators of (7.4.19) and (7.4.20) become very small at certain current levels and positions, which leads to give very large values for $\Delta\theta^s_q$ and $\Delta\theta^s_d$ terms. The simulation results in figure 7.29 illustrate this problem. The machine is ramped up to the rated speed using the actual rotor position for the controller and the position estimator operates in open-loop for this simulation. The load torque is increased to the machine at 2.5 s as shown in figure 7.29(b). The position estimating algorithm calculated $\Delta\theta^s_q$, $\Delta\theta^s_d$ and $\Delta\theta$ are shown in figure 7.29(c), figure 7.29(d) and figure 7.29(e) respectively. With or without load in the machine, the terms

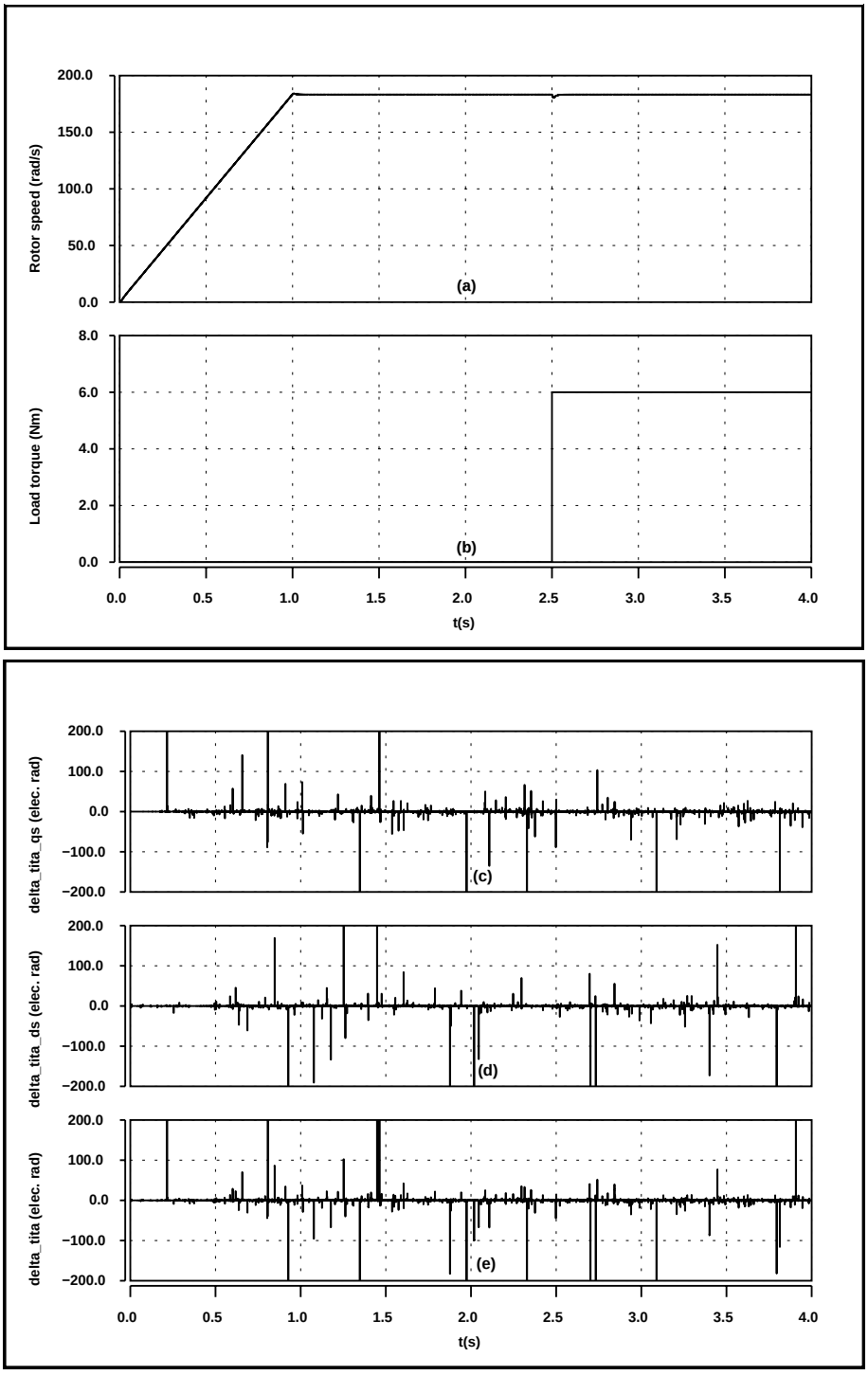

Figure 7.29: *Simulation results, when the stationary frame current errors are used for position correction in the position estimating algorithm. The machine is ramped up to the rated speed using the actual rotor position for the controller and the position estimating algorithm operates in open-loop. The load is increased to the machine at 2.5 s. (a) Rotor speed (b) Load torque (c) Position error $\Delta\theta_q^s$ (d) Position error $\Delta\theta_d^s$ (e) Average position error $\Delta\theta$.*

$\Delta\theta_q^s$ and $\Delta\theta_d^s$ become very large values in some situations, and therefore the $\Delta\theta$. Those large values are obviously wrong and the position correction becomes inaccurate at that situations.

In order to avoid the wrong position correction from very large values of $\Delta\theta$, one can add limits to the $\Delta\theta$. The rotor position variation during one sampling period depends on the speed of the rotor and it is given by $\omega_r T$, where, T is the sampling period. Therefore, the maximum value of $\Delta\theta$ can be limited to $\pm\omega_r T$. Figure 7.30 illustrates the simulation results when adding those limits to the position correction term $\Delta\theta$ at rated speed. The simulation is done with exactly the same conditions as the simulation in figure 7.29, but with limits to the $\Delta\theta$. Comparing the estimated rotor position and the actual rotor position in figure 7.30, it can be seen that even with limits to the $\Delta\theta$ the estimated rotor position does not track the actual position properly.

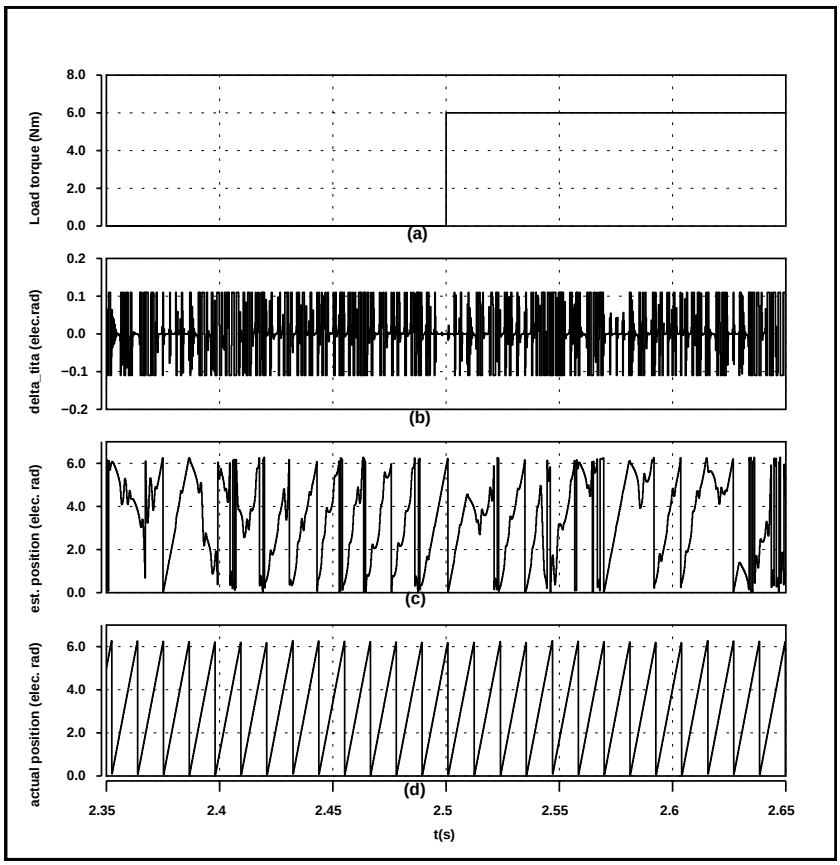

Figure 7.30: *Simulation results, with limits to the position correction term $\Delta\theta$. The stationary frame current errors are used and the simulations are at rated speed. The load is increased to the machine at 2.5 s. (a) Load torque (b) Position correction term $\Delta\theta$ (c) Estimated rotor position (d) Actual rotor position.*

Method 2:

The possibility of correcting the position using dq-transformed current errors instead of using stationary frame current errors is studied in this section.

Figure 7.31 illustrates the actual and predicted rotor reference frames. The flux in predicted rotor reference frame can be obtained as (see (2.4.7) of Chapter 2 for transformation)

$$\underline{\lambda}^{p}_{qds} = \underline{\lambda}_{abcs} e^{-j\hat{\theta}_{rp}} \tag{7.4.23}$$

Substituting $\underline{\lambda}_{abcs}$ from (2.3.11) of Chapter 2 to (7.4.23) one can obtain the flux components in predicted rotor reference frame as

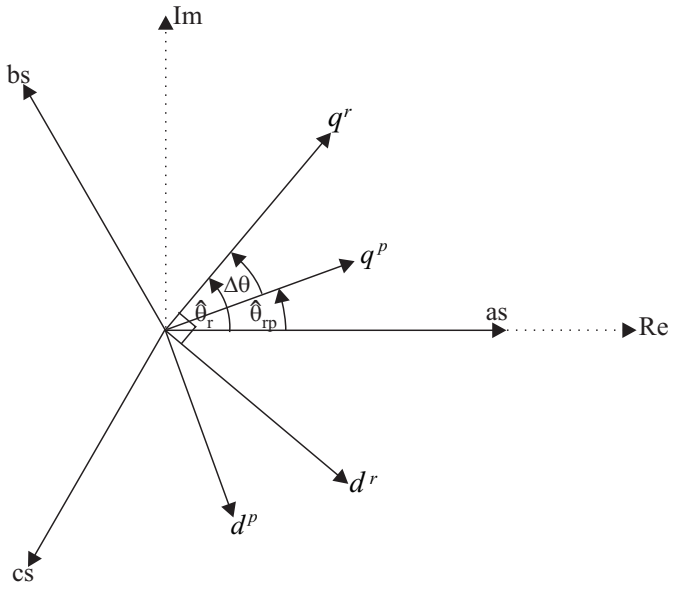

Figure 7.31: *Actual and predicted rotor reference frames.*

$$\lambda^{p}_{qs} = Li^{p}_{qs} + \Delta L[i^{p}_{qs} cos(2\Delta\theta) - i^{p}_{ds} sin(2\Delta\theta)] + \lambda_m sin(\Delta\theta) \tag{7.4.24}$$

$$\lambda^{p}_{ds} = Li^{p}_{ds} - \Delta L[i^{p}_{qs} sin(2\Delta\theta) + i^{p}_{ds} cos(2\Delta\theta)] + \lambda_m cos(\Delta\theta) \tag{7.4.25}$$

where, $\Delta\theta = \hat{\theta}_r - \hat{\theta}_{rp}$.

Assuming $\Delta\theta$ is very small and using the approximations

$$cos(2\Delta\theta) \approx 1 \tag{7.4.26}$$

$$cos(\Delta\theta) \approx 1 \tag{7.4.27}$$

$$sin(2\Delta\theta) \approx 2\Delta\theta \tag{7.4.28}$$

$$sin(\Delta\theta) \approx \Delta\theta \tag{7.4.29}$$

equations (7.4.24) and (7.4.25) can be written as

$$\lambda_{qs}^{p} = L_q i_{qs}^{p} - 2\Delta L i_{ds}^{p}(\Delta\theta) + \lambda_m(\Delta\theta) \tag{7.4.30}$$

$$\lambda_{ds}^{p} = L_d i_{ds}^{p} - 2\Delta L i_{qs}^{p}(\Delta\theta) + \lambda_m \tag{7.4.31}$$

The actual rotor frame flux equations are (see (2.4.32) and (2.4.33) of Chapter 2)

$$\lambda_{qs}^{r} = L_q i_{qs}^{r} \tag{7.4.32}$$

$$\lambda_{ds}^{r} = L_d i_{ds}^{r} + \lambda_m \tag{7.4.33}$$

Subtracting (7.4.30) and (7.4.32), and (7.4.31) and (7.4.33), one can obtain the relationships among the errors of variables due to the position deviation as

$$\Delta\lambda_q = L_q \Delta i_q - 2\Delta L i_{ds}^{p}(\Delta\theta) + \lambda_m(\Delta\theta) \tag{7.4.34}$$

$$\Delta\lambda_d = L_d \Delta i_d - 2\Delta L i_{qs}^{p}(\Delta\theta) \tag{7.4.35}$$

where, $\Delta\lambda_q = \lambda_{qs}^{p} - \lambda_{qs}^{r}$, $\Delta\lambda_d = \lambda_{ds}^{p} - \lambda_{ds}^{r}$, $\Delta i_q = i_{qs}^{p} - i_{qs}^{r}$ and $\Delta i_d = i_{ds}^{p} - i_{ds}^{r}$.

Assuming the flux estimation in step 1 of the algorithm is accurate, the position errors can be obtained substituting $\Delta\lambda_q = 0$ and $\Delta\lambda_d = 0$ into (7.4.34) and (7.4.35). They can be written as

$$\Delta\theta_q = \frac{L_q \Delta i_q}{2\Delta L i_{ds}^{p} - \lambda_m} \tag{7.4.36}$$

$$\Delta\theta_d = \frac{L_d \Delta i_d}{2\Delta L i_{qs}^{p}} \tag{7.4.37}$$

The current errors Δi_q and Δi_d in (7.4.36) and (7.4.37) can be obtained by transforming the stationary frame current errors Δi_{qs}^{s}, Δi_{ds}^{s} to the predicted rotor reference frame as

$$\Delta i_q = \Delta i_{qs}^{s} cos(\hat{\theta}_{rp}) - \Delta i_{ds}^{s} sin(\hat{\theta}_{rp}) \tag{7.4.38}$$

$$\Delta i_d = \Delta i_{qs}^{s} sin(\hat{\theta}_{rp}) + \Delta i_{ds}^{s} cos(\hat{\theta}_{rp}) \tag{7.4.39}$$

and i_{qs}^{p}, i_{ds}^{p} as

$$i_{qs}^{p} = i_{qs}^{s} cos(\hat{\theta}_{rp}) - i_{ds}^{s} sin(\hat{\theta}_{rp}) \tag{7.4.40}$$

$$i_{ds}^{p} = i_{qs}^{s} sin(\hat{\theta}_{rp}) + i_{ds}^{s} cos(\hat{\theta}_{rp}) \tag{7.4.41}$$

Again, two position errors ($\Delta\theta_q$ and $\Delta\theta_d$) exist and the position correction term $\Delta\theta$ may be calculated averaging these two terms as

$$\Delta\theta(k) = \frac{\Delta\theta_q(k) + \Delta\theta_d(k)}{2} \tag{7.4.42}$$

and the corrected rotor position is obtained as

$$\hat{\theta}_r(k) = \hat{\theta}_{rp}(k) + \Delta\theta(k) \tag{7.4.43}$$

The difficulty appears again when calculating $\Delta\theta_d$. For small values of i_{qs}^p, $\Delta\theta_d$ can become very large leading to wrong position correction. The simulation results in figure 7.32 illustrate this problem. The machine is ramped up to the rated speed using the actual rotor position for the controller and the position estimator operates in open-loop. The load torque is increased to the machine at 2.5 s as shown in figure 7.32(b). The position estimating algorithm calculated $\Delta\theta_q$, $\Delta\theta_d$ and $\Delta\theta$ are shown in figure 7.32(c), figure 7.32(d) and figure 7.32(e) respectively. Under no-load, the term $\Delta\theta_d$ becomes a very large value, and therefore, the $\Delta\theta$. Even though at high loads the problem does not appear, when the machine is operated under low loads the position correction becomes inaccurate leading to fail the position estimation.

As it is described when stationary frame current errors are used to correct the position, one can limit the $\Delta\theta$ in order to avoid wrong position correction from very large values of $\Delta\theta$. The simulation results with those limits to the $\Delta\theta$ are shown in figure 7.33. Compared to the method 1, an improvement in estimated rotor position can be seen in the simulation results shown in figure 7.33. However, at no-load the rotor position does not still track the actual rotor position accurately. It was found that during closed loop control (i.e. when estimated rotor position is used in the controller) there were severe instability problems in the system under no-load or light loads with this estimated position.

For non-salient pole machine

Since $\Delta L = 0$ for non-salient pole machines (SPMSMs), expressions (7.4.34) and (7.4.35) becomes

$$\Delta\lambda_q = L_q\Delta i_q + \lambda_m(\Delta\theta) \tag{7.4.44}$$

$$\Delta\lambda_d = L_d\Delta i_d \tag{7.4.45}$$

From (7.4.44) and (7.4.45), it can be seen that the position error term appears only in q-axis equation (7.4.44). This is different from previously discussed salient pole machine (IPMSM) case, where the position error appears in both q and d equations.

Assuming the flux estimation is accurate in step 1 of the algorithm a single position error correction term can be obtained substituting $\Delta\lambda_q = 0$ into (7.4.44) as

$$\Delta\theta = \frac{-L_q\Delta i_q}{\lambda_m} \tag{7.4.46}$$

Unlike salient pole machines, the denominator of (7.4.46) does not include any time varying variable. Therefore, position correction of non-salient pole machines does not face difficulties as it is seen for salient pole machines.

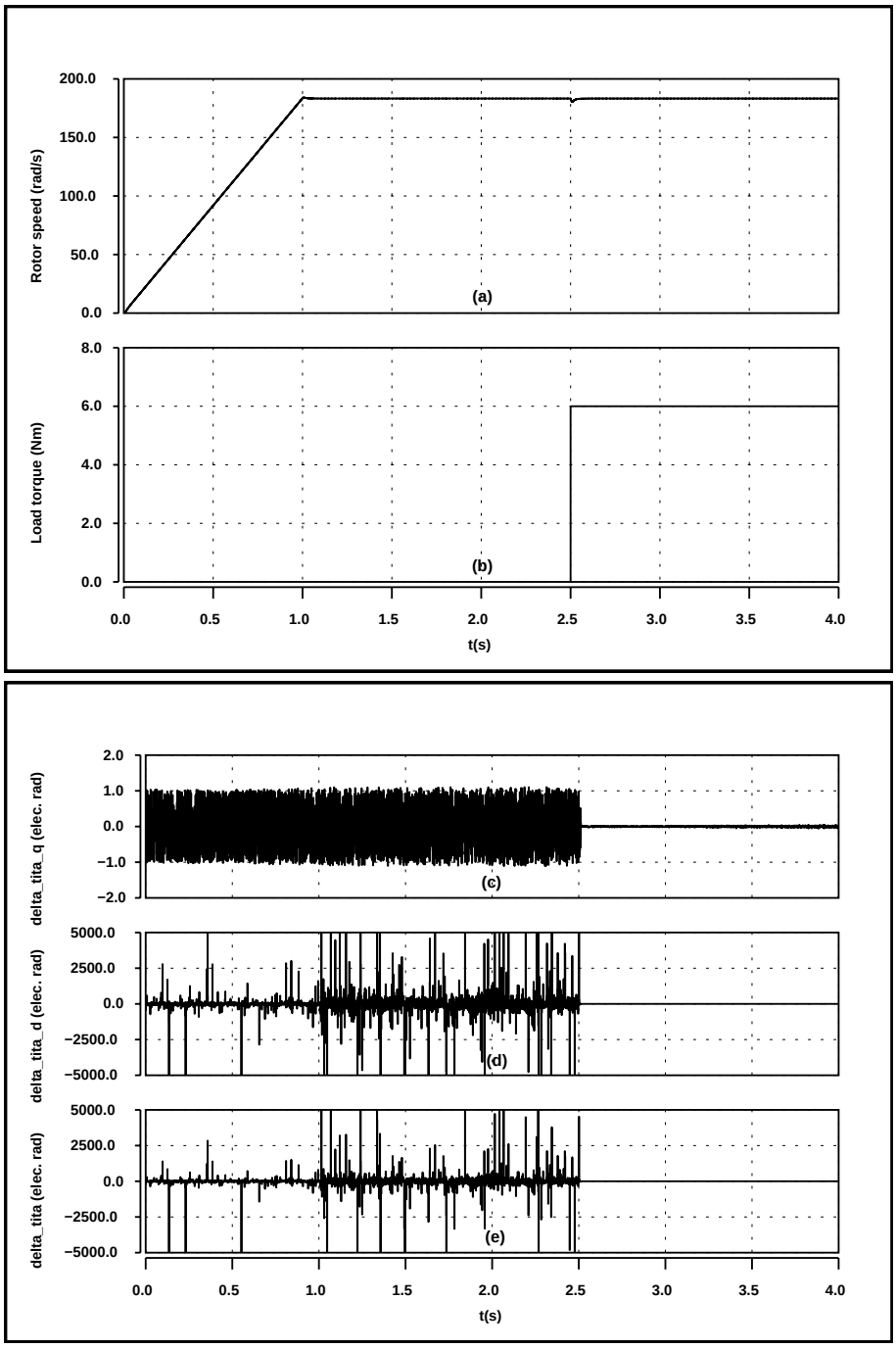

Figure 7.32: *Simulation results, when the d,q transformed current errors are used for position correction in the position estimating algorithm. The machine is ramped up to the rated speed using the actual rotor position for the controller and the position estimating algorithm operates in open-loop. The load is increased to the machine at 2.5 s. (a) Rotor speed (b) Load torque (c) Position error $\Delta\theta_q$ (d) Position error $\Delta\theta_d$ (e) Average position error $\Delta\theta$.*

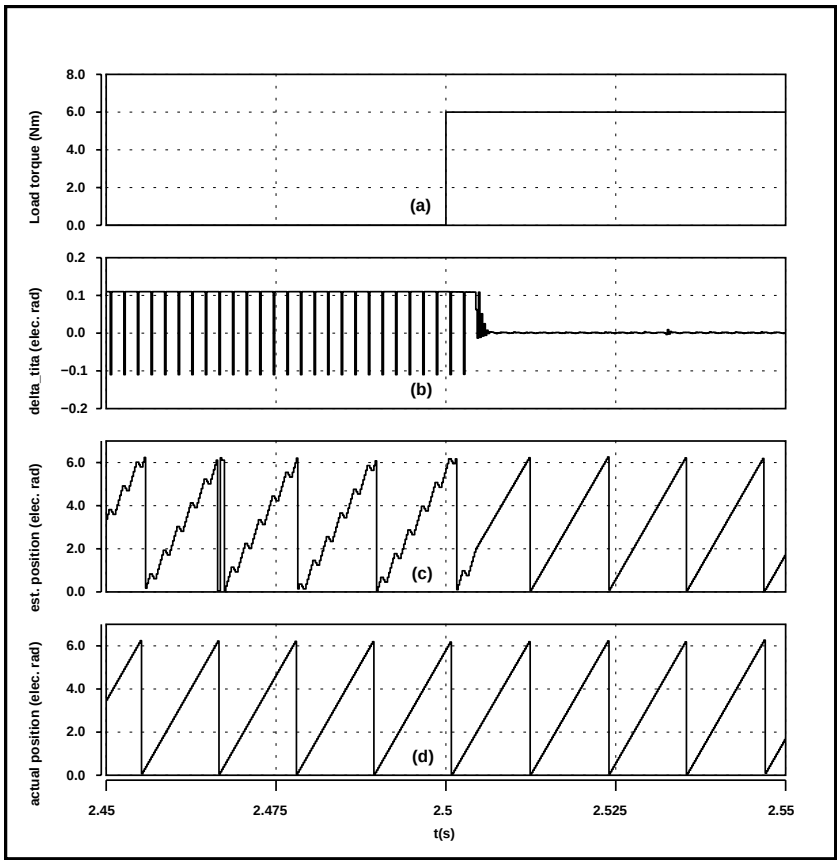

Figure 7.33: *Simulation results, with limits to the position correction term $\Delta\theta$. The d,q transformed current errors are used and the simulations are at rated speed. The load is increased to the machine at 2.5 s. (a) Load torque (b) Position correction term $\Delta\theta$ (c) Estimated rotor position (d) Actual rotor position.*

7.4.3 Simulation of the sensorless drive system

The IPMSM used for the analysis in this thesis has a lower saliency ratio ($\frac{L_q}{L_d} = 1.37$). Because of this reason and the difficulties for position correction in the position estimation algorithm for an IPMSM (Salient pole machine)using current errors for all operating conditions, the position estimation algorithm was investigated neglecting the saliency in the machine. That is,

1. When estimating the currents in step 2 of the algorithm (see figure 7.27), it is assumed that $\Delta L = \frac{L_q - L_d}{2} \approx 0$ in (7.4.3) and (7.4.4).

2. In step 3, the position is corrected using (7.4.46).

3. In step 4, when updating the flux linkages, it is assumed that $\Delta L = \frac{L_q - L_d}{2} \approx 0$ in (7.4.7) and (7.4.8).

The purpose of the simulations is to see the stability of the system and how much error exist in the position estimation when the small saliency exist in the machine is neglected during position estimation.

The sensorless drive system shown in figure 7.26 was simulated with all control functions, which use estimated rotor position and velocity. The estimated speed was filtered using 100 Hz low-pass filter and the initial simulations showed that for satisfactory operation of the drive with position and speed estimator the speed controller bandwidth should be reduced to about 15 Hz (This was about 44 Hz when actual position was used). The bandwidth of the current controllers remained unchanged. In all simulations the machine was started from a known initial position and the flux was initialized for the integration in step 1 of the position estimation algorithm according to that initial position.

Figure 7.34 shows simulation results when adding a 50% of rated load step to the drive at 50% rated speed. It can be seen that the stable operation of the drive with this load step. However, the position error increases when the machine is operated under load.

When adding the load step to the drive as shown in figure 7.34, variation of some variables related to the position estimation algorithm is shown in figure 7.35.

In figure 7.35, the q^s-, d^s-axis flux errors are calculated as

$$\Delta\lambda^s_{qs} = \lambda^s_{qs(actual)} - \hat{\lambda}^s_{qs} \tag{7.4.47}$$

$$\Delta\lambda^s_{ds} = \lambda^s_{ds(actual)} - \hat{\lambda}^s_{ds} \tag{7.4.48}$$

where, $\lambda^s_{qs(actual)}$, $\lambda^s_{ds(actual)}$ are actual flux from the machine and $\hat{\lambda}^s_{qs}$, $\hat{\lambda}^s_{ds}$ are estimated flux in step 1 of the algorithm. It should be mentioned that flux errors $\Delta\lambda^s_{qs}$ and $\Delta\lambda^s_{ds}$ are not calculated in the position estimation algorithm and in figure 7.35 they are shown for analysis purpose.

It can be seen from figure 7.35(a) and figure 7.35(b) the flux errors increase and they remain unchanged when the load is increased to the machine. The same for the

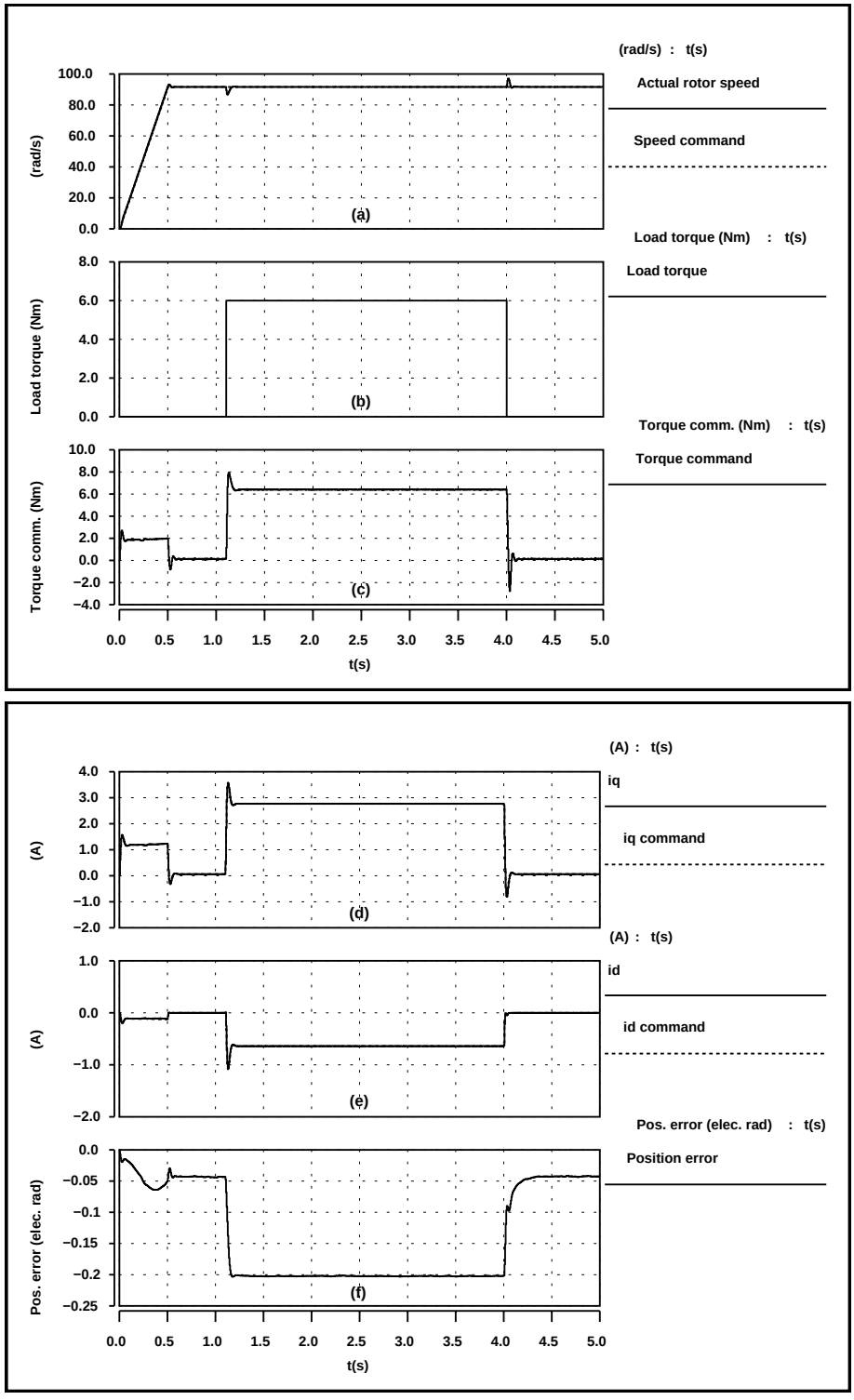

Figure 7.34: *The simulation results showing the performance of the sensorless drive, when adding a 50% load step at 50% rated speed. (a) Actual and commanded rotor speed (b) Applied load torque to the machine (c) Torque command (T_e^*) in the controller (d) Actual and commanded q-axis current in the controller (i_{qs}^r and i_{qs}^{r*}) (e) Actual and commanded d-axis current in the controller (i_{ds}^r and i_{ds}^{r*}) (f) Position error($\theta_r - \hat{\theta}_r$).*

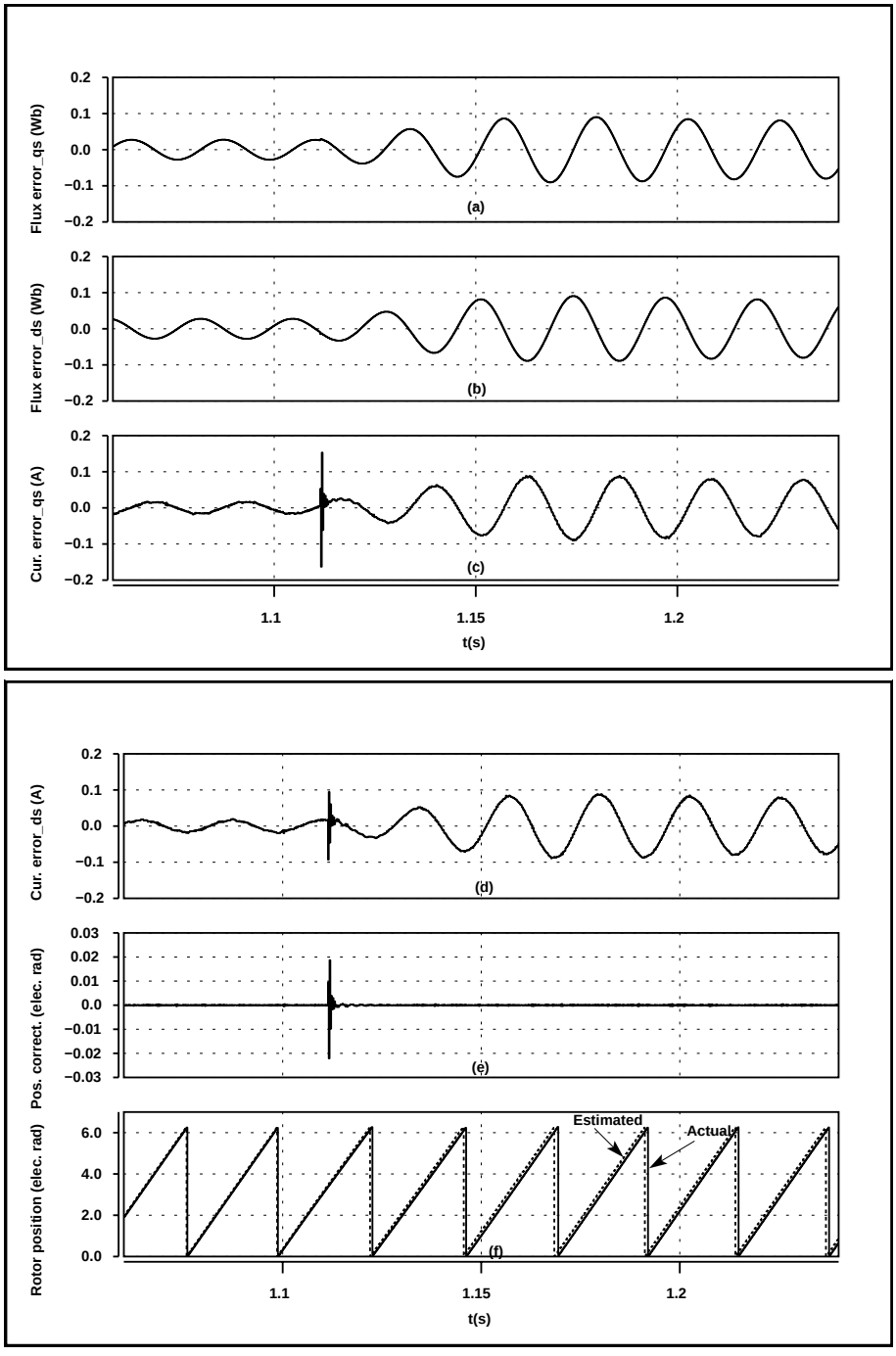

Figure 7.35: *When adding a load step to the sensorless drive as shown in the simulations in figure 7.34, the variation of variables related to the position estimation algorithm. (a) q^s-axis flux error ($\lambda^s_{qs(actual)} - \hat{\lambda}^s_{qs}$) (b) d^s-axis flux error ($\lambda^s_{ds(actual)} - \hat{\lambda}^s_{ds}$) (c) q^s-axis current error (Δi^s_{qs}) (d) d^s-axis current error (Δi^s_{ds}) (e) Position correction ($\Delta\theta$) (f) Actual and estimated rotor position.*

current errors. However, it can be seen that the position correction term does not try to correct the rotor position, even though there is a current error. Finally, there is an error in the estimated rotor position when the machine is loaded.

The reason for the position error when the load is increased is due to the assumptions made in the position estimation algorithm. The saliency is neglected when the currents are estimated in step 2 of the algorithm and when updating the flux linkages in step 4 of the algorithm. This makes errors in the current estimation and the updating of flux linkages. Moreover, in step 3, neglecting the saliency only a single position correction term given in (7.4.46) is used, which is also not accurate. The combination of these facts makes increased flux errors, increased current errors and inaccurate position correction when the load is increased in the machine as shown in figure 7.35.

Figure 7.36 shows the position errors with different load steps to the machine at 50% of rated speed. It can be seen that the position error is dependent on the load of the machine and when the load is increased the position error is also increased.

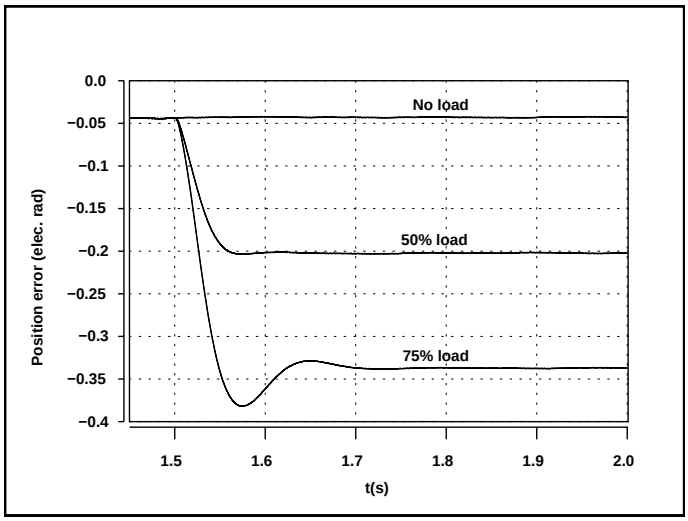

Figure 7.36: *Position error when the load is changed at 50% of rated speed.*

The response of the drive system when adding a 100% load step at 50% of rated speed is shown in figure 7.37. Due to the large position error with this load, the speed controller has to command a large torque to the machine, so that the machine can overcome the load. It can be seen that the torque command from the speed controller reaches to the limit, i.e. speed controller saturates, under this condition and the system becomes unstable. It should also be noted that the voltage command from the current controller does not go to the limit, i.e. the current controller does not saturate under this condition. Under the same conditions, another simulation was done increasing the torque limit of the speed controller to 150% of the nominal value. The results are shown in figure 7.38. The increased torque limit does not solve the problem. When the torque limit is increased the position error is increased to a value higher than the

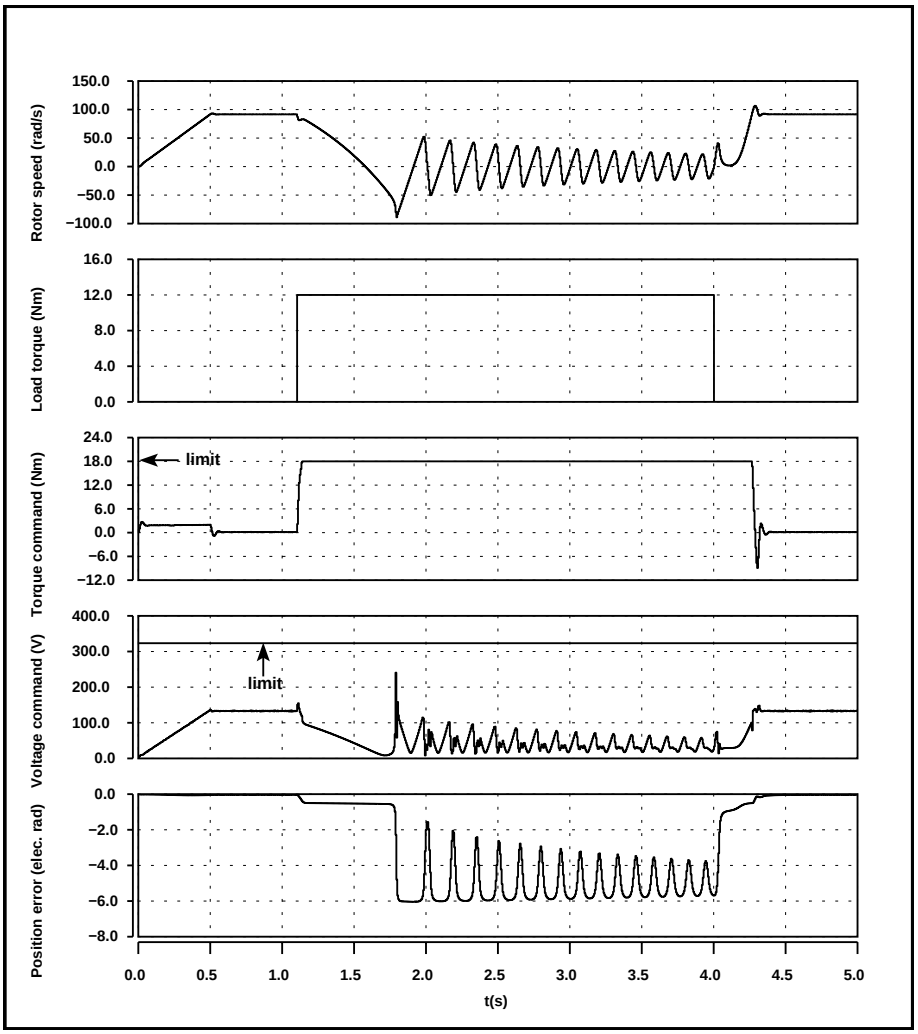

Figure 7.37: *Simulated variables, when adding a 100% load step to the sensorless drive at 50% of rated speed.*

value with nominal torque limit, as soon as the load step is added to the drive (see the position error in figure 7.38 as soon as the load step is added to the drive). This in turn requires higher torque command from the controller, which causes to saturate the speed controller again.

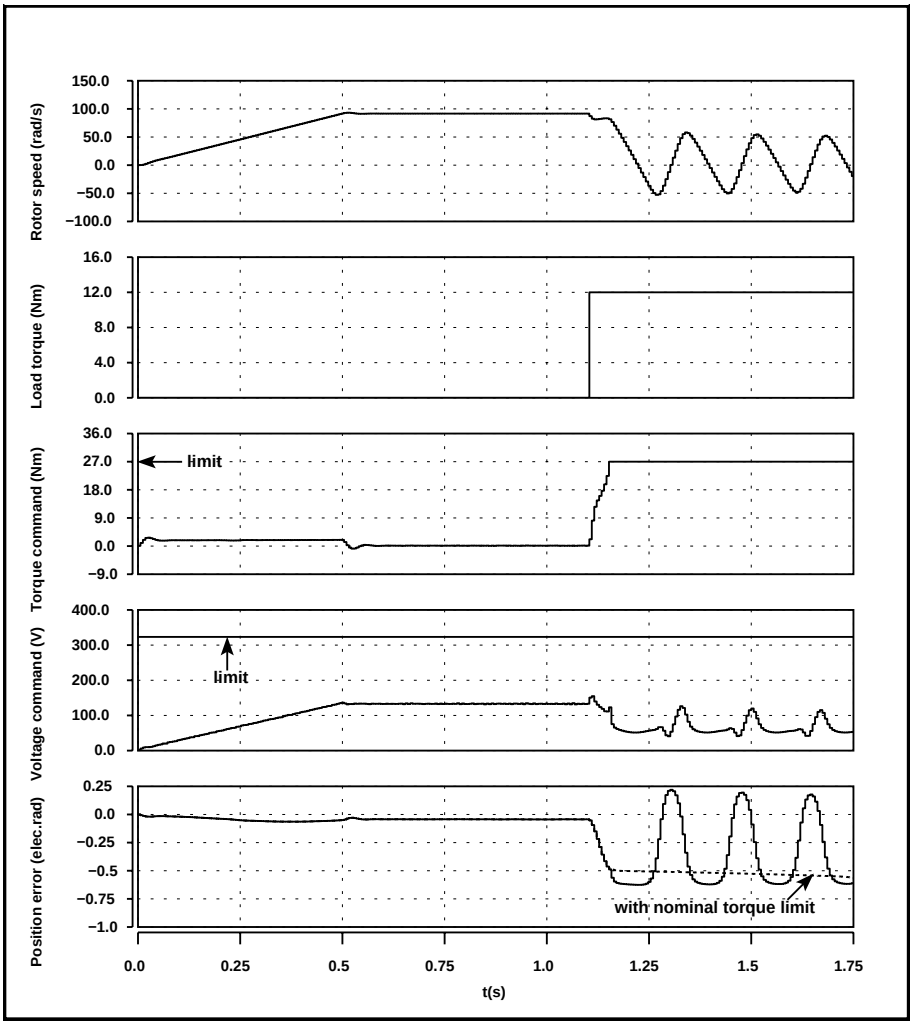

Figure 7.38: *Simulated variables, when adding a 100% load step to the sensorless drive at 50% of rated speed, increasing the torque limit of the speed controller to 150% of nominal value.*

Figure 7.39 shows the performance of the sensorless drive system at low speed (5% of rated speed). It seems the stable operation of the drive is possible under this speed with a load step, even though the position error increases under load.

The performance of the sensorless drive, when ramping up to the rated speed with quadratic load is shown in figure 7.40. Due to the increased position error with load, the speed controller has to command a much higher torque to the machine and it saturates at a certain speed. It should also be noted that the current controller does not saturate under this condition. The stable operation of the drive is still possible, however, finally,

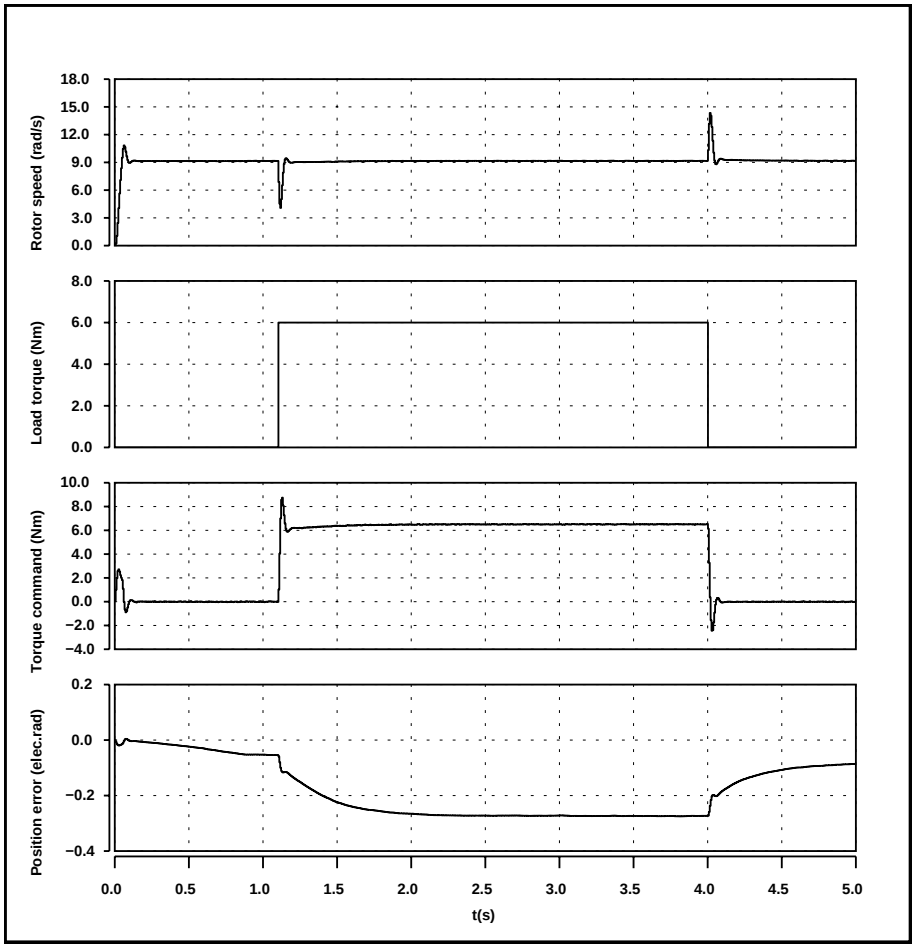

Figure 7.39: *Simulated variables, when adding a 50% load step at 5% of rated speed (4.4 Hz).*

there is an speed error in the system as it can be seen from figure 7.40(a). In order to see whether the speed error can be eliminated increasing the torque limit of the speed controller, another simulation was done increasing the torque limit of the speed controller to 24 Nm. The results are shown in figure 7.41. With increased torque limit the position error is increased again as it can be seen from figure 7.41(e), which in turn requires high torque command from the controller. Finally, the speed controller saturates again without solving the problem.

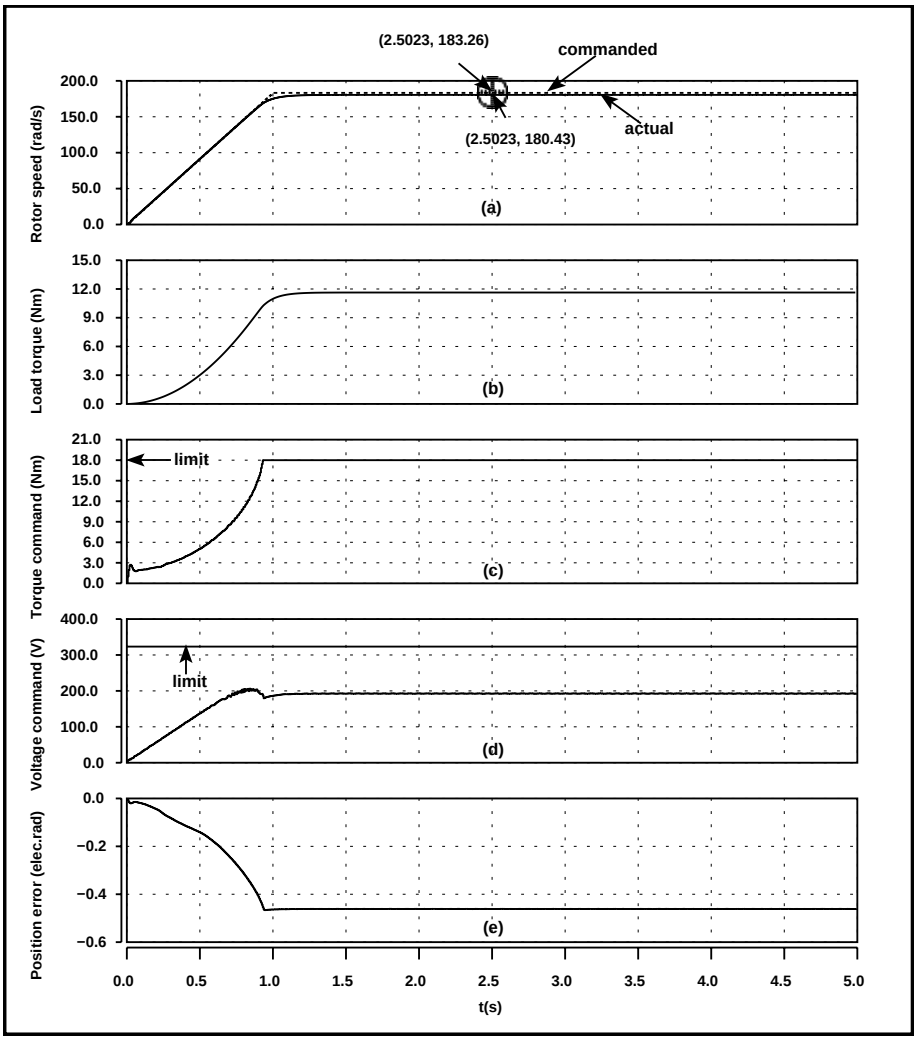

Figure 7.40: *Simulation results, when ramping up the sensorless drive to the rated speed with quadratic load. (a) Commanded and actual rotor speed (b) Applied load torque to the machine (c) Torque command (T_e^*) from the speed controller (d) Commanded magnitude of the voltage from the current controller (e) Position error.*

So far in the simulations the position estimator was started from a known initial rotor position. The flux was initialized for the integration in step 1 of the position estimation algorithm according to that known initial rotor position. The simulation

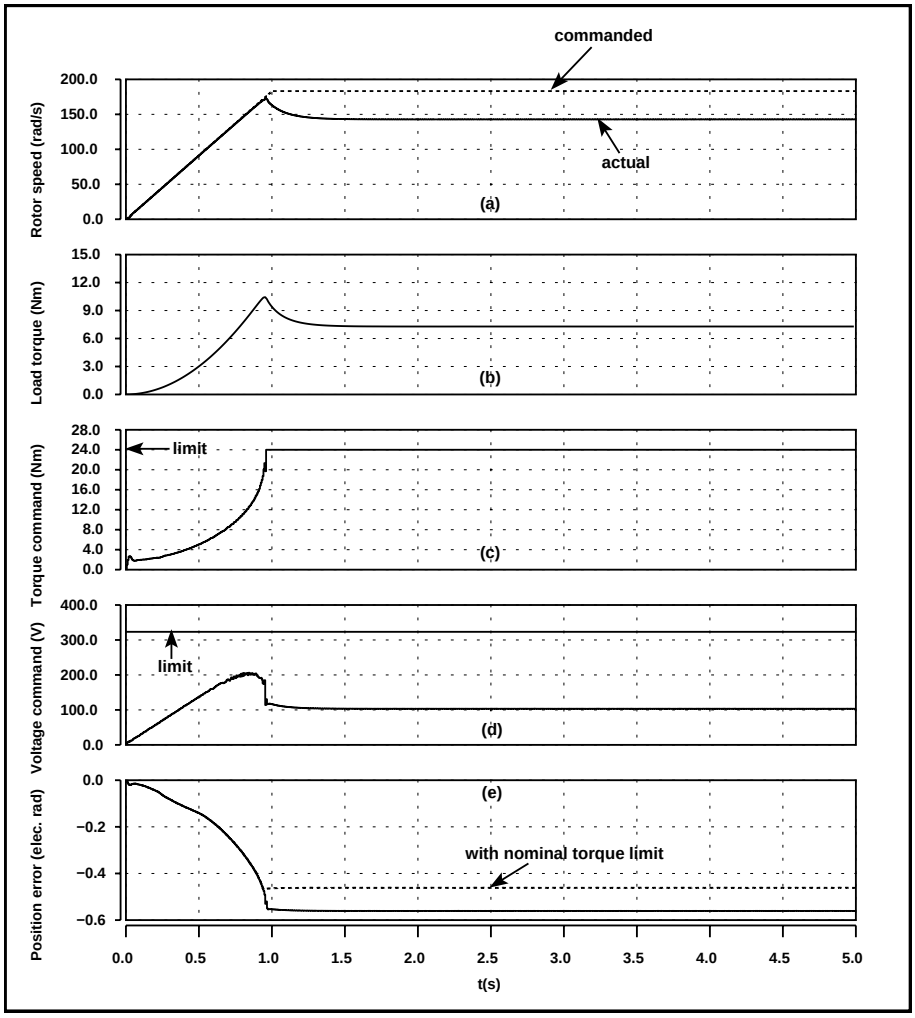

Figure 7.41: *Simulation results, when ramping up the sensorless drive to the rated speed with quadratic load, increasing the torque limit of the speed controller to 24 Nm. (a) Commanded and actual rotor speed (b) Applied load torque to the machine (c) Torque command (T_e^*) from the speed controller (d) Commanded magnitude of the voltage from the current controller (e) Position error.*

results in figure 7.42 show that the performance of the sensorless drive when there is a mismatch between the actual initial rotor position and the estimator started position. The estimator was started from 0 elec. rad position and the actual initial rotor position was set to $\frac{\pi}{2}$ elec. rad as shown in figure 7.42(c). The sensorless drive was ramped up to the 50% of rated speed and, as it can be seen from figure 7.42(b) the drive becomes unstable under this condition. It is evident that the position estimation algorithm requires actual initial rotor position in order to estimate the position accurately.

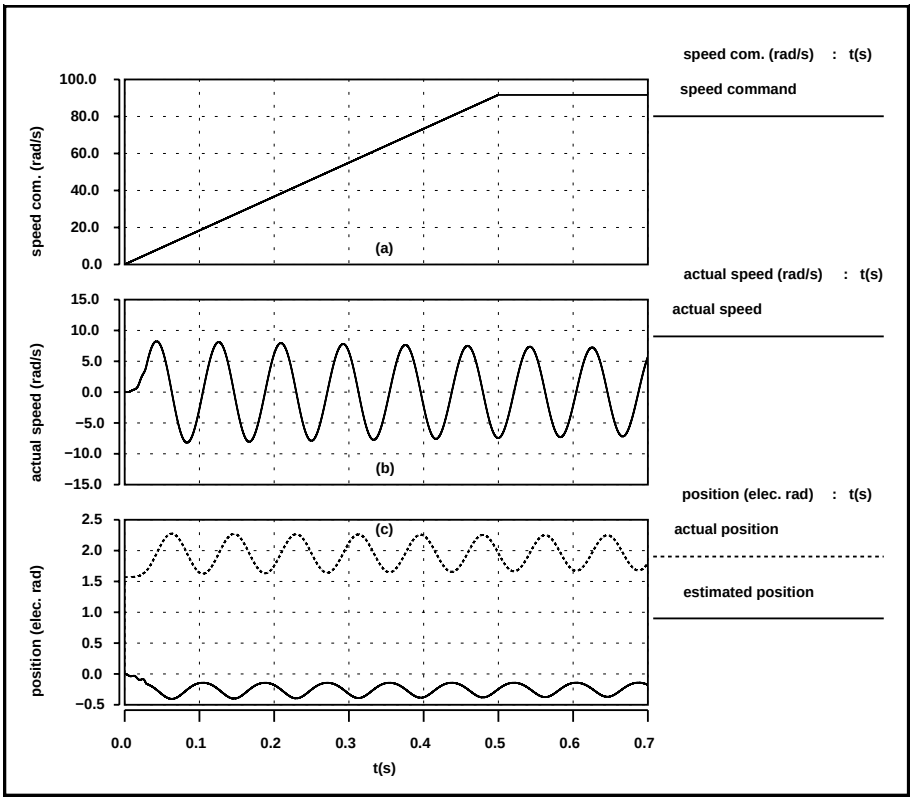

Figure 7.42: *Simulation results showing the instability in the sensorless drive when there is a mismatch between the actual initial rotor position and the estimator started position.*

7.4.4 V/f control and sensorless field-oriented control -*A performance comparison*

It is important to point out some differences seen in the performance of the V/f controlled drive discussed in Chapter 5 and the investigated sensorless field-oriented controlled drive in this chapter.

Figure 7.43 shows the simulated speed responses from the both drive systems when adding a 50% load step at 50% rated speed. It can be seen that the investigated sensorless field-oriented controlled drive has fast dynamic response compared to the

V/f controlled drive.

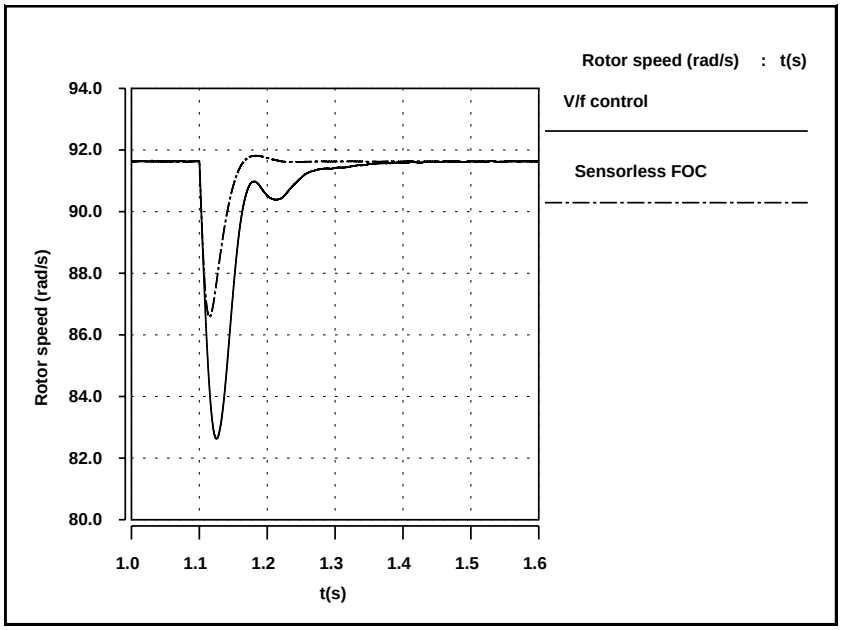

Figure 7.43: *Simulated speed responses from the V/f controlled drive system and the investigated sensorless field-oriented controlled drive system, when 50% load step is added at 50% rated speed.*

From figure 5.12 and figure 7.39, it can be seen that the stable operation of both drives at 5% rated speed with 50% load step. However, comparing figure 5.9, figure 5.10 with figure 7.37, one can see that the stable operation of the sensorless field-oriented controlled drive system is not possible at 50% rated speed with 100% load step. Another drawback in sensorless field-oriented controlled drive system can be seen when comparing figure 5.14 with figure 7.40. With quadratic load a speed error exists in the sensorless field-oriented controlled drive and that situation is not seen in V/f controlled drive.

With this comparison it can be seen that even though the dynamic response is slower in the V/f controlled drive system, from the overall performance point of view, it is better compared to the investigated sensorless field-oriented controlled drive system in this chapter.

7.5 Summary

The complete control structure of the rotor permanent-magnet flux oriented controlled PMSM drive system has been described in this chapter. In order to design the current and speed controller for the digital system the Z-domain root locus method can be used. The design of the controllers has been validated experimentally and the performance of the complete drive system with position sensor has been presented.

For position sensorless operation of the drive system a rotor position estimation technique has also been investigated. The investigated rotor position estimation technique uses predictor-corrector method, which uses current errors to correct the predicted rotor position. The investigation has been revealed that the correction of the predicted rotor position is difficult for salient pole machines using the current errors in the stationary reference frame. Using the predicted d-q reference frame current errors the position correction can be improved under high loads, however, at light loads there are still problems. For non-salient pole machines, position correction using current errors in the predicted d-q reference frame seems very convenient.

The difficulty of position correction in the position estimation algorithm for all operating conditions and the relatively low saliency exists in the IPMSM used for the analysis have lead to make assumptions to the position estimation algorithm. The simulation results have shown that the stable sensorless operation of the drive is possible, however, the existing load dependent position error has degraded the performance of the drive. In order to improve the performance of the drive, more investigations are still required for accurate rotor position estimation of the IPMSM.

Finally, the comparison has shown that the V/f controlled drive system proposed in Chapter 5 has better overall performance compared to the sensorless field-oriented controlled drive system investigated in this chapter.

Bibliography

[1] R.E. Betz, *Synchronous Reluctance and Brushless Doubly Fed Reluctance Machines*, Course Notes at Institute of Energy Technology, Aalborg University, Denmark, 1998.

[2] Dal Y. Ohm and Richard J. Oleksuk, *On Practical Digital Current Regulator Design for PM Synchronous Motor Drives*, Proceedings of APEC'98, Vol. 1, pp. 56-63, 1998.

[3] Shigeo Morimoto, Masayuki Sanada and Yoji Takeda, *Wide-Speed Operation of Interior Permanent Magnet Synchronous Motors with High-performance Current Regulator*, IEEE Transactions on Industry Applications, Vol. 30, No.4, pp. 920-926, July/August 1994.

[4] R.D. Lorenz, *Dynamics of Controlled Systems*, Course notes, The College of Engineering, University of Wisconsin-Madison, USA, 1998.

[5] Gene F. Franklin, J. David Powell and Michael L. Workman, *Digital Control of Dynamic Systems*, Second Edition, Addison-Wesley Publishing Company, Inc., 1990.

[6] Gene F. Franklin, J. David Powell and Abbas Emami-Naeini, *Feedback Control of Dynamic Systems*, Third Edition, Addison-Wesley Publishing Company, Inc., 1994.

[7] N. Mohan, *Designing Feedback Controllers for Motor Drives*, Chapter 8 in Electric Drives: An Integrative Approach, Published by MNPERE, 2001.

[8] D. Jouve, J.P. Rognon and D. Roye, *Effective Current and Speed Controllers for Permanent Magnet Machines: A Survey*, Proceedings of APEC'90, pp. 384 -393, 1990.

[9] Karl J. Åstrom and Tore Hagglund, *PID Controllers: Theory, Design, and Tuning*, Second edition, Instrument Society of America, 1995.

[10] Youbin Peng, Damir Vrancic and Raymond Hanus, *Anti-Windup, Bumpless, and Conditioned Transfer Techniques for PID Controllers*, IEEE Control Systems Magazine, Vol. 16, Issue 4, pp. 48-57, August 1996.

[11] Edward P. Cunningham, *Recursive Filter Design*, Chapter 4 in Digital Filtering: An Introduction, Houghton Mifflin Company, 1992.

[12] Nesimi Ertugrul and P.P. Acarnley, *A New Algorithm for Sensorless Operation of Permanent Magnet Motors*, IEEE Transactions on Industry Applications, Vol. 30, No.1, pp. 126-133, January-February 1994.

[13] Chris French and Paul Acarnley, *Control of Permanent Magnet Motor Drives Using a New Position Estimation Technique*, IEEE Transactions on Industry Applications, Vol. 32, No.5, pp. 1089-1097, September-Ocober 1996.

[14] Stefan Ostlund and Michael Brokemper, *Sensorless Rotor-Position Detection from Zero to Rated Speed for an Integrated PM Synchronous Motor Drive*, IEEE Transactions on Industry Applications, Vol. 32, No.5, pp. 1158-1165, September-Ocober 1996.

Part IV

Conclusions

Chapter 8

Conclusion

Mainly, due to the attractive efficiency characteristics, the PMSMs are good candidate for pumps and fans drives. This thesis has been focused on control of PMSMs for such drives.

In order to provide synchronization between machine's excitation frequency and rotor frequency, the rotor position information is essential during PMSM control. The direct approach to obtain the rotor position information is a rotor mounted angular position sensor. Because of the cost and the reduced reliability, a rotor mounted angular position sensor is not desirable in pumps and fans drives and sensorless control is needed. Two sensorless control approaches, i.e. sensorless V/f control approach and sensorless field-oriented control approach, have been investigated in this thesis. Moreover, the preliminary aspects, such as mathematical models, control properties of PMSMs, have also been discussed.

Based on the results presented in the thesis, the main conclusions can be summarized as below.

Mathematical models and control properties

- For an IPMSM, the rotor d,q model is the most convenient, since the position dependent inductances disappear in that model. In addition to the permanent-magnet produced torque, the reluctance torque also exist in IPMSMs, which makes important differences over SPMSMs.

- The comparison study made for the different control properties of the tested IPMSM has revealed that the constant stator flux linkage control has more advantages compared to the others, i.e. constant torque angle control, maximum torque per ampere control and unity power factor control.

Sensorless V/f control

- The design of sensorless V/f controlled drive has been started by investigating the stability characteristics of PMSMs under open-loop V/f control. The analysis made in Chapter 3 has revealed that the machine becomes unstable after exceeding a certain applied frequency under open-loop V/f control. Machine under no-load and under load with different control strategies have been investigated, and in any case the machine became unstable after the applied frequency exceeds about 15 Hz. Under open-loop V/f control, there is no synchronization between the machine's excitation frequency and the rotor frequency, and therefore, this instability behaviour can be expected.

- The stabilization of open-loop V/f controlled PMSMs can be achieved by modulating the applied frequency using input power perturbations or DC-link current perturbations. The simplified small signal dynamics model derived in Chapter 4 is the key to understand these stabilizing techniques. Moreover, the simplified small signal dynamics model has also shown how to select the gains for these frequency modulated stabilizing loops. To implement these stabilizing loops no rotor position sensor is required. The stabilizing loops in the system can also be seen as the signals, which provide synchronization between the machine's excitation frequency and the rotor frequency.

- In order to improve the performance, especially at low speeds, the compensation of stator resistance voltage drop is important in voltage magnitude of V/f controlled drive. It has been shown that measuring stator phase currents the voltage magnitude can be calculated with vector compensation of stator resistance voltage drop.

- With the proposed voltage control method to the drive, the power calculation was very convenient and the power perturbation stabilizing loop was the best solution to stabilize the drive. No rotor position sensor has been used to implement the complete drive system and the performance analysis in Chapter 5 have shown that the drive is suitable for pumps and fans applications.

Sensorless field-oriented control

- Unlike V/f control, the field-oriented control incorporates an inner torque controller and an outer speed controller in the control system. The torque control is achieved by controlling the currents in rotor d,q reference frame. The control system requires rotor position feedback in order to perform the self-synchronization function continuously. The basic PI controllers are sufficient for current and speed control in the drive system.

- In order to achieve sensorless operation of the drive, the position and velocity estimation is required and it is important to consider the type of the machine (SPMSM or IPMSM) and the application of the drive when investigating a rotor position and velocity estimating technique.

- The investigated rotor position estimating technique is predictor-corrector based, which uses current errors to correct the predicted rotor position. It has shown that, in theory, the expressions exist for both SPMSMs and IPMSMs to correct the predicted rotor position using current errors. However, the investigations have revealed that, for IPMSMs, there are implementation difficulties to correct the predicted rotor position using those expressions for all operating conditions. It has also revealed that, for SPMSMs, the best solution is the use of d,q transformed current errors to correct the predicted rotor position.

- The difficulty of correcting the predicted rotor position for an IPMSM for all operating conditions and the relatively low saliency exist in the machine used for investigation have lead to make some assumptions to the position estimating algorithm. The simulations have shown that the stable sensorless operation of the drive is possible, however, the performance of the drive system is greatly affected by the load dependent position error in the position estimation algorithm with those assumptions.

- It is believed that unlike SPMSMs simple model based approach is difficult for position estimation for an IPMSM. The use of saliency in the IPMSM to estimate the rotor position, e.g. high frequency signal injection, may be a better solution for an IPMSM.

Comparison of control methods

- In order to implement the sensorless V/f control the voltage magnitude calculation and the stabilizing loop is required (see figure 5.5 and figure 5.4 in Chapter 5). For sensorless field-oriented control, speed and current controllers are needed with position and speed estimation algorithm (see figure 7.26, figure 7.1 and figure 7.27 in Chapter 7). The overall calculation power required to implement the sensorless V/f controller is less compared to the sensorless field-oriented controller.

- The performance comparison has shown that the overall performance of the sensorless V/f controlled drive is better compared to the investigated sensorless field-oriented controlled drive.

- Considering the implementation simplicity and the overall performance of the drive, it can be concluded that the proposed V/f control method is the best

solution for pumps and fans applications between the two control methods investigated in the thesis.

8.1 Contributions in the thesis

The main contributions in the thesis can be summarized as below.

- The model for conventional salient-pole synchronous machine was widely discussed in the literature, however, for an IPMSM it was not directly derived. The derivation of the IPMSM model and the comparison of control properties are new contributions in the thesis.
- The detailed analysis provided to understand the stability and stabilization of open-loopV/f controlled PMSM drives are also new contributions in the thesis.
- The sensorless V/f controlled drive system developed in this work is considered as a new contribution to PMSM drive control strategies.
- The analysis made for the position correction methods for the position and speed estimation algorithm used in field-oriented controlled drive is a new contribution. The position correction in this position estimation algorithm was not clearly analyzed for SPMSMs and IPMSMs before.
- The previous work were mainly concentrated on sensorless field-oriented control of PMSMs and there were no attempts to compare V/f control with sensorless field-oriented control. The attempts made in the thesis to compare these two control strategies are novel.

8.2 Future work

Even though several topics have been addressed in the thesis, there are still some topics, which are interesting for future research. Some of those topics are summarized below.

- The variation of machine parameters was not considered for the developed control algorithm for V/f control. The machine parameter variation, how much effect give to the performance of this controller should be investigated.
- The control algorithm of V/f controlled drive system was implemented in a high performance DSP. The implementation of this algorithm in a low-cost microcontroller is beneficial for pumps and fans drives and the possibility of it should be investigated.

- The drives (both V/f controlled drive and the field-oriented controlled drive discussed in the thesis) are started after aligning the rotor to a known position by applying a DC voltage to the machine. The problem of this method is the movement of the rotor during aligning. In order to avoid this problem the investigations are required for direct detection of the initial rotor position.

- A study is needed for the effect of the machine parameter variation to the field-oriented controller discussed in the thesis.

- The rotor position estimation using the saliency in the IPMSM, e.g. high frequency signal injection method, may be a better solution compared to the method investigated in this thesis for sensorless operation of the field-oriented controlled drive. Therefore, an investigation of that method is needed for the field-oriented controlled drive system.

- The investigation of the flux-weakening regime operation of both V/f controlled and field-oriented controlled drive systems discussed in the thesis is also an interesting future research topic.

- The thesis only addressed the V/f control and the field-oriented control of PMSMs. The direct torque control is another control approach for PMSMs. The study of advantages and the disadvantages in the sensorless direct torque control approach compared to the two control approaches discussed in the thesis is another future research topic.

Part V

Appendices

Appendix A

Data for the IPMSM

Type	-	YASKAWA SSR1-42P2AFNL
Number of poles (n)	-	6
Rated power	-	2.2 kW
Rated speed	-	1750 rpm
Rated frequency	-	87.5 Hz
Rated torque	-	12 Nm
Rated phase to phase voltage	-	380 V(rms)
Rated phase current	-	4.1 A(rms)
Stator resistance per phase (r_s)	-	3.3 Ω
d-axis inductance (L_d)	-	41.59 mH
q-axis inductance (L_q)	-	57.06 mH
Rotor permanent-magnet flux (λ_m)	-	0.4832 V s rad^{-1}
Inertia of the rotating system (J)	-	10.07×10^{-3} kg m^2
Viscous friction coefficient (B_m)	-	20.44×10^{-4} Nm s rad^{-1}

Appendix B

Various Relationship Derivations Related to Chapter 3 and Chapter 4

B.1 The derivation of the transfer function for $\frac{\Delta T_e}{\Delta \delta}$ under open-loop V/f control of PMSMs

Under open-loop V/f control the linearized machine equations, which are given in matrix form in (3.3.3) of Chapter 3 are written here again as,

$$p\begin{bmatrix}\Delta i_{qs}^r \\ \Delta i_{ds}^r \\ \Delta \omega_r \\ \Delta \delta\end{bmatrix} = \begin{bmatrix} \frac{-1}{\sigma\tau_s} & \frac{-\omega_0}{\sigma} & \frac{-1}{\sigma}(\frac{\lambda_m}{L_d} + I_{ds}^r) & \frac{-V_s}{\sigma L_d} sin(\delta_0) \\ \sigma\omega_0 & \frac{-1}{\tau_s} & \sigma I_{qs}^r & \frac{-V_s}{L_d} cos(\delta_0) \\ \frac{3}{2}(\frac{n}{2})^2 \frac{1}{J}[\lambda_m + L_d(1-\sigma)I_{ds}^r] & \frac{3}{2}(\frac{n}{2})^2 \frac{1}{J} L_d(1-\sigma) I_{qs}^r & \frac{-B_m}{J} & 0 \\ 0 & 0 & -1 & 0 \end{bmatrix} \begin{bmatrix}\Delta i_{qs}^r \\ \Delta i_{ds}^r \\ \Delta \omega_r \\ \Delta \delta\end{bmatrix} + \begin{bmatrix} 0 \\ 0 \\ \frac{-n}{2J} \\ 0 \end{bmatrix} \Delta T_l \tag{B.1.1}$$

The first two equations and the last equation in this matrix equation can be written as

$$p(\Delta i_{qs}^r) = A(\Delta i_{qs}^r) + B(\Delta i_{ds}^r) + C(\Delta \omega_r) + D(\Delta \delta) \tag{B.1.2}$$

$$p(\Delta i_{ds}^r) = E(\Delta i_{qs}^r) + F(\Delta i_{ds}^r) + G(\Delta \omega_r) + H(\Delta \delta) \tag{B.1.3}$$

$$p(\Delta \delta) = -\Delta \omega_r \tag{B.1.4}$$

where,

$$A = \frac{-1}{\sigma\tau_s}, \quad B = \frac{-\omega_0}{\sigma}, \quad C = \frac{-1}{\sigma}(\frac{\lambda_m}{L_d} + I^r_{ds}), \quad D = \frac{-V_s}{\sigma L_d} sin(\delta_0) \tag{B.1.5}$$

$$E = \sigma\omega_0, \quad F = \frac{-1}{\tau_s}, \quad G = \sigma I^r_{qs}, \quad H = \frac{-V_s}{L_d} cos(\delta_0) \tag{B.1.6}$$

Substituting $\Delta\omega_r$ from (B.1.4) to the equations (B.1.2) and (B.1.3), and replacing p by s, the relationship between current perturbations and load angle perturbation can be obtained as

$$(s - A)(\Delta i^r_{qs}) = B(\Delta i^r_{ds}) + (D - sC)(\Delta\delta) \tag{B.1.7}$$

$$-E(\Delta i^r_{qs}) = (F - s)(\Delta i^r_{ds}) + (H - sG)(\Delta\delta) \tag{B.1.8}$$

Solving for Δi^r_{ds} and Δi^r_{qs},

$$\Delta i^r_{ds} = \frac{[(A - s)(H - sG) - E(D - sC)]}{(s - A)(F - s) + BE}\Delta\delta \tag{B.1.9}$$

$$\Delta i^r_{qs} = \frac{[(F - s)(D - sC) - B(H - sG)]}{(s - A)(F - s) + BE}\Delta\delta \tag{B.1.10}$$

Linearizing the torque equation (2.5.7) in Chapter 2 one obtains,

$$\Delta T_e = X_1\Delta i^r_{qs} + Y_1\Delta i^r_{ds} \tag{B.1.11}$$

where,

$$X_1 = \frac{3}{2}\frac{n}{2}[\lambda_m + (L_d - L_q)I^r_{ds}] \tag{B.1.12}$$

$$Y_1 = \frac{3}{2}\frac{n}{2}(L_d - L_q)I^r_{qs} \tag{B.1.13}$$

Substituting Δi^r_{ds} and Δi^r_{qs} from (B.1.9) and (B.1.10) to the linearized torque equation (B.1.11), finally, the transfer function for $\frac{\Delta T_e}{\Delta\delta}$ under open-loop V/f control can be obtained as,

$$\frac{\Delta T_e}{\Delta\delta} = X_1\frac{[(F - s)(D - sC) - B(H - sG)]}{(s - A)(F - s) + BE} + Y_1\frac{[(A - s)(H - sG) - E(D - sC)]}{(s - A)(F - s) + BE} \tag{B.1.14}$$

B.2 The derivation of T_{e0} as a function of V_s, ω_0 and δ_0

The steady state voltage equations in the rotor d,q frame can be written as (see (2.7.1) and (2.7.2) of Chapter 2)

$$V^r_{qs} = r_s I^r_{qs} + \omega_0 L_d I^r_{ds} + \omega_0\lambda_m \tag{B.2.1}$$

$$V^r_{ds} = r_s I^r_{ds} - \omega_0 L_q I^r_{qs} \tag{B.2.2}$$

The relationship between the load angle and the voltages from (3.2.3) and (3.2.4) of Chapter 3 is

$$V_s cos(\delta_0) = V_{qs}^r \quad \text{(B.2.3)}$$
$$-V_s sin(\delta_0) = V_{ds}^r \quad \text{(B.2.4)}$$

Substituting those two relationships to the (B.2.1) and (B.2.2) the following two equations are obtained.

$$V_s cos(\delta_0) = r_s I_{qs}^r + \omega_0 L_d I_{ds}^r + \omega_0 \lambda_m \quad \text{(B.2.5)}$$
$$-V_s sin(\delta_0) = r_s I_{ds}^r - \omega_0 L_q I_{qs}^r \quad \text{(B.2.6)}$$

Solving for I_{ds}^r and I_{qs}^r from these two equations,

$$I_{ds}^r = \frac{\omega_0 L_q V_s cos(\delta_0) - r_s V_s sin(\delta_0) - \omega_0^2 L_q \lambda_m}{r_s^2 + \omega_0^2 L_q L_d} \quad \text{(B.2.7)}$$

$$I_{qs}^r = \frac{V_s sin(\delta_0)}{\omega_0 L_q} + \frac{r_s}{\omega_0 L_q}\left(\frac{\omega_0 L_q V_s cos(\delta_0) - r_s V_s sin(\delta_0) - \omega_0^2 L_q \lambda_m}{r_s^2 + \omega_0^2 L_q L_d}\right) \quad \text{(B.2.8)}$$

The steady state torque expression from (2.7.3) of Chapter 2 is,

$$T_{e0} = \frac{3}{2}\frac{n}{2}[\lambda_m + (L_d - L_q) I_{ds}^r] I_{qs}^r \quad \text{(B.2.9)}$$

Substituting the current expressions (B.2.7) and (B.2.8) to the torque expression in (B.2.9) one can obtain the following equation, which expresses the T_{e0} as a function of V_s, ω_0 and δ_0.

$$T_{e0} = \frac{3}{2}\frac{n}{2}[\lambda_m + (L_d - L_q)\left(\frac{\omega_0 L_q V_s cos(\delta_0) - r_s V_s sin(\delta_0) - \omega_0^2 L_q \lambda_m}{r_s^2 + \omega_0^2 L_q L_d}\right)]\left[\frac{V_s sin(\delta_0)}{\omega_0 L_q} + \frac{r_s}{\omega_0 L_q}\left(\frac{\omega_0 L_q V_s cos(\delta_0) - r_s V_s sin(\delta_0) - \omega_0^2 L_q \lambda_m}{r_s^2 + \omega_0^2 L_q L_d}\right)\right] \quad \text{(B.2.10)}$$

B.3 The derivation of the expression for k_e

The above §B.2 obtained the expression (B.2.10) for the torque can be written as

$$T_{e0} = \frac{3}{2}\frac{n}{2}[\lambda_m + (L_d - L_q) I_{ds}^r]\left[\frac{V_s sin(\delta_0)}{\omega_0 L_q} + \frac{r_s}{\omega_0 L_q} I_{ds}^r\right] \quad \text{(B.3.1)}$$

where,

$$I_{ds}^r = \frac{\omega_0 L_q V_s cos(\delta_0) - r_s V_s sin(\delta_0) - \omega_0^2 L_q \lambda_m}{r_s^2 + \omega_0^2 L_q L_d} \quad \text{(B.3.2)}$$

Taking the partial derivative of (B.3.1) respect to δ_0 one can obtain the k_e as,

$$k_e = \frac{\partial T_{e0}}{\partial \delta_0} = \frac{3}{2}\frac{n}{2}[\lambda_m + (L_d - L_q)I^r_{ds}][\frac{V_s cos(\delta_0)}{\omega_0 L_q} + \frac{r_s}{\omega_0 L_q}(\frac{\partial I^r_{ds}}{\partial \delta_0})]+ \frac{3}{2}\frac{n}{2}[(L_d - L_q)(\frac{\partial I^r_{ds}}{\partial \delta_0})][\frac{V_s sin(\delta_0)}{\omega_0 L_q} + \frac{r_s}{\omega_0 L_q} I^r_{ds}] \quad \text{(B.3.3)}$$

where,

$$\frac{\partial I^r_{ds}}{\partial \delta_0} = \frac{-\omega_0 L_q V_s sin(\delta_0) - r_s V_s cos(\delta_0)}{r_s^2 + \omega_0^2 L_q L_d} \quad \text{(B.3.4)}$$

B.4 The elements of the matrix $A_2(X)$

$A_{11} = \frac{-1}{\sigma\tau_s}$, $A_{12} = \frac{-\omega_0}{\sigma}$, $A_{13} = \frac{-1}{\sigma}(\frac{\lambda_m}{L_d} + I^r_{ds})$, $A_{14} = \frac{-V_s sin(\delta_0)}{\sigma L_d}$, $A_{15} = 0$

$A_{21} = \sigma\omega_0$, $A_{22} = \frac{-1}{\tau_s}$, $A_{23} = \sigma I^r_{qs}$, $A_{24} = \frac{-V_s cos(\delta_0)}{L_d}$, $A_{25} = 0$

$A_{31} = \frac{3}{2J}(\frac{n}{2})^2[\lambda_m + L_d(1-\sigma)I^r_{ds}]$, $A_{32} = \frac{3}{2J}(\frac{n}{2})^2 L_d(1-\sigma)I^r_{qs}$, $A_{33} = \frac{-B_m}{J}$,
$A_{34} = A_{35} = 0$

$A_{41} = A_{42} = 0$, $A_{43} = -1$, $A_{44} = 0$, $A_{45} = 1$

$A_{51} = c[\frac{cos(\delta_0)}{\sigma\tau_s} + \omega_0\sigma sin(\delta_0)]$, $A_{52} = c[\frac{\omega_0 cos(\delta_0)}{\sigma} - \frac{sin(\delta_0)}{\tau_s}]$,

$A_{53} = c[(\sigma-1)I^r_{qs}sin(\delta_0) + \frac{1}{\sigma}(\frac{\lambda_m}{L_d} + (1-\sigma)I^r_{ds})cos(\delta_0)]$,

$A_{54} = c[(\omega_0\sigma I^r_{qs} - \frac{1}{\tau_s}I^r_{ds})cos(\delta_0) - \frac{V_s(\sigma-1)sin(2\delta_0)}{\sigma L_d} - (\frac{\omega_0}{\sigma}(\frac{\lambda_m}{L_d} + I^r_{ds}) + \frac{I^r_{qs}}{\sigma\tau_s})sin(\delta_0)]$,

$A_{55} = c[I^r_{qs}sin(\delta_0) + I^r_{ds}cos(\delta_0)] - \frac{1}{\tau_h}$

where, $\sigma = \frac{L_q}{L_d}$, $\tau_s = \frac{L_d}{r_s}$, $c = \frac{3}{2}k_p V_s$.

Appendix C

Generation of PWM

After the voltage vector to the machine is decided from the control section of the V/f controlled drive or the field oriented controlled drive, this voltage vector is applied to the stator of the machine through the inverter. For this purpose, the inverter creates the three-phase stator voltages via Pulse Width Modulation (PWM). There are several approaches to generate inverter control signals to achieve PWM [1]. The space vector modulation (SVM) approach is used in both of the V/f controlled and field oriented controlled drive systems discussed in this thesis. The implementation of this approach in a digital system is very convenient. The space vector modulation approach and inverter nonlinearity compensation are briefly discussed in this Appendix.

C.1 Space vector modulation

The basis for the space vector modulation is, the ability of generating fixed voltage space vectors from a three phase inverter, which is shown in figure C.1. This type of

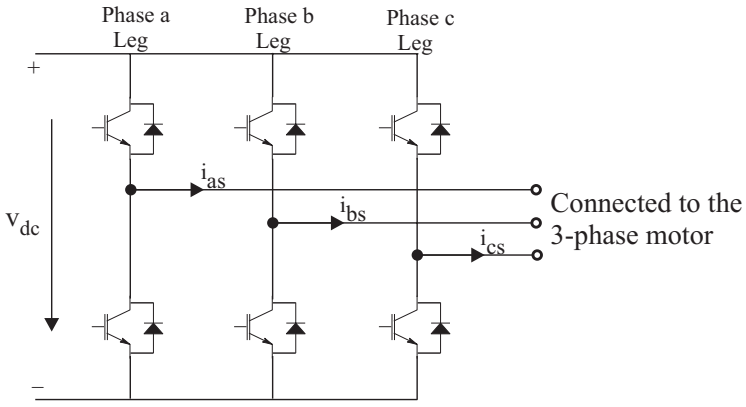

Figure C.1: *Three-phase inverter.*

inverter can produce a total of six non-zero voltage space vectors and two zero voltage vectors [1]. They are correspondent to the 8 switching states of this inverter. These

voltage space vectors correspond to the switching states of the inverter are shown in figure C.2(a) with the notation $\underline{v}_{100}, \underline{v}_{110}, \underline{v}_{010}, \underline{v}_{011}, \underline{v}_{001}, \underline{v}_{101}, \underline{v}_{000}$ and $\underline{v}_{111}$. In this notation of voltage space vectors, the subscript denotes the state of the switches and they are represented by a binary pattern, where 'one' represents the top switch is closed and the bottom switch is opened for a particular leg of the inverter and a 'zero' the opposite. The most left position in the pattern is leg 'a', the middle is leg 'b' and the right position is leg 'c'.

According to the states of the switches, one can decide the polarity and the magnitude of the voltages, which produce in the three phase stator windings of the machine, connected to the inverter. The magnitude of those produced phase voltages on the star connected windings are either $\frac{2v_{dc}}{3}$ or $\frac{v_{dc}}{3}$. With those produced phase voltages and using the definition for the voltage space vector given in (C.1.1) (See (2.3.1) in Chapter 2), one can obtain the eight voltage space vectors correspond to the eight switching states as shown in figure C.2(a). The magnitude of each of these voltage space vectors is $\frac{2v_{dc}}{3}$.

$$\underline{v}_{abcs} = \frac{2}{3}[v_{as} + \underline{a}v_{bs} + \underline{a}^2 v_{cs}] \tag{C.1.1}$$

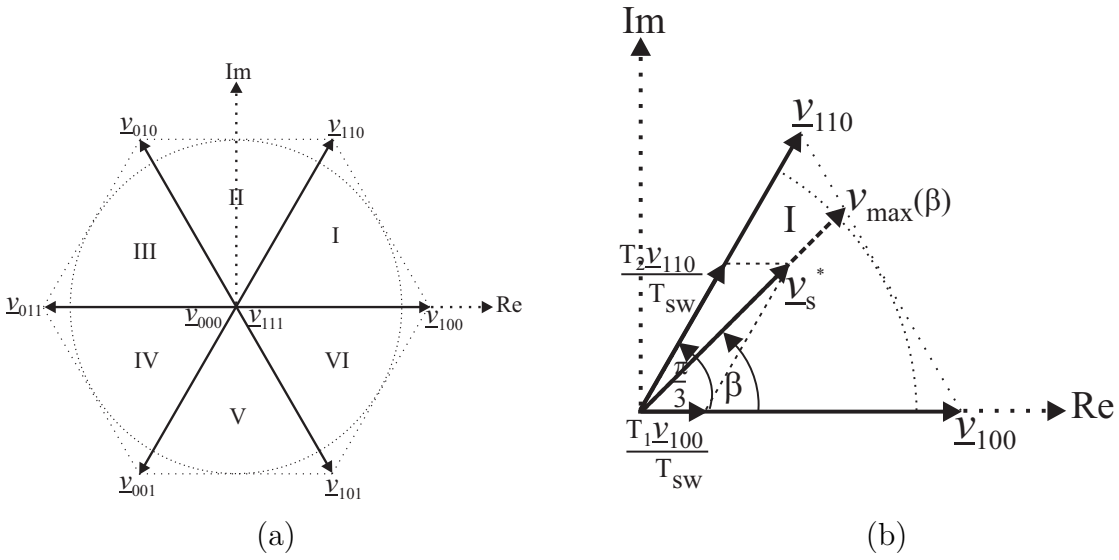

Figure C.2: *(a) Voltage space vectors correspond to the eight switching states of the three-phase inverter. (b) Representation of the commanded voltage vector from two adjacent voltage space vectors.*

In the following, the generation of inverter control signals from SVM is discussed assuming the commanded voltage vector $\underline{v}_s^*$, which is in the stationary reference frame, locates in the first sector of the space vector diagram shown in figure C.2(a).

Since the commanded voltage vector is in the first sector, the adjacent two voltage space vectors are $\underline{v}_{100}$ and $\underline{v}_{110}$. The change in flux over one switching period can be

written as

$$\int_0^{T_{sw}} \underline{v}_s^* dt = \int_0^{T_1} \underline{v}_{100} dt + \int_{T_1}^{T_1+T_2} \underline{v}_{110} dt + \int_{T_1+T_2}^{T_{sw}} \underline{v}_0 dt \tag{C.1.2}$$

where,

T_{sw} - The switching period

T_1 - The time for the $\underline{v}_{100}$ vector

T_2 - The time for the $\underline{v}_{110}$ vector

$\underline{v}_0$ - The zero vector (either $\underline{v}_{000}$ or $\underline{v}_{111}$).

From (C.1.2) the following result can be obtained.

$$\underline{v}_s^* T_{sw} = \underline{v}_{100} T_1 + \underline{v}_{110} T_2 \tag{C.1.3}$$

$$\therefore \underline{v}_s^* = \frac{\underline{v}_{100} T_1}{T_{sw}} + \frac{\underline{v}_{110} T_2}{T_{sw}} \tag{C.1.4}$$

The result in (C.1.4) is illustrated in the vector diagram shown in figure C.2(b).

From (C.1.4) one can obtain the switching times T_1 and T_2 for the adjacent two vectors as

$$T_1 = \frac{\sqrt{3} T_{sw} v_s^*}{v_{dc}} sin(\frac{\pi}{3} - \beta) \tag{C.1.5}$$

$$T_2 = \frac{\sqrt{3} T_{sw} v_s^*}{v_{dc}} sin(\beta) \tag{C.1.6}$$

where β is the angle between $\underline{v}_{100}$ and $\underline{v}_s^*$. During the remaining time in the switching period, the zero vectors should be applied. Therefore, the time for zero vectors (T_0) becomes

$$T_0 = T_{sw} - T_1 - T_2 \tag{C.1.7}$$

The implemented SVM scheme the T_0 is divided into four parts of equal duration and, in the first sector the switching sequence is selected as

$$\begin{aligned} &\underline{v}_{000}\langle T_0/4\rangle \rightarrow \underline{v}_{100}\langle T_1/2\rangle \rightarrow \underline{v}_{110}\langle T_2/2\rangle \rightarrow \underline{v}_{111}\langle T_0/4\rangle \rightarrow \\ &\underline{v}_{111}\langle T_0/4\rangle \rightarrow \underline{v}_{110}\langle T_2/2\rangle \rightarrow \underline{v}_{100}\langle T_1/2\rangle \rightarrow \underline{v}_{000}\langle T_0/4\rangle. \end{aligned} \tag{C.1.8}$$

In (C.1.8), the duration for the associated vector is given in brackets. The switching signals correspond to the sequence given in (C.1.8) are shown in figure C.3. Note that each leg of the inverter is switched twice during one switching period and switching signals are symmetric around $\frac{1}{2}T_{sw}$.

When the commanded voltage vector is in other sectors, the expressions (C.1.5) and (C.1.6) remain valid. Then, β should be the angle between the commanded voltage vector and the first vector applied from the adjacent two vectors.

The implemented drive systems, first, the duty cycles are calculated for the switching signals shown in figure C.3, with the help of (C.1.5), (C.1.6) and (C.1.7). Knowing those duty cycles, a micro-controller generates the switching signals to the inverter.

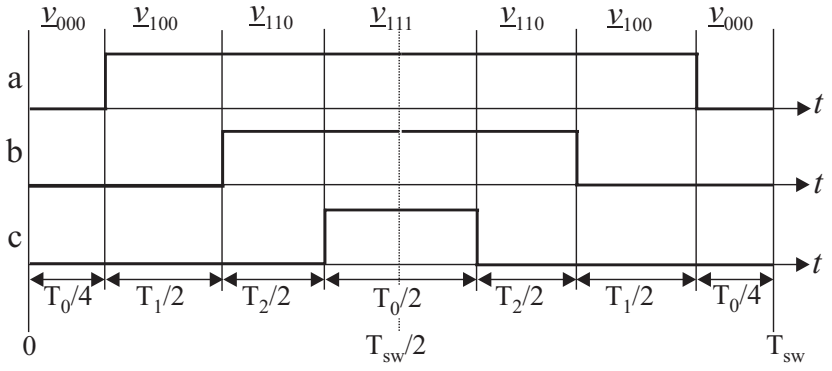

Figure C.3: *Switching signals produced by SVM for the three legs of the three phase inverter. It is assumed that the commanded voltage vector is in first $0^0 - 60^0$ sector.*

C.1.1 Voltage limit

The magnitude of the maximum voltage, which can be obtained from SVM is dependent on the position of the commanded voltage vector and it can be found using the constraint

$$T_1 + T_2 = T_{sw}. \tag{C.1.9}$$

After substituting T_1 and T_2 from (C.1.5) and (C.1.6), the expression (C.1.9) becomes

$$\frac{\sqrt{3}T_{sw}v_{max}(\beta)}{v_{dc}}sin(\frac{\pi}{3} - \beta) + \frac{\sqrt{3}T_{sw}v_{max}(\beta)}{v_{dc}}sin(\beta) = T_{sw} \tag{C.1.10}$$

where, $v_{max}(\beta)$ is the magnitude of the maximum voltage at reference angle β.

From (C.1.10), $v_{max}(\beta)$ can be obtained as

$$v_{max}(\beta) = \frac{v_{dc}}{\sqrt{3}cos(\frac{\pi}{6} - \beta)}, \quad 0 \leq \beta \leq \frac{\pi}{3} \tag{C.1.11}$$

When β varies, the value of $v_{max}(\beta)$ lies on the line, which is connected the tips of the vectors $\underline{v}_{100}$ and $\underline{v}_{110}$ (see figure C.2(b)). If it is considered the other sectors also, this means that $v_{max}(\beta)$ constitutes the hexagon shown in figure C.2(a).

One can limit the voltage vector to the hexagon. However, this results in different maximum voltages depending on the angle of the commanded voltage vector, increasing the calculation time. Alternatively, one can also limit the voltage vector to the largest circle that fits in the hexagon (This circle is shown in figure C.2(a)). The advantage of this circular limit is that the magnitude of the voltage vector is limited to a constant length regardless of the position of the voltage vector, reducing the calculation time required. With this circular limit, the maximum voltage (v_{max}) becomes the radius of the circle and

$$v_{max} = \frac{v_{dc}}{\sqrt{3}}. \tag{C.1.12}$$

This circular limit is used in the implemented drive systems.

C.2 Inverter nonlinearity compensation

There are three nonlinearities in PWM voltage source inverters [2]. They are

- DC-link voltage ripple
- Dead-time
- Components voltage drop (Diodes and transistors voltage drop in the inverter).

The compensation methods of these nonlinerities are discussed in detail in [2]. The same methods are used to implement and they are discussed briefly in subsequent sections.

C.2.1 DC-link voltage ripple

Due to the behaviour of diode rectifier the ripples appear in the DC-link voltage, i.e. the DC-link voltage is not a constant value. When generating PWM, if it is assumed the DC-link voltage is constant in (C.1.5) and (C.1.6), it will cause undesirable variations in stator voltages. In order to overcome this problem, the DC-link voltage is measured instantaneously, and this measured DC-link voltage is used in (C.1.5) and (C.1.6) during PWM generation.

C.2.2 Dead-time

In order to avoid short-circuit in the DC-link, it should always be considered a short period of delay between one transistor is turned-off and the other is turned-on in each leg of the inverter. This short period of delay is referred to as dead-time. Due to the dead-time, there is a difference between the actual output voltage and the commanded voltage to a phase. The influence to the output voltage is dependent on the direction of phase current. Assuming the switching of the power semiconductor devices is ideal (i.e. no delays), the magnitude of the average voltage error in one switching period due to the dead-time is given by [2]

$$\Delta v = \frac{t_d}{T_{sw}} v_{dc} \tag{C.2.1}$$

where Δv is the average voltage error in one switching period and t_d is the dead-time.

The commanded voltage to a phase can be corrected to compensate the dead-time effect by knowing the sign of the current and using the relationship

$$v^*_{as(c)} = v^*_{as} + sign(i_{as}) t_d f_{sw} v_{dc} \tag{C.2.2}$$

where $v^*_{as(c)}$ is the corrected voltage for phase a, v^*_{as} is the commanded voltage for phase a and f_{sw} is the switching frequency. Equation (C.2.2) can be written in duty cycles for the upper transistor of a-phase leg as

$$D^*_{a(c)} = D^*_a + sign(i_{as}) t_d f_{sw} \tag{C.2.3}$$

where $D^*_{a(c)}$ is corrected duty cycle and D^*_a is commanded duty cycle, i.e. calculated duty cycle from SVM. For the other two phases same relationships are applied (Only changing a to b and c).

When implementing, the duty cycles calculated from SVM for the three legs of the inverter are corrected using the relationship in (C.2.3), in order to compensate the dead-time effects to the output voltage.

C.2.3 Components voltage drop

The voltage drop across the power semiconductor devices of the inverter causes to deviate the actual output voltage from the commanded voltage. The effect to the output voltage from voltage drops of the power semiconductor devices is dependent on the magnitude and the direction of the phase current [2].

Considering a-phase leg, the transistor and the diode voltage drop can be expressed as

$$v_T = R_T|i_{as}| + v_{T,0} \tag{C.2.4}$$

$$v_D = R_D|i_{as}| + v_{D,0} \tag{C.2.5}$$

where,

- v_T - Transistor voltage drop
- v_D - Diode voltage drop
- R_T - Dynamical resistance of transistor
- R_D - Dynamical resistance of diode
- $v_{T,0}$ - Voltage drop at zero current in transistor
- $v_{D,0}$ - Voltage drop at zero current in diode.

According to the analysis in [2], the commanded voltage can be corrected to compensate the transistor and the diode voltage drop, knowing the direction of the current and using the relationships

$$v^*_{as(c)} = v^*_{as} - v_T - (v_D - v_T)D^*_a, \quad \text{for} \quad i_{as} < 0 \tag{C.2.6}$$

$$v^*_{as(c)} = v^*_{as} + v_D + (v_T - v_D)D^*_a, \quad \text{for} \quad i_{as} > 0 \tag{C.2.7}$$

Expressions (C.2.6) and (C.2.7) can be written in duty cycles as

$$D^*_{a(c)} = D^*_a - \frac{[v_T + (v_D - v_T)D^*_a]}{v_{dc}}, \quad \text{for} \quad i_{as} < 0 \tag{C.2.8}$$

$$D^*_{a(c)} = D^*_a + \frac{[v_D + (v_T - v_D)D^*_a]}{v_{dc}}, \quad \text{for} \quad i_{as} > 0 \tag{C.2.9}$$

Same relationships can be obtained for the other phases. When implementing, the duty cycles calculated from SVM for the three legs of the inverter are corrected using the relationships in (C.2.8) and (C.2.9), in order to compensate the effects from transistor and diode voltage drops to the output voltage. The transistor and diode parameter values used in (C.2.4) and (C.2.5) are, $R_T = 80$ mΩ, $R_D = 80$ mΩ, $v_{T,0} = 1.6$ V and $v_{D,0} = 0.8$ V. These values are obtained from the data sheets provided by the inverter IGBT module manufacturer.

Bibliography

[1] J. Holtz, *Pulse Width Modulation for Electronic Power Conversion*, Chapter 4 in Power Electronics and Variable Frequency Drives. Technology and Applications, B. K. Bose, Ed., pp. 138-208, IEEE Press, 1997.

[2] Frede Blaabjerg, John K. Pedersen and Paul Thøgersen, *Improved Modulation Techniques for PWM-VSI Drives*, IEEE Transactions on Industrial Electronics, Vol. 44, No. 1, pp. 87-95, February 1997.

Appendix D

The Laboratory Test System

The laboratory test system, which is used for experiments in this project, is described in this Appendix. The overview of the laboratory test system is shown in figure D.1. It consists of a converter, a digital control system, sensors to obtain various signals, a load control system and an IPMSM. The IPMSM is the test machine used throughout the project and details of this machine can be found in Appendix A. More details of other parts of the laboratory test system are given in subsequent sections.

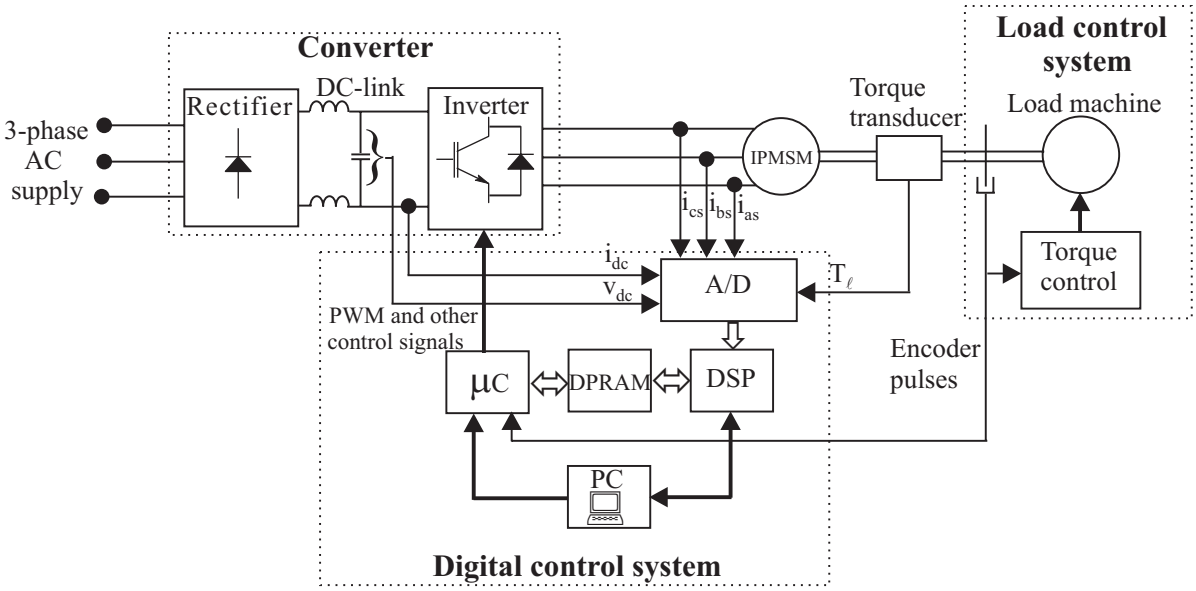

Figure D.1: *Overview of the laboratory test system.*

D.1 Converter

The power electronic converter configuration used in the laboratory test system is shown in figure D.2. This converter is, a modified version of Danfoss VLT 3004 frequency converter. The control board was removed from original VLT 3004 and the

gate pulses and other control signals were supplied from the external digital control system through fiber-optic interface as shown in figure D.2. It should be mentioned that remaining control electronics, snubber circuits and power supplies in the converter are not shown in figure D.2.

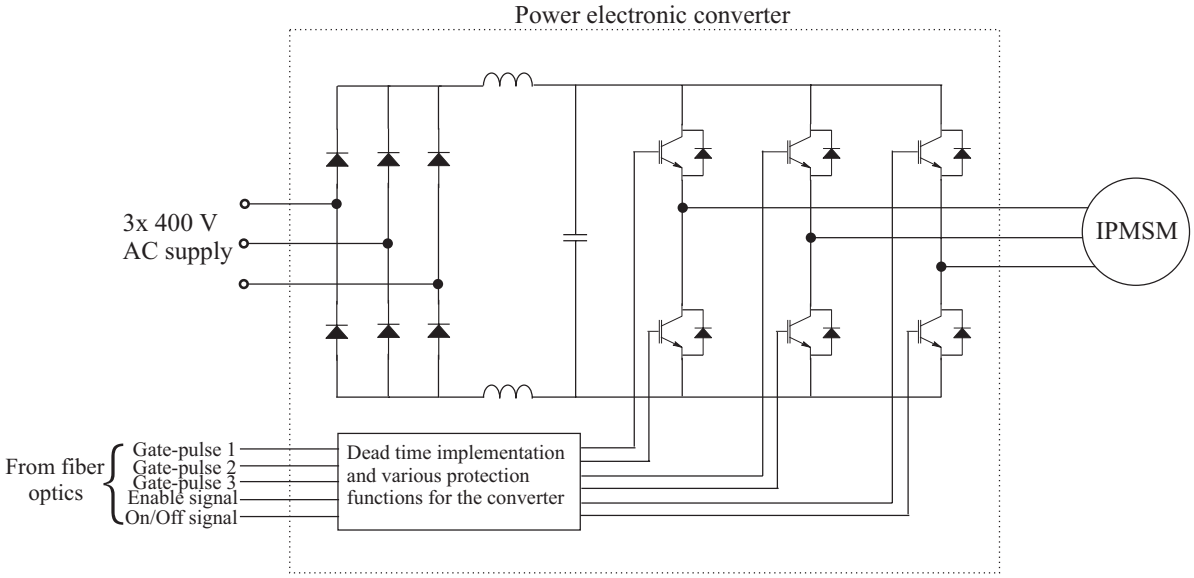

Figure D.2: *Power electronic converter configuration used to control the test machine in the laboratory test system.*

As shown in figure D.2 the supplied signals to the converter include 3 gate-pulses (one for each leg of the IGBT inverter), enable signal (a square-wave signal with a frequency of 1-5 kHz, which is required for control electronics of the converter) and converter on/off signal. Each gate-pulse is split into two signals in the converter (one for upper IGBT and the other for lower IGBT of each leg) incorporating dead time. The value of the dead time is 2 μs.

The protection functions, which include in the VLT 3004 is also used in the converter. They are, protection against short-circuit and over-load currents, and thermal protection of power modules. The DC-link voltage is also measured in VLT 3004 and the converter trips, if DC-link voltage is not within the required range. This function is also used in the laboratory test system converter.

D.2 Digital control system

The digital control system handles all the calculations in the control algorithm with the knowledge of various measured signals from other parts of the system, and generates gate pulses and other control signals for the converter. The block diagram in figure D.3 outlines the digital control system.

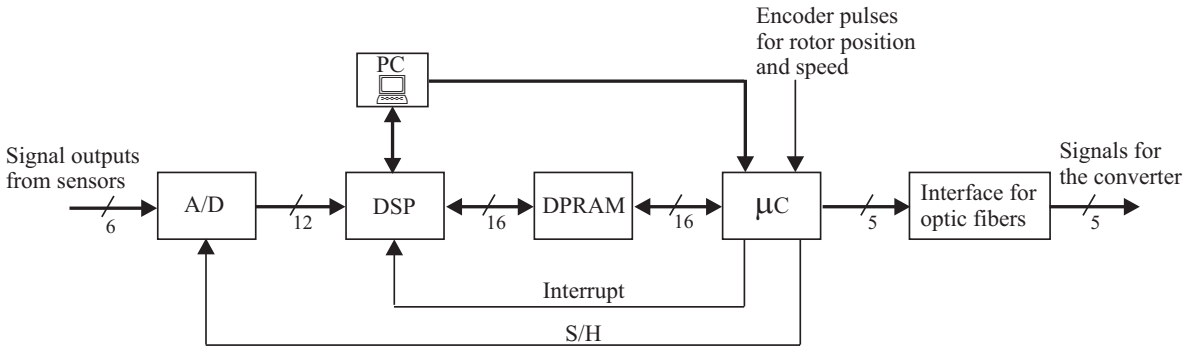

Figure D.3: *Block diagram of the digital control system.*

The measured variables for the A/D converter are, motor phase currents, DC-link current, DC-link voltage and torque on the rotor shaft (see figure D.1). The LEM modules are used to measure the phase currents and DC-link current, and an isolation amplifier (Hewlett-Packard HCPL-7800) is used for the DC-link voltage. The torque on the rotor shaft is measured using Staiger Mohilo (Model no. 0130/03AE-01-F-A) torque transducer.

The A/D converter (Analog Devices AD7891) has 8 channels giving facilities to measure up to 8 analogue signals, even though only 6 signals are used in this project. All channels are sampled and held simultaneously by two four-channel sample-hold circuits (Analog Devices AD684), when a signal is given from the micro-controller (μc). This signal is shown as S/H in figure D.3. The resolution of the A/D converter is 12 bit, and the conversion time is 1.6 μs per channel. The digitized values from the A/D converter are read by the digital signal processor (DSP) when it receives the interrupt signal.

The DSP (Analog Devices SHARC ADSP-21062, 33 MHz clock frequency), which performs floating point calculations with 32/40 bit resolution, is installed in EZ-LAB Development System evaluation board designed by BittWare Research Systems. This board is physically installed in the PC, and the PC can communicate with the DSP. All control algorithms are programmed using C programming language and they are compiled using C-compiler, which includes in the DSP software tools. The compiled programmes are downloaded to the DSP, whenever the control algorithms are needed to execute in real time. If it is required, variables in control algorithms can be saved in the DSP memory and they can be transferred to the hard disk of the PC so that they can be viewed off-line.

At the beginning of each PWM switching period, the micro-controller generates the interrupt signal to the DSP. With this interrupt signal, the DSP executes the calculations in the control algorithm. Finally, the DSP outputs the calculated duty-cycles for the three gate pulses and the on/off status of the converter. They are written

to the dual-port ram (DPRAM) in 16-bit format. The micro-controller reads these values and generates the gate pulses and on/off signal for the converter in the beginning of next PWM switching period.

In addition to the three gate pulses and on/off signal, the micro-controller also generates the DSP interrupt signal and A/D converter S/H signal in the beginning of each PWM switching period. The S/H signal is also used as the enable signal to the converter.

Since the DSP interrupt signal and A/D converter S/H signal are generated in the beginning of each PWM switching period, the sampling period of the digital control system is essentially the same as the PWM switching period. It should also be noted that, since the gate pulses are generated in the beginning of next sampling period after the calculations, there is one sampling period delay between the analog values are sampled and the voltage is applied to the machine.

The micro-controller is from Siemens, SAB 80C167, with 20 MHz clock frequency. It performs calculations in 16-bit fixed-point format. It has PWM channels, which are dedicated for generating gate pulses for a converter. When duty cycles are known those PWM channels can be used to generate gate pulses. The programme for the micro-controller is also written in C programming language. The micro-controller communicates with the PC via a serial port.

As it is shown in figure D.3, the micro-controller also counts pulses, which are generated by an encoder according to the revolution of the rotor shaft. The counted value of the pulses during one sampling period are written to the DPRAM and it is read by the DSP. The resolution of the counted pulses is: 8192 pulses/rev.

The micro-controller generated 5 signals for the converter (i.e. 3 gate pulses, enable signal, on/off signal) are send via fiber-optic cables to the converter. This fiber-optic cable link provides electrical isolation between digital control system and the converter.

More description about different components used in the digital control system can be found in manuals published by the manufactures. For EZ-LAB Development System evaluation board, more details can be found in [1]. Detailed descriptions for the DSP and the micro-controller are documented in [2] and [3] respectively.

D.3 Load control system

Figure D.4 outlines the load control system in the laboratory test setup. This load control system was built using Siemens SIMOVERT MASTERDRIVES converters.

The rectifier/regenerative unit provides facility to power flow from grid to the DC-link and regenerative power flow from DC-link to the grid. Two independent thyristor bridges in this unit provide this facility. This rectifier/regenerative unit is connected to the IGBT inverter via the DC-link. The load machine is a SPMSM. It is also from Siemens and the type is ROTEC 1FT6. This machine is fitted with an encoder in

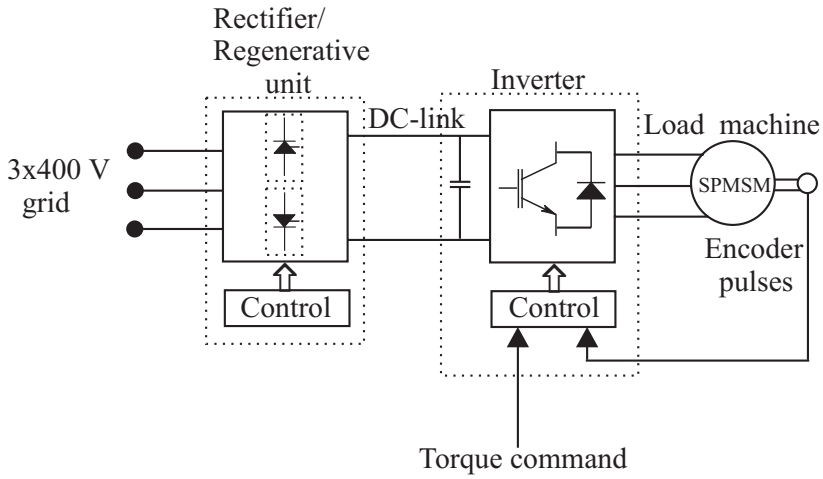

Figure D.4: *Block diagram illustrating sections of the load control system.*

order to provide position and velocity information of the rotor. The rated speed and the rated torque of this machine are 3000 rpm and 14.7 Nm respectively.

Control of the rectifier/regenerative unit and the inverter is provided by Siemens. In addition, those units are provided with software so that the user can programme them via parameters in order to adapt to a specific application. Key-pads with displays are also included so that the user can programme them easily. The torque command, which is needed to control the torque of the load machine, can be given to the inverter from the key-pad or using an analog voltage signal (0-10 V).

Detailed description of the rectifier/regenerative unit and the inverter used in the load control system can be found in [4] and [5] respectively. More details about load machine can be found in [6].

Bibliography

[1] BittWare Research Systems, *EZ-LAB Development System Manual*, BittWare Research Systems, Inc., Hardware Rev. 3, April, 1996.

[2] Analog Devices, *ADSP-2106x SHARC User's Manual*, Analog Devices, Inc., Second Edition, May, 1997.

[3] Siemens, *C167 Derivatives User's Manual*, Siemens AG, Edition 03.96, Version 2.0, 1996.

[4] Siemens, *SIMOVERT MASTERDRIVES, Rectifier/Regenerating Unit (Sizes C to K), Operating Instructions*, Siemens AG, Edition H, 1994.

[5] Siemens, *SIMOVERT MASTERDRIVES, Frequency Inverter (DC-AC) Compact Type, Operating Instructions*, Siemens AG, Edition AB, 1997.

[6] Siemens, *ROTEC, Low-Voltage Motors for Variable-Speed Drives*, Siemens AG, Advance Catalog DA 65.3, 1997.